Gas retention and release from nuclear legacy waste

Michael Charles Johnson

School of Chemical and Process Engineering

University of Leeds

Submitted in accordance with the requirements for

the integrated degree of Doctor of Philosophy

and Master of Science

2nd May, 2018

Intellectual Property and Publication Declaration

I, the candidate, confirm that the work submitted is my own, except where work which has formed part of jointly authored publications has been included. Details of five jointly authored journal and conference proceedings publications are provided and the contributions of myself and the other authors to these works has been explicitly indicated below. Appropriate credit has been given within the thesis where reference has been made to the work of others.

Jointly authored journal publications

1. Johnson, M., Peakall, J., Fairweather, M., Biggs, S., Harbottle, D. & Hunter, T.N. (2016). Characterization of multiple hindered settling regimes in aggregated mineral suspensions. *Ind. Eng. Chem. Res.* **55** 9983–9993

2. Johnson, M., Fairweather, M., Harbottle, D., Hunter, T.N., Peakall, J. & Biggs, S. (2017). Yield stress dependency on the evolution of bubble populations generated in consolidated soft sediments. *AIChE J.* **63** 3728–3742

3. Johnson, M., Peakall, J., Fairweather, M., Biggs, S., Jia, X., Harbottle, D. & Hunter, T.N. (2017). Enhanced gas migration through permeable bubble networks within consolidated soft sediments. *AIChE J.* [under review]

Jointly authored conference proceedings publications

4. Johnson, M., Peakall, J., Fairweather, M., Biggs, S., Harbottle, D. & Hunter, T.N. (2016) Gas retention and release from nuclear legacy waste. In *Proceedings of Waste Management*. March 2016. Phoenix, USA

5. Johnson, M., Peakall, J., Fairweather, M., Biggs, S., Harbottle, D. & Hunter, T.N. (2016) An x-ray tomography study of gas retention in nuclear legacy waste. In *Proceedings of Chemeca*. September 2016. Adelaide, Australia

Within this thesis, chapter 3 contains particle size and shape analysis also presented in paper 1, shear yield stress data presented in paper 2 and Langmuir-Blodgett experiments presented in paper 5. Chapter 4 contains x-ray tomography data which was first presented in paper 4 at Waste Management 2016 and is used extensively throughout paper 2. Chapter 5 forms the basis of paper 3 which has recently been submitted for review.

The contribution of co-authors to these publications has been advisory, consistent with their role as academic supervisors of this PhD. I, the candidate, confirm that the experimental data acquisition, analysis and written work within this thesis has been my own and that any contributions from colleagues are explicitly referenced in the text.

Signed

Michael Johnson

2nd May, 2018

Acknowledgements

I owe enormous gratitude to my primary supervisor Dr Timothy Hunter for his time, expertise and encouragement throughout this project. I have been lucky to benefit from exceptional academic support throughout this research at the University of Leeds also from Dr David Harbottle and Professors Mike Fairweather and Jeff Peakall, with whom I hope to continue collaborating for many years. Thanks are also due to Prof. Simon Biggs who first introduced me to this topic and has retained a keen interest ever since his departure to the University of Queensland, his enthusiasm for the project has been greatly appreciated. The advice of Dr Xiaodong Jia has been a great help for the image processing, Lattice Boltzman and Monte Carlo modelling components of this research. Martin Barnes and Prof. Geoff Randall have been invaluable as industrial supervisors, providing technical context and facilitating access to research equipment whenever I have called upon them, while also endeavouring to support me with professional development opportunities beyond this PhD research. Special thanks are also reserved for Prof. Peter Heggs who has been a mentor since my Masters research project and to whom I owe this research opportunity.

Many thanks go to the Nuclear Decommissioning Authority (NDA), Sellafield Ltd. and the Engineering and Physical Sciences Research Council (EPSRC) for funding this work through an industrial case award (Grant EP/K504440). This work is also affiliated with the Decommissioning, Immobilisation and Storage Solutions for Nuclear Waste Inventories (DISTINCTIVE) consortium (Grant EP/L014041/1).

A number of technical support staff have been invaluable in helping to collect the large tomographic datasets at the heart of this research. Thank you to Samuel Allshorn and Carlos Grattoni of the University of Leeds Wolfson Laboratory for their assistance in computed tomography, nuclear magnetic resonance and mercury intrusion porosimetry, and Tony Windross for manufacturing the experimental rigs used throughout this study. Thank you to Dr Karine Mardon at the University of Queensland's Centre for Advanced Imaging for allowing me access to her tomography facilities in Brisbane. Thank you to Dr Adam

Qaisar of the National Nuclear Laboratory for his assistance collecting the microtography data and Stuart Micklethwaite at the Leeds Electron Microscopy and Spectroscopy Centre for his assistance with cryo-FIB microscopy.

On a personal level, thank you to all the family and friends who have supported me and kept me company through this PhD. I'm enormously grateful to my parents Jean and Richard, particularly for hosting me during the final stages of my write up, and to my younger sister Catherine for her encouragement. Finally, thank you to Robbie, Tom, James, Calum, Jess, Gerard and all the people who have made the last 4 years in Leeds such a pleasure.

Abstract

Many consolidated sediments experience *in situ* gas generation from methanogenesis, corrosion or radiolysis reactions, while the strength of the sediment matrix can immobilise bubbles for long periods. Particular research interest is motivated by the need to mitigate against periodic acute release of flammable hydrogen from nuclear legacy waste sludge at Sellafield, UK and Hanford, USA to ensure safe decommissioning of ageing facilities. Gas retention within nuclear legacy waste silos is mimicked at laboratory scale by decomposing hydrogen peroxide within $Mg(OH)_2$ sediments, using clinical x-ray computed tomography to capture the bubbles' size, shape and mobility. Tomography revealed that modest yield stresses of 7 Pa were sufficient for sediments to inhibit buoyant migration of relatively large 6-9 mm diameter bubbles during 8 h of imaging, causing the bed to swell to significant voidages in the order of 30 %. Sediments up to 800 Pa yield stress exhibited sufficient gas holdup to reduce the bulk sediment density to below that of an aqueous supernatant, raising the potential for acute gas release through Rayleigh-Taylor instabilities. In the absence of buoyant migration or deep drainage channels, chronic gas release from low-intermediate strength (7-1112 Pa) sediments appears to be governed by diffusion along extensive networks of partially coalesced submillimetre *microvoids*, observed here for the first time. Lattice Boltzmann and Monte Carlo simulations reveal these networks to be highly gas-pervious, with permeabilities in the $10.1\text{-}151.6 \times 10^{-12}\,m^2$ range and effective hydrogen diffusivities of $3.7\text{-}12.5 \times 10^{-5}\,m^2\,s^{-1}$. Bubbles within kiloPascal strength sediments were observed to grow by the induction of high aspect ratio lateral fractures, promoting low-tortuosity pathways for efficient gas migration and reduced holdup. Conversely, a 30 Pa sediment with an additional coarse (100−800 µm) particle fraction and constricted pore throats supported large 1-8 mm bubbles of high sphericity, forming short range *ganglia* of < 42 bubbles which spanned < 25 mm in range, thereby truncating the avenues for chronic hydrogen release.

Contents

List of Figures xvii

List of Tables xviii

Nomenclature xxiii

1 Introduction 1

2 Literature review 5

2.1 Nuclear legacy waste in the UK . . . 5

2.1.1 First generation Magnox storage pond (FGMSP) . . . 5

2.1.2 Magnox swarf storage silos (MSSS) . . . 6

2.1.3 CMS characterisation . . . 7

2.2 Nuclear legacy waste in the USA . . . 9

2.3 Evidence of gas retention and periodic release from nuclear legacy waste . . . 10

2.3.1 Ignition of temporary $H_2 - O_2 - N_2$ atmospheres . . . 12

2.3.2 Alternative hydrogen hazards . . . 13

2.4 Sources of gas generation in consolidated soft sediments . . . 13

2.4.1 Magnox corrosion . . . 14

2.4.2 Radiolysis of water . . . 16

2.4.3 Observed gas generation rates . . . 17

2.5 Clarification on nomenclature for consolidated sediments and sedimentary bubbles . . . 18

2.6 Bubbles observed within consolidated soft sediments . . . 19

2.7 Mechanisms of bubble growth and retention in consolidated soft sediments . . . 22

Capillary invasion . . . 23

Cavity expansion . . . 24

Tensile fracture . . . 25

2.7.1 The mathematics of deformation at the boundary of a spherical bubble (cavity expansion) . . . 25

2.7.2 The mathematics of crack propagation under linear elastic fracture mechanics (LEFM) . . . 28
2.8 Mechanisms of gas release . . . 31
2.8.1 Chronic release mechanisms . . . 31
Aqueous diffusion . . . 31
Buoyant bubble ebullition . . . 31
Bubble rise by viscoelastic fracture . . . 34
Channel formation . . . 35
2.8.2 Acute release mechanisms . . . 36
Bubble cascades . . . 36
Rollover events . . . 37
2.9 Conclusions . . . 38

3 Characterisation of Magnox legacy waste test materials 41
3.1 Introduction . . . 41
3.2 Materials and methods . . . 42
3.2.1 Materials . . . 42
3.2.2 Particle characterisation techniques . . . 43
Zeta potential and pH characterisation . . . 43
Particle sizing . . . 43
Particle imaging techniques . . . 44
X-ray microtomography (μCT) . . . 44
Energy dispersive x-ray spectroscopy (EDX) . . . 44
X-ray diffraction (XRD) . . . 45
3.2.3 Soft sediment mechanical and rheological behaviour . . . 45
3.2.4 Characterisation of the three phase interface . . . 46
Langmuir-Blodgett experiments . . . 46
Bikerman foam tests . . . 47
3.3 Results and discussion . . . 49
3.3.1 Particle size, structure and composition . . . 49
3.3.2 Mechanical deformation behaviour of magnesium hydroxide soft sediments . . . 55
3.3.3 Behaviour at the three phase interface . . . 62
3.4 Conclusions . . . 65

4 The evolution of bubble populations retained by magnesium hydroxide soft sediments experiencing *in situ* gas generation 67
4.1 Introduction . . . 67
4.2 Materials and methods . . . 68
4.2.1 Laboratory scale gas retention tests . . . 68
4.2.2 X-ray computed tomography . . . 70

X-ray CT image analysis . . . 72
4.3 Results . . . 73
4.3.1 Laboratory scale gas retention tests . . . 73
Acute gas releases in the presence of a supernatant . . . 76
4.3.2 X-ray computed tomography . . . 81
Evolution in the bubble size and shape . . . 81
Bubble mobility, residence times and release . . . 88
Gas release during heterogeneous gas generation . . . 92
4.4 Conclusions . . . 94

5 Enhanced gas migration through permeable bubble networks within consolidated soft sediments 97
5.1 Introduction . . . 97
5.2 Materials and methods . . . 98
5.2.1 Soft sediment microstructure characterisation . . . 99
5.2.2 Imaging *in situ* bubbles within soft sediments with high resolution x-ray computed tomography (CT) . . . 101
X-ray CT post processing . . . 102
Characterising partially coalesced or networked bubbles . . . 102
5.2.3 Simulating gas transport through permeable bubble networks 102
Lattice Boltzmann Method (LBM) . . . 103
Monte Carlo gas diffusion . . . 105
5.3 Results and discussion . . . 107
5.3.1 Soft sediment microstructure . . . 107
5.3.2 X-ray computed tomography . . . 111
5.3.3 Characterising the permeability of bubble networks with LBM 116
5.3.4 Characterising effective diffusivity through permeable bubble networks with Monte Carlo simulations . . . 118
5.4 Conclusions . . . 125

6 Gas retention and release from corroded magnesium sludge 126
6.1 Introduction . . . 126
6.2 Materials and methods . . . 127
6.2.1 Microstructure characterisation . . . 127
6.2.2 Laboratory scale gas retention tests . . . 127
6.2.3 X-ray computed tomography . . . 128
6.3 Results and discussion . . . 129
6.3.1 CMgS microstructure . . . 129
6.3.2 Bubble populations within CMgS observed using high resolution clinical x-ray CT . . . 132
6.3.3 Laboratory scale gas retention tests . . . 137

6.3.4 Large scale x-ray computed tomography 140
Bubble mobility 145
6.4 Conclusions 148

7 Conclusions **150**

8 Future work **153**

References **156**

List of Figures

2.1 The two principal Magnox-era legacy buildings at Sellafield: (a) the first generation Magnox storage pond (FGMSP, Hastings *et al.* (2007)) and (b) the Magnox swarf storage silos (MSSS, Forepoint Ltd. (2016)) 6

2.2 Images from the life-cycle of CMS including (a) partially corroded Magnox cladding, (b) highly consolidated CMS (both Hastings *et al.* (2007)) and environmental scanning electron micrographs (ESEM) of aggregates from corroded, unirradiated Magnox(Gregson *et al.*, 2011) at (c) 3750 and (d) 21000 times magnification 8

2.3 Evidence of gas retention and periodic gas releases from underground waste storage tanks at Hanford, USA, including (a) evolution in waste level over a 7 yr period (Allemann, 1992), (b) changes in waste level with ambient pressure (Kam *et al.*, 2001b), (c) periodic spikes in hydrogen concentration within a tank ullage over a 2 yr period (Whitney *et al.*, 1996) and (d) evolution in waste temperature profile coinciding with spikes in hydrogen concentration (Allemann, 1992) . 11

2.4 (a) Image demonstrating propagation of a black corrosion filament and hydrogen evolution from a Magnox substrate (Burrows *et al.*, 2005) and (b) hydrogen evolution rates during magnesium alloy corrosion at solution pH of (i) 2, (ii) 4, (iii) 7, (iv) 10, (v) 12 and (vi) 13 (Williams *et al.*, 2013) 15

2.5 Evolution in the molecular yield of radiolysis products for water exposed to 1 h of 25 rad s^{-1} γ-radiation (Pastina & Laverne, 2001) . 16

2.6 Examples of bubbles observed within various consolidated soft sediments using x-ray CT including (a) a cornflake or penny shaped crack within mud from Cole Harbour, Nova Scotia, Canada (Best *et al.*, 2006; Boudreau *et al.*, 2005), (b) spherical and oblate spheroid bubbles within layered carbonate sand (A) and clay (B) layers respectively (Boudreau *et al.*, 2005), and bubbles within (c) 38 and (d) 680 Pa yield stress kaolin (Gauglitz *et al.*, 2012) 21

2.7 Schematics of bubble growth by (a) capillary invasion and (b) elastic cavity expansion(Kam *et al.*, 2001b) 23
2.8 Schematics of (a) a large spherical bubble within a soft sediment consistent with growth by cavity expansion (Terrones & Gauglitz, 2003) and (b) a unit cell for an elastic-perfectly plastic cavity expansion model, treating the sediment (solids and pore water) as a continuum (adapted from Wheeler *et al.* (1989)) 26
2.9 Schematic (a) of a crack of length $2a$ within an infinite plate under an imposed tensile stress normal to the crack of magnitude σ, demonstrating the coordinates, r and θ, used to describe the local stress field and (b) deviation of the assumed stress field within the plastic region close to the crack tip (Broek, 1982); here σ_{ys} denotes the yield stress rather than τ and r_p represents the size of the plastic deformation region 28
2.10 Correlation between gas flux from marine soft sediments by bubble ebullition (bars) and wind velocity (lines) (Keller & Stallard, 1994) 34
2.11 Schematic demonstrating a cascade of bubbles liberated by the motion of a local buoyant bubble (Gauglitz *et al.*, 2015) 36

3.1 Image of the 80 cm^2 Langmuir-Blodgett trough used to prepare and compress $Mg(OH)_2$ monolayers while monitoring changes in surface pressure 47
3.2 Schematic of a Bikerman column with an in-line rotameter for dynamic foam height analysis, modified from Fryer *et al.* (2011) 48
3.3 Laser scattering particle size distributions for commercial $Mg(OH)_2$ (Versamag) and corroded magnesium sludge (CMgS) test materials acquired using a Malvern Mastersizer 2000 49
3.4 Images of $Mg(OH)_2$ acquired (with decreasing magnification from left to right) using (a) scanning electron microscopy (SEM), (b) Sysmex flow particle image analysis (FPIA) and (c) particle vision and measurement (PVM) 50
3.5 Three dimensional x-ray micro-tomography reconstructions of (a, b) dried $Mg(OH)_2$ soft sediments and (c, d) dired CMgS. The opacity of the bulk material has been minimised in (b) and (d) to observe high radiodensity heterogeneities within each test material. 51

3.6 Four scanning electron micrographs of the bulk phase of (a) Versamag and (b) CMgS, (c) a large crystal impurity within the CMgS and (d) a very large, dense millimetre scale particle within CMgS; the black box regions were analysed for their atomic composition using energy-dispersive x-ray specroscopy (EDX), presented in Figure 3.7 and table 3.1 53
3.7 Four EDX spectra corresponding to the micrographs in Figure 3.6 indicating the elements which best account for each EDX peak . . . 53
3.8 X-ray diffraction (XRD) patterns for commercial $Mg(OH)_2$ (Versamag) and corroded magnesium sludge (CMgS) [XRD measurements undertaken with Wei Ding and Johannes Botha, University of Leeds] 55
3.9 Example torque-time profile from the 0.5 rpm rotation of a four blade vane within % w/w $Mg(OH)_2$ soft sediment demonstrating the maximum torque and maximum torque gradient 56
3.10 Stress controlled flow curves passing through an observed yield stress for (a) Versamag $Mg(OH)_2$ soft sediments and (b) CMgS 57
3.11 Comparative yield stress determination from (1) the imposed stress immediately prior to a decrease in viscosity by several orders of magnitude or (2) extrapolation to the point of near-zero strain rate 57
3.12 Commercial $Mg(OH)_2$ (Versamag) and CMgS soft sediment shear yield stresses within the 28-52 % w/w concentration range, acquired using a Brookfield DV-II Pro viscometer and Bohlin Gemini rheometer shown on (a) linear and (b) semilog axes in order to highlight the disparity between the test materials in the low concentration regime. The Brookfield yield stress data was acquired using two vanes (72 and 73) of 10.8 and 6.3 mm diameter respectively, with the smaller vane employed for sediment concentrations above 40 % w/w 58
3.13 Creep profiles at a series of constant stress conditions for (a) 36.0 % w/w $Mg(OH)_2$ soft sediment and (b) 38.9 % w/w CMgS 60
3.14 The shear modulus of magnesium hydroxide soft sediments obtained using the vane method 62
3.15 Three Langmuir-Blodgett isotherms observed during compression (solid) and expansion (dashed) of a $Mg(OH)_2$ monolayer at an air-water interface 63
3.16 Image from a dynamic foam test within a Bikerman column taken while bubbling air through a 2 % v/v $Mg(OH)_2$ suspensions at 122.1 ml min^{-1} 64

4.1 Schematic of the laboratory scale gas retention tests identifying two alternative hydrogen peroxide injection points, 1 and 2; the dashed line represents the surface of the soft sediment at time t 69
4.2 Schematic of the modified gas retention tests for optimised CT imaging, identifying two alternative hydrogen peroxide injection points, 1 and 2, and two alternative imaging fields of view in red 71
4.3 Sensitivity of bubble population statistics to the threshold radiodensity value used during image post-processing; the statistics relate to bubbles within the large FOV of a 40 %w/w sediment after 6 h of gas generation 73
4.4 Laboratory scale gas retention test profiles achieved by injecting hydrogen peroxide at point 2 in Figure 4.2, including (a) example gas generation profiles within 28-40 %w/w (4-85 Pa) soft sediments and (b) gas generation, retention and release profiles within 35 %w/w (27 Pa) soft sediment 74
4.5 The maximum void fractions observed under different shear yield stress conditions and alternative gas generation methods: (1) injection at the sample homogenisation stage and (2) continuous injection into the flow during transfer to the test vessel (see Figure 4.2); the density countour map demonstrates the feasibility of periodic rollover events 75
4.6 Image sequences recoded to demonstrate bed swell and release events exhibited by (a) 30 %w/w (7 Pa) and (b) 45 %w/w (238 Pa) $Mg(OH)_2$ soft sediments subject to *in situ* gas generation by hydrogen peroxide decomposition 77
4.7 Summary of the void fractions at which four sediments of 7-238 Pa yield stress exhibited their first partial rollover event, aggregated with the gas retention tests in the absence of a supernatant from Figure 4.5 79
4.8 Imaging post-processing steps prior to quantitative bubble population analysis demonstrating (a) a typical x-ray CT slice in 8-bit greyscale, (b) the bi-level thresholded slice revealing black voids against white bulk sediment and (c) identification and labelling of discrete objects in three-dimensional space using the Bolte & Cordelières (2006) algorithm (excluding those in contact with the edge of the field of view); the images relate to 54 %w/w sediment after 6 h *in situ* gas generation 82

4.9 The evolution of retained bubble populations within 1112 Pa yield stress soft sediment including (a) side-on x-ray *scout* images of half the bed showing bulk waste swell during 0-8 h gas generation and (b) the evolution of bubble size and number density with time within the small FOV . . . 83
4.10 X-ray tomographs of bubbles within the large FOV of (a) 7 (b) 86 (c) 234 and (d) 1112 Pa yield stress magnesium hydroxide soft sediments after 6 h gas generation; the values in the top left corner of each image represent the axial distance from the centre of the test vessel . . . 84
4.11 Histograms of (a) bubble diameter (volume weighted, bubbles < 5 voxels excluded) and (b) bubble sphericity (count weighted, bubbles < 80 voxels excluded) within 7-1112 Pa soft sediments after 2 and 6 h gas generation . . . 85
4.12 *Hyperstacked* x-ray tomographs of bubbles in 7 and 1112 Pa soft sediments using a colour legend to represent bubbles across multiple time-frames, showing (a) bubbles at 15 minute intervals within the small FOV of a 7 Pa soft sediment and (b) bubbles at 0, 2 and 6 h within the large FOV of a 1112 Pa soft sediment (as the sediment expands due to its increasing voidage the bulk sediment changes from black to green to orange as shown in the legend) . . . 89
4.13 X-ray tomographs at two depths within the large FOV of 7 Pa sediment after 6 h gas generation following hydrogen peroxide addition at injection point 2 (see Figure 4.6a) . . . 93

5.1 Schematic of the D3Q19 lattice structure (left), reproduced from Guan *et al.* (2017), and a summary of the governing *propagation* (Guan *et al.*, 2017) and *collision* (Quispe *et al.*, 2005; Succi, 2001) models which redistribute the MPFs at each computational time step 103
5.2 (a) Mercury intrusion porosimetry (MIP) and (b) low-field nuclear magnetic resonance (LFNMR) spectrograms for dried $Mg(OH)_2$ soft sediments . . . 107
5.3 Pore throat size distributions for $Mg(OH)_2$ soft sediments of 35-54 % w/w solids concentration obtained by low-field nuclear magnetic resonance (LFNMR) spectroscopy with a mercury intrusion porosimetry (MIP) calibrated *corrected transverse relaxation strength* 108
5.4 Focused ion beam (FIB) micrographs of (a-b) the topography of a fractured surface and (c) a vertical FIB cross-section of cryogenically frozen $Mg(OH)_2$ soft sediment . . . 110

5.5 Example x-ray tomographs through the cylindrical cross-section of three $Mg(OH)_2$ soft sediments of (a) 30 Pa, (b) 238 Pa and (c) 1112 Pa yield stress following 6 h in-situ gas generation. The 600×600 pixel region of interest outlined in (a) has been processed and thresholded in (d) to show white bubbles against black sediment 112
5.6 Three-dimensional views of *partially eroded* bubble networks indicating the size and shape of individual bubbles within (a) 30 (b) 234 and (c) 1112 Pa soft sediments together with (d) bubble size distribution histograms from chord length analysis 114
5.7 LBM simulations of flow through sedimentary void-networks given a 1.65 $Pa\,m^{-1}$ lateral pressure gradient, including (a) an example velocity field in the x-y plane through the bubble networks of a 30 Pa yield stress soft sediment, white pixels represent regions of zero flow, including the bulk sediment (solids and porewater) sites and bubbles not connected to the continuous void-network, velocities through the void network are represented using a blue-red colour map with velocity increasing with the colour warmth, and (b) the evolution in superficial velocity at the mid-point of the porous volume in the lateral (solid line) and vertical (dashed line) directions 116
5.8 An example two-dimensional slice (normal to the z-direction) through the constructed domain for the Monte Carlo gas diffusion (MCGD) simulations at the initial condition; the three regions from left to right represent the source, porous medium and sink regions, where the porous medium is generated from a void-thresholded CT reconstruction of the 54 % w/w sample 119
5.9 Evolution of oxygen tracer molecule concentration in time and space, $\phi(x,t)$, during Monte Carlo gas diffusion simulations within (a) an open duct and (b) the permeable void networks within 54 % w/w $Mg(OH)_2$ soft sediment (see Figure 5.8); the dotted line profiles are obtained from the simulations, $\phi(x,t)$, the thick dashed lines represent optimised analytical solutions, $\tilde{\phi}(x,t)$, and the vertical dashed lines demarcate the source, porous and sink regions 120
5.10 Summary of the effective diffusivities for oxygen tracer molucules through an empty duct and through permeable bubble networks within 35-54 % w/w $Mg(OH)_2$ soft sediments 121

5.11 Schematic demonstrating alternative chronic gas release mechanisms from consolidated soft sediments under various yield stress and gas holdup conditions, including: (a) buoyant bubble ebullition, possibly inducing (b) bubble cascades (Gauglitz *et al.*, 2015; Sherwood & Eduardo Sáez, 2014), gas migration through (c) discrete ganglia of partially coalesced bubbles or (d) vessel-spanning continuous bubble networks at higher voidages, (e) permeable pathways through coalesced micro-cracks and (f) deep vertical drainage channels (van Kessel & van Kesteren, 2002) 124

6.1 Schematic of the laboratory scale gas retention tests used to observe evolution in gas holdup with time during hydrogen peroxide decomposition within CMgS; hydrogen peroxide is well mixed through the sediment using an axial flow impeller 128

6.2 (a) Mercury intrusion porosimetry (MIP) and (b) low-field nuclear magnetic resonance (LFNMR) spectra for dried CMgS soft sediments along with (c) a pore size distribution for 42.3 % w/w (156 Pa) CMgS and (d) comparison of pore size distributions for CMgS and commercial $Mg(OH)_2$ sediments of 30-1112 Pa yield stress; the $Mg(OH)_2$ sediment data has been reproduced from Figure 5.3 130

6.3 Focused ion beam micrographs of (a-b) the topography of a fractured and sublimed surface and (c) a vertical FIB cross-section of a cryogenically frozen sample of 42 % w/w CMgS 132

6.4 Typical x-ray computed tomography (CT) slices at two axial depths through (a) 30 Pa yields stress CMgS and (b) 30 Pa $Mg(OH)_2$ soft sediment (previously presented in Figure 5.5a) following 6 h *in situ* gas generation; the test materials were imaged within a 7.1 cm diameter side-mounted cylinder using an Inveon PET/CT (Siemens, Germany) 133

6.5 Bubble size distributions, translated from chord length distributions, for populations within 30 Pa CMgS and 30, 234 and 1112 Pa $Mg(OH)_2$ soft sediments; the $Mg(OH)_2$ sediment data has been reproduced from Figure 5.6d 134

6.6 Magnified sections of the micrographs in Figure 6.4a demonstrating the imact of large, dense particles at the growing bubble front 136

6.7 Three-dimensional reconstruction of the 16 larges bubble networks within 29 Pa yield stress CMgS; warmer colours represent less voluminous bubble networks 136

6.8 Gas generation, retention and implied release profiles during hydrogen peroxide decomposition within 1 l samples of (a) 11 and (b) 88 Pa yield stress CMgS 138
6.9 Summary of gas holdup within CMgS (red) and commercial $Mg(OH)_2$ (blue) soft sediments across three scales of (1) 0.36 l sideways mounted cylinders, (2) 1 l vertically mounted cylinders and (3) 6.5 l sideways mounted cylinders 139
6.10 Montage of x-ray CT *scout* profiles of 132 Pa CMgS during 8 h *in situ* gas generation 140
6.11 Example x-ray tomographs of bubbles retained by 132 Pa CMgS within a 300 mm diameter sideways mounted cylinder 141
6.12 Evolution in (a) the size distribution, as well as the number and sphericity of bubbles of (b) 1.42-2.58 mm, (c) 2.58-3.57 mm and (d) > 3.57 mm diameter retained by 132 Pa CMgS 143
6.13 Flattened *hyperstacks* of x-ray tomographs at (a) 5 min intervals for the first 15 min gas generation and (b) a larger FOV at 0, 2 and 6 h gas generation for 132 Pa yield stress CMgS within a 300 mm diameter cylinder 146

List of Tables

3.1 A summary of the relative atomic abundance of each element identified from the four EDX spectra in Figure 3.7 54
3.2 Summary of the major intensity peaks identified from the XRD spectra in Figure 3.8; the respective brucite crystal planes are identified from Henrist *et al.* (2003) 56

4.1 X-ray CT imaging parameters for two imaging fields of view 71
4.2 Estimation of buoyant potential energy ratios for *gobs* of liberated sediment following partial rollover at various supernatant depths according to eq. (4.10) (Stewart *et al.*, 1996); the conditions most likely to result in acute gas release are shown in bold 80
4.3 Contribution of the observable (d_b > 0.83 mm) and sub-resolution bubble populations to the total voidage 91

5.1 Summary of x-ray CT scanning parameters and comparison with the scanning protocol used in Chapter 4 101
5.2 Summary of modal pore throat radii, $\bar{r}_{th}$, and free water content within $Mg(OH)_2$ soft sediments estimated using LFNMR 109
5.3 Characterisation of the voidage properties within 30-1112 Pa yield stress $Mg(OH)_2$ soft sediments following 6 h *in situ* gas generation . 113
5.4 The gas permeabilities of bubble networks retained within $Mg(OH)_2$ soft sediments of 30-1112 Pa yield stress 117

6.1 Summary of x-ray CT scanning parameters and comparison with the scanning protocol used in Chapter 4 129
6.2 Modal pore throat radii, $\bar{r}_{th}$, and free water content within $Mg(OH)_2$ and CMgS soft sediments estimated using LFNMR 131
6.3 Contribution of the observable (d_b > 0.83 mm) and sub-resolution bubble populations to the total voidage within commercial $Mg(OH)_2$ sediments (reproduced from Table 4.3) and CMgS 142

Nomenclature

Acronyms

Symbol	Description
μCT	X-ray microtomography
BFS	Blast funace slag
CMgS	Corroded magnesium sludge
CMS	Corroded Magnox sludge
CT	Computed tomography
EDX	Energy dispersive x-ray analysis
ESD	Equivalent spherical diameter
ESEM	Environmental scanning electron microscopy
FGMSP	First generation Magnox storage pond
FIB	Focused ion beam
FT-IR	Fourier transform infra-red spectroscopy
GDF	Geological disposal facility
LFL	Lower flammability limit
LFNMR	Low field nuclear magnetic resonance
MIP	Mercury intrusion porosimetry
MSSS	Magnox swarf storage silos
NNL	National Nuclear Laboratory
OPC	Ordinary Portland cement

PNNL	Pacific Northwest National Laboratory
SEM	Scanning electron microscope
SPP1	Sludge packaging plant 1
WIPP	Waste isolation pilot pant

Dimensionless Numbers

Symbol	Description	Definition
Y_g	Yield parameter	$\frac{\text{yield stress}}{\text{buoyant stress}} = \frac{\tau}{\rho_l g r_b}$
Bn	Bingham number	$\frac{\text{yield stress}}{\text{viscous stress}} = \frac{\tau r_b}{\mu_0 u_b}$
Bo	Bond number	$\frac{\text{buoyancy}}{\text{surface tension}} = \frac{\rho_l g r_b^2}{\gamma}$
Fr	Froude number	$\frac{\text{inertia}}{\text{gravity}} = \frac{u_b}{\sqrt{g r_b}}$
Re	Reynolds number	$\frac{\text{inertia}}{\text{viscosity}} = \frac{\rho u d}{\mu}$

Greek Symbols

Symbol	Description	Dimensions	Units
$\boldsymbol{\nu}$	Kinematic viscosity	A/t	$\mathrm{m^2\,s^{-1}}$
$\boldsymbol{\tau}$	Relaxation constant	-	-
δ_t	Computational time step	t	-
δ_x	Voxel width	L	-
ΔP	Excess bubble pressure	F/A	Pa
$\dot{\varepsilon}$	Strain rate	1/t	$\mathrm{s^{-1}}$
γ	Surface tension	F/L	$\mathrm{N\,m^{-1}}$
κ	Permeability	1/A	$\mathrm{m^{-2}}$
ν	Void fraction or gas holdup	-	-
ω	Weight fraction	-	-
Φ	Porosity	-	-
ϕ	Concentration	n/V	$\mathrm{mol\,dm^{-3}}$
Ψ	Sphericity	-	-

ρ	Density	m/V	$\mathrm{kg\,m^{-3}}$
ρ_2	Transverse relaxation strength	L/t	$\mathrm{m\,s^{-1}}$
σ	Stress	F/A	Pa
τ	Shear yield stress	F/A	Pa
θ	Three-phase contact angle	-	$^\circ$
ε_T	Strain and thrixotropic transition	L/L	-

Roman Symbols

Symbol	Description	Dimensions	Units
a	Crack length (longest axis)	L	m
AR	Aspect ratio	L/L	-
COD	Crack opening displacement	L	m
D	Diffusivity	A/t	$\mathrm{m^2\,s^{-1}}$
d	Diameter	L	m
E	Young's modulus	F/A	Pa
e_i	Directional vector	-	-
f_i	Mass probability function	-	-
G	Shear modulus	F/A	Pa
J	Molar flux	n/A t	$\mathrm{mol\,m^{-2}\,s^{-1}}$
k	Reaction first order kinetic constant	1/T	$\mathrm{s^{-1}}$
K_h	Henry's law constant	n/VP	$\mathrm{mol\,m^{-3}\,Pa^{-1}}$
K_0	Coefficient of earth pressure at rest, ratio of horizontal to vertical effective stress	-	-
K_{1c}	Fracture toughness	$\mathrm{F\,L^{1/2}}$	$\mathrm{Nm^{1/2}}$
K_1	Stress intensity factor	$\mathrm{F\,L^{1/2}}$	$\mathrm{Nm^{1/2}}$
K_ν	Poisson's ratio	-	-
L	Length	L	m
L_D	Diffusion length	L	m

P	Pressure	F/A	Pa
r	Radius	L	m
R_1	Radial distance from bubble	L	m
S	Surface area	A	m^2
S_0	Gas source term	n/V	$mol\,m^{-3}$
t	Time	t	s
T_2	Transverse relaxation time	T	s
u	Velocity	L/t	$m\,s^{-1}$
V	Volume	L^3	m^3
W	Energy or Work	F L	J
x	Distance	L	m

Superscripts

Symbol	Description
$\bar{}$	Average
$\hat{}$	Simulation solution (lattice units)
$\tilde{}$	Analytical solution

Subscripts

Symbol	Description
0	Initial
τ	Yield
a	Ambient
a	Atmospheric (ambient)
aq	Aqueous
B	Boundary
b	Bubble
BP	Buoyant potential

by	Buoyancy
c	Critical
cor	Corrected
dig	Digital
E	Released (escaped)
e	Elastic cavity expansion
eff	Effective
eq	Equilibrium
f	Tensile fracture
G	Generated
g	Gas
H	Horizontal
h	Hydrostatic head
i	Capillary invasion
l	Liquid
max	Maximum
min	Minimum
NB	Neutral buoyancy
nuc	Nucleation
p	Plastic region
pb	Pore body
pw	Pore water
R	Retained
r	Rise
s	Source
th	Pore throat
tom	Tomography
V	Vertical

Chapter 1

Introduction

Many natural water systems, including shallow marine beds (Johnson *et al.*, 2002; Wheeler, 1988a), lakes (Keller & Stallard, 1994; van Kessel & van Kesteren, 2002), rivers (Sills & Gonzalez, 2001), and wetlands (Algar *et al.*, 2011a), experience *in situ* methane, nitrogen and carbon dioxide production, retention and release as a result of biogenic decomposition of organic matter. This has received significant research interest due to the significant contribution towards global greenhouse gas emissions (Katsman *et al.*, 2013; Keller & Stallard, 1994), while the impact of retained gas pockets on the bulk strength (Wheeler, 1988b) and elasticity (Wheeler & Gardner, 1989) of marine sediments is also likely to have significant implications for offshore construction. Alternatively, methanogenesis can be effectively exploited for commercial biogas production from the anaerobic digestion of wastewater sludges in order to offset the economic and carbon cost of the treatment (Chan *et al.*, 2009). A further example of *in situ* gas retention within aqueous soft sediments, which forms the basis of this research, is encountered within historic nuclear waste deposits, where highly consolidated sediments of fuel and cladding corrosion products, contaminated with depleted fuel, leached actinides and fission products (Fairhall & Palmer, 1992), trap bubbles of hydrogen (Kam *et al.*, 2001b). The hydrogen is formed by a combination of corrosion reactions and radiolysis, triggered by the radioactive decay of water soluble fission products such as caesium and strontium (Gregson *et al.*, 2011; Terrones & Gauglitz, 2003).

Substantial inventories of radioactive *sludge* wastes have accumulated at Sellafield, UK (Hastings *et al.*, 2007) and Hanford, USA (Kam *et al.*, 2001a; Sherwood & Eduardo Sáez, 2014; Terrones & Gauglitz, 2003) from legacy civil and defence reactors which employed metallic uranium fuel and either aluminium or Magnox alloy cladding, all of which are vulnerable to corrosion during long term underwater storage (Delegard *et al.*, 2014; Parry *et al.*, 2011). Further consolidated particulate wastes have been accrued within vast underground storage tanks at Hanford from historic reprocessing and decontamination activities (Watson & Ellwood, 2003).

Much of the hydrogen within these wastes is released at a chronic rate and safely ventilated, however, trapped hydrogen still presents a number of potential hazards which must be considered ahead of decommissioning legacy waste silos and storage ponds:

1. Sediments prone to significant gas holdup stored beneath a convective aqueous supernatant pose a perpetual risk of acute hydrogen release from Rayleigh-Taylor instabilities, which may occur if bed swell reduces the bulk waste density below that of the supernatant (Allemann, 1992; Kam *et al.*, 2001b). Large acute gas releases have the potential to raise the hydrogen concentration in the ullage above the lower flammability limit, which could result in breach of containment on ignition.

2. Exposure of dried regions of uranium metal within the waste to hydrogen can result in uranium hydride formation, a pyrophoric compound which has caused a number of fires and radioactive releases (Orr *et al.*, 2017; Solbrig *et al.*, 1994).

3. Evacuation of legacy waste silos into $3\,\mathrm{m}^3$ modular containers for transport and interim storage presents additional challenges. Mechanical perturbations during transport may induce acute hydrogen releases. Overfilling these boxes raises the potential to *blind* the gas ventilation filters and cause the container to pressurise with hydrogen, while underfilling incurs substantial expense and delays in evacuating the legacy buildings, which have already reached the end of their designed operating lifetime (Hastings *et al.*, 2007).

Two significant obstacles complicate the study of gas bubbles within these wastes. First, monitoring Magnox Swarf Storage Silos at Sellafield is greatly inhibited by local radioactivity levels. In some areas, doses in the order of $200\,\mathrm{REM\,h^{-1}}$ correspond to a permissible daily working time of less than a second (Smith, 2006). Second, the optical opacity of consolidated particulate sludge wastes renders the bubble population invisible (Hunter *et al.*, 2011). To overcome this issue, x-ray computed tomography (CT) has been employed to observe detailed bubble growth within marine sediments (Abegg & Anderson, 1997; Best *et al.*, 2006; Boudreau *et al.*, 2005; Sills & Gonzalez, 2001), revealing various void geometries including cornflake or disk-shaped fractures (Best *et al.*, 2006; Gardiner *et al.*, 2003), oblate spheroid (Boudreau *et al.*, 2005) and inverted teardrop bubbles Algar *et al.* (2011a); Katsman (2015). Recent advances in this field provide further promise: commercial microtomography can visualise features to spatial resolutions close to a micron for small experimental scales and 20-30 min scan times (Selomulya *et al.*, 2006), while ultrafast benchtop tomography has enabled imaging of centimetre scale bubbles within fluidised beds at frequencies of 10 000 Hz (Muddle, 2011). In recent years,

synchrotron x-ray tomography has addressed the compromise between spatial and temporal resolution to enable visualisation of transient behaviour at the micro-scale (Dobson *et al.*, 2016), including dynamic bubble connectivity within porous media (Reynolds *et al.*, 2017) and Haines jumps (Berg *et al.*, 2013).

On the assumption that bubbles quickly grow to the scale of interstitial pores within fine grained consolidated soft sediments (Boudreau, 2012), a bubble may (1) create space for further growth by displacing the sediment skeleton and expanding its host cavity (Terrones & Gauglitz, 2003), (2) the bubble may be deformed by the sediment and intrude into adjacent pore-space by capillary invasion (Kam *et al.*, 2001b), or (3) the excess bubble pressure may induce tensile fracture (Johnson *et al.*, 2002) resulting in high aspect ratio cracks. Dendritic bubbles resulting from capillary invasion appear the least realistic within fine grained sediments of metallic corrosion products as the capillary entry pressures scale with inverse pore throat radius (Jain & Juanes, 2009). Near spherical bubbles resulting from cavity expansion are anticipated within low strength sediments, which exert least resistance to deformation at the bubble-sediment interface. Fracture toughness scales with inverse yield stress (Broek, 1982), increasing the probability of fracture within kilopascal yield stress sediments. Merging of fracture sites and pore-water drainage channels can provide deep stable channels for continuous chronic gas release from highly consolidated sediments of high yield stress (van Kessel & van Kesteren, 2002). Conversely, the ratio of buoyant stress to sediment yield stress is most favourable to bubble release by ebullition within low yield stress materials (Dubash & Frigaard, 2004). The mechanisms for chronic gas release are least certain for intermediate strength sediments, making yield stress conditions in the order of $50 < \tau < 500\,\mathrm{Pa}$ potentially vulnerable to the large holdup conditions at risk of acute flammable gas release.

At present, the waste silos at Sellafield represent somewhat of a *black box*. Designing a decommissioning safety case which mitigates against the hazards detailed requires much greater clarity in (1) the realistic extent of gas holdup across a range of sediment yield stress conditions, (2) the potential avenues for chronic gas release and (3) the conditions most susceptible to acute quiescent gas release. In order to address these uncertainties, this thesis presents a methodology to imitate *in situ* bubble generation within consolidated nuclear soft sediments at laboratory scale using the decomposition of hydrogen peroxide (Sherwood & Eduardo Sáez, 2014) to form oxygen bubbles within non-active analogues for Magnox-era legacy waste (Blackburn & Thompson, 2013). Clinical x-ray CT (Constantinescu & Mukherjee, 2009) will be employed to non-destructively observe the evolution of bubble size and shape and to assess the mobility of retained bubbles. This experimental approach addresses a limitation of tomography studies which have focused on individual bubbles formed at a submerged orifice (Best *et al.*, 2006; Johnson *et al.*,

2002), and hence fail to capture the diversity of a bubble population, interaction between bubbles or macroscopic bubble features which may facilitate enhanced rates of chronic gas release.

X-ray tomography will be coupled with Lattice Boltzmann and Monte Carlo simulations (Abbasi & Evans, 1983; Quispe *et al.*, 2005) to investigate possible mechanisms for gas migration through the sediment. Sediment response to bubble growth is considered to be governed by complex functions of the sediment deformation mechanics (Johnson *et al.*, 2002; Terrones & Gauglitz, 2003), microstructure (Kam *et al.*, 2001b; Rossen & Gauglitz, 1990; Wheeler, 1988a) and three-phase interfacial behaviour (Jain & Juanes, 2009; Kam & Rossen, 1999). These sediment behaviours will be investigated using vane rheology (Nguyen & Boger, 1992), low field nuclear magnetic resonance (Xiao *et al.*, 2017) and Langmuir-Blodgett experiments (Kundu *et al.*, 2005) respectively, providing a framework to interpret the various bubble geometries (Gardiner *et al.*, 2003; Katsman, 2015) observed under x-ray CT. First, Chapter 2, reviews the existing literature to consider (1) the chemical and physical composition of nuclear legacy waste in the UK and USA, (2) the evidence for periodic flammability hazards within nuclear storage tanks and silos and (3) the various mechanisms for bubble growth and release proposed in relation to biogenic methane bubbles within marine sediments (Boudreau, 2012).

Chapter 2

Literature review

2.1 Nuclear legacy waste in the UK

The UK has a substantial legacy of radioactive waste from its first generation civil reactors and early defence programmes, the majority of which is currently stored at the Sellafield site in Cumbria (Horsley & Hallington, 2005). The earliest of the UK's first generation of nuclear reactors, such as the Windscale Piles and Calder Hall, used metallic natural uranium for fuel, with the aforementioned two clad with aluminium (Baldwin, 2003) and Magnox alloy (Watson & Ellwood, 2003) respectively. Magnox cladding, an alloy of magnesium (>99 %) with aluminium (Fairhall & Palmer, 1992; Morris *et al.*, 2009), was adopted by the subsequent first generation civil nuclear fleet as its very low neutron capture cross-section (Burrows *et al.*, 2005; Jackson *et al.*, 2014) provided exceptional compatability with non-enriched fuel. However, the Magnox alloy, like aluminium and uranium, is particularly vulnerable to corrosion during long term underwater storage (Hastings *et al.*, 2007; Parry *et al.*, 2011), with the predominantly brucite, $Mg(OH)_2$, (Gregson *et al.*, 2011) corrosion product accumulating and consolidating into the current inventory of intermediate level waste (ILW) *corroded Magnox sludge* (CMS).

2.1.1 First generation Magnox storage pond (FGMSP)

Following a period of at least 150 days of underwater storage within reactor adjacent cooling ponds to remove decay heat from short lived radionuclides (Morris *et al.*, 2009), spent Magnox fuel cannisters were transported to the First Generation Magnox Storage Pond (FGMSP) at Sellafield, pictured in Figure 2.1a (Hastings *et al.*, 2007). The exceptions to this strategy were the two Magnox reactors at Wylfa where spent fuel rods have been stored in CO_2-filled dry-storage cells prior to reprocessing (Morris *et al.*, 2009). Within the FGMSP, spent fuel rods undergo

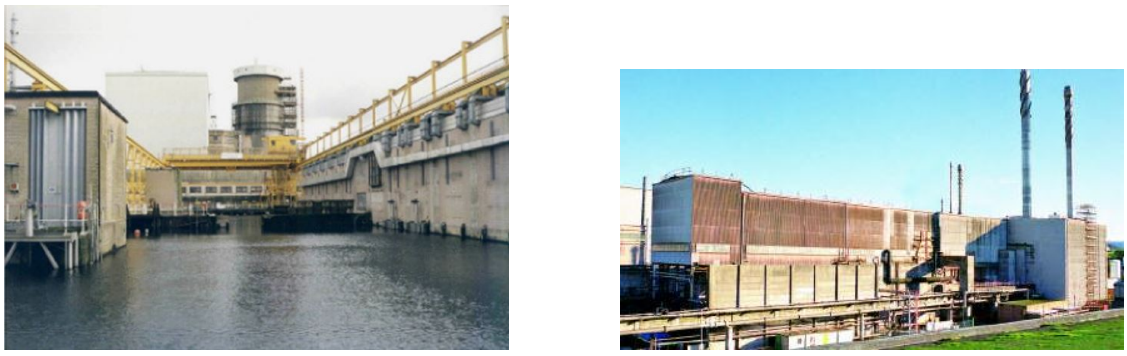

(a) (b)

Figure 2.1: The two principal Magnox-era legacy buildings at Sellafield: (a) the first generation Magnox storage pond (FGMSP, Hastings *et al.* (2007)) and (b) the Magnox swarf storage silos (MSSS, Forepoint Ltd. (2016))

a further period of cooling before the shear removal, or *decanning*, of the outer cladding in order to liberate the fuel for reprocessing (Jackson *et al.*, 2014).

The FGMSP is an open air pond constructed in the 1950s, which received irradiated Magnox fuel until 1992 (Jackson *et al.*, 2014). Although alkaline pond chemistry is carefully maintained with sodium hydroxide dosing in order to minimise Magnox corrosion (Burrows *et al.*, 2005; Parry *et al.*, 2011), a prolonged shut-down period in the 1970s resulted in substantial corrosion, leading to escalating radiation levels and deteriorating water visibility (Jackson *et al.*, 2014) to the extent that radiation workers can currently spend less than an hour a day in the vicinity (Reddy *et al.*, 2012). Up to 2000 m^3 (Parry *et al.*, 2011) of CMS, including corroded cladding, fuel fragments and pond *furniture* (Baldwin, 2003), wind-blown debris and organic matter (Jackson *et al.*, 2014), has accumulated in a layer, up to a metre deep, at the base of the pond.

In 2011, £7 billion was committed to decommissioning the FGMSP (Jackson *et al.*, 2014; Reddy *et al.*, 2012). The age and deteriorating condition of the FGMSP have made waste retrieval and decommissioning priority activities and the settled sludge is currently undergoing pumped transfer to a new sludge packaging plant (SPP1), containing three $33 \times 3 \times 7$ m stainless steel containers, for interim storage. A 14 000 m^3 volume of active effluent (Le Clere, 2011) must also be treated in parallel with the evacuation of the FGMSP and dewatering of sludge within SPP1.

2.1.2 Magnox swarf storage silos (MSSS)

The decanning operations within the FGMSP generate a *swarf* waste of shards of metallic cladding, which has subsequently been stored in the Magnox Swarf Storage Silos (MSSS), shown in Figure 2.1b. Since decanning had to ensure that absolutely no cladding material entered the reprocessing plant, swarf is routinely contaminated with 1-3 % depleted fuel and fission products (Fairhall & Palmer, 1992; Morris *et al.*,

2009). Since the MSSS were commissioned in 1964, the 22 compartments, each with around 600 m^3 capacity, have received between 9700 m^3 (Baldwin, 2003) and 11 000 m^3 (Le Clere, 2011) of solid waste, including Magnox swarf, fuel debris and 300 tonnes of irradiated equipment (Baldwin, 2003; McCracken & Eilbeck, 2005; Smith, 2006).

The condition of waste within each container varies greatly. Corrosion was actively promoted in the original 6 containers by the addition of sodium chloride, while subsequent containers were dosed with sodium hydroxide in order to retard corrosion (Baldwin, 2003) and so the extent of uncorroded swarf within the MSSS is uncertain. At the time of writing, the proposal for evacuation of the MSSS is to mechanically grab sludge waste from the containers for transfer to 1 m^3 skips within 3 m^3 boxes, which can be stacked in a suitable warehouse for interim storage. The prefered ultimate waste form is to encapsulate CMS and any uncorroded swarf within a cementitious grout of blast furnace slag (BFS) and ordinary Portland cement (OPC) for long term storage in a geological disposal facility (GDF) (Cronin & Collier, 2012; Fairhall & Palmer, 1992)

2.1.3 CMS characterisation

The substantial dose emitted by the FGMSP liquor makes sampling and characterisation of CMS a far from trivial task. The most comprehensive published CMS characterisation studies can be found in Gregson *et al.* (2011) and Parry *et al.* (2011), where sludge samples from the FGMSP, aqueous pond effluents and a test material of corroded, unirradiated Magnox cladding were assessed by:

- environmental scanning electron microscopy with energy dispersive x-ray analysis (ESEM/EDX) of filtered particles from liquor and sludge samples
- micro-Raman spectroscopy of filtered particles from liquor and sludge samples
- Fourier transform infra-red spectroscopy (FT-IR) of sludge

The dominant phase observed under ESEM consisted of aggregates of hexagonal platelets typical of brucite, $Mg(OH)_2$, as demonstrated by Figures 2.2c and 2.2d (Gregson *et al.*, 2011). The aggregate in Figure 2.2c is 22 µm in length, while Figure 2.2d shows hexagonal platelets with facial dimensions of 1-2 µm and a thickness of 20-40 nm. The formation of $Mg(OH)_2$ at the surface of partially corroded Magnox cladding and the consolidation of CMS into a dense sludge are also shown by Figures 2.2a and 2.2b (Hastings *et al.*, 2007). EDX analysis of CMS revealed further magnesium rich phases including rod-shaped artinite, $Mg_2CO_3(OH)_2.3H_2O$ crystals, hydrotalcite, $Mg_6Al(CO_3)(OH)_{16}.4H_2O$ (Gregson *et al.*, 2011; Parry *et al.*,

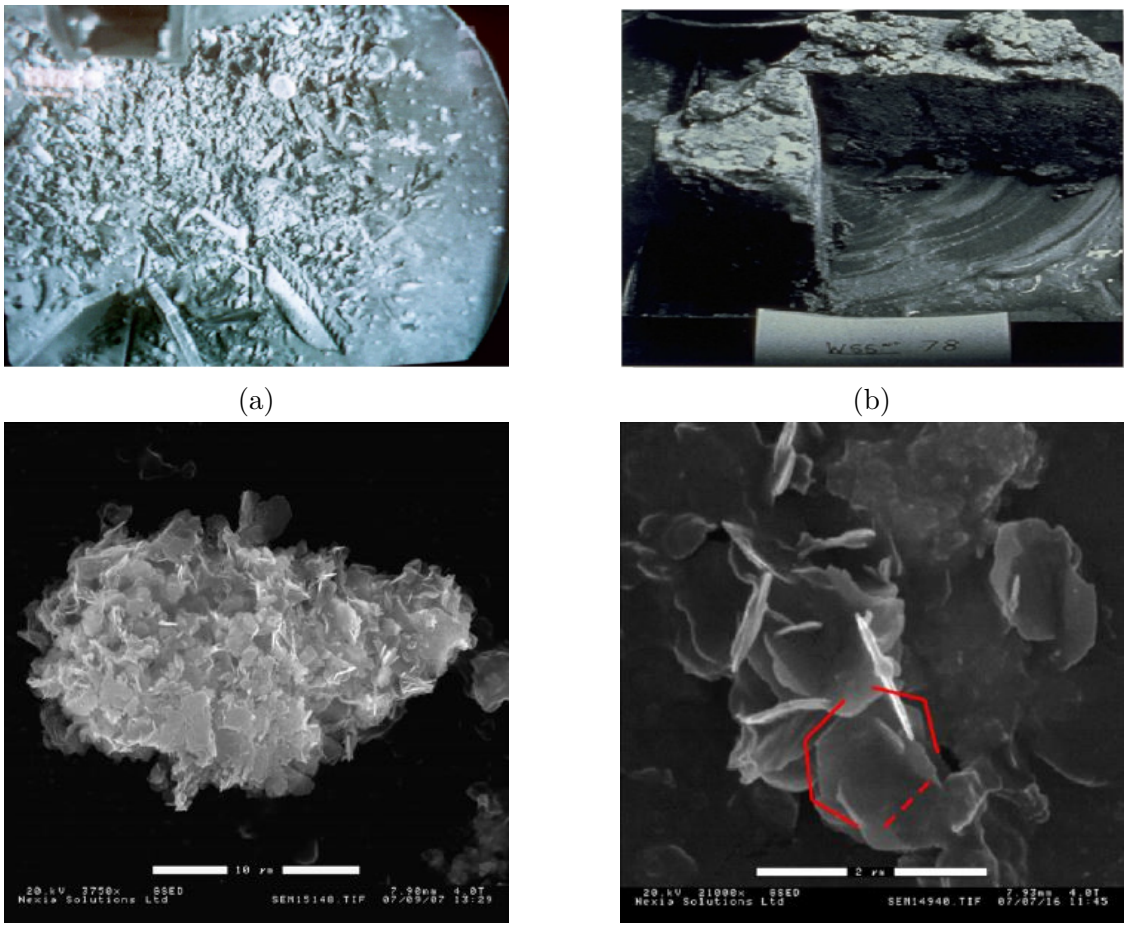

(a) (b)

(c) (d)

Figure 2.2: Images from the life-cycle of CMS including (a) partially corroded Magnox cladding, (b) highly consolidated CMS (both Hastings *et al.* (2007)) and environmental scanning electron micrographs (ESEM) of aggregates from corroded, unirradiated Magnox(Gregson *et al.*, 2011) at (c) 3750 and (d) 21000 times magnification

2011) and various magnesium hydroxy-carbonates, $Mg_5(CO_3)_4(OH)_2.nH_2O$ (Gregson *et al.*, 2011).

The dark grey colour of CMS in Figure 2.2b (Hastings *et al.*, 2007), despite its major component being white $Mg(OH)_2$, results from < 5 µm aggregates of 30-50 nm black particulates identified by EDX as rich in uranium and oxygen, believed to be uranium oxide (Gregson *et al.*, 2011). In addition to uranium, EDX, FT-IR and raman spectroscopy revealed calcium, silicon, titanium and iron phases within the CMS matrix (Gregson *et al.*, 2011), however this barely begins to reflect the chemical heterogeneity of the pond and silo sludge. Leached trivalent fission products including samarium and europium are known to readily substitute for aluminium in hydrotalcites, while pertechnate substitutes for its various anions (Gregson *et al.*, 2011). Plutonium, americium and other actinides associate with brucite colloids within the settled sludge and suspended in the supernatant (Maher *et al.*, 2016; Parry *et al.*, 2011). The open air FGMSP is further contaminated by humic and fulvic acids from decayed organic matter, which also associate with hydrotalcites (Amin & Jayson, 1996; Gregson *et al.*, 2011).

2.2 Nuclear legacy waste in the USA

Characterisation of legacy waste in the USA represents an even more extensive task than for UK waste and so this section is limited to a brief overview, sufficient to contextualise the relevant research into gas retention undertaken by the American National Laboratories and universities. The major inventories of American legacy waste include the accumulated corrosion products in ponds, such as the K-basins (Delegard *et al.*, 2014; Phillips & Knollmeyer, 2006), adjacent to second world war-era plutonium production reactors, and secondary waste streams from historic reprocessing activities stored in large underground single and double-shell tanks (Krupka *et al.*, 2006; Singer *et al.*, 2009).

The two K-basins received 2300 t (Knollmeyer, 2006) spent aluminium clad uranium metal fuel from two historic reactors at the Hanford site, corroding to leave a legacy of around 50 m^3 sludge within cannisters and coating the floors, walls and discarded equipment (Knollmeyer, 2006). The sludge is predominantly comprised of uranium corrosion products (≈ 82 %), alongside uncorroded uranium (≈ 6 %), iron corrosion products (≈ 1 %), and the remainder being aluminium, its corrosion products, wind blown sand and spalled concrete (Schmidt & Zacher, 2007) contaminated with transuranics and fission products (Knollmeyer, 2006). The abrasive qualities of uncorroded uranium complicate the transport of K-basin sludge, confounding the ongoing hydrogen flammability risk (Delegard *et al.*, 2014; Gerber, 2008). The bulk of the sludge was cleaned out in 2007 (Gerber, 2008) and

is now awaiting treatment and packaging for disposal at a waste isolation pilot pant (WIPP) in New Mexico (Witwer, 2011).

A vastly greater quantity of sludge waste and a similarly greater hydrogen safety risk is associated with the underground storage tanks at Hanford. 200 000-250 000 m^3 (Gephart & Lundgren, 1998; Watson & Ellwood, 2003) is stored within 149 single and 28 double-shell tanks (Prugue, 2013). These underground concrete tanks are many times larger than the MSSS containers, at up to 23 m in diameter and 3800 m^3 in capacity (Prugue, 2013). The waste exists as three main phases, a sludge containing oxides, aluminates, silicates and the vast majority of the radionuclides which are insoluble within the alkaline storage environment, a supernatant layer, dense with dissolved sodium nitrite and sodium hydroxide, and contaminated with water soluble caesium, strontium and technetium, and a chromium, fluoride, oxalate and sulfate rich saltcake (Lukens *et al.*, 2004; Mashal *et al.*, 2004; Watson & Ellwood, 2003). Some tanks also exhibit a carbonate rich mineral crust (Bryan *et al.*, 1992) at the top of the waste layer including dawsonite, $NaAlCO_3(OH)_2$ and cejkaite, $Na_4(UO_2)(CO_3)_4$, cemented together by trona, $Na_2CO_3 \cdot NaHCO_3 \cdot 2H_2O$ (Page *et al.*, 2018).

There is great uncertainty in the concentration and composition of waste within the underground tanks and the contents vary greatly between the four tank *farms* (Mashal *et al.*, 2004). The U-farm contains bismuth, sodium and nitrate rich secondary reprocessing wastes from lanthanum fluoride decontamination (Rassat *et al.*, 2003). The S and SX-farms contain waste from early REDOX reprocessing operations, with higher activity waste in the SX-farm tanks, while the BY-farms contain metal and caesium scavenging wastes (Rassat *et al.*, 2003). Much of the pumpable waste has been transferred to larger double-shell tanks after discovering that 67 of the single-shell tanks were leaking a highly alkaline leachate rich in sodium, aluminium, hydroxides and nitrates (Chen *et al.*, 2005; Deng *et al.*, 2006). The Hanford tank waste is as physically heterogeneous as it is chemically diverse, with yield stresses measured as low as 30 Pa or as high as 6 kPa (Rassat *et al.*, 2003; Wells *et al.*, 2010).

2.3 Evidence of gas retention and periodic release from nuclear legacy waste

The Pacific Northwest National Laboratory (PNNL) have published a wealth of data from their underground storage tanks demonstrating a propensity for legacy waste to generate, retain and periodically release flammable gases (Whitney *et al.*, 1996); selected findings are presented in Figure 2.3 (Allemann, 1992; Kam *et al.*, 2001b; Whitney *et al.*, 1996). Figure 2.3a demonstrates the evolution in waste

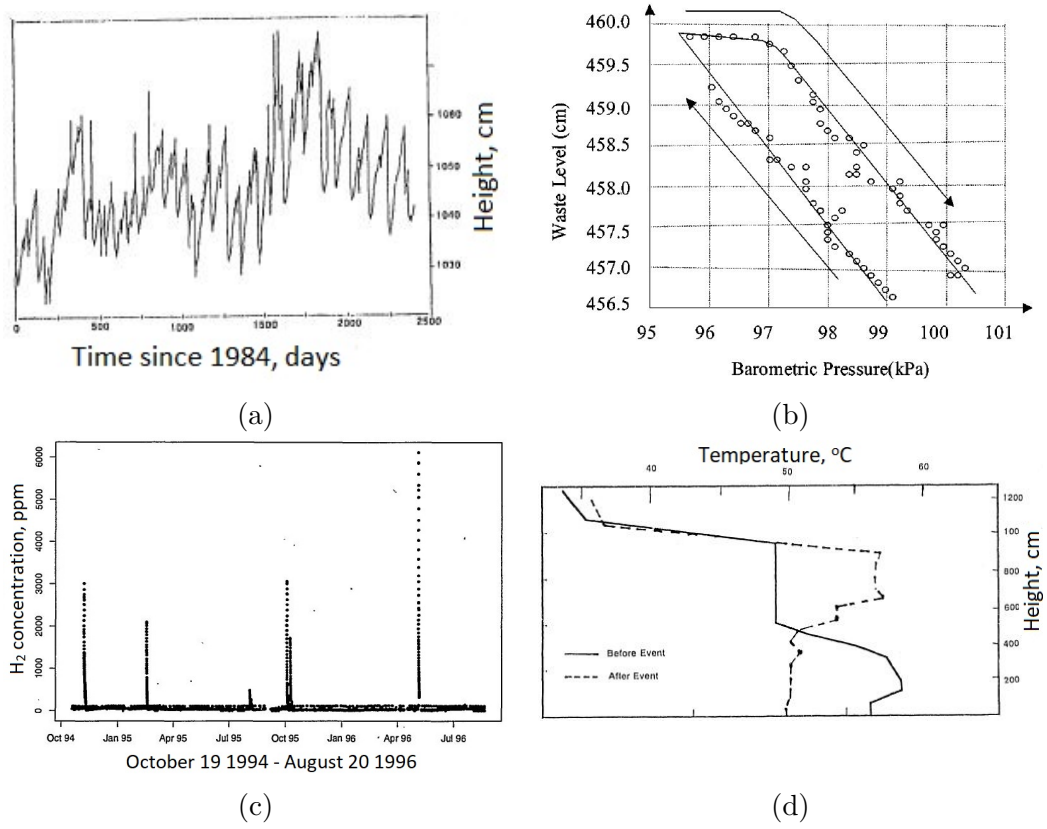

Figure 2.3: Evidence of gas retention and periodic gas releases from underground waste storage tanks at Hanford, USA, including (a) evolution in waste level over a 7 yr period (Allemann, 1992), (b) changes in waste level with ambient pressure (Kam *et al.*, 2001b), (c) periodic spikes in hydrogen concentration within a tank ullage over a 2 yr period (Whitney *et al.*, 1996) and (d) evolution in waste temperature profile coinciding with spikes in hydrogen concentration (Allemann, 1992)

level within tank 241-SY-101 (Allemann, 1992), indicating fluctuations within a 0.6 m range over a 7 yr period. The high frequency changes in waste volume are readily explained by a response in retained gas volume to ambient temperature and pressure. This is reinforced by Figure 2.3b which demonstrates a hysteresis profile of waste level response to barometric pressure during a storm (Kam *et al.*, 2001b). A 4 % decrease in ambient pressure manifested in a 4 cm rise in waste level, before returning to the original waste height during the subsequent pressure re-adjustment. This is only explicable by the presence of a significant, compressible gas volume within the waste.

The waste level hysteresis exhibited in response to changes in ambient pressure is also interesting as it implies irreversible changes in the retained bubble population during a sudden expansion. This could result from *snap-off* Gauglitz *et al.* (1988) as expanding bubbles intrude through water-filled pores in the consolidated bed, breaking into multiple bubbles at pore throats, thereby irreversibly changing the size distribution of the retained bubble population. Alternatively, the stress imposed on the sediment by the expanding bubble may induce an irreversible plas-

tic response from the sediment (Terrones & Gauglitz, 2003), a possibility which is discussed in Section 2.7.

Lower frequency cyclical changes in waste level in Figure 2.3a, beyond the timescale of seasonal and daily changes in ambient conditions, are better explained by chronic *in situ* gas generation, much of which is retained leading to *waste swell*, punctuated by large periodic gas release events. The occurance of periodic gas release is supported by continuous monitoring of volatiles in tank ullages. Figure 2.3c (Whitney *et al.*, 1996) shows six 500-6000 ppm spikes in hydrogen concentration within the ullage of Hanford tank AN-104 with a periodicity of 2-7 month, each coinciding with sudden drops in waste level. One exceptional case was observed in October 1995, where a gas release appears to have induced a second, lesser release shortly afterward. The brevity of the spikes in hydrogen concentration demonstrates that hydrogen is rapidly ventiliated from the ullage and so either a continuous, or highly coincidental ignition source would be required for an explosive event. Furthermore, the magnidude of the concentration spikes, < 6000 ppm, indicates that the ullage never exceeds 15 % of the lower flammability limit for hydrogen within this tank during the time period represented.

Finally, Figure 2.3d (Allemann, 1992) presents two temperature profiles along the height of Hanford tank 241-SY-101 immediately before and after a release of the kind demonstrated in Figure 2.3c. This inversion of the temperature profile with height demonstrates a sudden upward transfer of thermal energy from the bottom half of the tank to the top half. Inititally, the elevated temperatures in the lower half of the tank are explained by the decay heat generated by fission products within a settled and consolidated waste layer, while the overlying supernatant has a lower, uniform temperature around 48 °C. Retained gas trapped within the consolidated waste layer causes the waste to swell and its bulk density to decrease over time. The release event can be explained by bed swell causing the waste density to drop below that of the supernatant, resulting in a large Rayleigh-Taylor instability, or *rollover* event (Allemann, 1992), as this accounts for both the liberation of hydrogen and the substantial upward transfer of decay heat. It is also noted that the temperature profile after release implies a total waste height tens of centimetres lower than before the event, confirming that a significant volume of gas has been transferred from the waste to the ullage.

2.3.1 Ignition of temporary $H_2 - O_2 - N_2$ atmospheres

Acute hydrogen releases result in a temporary $H_2 - O_2 - N_2$ atmosphere within the tank ullage which can potentially exceed the lower flammability limit (LFL) for hydrogen of 4 % (Gauglitz *et al.*, 2015) for a period until the headspace is ventilated. These mixtures require a coincidental ignition source for the flammability hazard to

manifest. Ingram *et al.* (2014) considered the possibility of an electrostatic ignition from the charge generated by a bursting bubble, but concluded the magnitude of the charge was insufficient to provoke ignition. Alternatively, surface friction from hydraulically powered apparatus used during decommissioning could present a mechanical stimulus for ignition (Averill *et al.*, 2014, 2015). The possibility for spark generation was found to be exacerbated for equipment surfaces contaminated with either wet CMS containing magnesium fines or pyrophoric materials (discussed in Section 2.3.2), indicating potential for ignition of 12 % hydrogen mixtures (Averill *et al.*, 2014, 2015).

2.3.2 Alternative hydrogen hazards

In addition to the flammability risk associated with acute release of hydrogen from nuclear legacy wastes, retained hydrogen poses further risks on reaction with *dewetted* uranium to form uranium hydride according to eq. (2.1) (Orr *et al.*, 2017; Solbrig *et al.*, 1994).

$$2\,\mathrm{U} + 3\,\mathrm{H_2} \longrightarrow 2\,\mathrm{UH_3} \tag{2.1}$$

As long as uranium is wetted by pore water within the soft-sediment, it will preferentially react to form uranium oxide. However, hydride formation at dry spots within the sediment pose an inherent flammability risk due to its pyrophoricity, which has resulted in a number of fires and radioactive releases (Solbrig *et al.*, 1994; Totemeier, 2000). Uranium hydride reacts violently with both oxygen (Solbrig *et al.*, 1994) and anoxic water (Orr *et al.*, 2017):

$$\begin{aligned} 2\,\mathrm{UH_3} + 3.5\,\mathrm{O_2} &\longrightarrow 2\,\mathrm{UO_2} + 3\,\mathrm{H_2O} \\ \mathrm{UH_3} + 2\,\mathrm{H_2O} &\longrightarrow \mathrm{UO_2} + 3.5\mathrm{H_2} \end{aligned} \tag{2.2}$$

Stakebake (1981) notes that flammability hazards similarly pertain to pyrophoric hydrides of plutonium and other actinides.

2.4 Sources of gas generation in consolidated soft sediments

While *in situ* gas generation within consolidated Magnox legacy waste in the UK forms the subject of this research, the bulk of published literature relates to issues of retained gas within natural aquatic sediments and historic American nuclear waste. Hence, in order to better understand the body of available research, it is

useful to briefly outline the various sources of free gas in each of these environments. Marine and other aquatic soft sediments experience *in situ* gas generation from the bacterially mediated decomposition of organic matter, or methanogenesis (Algar & Boudreau, 2010; Boudreau *et al.*, 2001):

$$2\,CH_2O \longrightarrow CH_4 + CO_2 \tag{2.3}$$

where CH_2O represents stoichiometric organic matter.

Equally, all aqueous radioactive wastes of sufficient activty will exhibit some degree of chronic gas generation due to radiolysis, whereby incident ionising radiation causes water molecules to dissociate to highly oxidising free radicals, which in turn react to form volatile species such as hydrogen and oxygen. However, *in situ* hydrogen production is enhanced for historic nuclear wastes due to the nature of materials used in first generation reactors. Uranium metal fuel and aluminium and Magnox alloy cladding are vulnerable to much more extensive corrosion than ceramic uranium dioxide pellets or stainless steel and zirconium alloy cladding used in subsequent designs. Corrosion greatly enhances the problems surrounding *in situ* gas generation in a number of ways, (1) the formation and consolidation of corrosion products gives rise to sludge wastes, as detailed in Section 2.1.3, which trap flammable gas and inhibit its safe ventilation, (2) corrosion weakens and breaches the cladding used to contain fission products and actinides greatly increasing the potency of the radiation field and enhancing hydrogen production by radiolysis, and (3) metal corrosion is itself a reactive source of hydrogen within consolidated sediments. The mechanisms of Magnox corrosion and water radiolysis are discussed in more detail below:

2.4.1 Magnox corrosion

Magnesium corrodes in aqueous environments at ambient temperatures by an electrochemical reaction with water to produce magnesium hydroxide and gaseous hydrogen according to eq. (2.4) (Bradford *et al.*, 1976; Makar, 1990):

$$Mg + 2\,H_2O \longrightarrow Mg(OH)_2 + H_2 \tag{2.4}$$

This net reaction represents the result of two electrochemical half reactions, the cathodic reduction of water to hydrogen and anodic dissolution of magnesium, before the dissolved magnesium and hydroxide ions combine to precipitate brucite

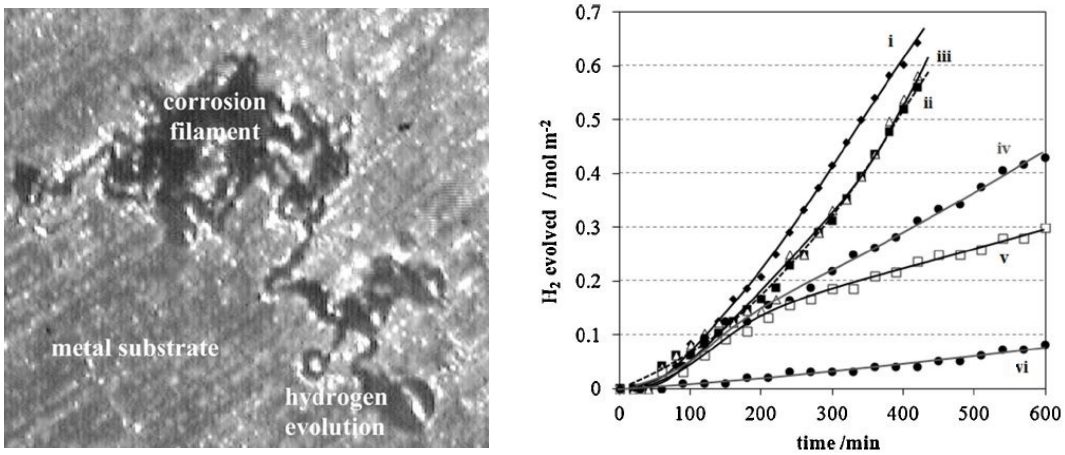

(a) (b)

Figure 2.4: (a) Image demonstrating propagation of a black corrosion filament and hydrogen evolution from a Magnox substrate (Burrows *et al.*, 2005) and (b) hydrogen evolution rates during magnesium alloy corrosion at solution pH of (i) 2, (ii) 4, (iii) 7, (iv) 10, (v) 12 and (vi) 13 (Williams *et al.*, 2013)

(Makar, 1990; Williams *et al.*, 2013):

$$\begin{aligned} \mathrm{Mg} &\longrightarrow \mathrm{Mg^{2+}} + 2\,\mathrm{e^-} \\ 2\,\mathrm{H_2O} + 2\,\mathrm{e^-} &\longrightarrow \mathrm{H_2} + 2\,(\mathrm{OH})^- \\ \mathrm{Mg^{2+}} + 2\,(\mathrm{OH})^- &\longrightarrow \mathrm{Mg(OH)_2} \end{aligned} \tag{2.5}$$

Magnox cladding undergoes oxidation within the high temperature carbon dioxide environment of a gas cooled reactor, developing an oxide film containing some carbon, carbonate and traces of carbide and fluoride (Bradford *et al.*, 1976). This oxide layer too hydrates to brucite during underwater storage and is expelled from the surface, exposing magnesium metal:

$$\mathrm{MgO} + \mathrm{H_2O} \longrightarrow \mathrm{Mg(OH)_2} \tag{2.6}$$

Laboratory scale corrosion tests in Burrows *et al.* (2005) revealed three processes occurring at the metal surface, the formation of a uniform, grey/white hydroxide layer, formation of the black *filaments* shown in Figure 2.4a (Burrows *et al.*, 2005) of magnesium oxide with a hydroxide membrane and the formation of *pits* where magnesium hydroxide is expelled from the surface. The $Mg(OH)_2$ film formed at the surface passivates at high pH (Makar, 1990), maintained in the FGMSP by sodium hydroxide doping (Kirby, 1987), slowing, but not extinguishing, hydrogen production as shown in Figure 2.4b; however the hydroxide film is much less stable than passive films formed on other metals, such as iron, making magnesium alloys particularly vulnerable to pitting (Bradford *et al.*, 1976; Makar, 1990).

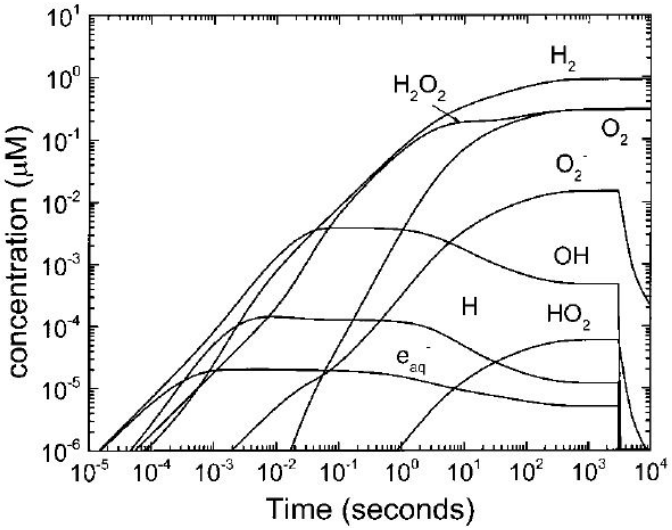

Figure 2.5: Evolution in the molecular yield of radiolysis products for water exposed to 1 h of 25 rad s^{-1} γ-radiation (Pastina & Laverne, 2001)

Magnox corrosion rates are also exacerbated by internal *galvanic* attack due to ppm concentrations of iron impurities within even high purity magnesium (Makar, 1990) and external galvanic attack due to contact between Magnox cladding and exposed steel from the abraded skips in the FGMSP (Kirby, 1987). The rate of corrosion greatly accelerates with increased temperature and with local breaching of the hydroxide film by aggressive anions such as chloride, sulphate and silicate (Kirby, 1987). Conversely, the presence of fluoride ions has been observed to stabilise the hydoxide film by substituting for hydroxide ions and thus inhibit corrosion(Bradford *et al.*, 1976; Burrows *et al.*, 2005).

2.4.2 Radiolysis of water

Molecular dissociation of water by ionising radiation, or radiolysis, produces an array of products including hydrogen atoms, molecular hydrogen, oxygen and hydrogen peroxide. A time-dependent product distribution for water exposed to 25 rad s^{-1} γ-radiation is presented in Figure 2.5 (Pastina & Laverne, 2001), demonstrating that hydrogen is the main product for time-scales greater than 1×10^{-1} s. Radiolysis presents a number of reaction routes for hydrogen production within aqueous radioactive environments. The spur diffusion model (Faraggi, 1973; Hamill, 1970; Hayon & Moreau, 1965; Schwartz, 1969) considers the following reaction set to account for the bulk of the hydrogen yield:

$$\begin{aligned} e^-(aq) + e^-(aq) + 2\,H_2O &\longrightarrow H_2 + 2\,OH^- \\ e^-(aq) + H + H_2O &\longrightarrow H_2 + OH^- \\ H + H &\longrightarrow H_2 \end{aligned} \tag{2.7}$$

Product yields from radiolysis are typically presented using G-values, representing the number of molecules produced per 100 eV incident radiation. Both the product distribution and the magnitude of the G-values differ for ionisation by α, β or $\gamma-$radiation (Dzaugis *et al.*, 2015), however $\gamma-$radiolysis has been the most comprehensively studied. Hydrogen G-values for pure water exposed to γ – radiation, $G(H_2)_\gamma$, are typically reported at 0.44-0.45 (Draganic & Draganic, 1971; Hamill, 1970; Hayon & Moreau, 1965; Pastina & Laverne, 2001) and the hydrogen yields for each form of incident radiation obey the following hierarchy (Dzaugis *et al.*, 2015; Kohan *et al.*, 2013; Mustaree *et al.*, 2014; Pastina & Laverne, 2001):

$$G(H_2)_\alpha \approx \frac{4}{3} G(H_2)_\beta \approx \frac{8}{3} G(H_2)_\gamma \tag{2.8}$$

Of the reactions in Equation (2.7), the first equation is said to account for over 75 % of the hydrogen yield in pure water (Hayon & Moreau, 1965), however this reaction route can be inhibited by competition for electrons and atomic hydrogen with a number of solutes, for instance NO_2^-, NO_3^-, H_2O_2, Cu^{2+}, acrylamide and Ce^{4+}, causing $G(H_2)_\gamma$ to tend to 0.1 at elevated concentrations of these solutes (Hayon & Moreau, 1965). Mercury, lead, chromium, copper and cadmium ions have also been shown to scavenge the atomic hydrogen and electron precursors to molecular hydrogen production from solution and diminish the hydrogen yield (Faraggi, 1973).

2.4.3 Observed gas generation rates

Methanogenic gas generation rates, S_{CH_4}, within marine sediments vary greatly depending on the availability of organic matter (Christensen *et al.*, 2003), spanning five orders of magnitude from 1 µmol m^{-3} d^{-1} to 100 mmol m^{-3} d^{-1}Winterwerp & van Kesteren (2004). Methane generation rates are sometimes reported as a flux per unit surface area of sediment. The organic rich coastal sediments at Cape Lookout Bright, USA (Boudreau *et al.*, 2001; Crill & Martens, 1986) and Eckenforde, Germany (Boudreau *et al.*, 2001; Martens & Albert, 1995) are reported to generate methane at 1.40 ± 0.19 mM m^{-2} h^{-1} and 2.0 mM m^{-2} h^{-1} respectively. Given the orders of magnitude, gas generation can be considered a chronic process; at the fastest gas generation rates in the order of 100 mmol m^{-3} d^{-1} a cubic metre of sediment would require 41 d to generate sufficient volatiles to occupy 0.1 m^3 at ambient temperature and pressure, but would occupy a substantially lower volume still under realistic hydrostatic loads.

Sludge waste within underground tanks at Hanford generates hydrogen, methane and nitrous oxide at rates near the middle of this range, in the order of 1 mmol m^{-3} d^{-1} (Sherwood & Eduardo Sáez, 2014). The 241-SY-101 tank has long been associated

with the fasted gas generation rates, typically recorded around $4\,m^3\,d^{-1}$ (Allemann, 1992). Based on its 23 m tank radius (Allemann, 1992) and an assumed sludge height of 5 m based on the profile of trapped decay heat profile at rest in Figure 2.3d, this would correspond to a hydrogen production rate of $8.02 \times 10^{-5}\,m^3\,m^{-3}\,h^{-1}$.

Hydrogen generation rates within corroded magnox sludge at Sellafield are anticipated to be higher due to the presence of uncorroded metallic cladding swarf. Typical hydrogen generation rates in the MSSS have been measured in the range of 0.004-0.334 $m^3\,h^{-1}$, with the most recently filled compartments, 16-18, having the highest generation rates (Diggle, 2012). The highest recorded hydrogen generation rate during normal operating conditions was $2.5\,m^3\,h^{-1}$, however, elevated rates $> 10\,m^3\,h^{-1}$ were observed during temperature excursions in the 1980s (Diggle, 2012). The MSSS containers are much smaller than the Hanford double shell tanks. For a crude estimate of gas generation rate per unit volume of sludge, it is assumed that each of the MSSS containers are half-occupied by CMS; this would imply hydrogen production rates under standard operating conditions of $5.63 \pm 7.78 \times 10^{-4}\,m^3\,m^{-3}\,h^{-1}$. For comparison with the methanogenic rates of 1×10^{-3}-$1 \times 10^{2}\,mmol\,m^{-3}\,d^{-1}$, $5.63 \times 10^{-4}\,m^3\,m^{-3}\,h^{-1}$ corresponds to an average hydrogen generation rate on a molar basis of $552\,mmol\,m^{-3}\,d^{-1}$, based on the occupancy of a mole of gas at ambient temperature and pressure.

Hydrogen production in the presence of uncorroded metallic swarf is therefore fast relative to methanogenesis and very fast relative to the Hanford underground storage tanks. Given that the Hanford double-shell tanks contain highly active waste by-product from reprocessing, with a potent radiation field to drive radiolysis, this would imply that cladding corrosion supersedes radiolysis as the dominant mechanism of hydrogen generation within the swarf containing wastes, a conclusion which was similarly reached in Streatfield & Hebditch (2006).

2.5 Clarification on nomenclature for consolidated sediments and sedimentary bubbles

In Sections 2.6 and 2.7, observations of bubbles within consolidated sediments and the mechanisms underpinning the different modes of *in situ* bubble growth are discussed. This review draws from both chemical engineering and environmental science research and so, before proceeding, some clarifications are provided on the chosen nomenclature given the disparities in certain key definitions between the disciplines.

Sludge, soft sediment, and sediment are used interchangeably through this thesis in reference to consolidated aqueous particulate beds. Hence, sediment refers to a two-phase material rather than just the solid particulate component. The strength

of these sediments is characterised by their shear yield stress; references to yield stress or yield strength will always relate to the shear yield strength unless tensile yield strength is expressly referred to in the text. The term *pore* is used to refer to the water-filled interstitial gaps between particles within the two-phase sediment and the porosity refers to the volume fraction of the sediment occupied pore water. Since it is difficult to determine the content of water immobilised within aggregates forming the sediment skeleton and the free inter-aggregate water occupying the interstitial pores, the solids content will be characterised simply by the total weight fraction of solids or *solids concentration*, ω, which may also be expressed as a percentage. Assuming the mass of retained gas within the sediment to be negligible, this solids concentration does not evolve during bed swell.

The term *void* is used interchangeably with bubble to refer to pockets of gas within the sediment after the onset of *in situ* gas generation. The voidage or void fraction, ν, represents the instantaneous retained free gas volume normalised by the total instantaneous bed volume, $\nu = \frac{V_g(t)}{V(t)}$. This contrasts with environmental science studies where the terms void and pore are typically synonymous and thus may be occupied by either gas or water.

2.6 Bubbles observed within consolidated soft sediments

Quintessential to the study of bubble growth and release in consolidated sediment is the ability to observe their size, geometry and mobility, however the high solids concentrations prevent the use of optical methods for visualising the bubbles. Acoustic profiling of marine sediments is effective in revealing the presence and extent of retained gas (Anderson *et al.*, 1998; Yuan *et al.*, 1992) as bubbles are effective in reflecting ultrasound, however this is not a realistic approach for gaining detailed size and shape information for individual bubbles. Visual techniques can be employed when clear viscoplastic and viscoelastoplastic gels such as gelatin (Johnson *et al.*, 2002) or Carbopol (Astarita & Apuzzo, 1965) are used as analoges for consolidated sediments. Johnson *et al.* (2002) observed oblate spheroidal bubble growth from a submerged orifice within gelatin solutions and determined from the sawtooth evolution in internal bubble pressure that growth was dictated by fracture propagation. Carbopol cross-linked polymer solutions have been useful in studying the competition between yield stress and buoyant stress as well as the subsequent bubble rise dynamics (Dubash & Frigaard, 2007; Tripathi *et al.*, 2015). However, adoption of these clear gels assumes the two-phase sediment microstructure plays a limited role in bubble growth dynamics. Deformation at the sediment

grain-scale, density heterogeneity and anisotropy of the stress field at the bubble interface are all sacrificed in order to achieve optical transparency.

X-ray computed tomography (CT) represents a non-destructive approach for viewing bubbles within consolidated soft sediments *in situ*, exploiting the large disparity in radiodensity between gas and bulk sediment. Figure 2.6 presents four examples of gas observed within sediments under x-ray CT. The tomographs reveal a conflake shaped fracture in Figure 2.6a, spherical and oblate spheroidal bubbles in Figure 2.6b, a bimodal size distribution of bubbles within Figure 2.6c and departure from spherical geometries within increased shear yield stress and with depth in Figure 2.6d. In addition to the clear influence of sediment strength and depth within the sediment on bubble geometry, the banded regions of light and dark sediment within Figure 2.6b, representing coarse grained sand and fine grained clay respectively, demonstrate a clear influence of particle size on the aspect ratio of retained bubbles (Boudreau *et al.*, 2005; Jain & Juanes, 2009). The physical justification for these unusual bubble geometries will become clearer once the established mechanisms for bubble growth are introduced in Section 2.7.

X-ray CT clearly represents a powerful technique for generating high resolution images of individual bubbles, and for characterising diverse bubble populations, however there is scope for much more extensive use of the technique for analysing bubbles within soft sediments. X-ray CT enables comprehensive quantitative three-dimensional analysis of the evolution of bubble size and shape with time, however this detailed analysis has typically been applied to the case of the individual bubble grown from a submerged orifice, as demonstrated in Figure 2.6a. This doesn't fully capture the diversity of bubble populations as demonstrated by Figures 2.6b to 2.6d, however, the analysis of these larger scale tomography data has been two-dimensional and largely qualitative.

Some recent progress has been made in more determining detailed size distributions for *in situ* bubble populations in Liu *et al.* (2016) and Liu *et al.* (2018), where x-ray tomography was used to observe and characterise methane bubbles within natural clay, silt and sand sediments. The former study was limited by its millimeter scale spatial resolution and 4 mm slice separation (or resolution in third dimension), however, bubbles of roughly 2-18 mm were observed and assessed in relation to their different particle size distributions and nuclear magnetic resonance (NMR) derived pore size distributions. The largest bubbles, in excess of 10 mm, were limited to the clay and slit samples with smaller grain-sizes and finer pore dimensions for reasons which will be discussed in Section 2.7. The CT configuration in Liu *et al.* (2016) was also able to profile gas content with depth on a scale of 0.3 m, revealing a concentration of free gas in the shallow bed region, particularly for the silt and sand samples. The configuration in Liu *et al.* (2018), achieving greater imaging resolution and shorter imaging intervals, demonstrated that gas

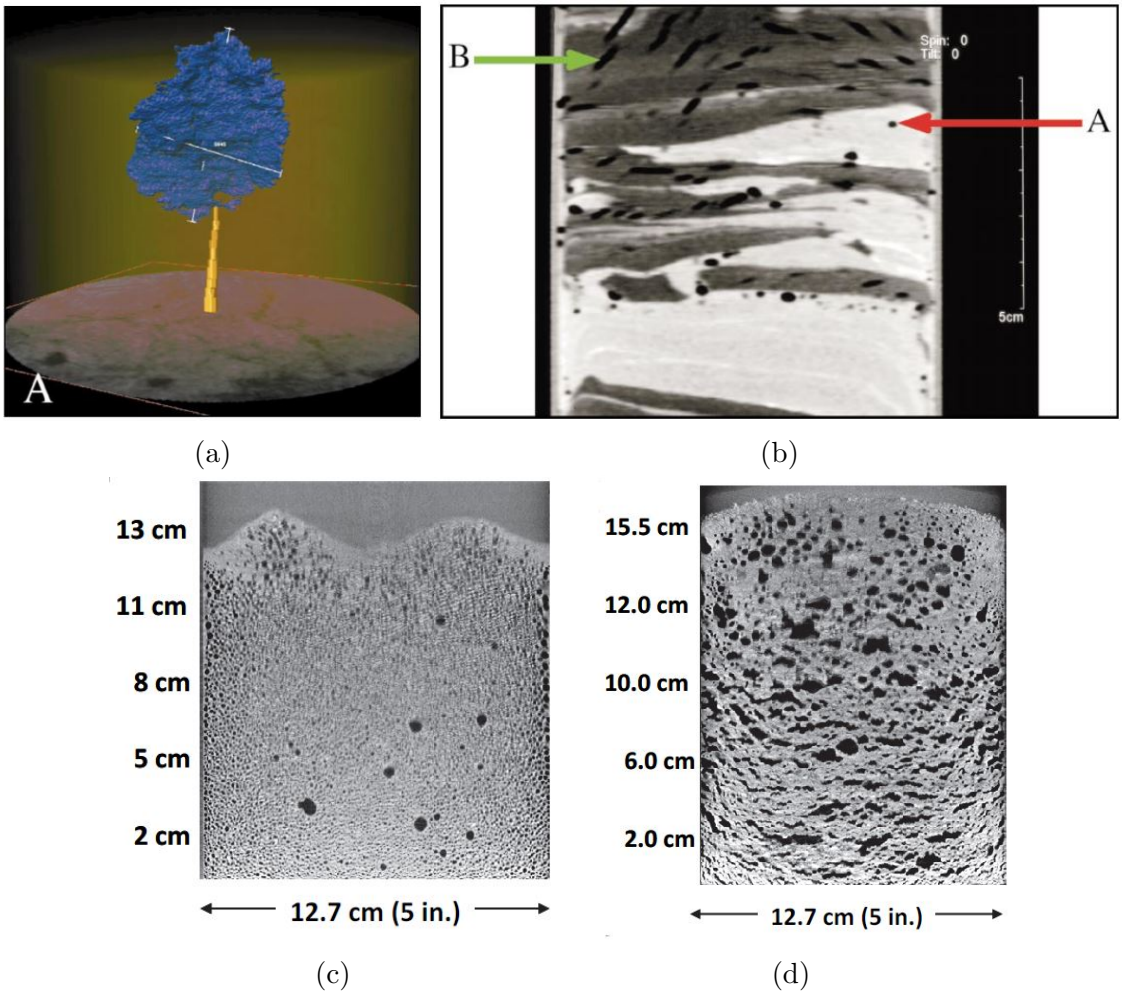

Figure 2.6: Examples of bubbles observed within various consolidated soft sediments using x-ray CT including (a) a cornflake or penny shaped crack within mud from Cole Harbour, Nova Scotia, Canada (Best *et al.*, 2006; Boudreau *et al.*, 2005), (b) spherical and oblate spheroid bubbles within layered carbonate sand (A) and clay (B) layers respectively (Boudreau *et al.*, 2005), and bubbles within (c) 38 and (d) 680 Pa yield stress kaolin (Gauglitz *et al.*, 2012)

release in response to a reduction in hydrostatic head was governed the mobility of the smallest bubbles along the largest macropore networks, rather than by buoyant bubble rise.

Algar *et al.* (2011a) discusses how bubble growth by fracture can enable otherwise stable bubbles to migrate upwards through the sediment by a *burrowing* (Dorgan *et al.*, 2005) mechanism, while (Boudreau *et al.*, 2005) discusses the possibility of small bubbles moving slowly through the connected void-spaces. Tomography can achieve the spatial and temporal resolutions necessary to track bubble migration by fracture mechanics, however the attachment forces at the nozzle of the submerged orifice in Figure 2.6a mask the onset of bubble migration. Connectivity within the void-space certainly appears plausible from Figures 2.6c and 2.6d (Gauglitz *et al.*, 2012) and from tomographs presented in Liu *et al.* (2016), however limitations in resolution, and artefacts due to bubble growth during the scan in the former instance, prevent a clear gas migration pathway from being established.

Recent advances in tomography are likely to overcome many of these issues. Commercial microtomography can visualise features to spatial resolutions close to a micron for small experimental scales and 20-30 min scan times (Selomulya *et al.*, 2006). Clinical CT is often much faster, with scan times in the order of a second, than the *cone-beam* tomography employed by each example image in Figure 2.6, while ultrafast benchtop tomography has enabled imaging of centimetre scale bubbles within fluidised beds at frequencies of 10 000 Hz (Muddle, 2011). In recent years, synchrotron x-ray tomography has overcome the compromise between spatial and temporal resolution to enable visualisation of transient behaviour at the micro-scale (Dobson *et al.*, 2016), including dynamic bubble connectivity within porous media (Reynolds *et al.*, 2017) and Haines jumps (Berg *et al.*, 2013).

2.7 Mechanisms of bubble growth and retention in consolidated soft sediments

Immediately after nucleation, growth in equivalent spherical bubble radius, $r_b(t)$, will be governed by diffusion to the bubble, and is characterised by a square root dependence on time, t (Boudreau, 2012):

$$r_b(t) \approx 0.31 \left(\frac{2(\phi_\infty - \phi^*) D_{eff} t}{\phi_g} \right)^{\frac{1}{2}} \tag{2.9}$$

where ϕ_∞ is the gas concentration in the porewater far from the bubble, ϕ^* is the porewater gas solubility, ϕ_g is the concentration in the bubble and D_{eff} is the effective diffusivity of volatiles through the porewater, corrected for the

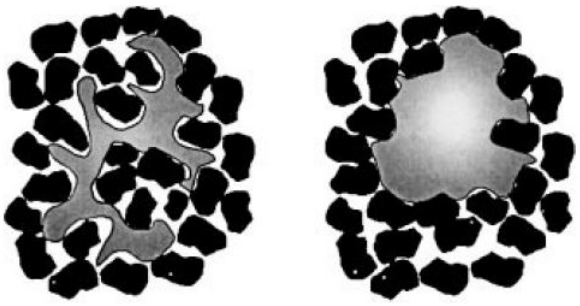

(a) (b)

Figure 2.7: Schematics of bubble growth by (a) capillary invasion and (b) elastic cavity expansion(Kam *et al.*, 2001b)

tortuosity of the sediment. This stage is likely to be brief as bubbles quickly grow to the scale of fine pores or capillaries within soft sediments, at which point the bubble encounters the sediment matrix and the mechanics of bubble growth will depart from those in conventional clear Newtonian fluids (Boudreau, 2012). Soft sediments, unlike Newtonian fluids, are able to support a stress and so the bubbles internal pressure will rise as the sediment matrix resists bubble expansion (Algar & Boudreau, 2010). The excess internal bubble pressure, ΔP, given by the difference in internal bubble pressure, P_b, and surrounding sediment, P_0, can be relieved by bubble growth. Once the bubble occupies the body of its host pore, subsequent growth requires that either the bubble must displace the sediment to create space, or the sediment must deform the bubble for intrusion into adjacent pore space; these two possibilities are represented schematically in Figure 2.7 (Kam *et al.*, 2001b).

Three mechanisms are discussed in relation to macroscopic, beyond the pore-scale, bubble growth within soft sediments. These are *capillary invasion*, *cavity expansion*, and *tensile fracture*. The relevant mechanism will be governed by the mechanical properties, microstructure and wetting characteristics of the soft sediment (Boudreau, 2012).

Capillary invasion

Capillary invasion occurs when the growing bubble encounters the sediment matrix and the sediment structure remains rigid, forcing the bubble to intrude into the dendritic pore network, as demonstrated by Figure 2.7a. Resistance to capillary invasion is governed by the Young-Laplace equation, eq. (2.10) (Kam & Rossen, 1999):

$$\Delta P_i = P_b - P_{pw} = \frac{2\gamma cos(\theta)}{r_{th}} \tag{2.10}$$

where ΔP_i is the excess bubble pressure required to intrude through a capillary throat, given by the difference between the bubble pressre, P_b, and the pore water pressure, P_{pw}; θ is the three-phase contact angle, γ is the interfacial surface tension between porewater and gas, and r_{th} is the radius of sedimentary pore throats. Equation (2.10) implies that soft sediments with small grain sizes and correspondingly small pore throat radii will resist capillary invasion due to the high pore entry pressures. Likewise, if the sediment is well wetted by the porewater, with negligible contact between solid and gas, capillary invasion will be energetically unfavourable (Boudreau, 2012) as $\Delta P_i \rightarrow$ maximum as $cos(\theta) \rightarrow 1$.

Cavity expansion

Cavity expansion occurs when the bubble cannot invade adjacent pore space by capillary invasion and so the bubble creates space for growth by expanding its host cavity; this mechanism is characterised by more spherical bubble geometries as indicated by Figure 2.7b (Kam *et al.*, 2001b). Wheeler (1988a) proposed that, as the bubble displaces sediment grains to create space, the combined sediment and pore water within the soft sediment behave as one continuous phase. Cavity expansion theory states that the greater the mechanical strength of the soft sediment, characterized according to its shear yield stress, τ, and shear modulus, G, the greater the resistance to expansion of the host pore (Katsman *et al.*, 2013; van Kessel & van Kesteren, 2002). An expression for the excess bubble pressure required to expand the cavity, ΔP_e, given by the difference between the bubble pressure and the opposing mean total stress acting on the sediment, σ (Wheeler *et al.*, 1989) is provided in eq. (2.11) (van Kessel & van Kesteren, 2002), however, a more comprehensive mathematical model for cavity expansion is detailed in Section 2.7.1.

$$\Delta P_e = P_b - \sigma = \frac{4}{3}\tau\left(1 + ln\left|\frac{G}{\tau}\right|\right) \tag{2.11}$$

The relative contibutions of bubble growth by cavity expansion and capillary invasion to total hold up can be determined experimentally as the former manifests in bulk bed expansion whereas instances of capillary invasion manifest in water displacement from the bed (Liu *et al.*, 2016, 2018). These studies determined that weak (< 15 Pa) clay with fine sedimentary pores exhibited over 80 % of its bubble growth by cavity expansion, whereas high strength (< 5 kPa) consolidated sand with much coarser sedimentary pores promoted over 80 % capillary invasion and expanded to lower ultimate void fractions (Liu *et al.*, 2016, 2018). This accords well with eqs. (2.10) and (2.11) which state that cavity expansion and capillary invasion scale with yield strength and pore throat radius respectively.

Tensile fracture

Many natural marine sediments (Algar *et al.*, 2011a; Boudreau *et al.*, 2005) and wastes in long-standing nuclear legacy facilities (Burrows *et al.*, 2005; Gregson *et al.*, 2011; McCracken & Eilbeck, 2005) are characterised by fine grain sizes and many have consolidated to high yield stresses ($\tau > 1\,\text{kPa}$) over several decades (Hastings *et al.*, 2007; van Kessel & van Kesteren, 2002) and thus present considerable resistance to the above two mechanisms. However, while the resistance to elastic cavity expansion scales with the yield stress, a material's resistance to tensile fracture typically diminishes with increased yield stress as high strength materials are, in general, less prone to plastic deformation in the vicinity of pre-formed cracks (Broek, 1982; Mughrabi, 1992).

Hence, for fine grained, high strength materials, the excess bubble pressure may rise until it exceeds the combined compressive and tensile strengths of the sediment, forming cracks along the direction of minimum compressive stress (Boudreau, 2012) which may expand by a process of *tensile fracture* (Boudreau, 2012; Dorgan *et al.*, 2005; Johnson *et al.*, 2002). A rock mechanics study by Potyondy & Cundall (2004) proposed that the internal length scale of the fracture toughness is determined by the grain size, leading Jain & Juanes (2009) to conclude that the excess bubble pressure for fracture, $\Delta P_f = P_b - \sigma$, scales with the inverse square root of the grain size, implying that fracture will be energetically favourable in comparison to capillary invasion in very fine grained sediments. In addition to very high strength sediments exhibiting reduced fracture toughness, K_{1c}, it is anticipated that significant yield strength is required to support open fractures for long timescales under substantial lithostatic and hydrostatic loads (van Kessel & van Kesteren, 2002). A linear elastic fracture mechanics (LEFM) model has been used to describe the stress distribution in the proximity of a crack (Broek, 1982; Johnson *et al.*, 2002), as detailed in Section 2.7.2.

2.7.1 The mathematics of deformation at the boundary of a spherical bubble (cavity expansion)

Wheeler (1988a) presents a useful schematic of a large spherical bubble, much larger than the particles or interstitial pores, consistent with bubble growth within soft sediments by cavity expansion. The excess internal bubble pressure, ΔP, (above that of the surrounding pore water, P_{pw}) can be determined from the radii of curvature, r_m, of the menisci bridging the grains at the bubble sediment interface according to eq. (2.12) (Wheeler, 1988a):

$$\Delta P = P_b - P_{pw} = \frac{2\gamma}{r_m} \tag{2.12}$$

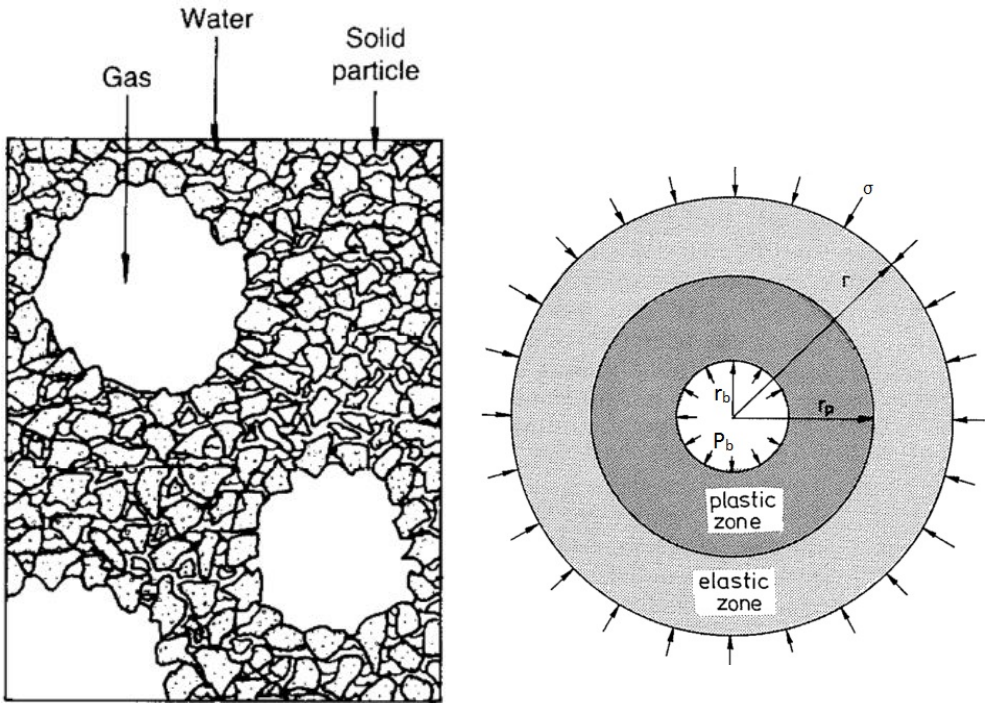

(a) (b)

Figure 2.8: Schematics of (a) a large spherical bubble within a soft sediment consistent with growth by cavity expansion (Terrones & Gauglitz, 2003) and (b) a unit cell for an elastic-perfectly plastic cavity expansion model, treating the sediment (solids and pore water) as a continuum (adapted from Wheeler *et al.* (1989))

However, a simpler model, presented by Wheeler *et al.* (1989), considers a perfectly spherical bubble within a spherical unit cell of sediment treated as a single continuous phase. If the sediment is treated as an elastic-perfectly plastic material, and its response to the excess bubble pressure (above that of the mean stress acting on the unit cell) is linearly elastic until it yields, the sediment will first begin to yield at the bubble surface when the excess bubble pressure exceeds the value determined by eq. (2.15) (Wheeler *et al.*, 1989):

$$\Delta P = P_b - \sigma > \frac{4}{3}\tau\left(\frac{r^3 - {r_b}^3}{r^3}\right) = \frac{4}{3}\tau(1-\nu) \tag{2.13}$$

This, condition can be achieved either by (1) a reduction in the mean stress acting on the unit cell (Chadwick, 1959), possibly arising due to fluctuations in hydrostatic head above the bed, or (2) an increasing internal bubble pressure due to diffusive supply of volatiles to the bubble (Chadwick, 1959). Once this critical excess bubble pressure for yielding is exceeded, a plastic region spreads from the surface of the bubble as indicated by Figure 2.8b (Wheeler *et al.*, 1989). As the plastic region spreads, and assuming a perfectly plastic reponse on yielding, the excess bubble pressure relates to the radius of the plastic region, r_p, according to

eq. (2.14) (Wheeler *et al.*, 1989):

$$\begin{aligned}\Delta P &= \frac{4}{3}\tau\left(\frac{r^3 - {r_p}^3}{r^3} + \ln\left(\frac{r_p}{r_b}\right)\right) \\ &= \frac{4}{3}\tau\left(1 - \nu\frac{G}{\tau} + \ln\left(\frac{G}{\tau}\right)\right)\end{aligned} \tag{2.14}$$

When the plastic region extends to the boundary of the unit cell, analogous to the overlapping of plastic regions between neighbouring bubbles, a *collapse mechanism* is instigated, at which point eq. (2.14) simplifies to (Wheeler *et al.*, 1989):

$$\Delta P = \frac{4}{3}\tau\ln\left(\frac{1}{\nu}\right) \tag{2.15}$$

This model represents a greatly simplified model of cavity expansion, relying on the assumptions of an isotropic stress acting at the unit cell boundary and an initial stress condition which is independent of the stress history experienced by the sediment. Furthermore, the elastic-perfectly plastic continuum model does not capture the full complexity of a soft sediment's response to stress. Terrones & Gauglitz (2003) describes soft sediments more realistically as *elastoviscoplastic* solids with a dominant elastic modulus at small finite strains, and as a non-Newtonian fluid at elevated strains and strain-rates. The introduction of an elastoviscoplastic mechanical model, along with anisotropic deformation through Poisson's ratio, results in a significantly more complex mathematical framework for cavity expansion in Terrones & Gauglitz (2003). However, the introduction of surface tension dependency is curious. Surface tension only becomes relevant if the internal bubble pressure is expressed relative to the pore fluid pressure, which is a difficult property to characterise and would not be relevant to a continuum based sediment deformation model (Wheeler *et al.*, 1989).

Each of these models of cavity expansion would benefit greatly from experimental validation of the evolution in internal bubble pressure during growth. These measurements have been achieved in Johnson *et al.* (2002) by gas injection from a submerged orifice with a highly responsive and accurate in-line pressure sensor, but only for high strength sediments prone to growth by fracture. There is no reason that the same methodology could not be applied to a sediment of reduced yield strength and greater fracture toughness to validate the mathematics of cavity expansion. For an initial investigation to generate concurrent strain measurements, along with bubble pressure data, a clear elastoviscoplastic gel such as Carbopol or gelatin could be used as an analogue as two phase consolidated sediments would require spatial and temporal resolutions consistent with synchrotron x-rays to generate strain data with adequate frequency. Clear elastoviscoplastic gels would also enable photoelastic stress analysis of the stress field surrounding the bubble as outlined by Dorgan *et al.* (2005).

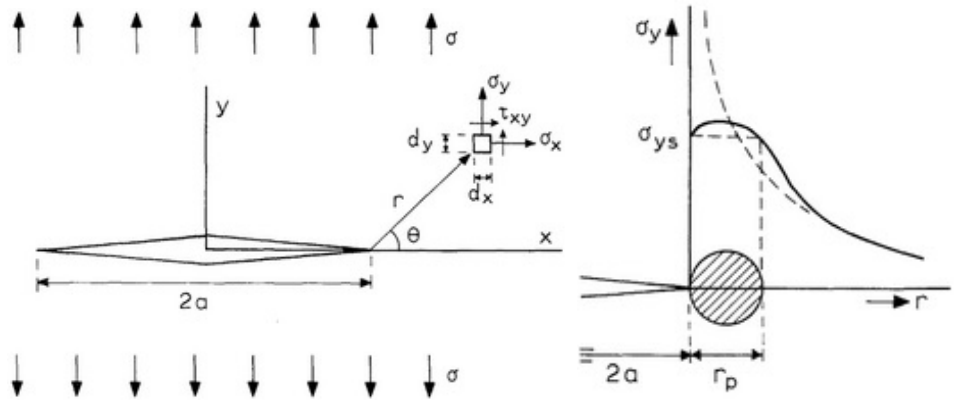

(a) (b)

Figure 2.9: Schematic (a) of a crack of length $2a$ within an infinite plate under an imposed tensile stress normal to the crack of magnitude σ, demonstrating the coordinates, r and θ, used to describe the local stress field and (b) deviation of the assumed stress field within the plastic region close to the crack tip (Broek, 1982); here σ_{ys} denotes the yield stress rather than τ and r_p represents the size of the plastic deformation region

2.7.2 The mathematics of crack propagation under linear elastic fracture mechanics (LEFM)

LEFM was first employed in relation to soft sediments in Johnson *et al.* (2002) to explain crack propagation within marine sediments after concluding that the *sawtooth* evolution in bubble volume and internal bubble pressure observed during bubble growth implied growth dictated by fracture. LEFM was originally developed for more brittle glass and ceramic materials, however the application was deemed to be much broader after it was subsequently observed that low stress fractures induced by small cracks in high strength materials were also brittle in nature (Broek, 1982). LEFM has since been used in a number of environmental research studies to rationalise complex bubble geometries, including penny or disk shaped cracks, observed within softer test materials using x-ray computed tomography (Abegg & Anderson, 1997; Algar *et al.*, 2011a; Barry *et al.*, 2010; Best *et al.*, 2006; Gardiner *et al.*, 2003; Katsman, 2015).

The model considers the stress field, σ_{ij}, around the tip of a crack within a material subjected to a tensile stress, σ, normal to the orientation of the crack, as demonstrated by the schematic in Figure 2.9a (Broek, 1982). For a crack of length $2a$ within an infinite plate, the stress field near the crack tip, at coordinates r and θ, is governed by the stress intensity factor, K_1, which itself is dictated by length of the crack and the applied stress, according to eq. (2.16):

$$\sigma_{ij}(r,\theta) = \frac{K_1}{2\pi r} f_{ij}(\theta)$$
$$K_I = \sigma\sqrt{\pi a} \tag{2.16}$$

Hence, a crack of length $4a$ will demonstrate the same stress field under an applied stress of σ as a crack of length a under a stress of 2σ. For a gas filled crack within a consolidated soft sediment, the tensile stress is dictated by the crack's excess internal pressure, ΔP. For a penny shaped, or spheroidal, crack, the stress intensity factor would be (Johnson *et al.*, 2002):

$$K_I = \frac{2}{\pi}\Delta P\sqrt{\pi a} \tag{2.17}$$

The scaling of the stress field with inverse distance from the crack tip, as predicted by eq. (2.16) and demonstrated in Figure 2.9b (Broek, 1982), represents an elastic response and breaks down within the *plastic region* close to the crack tip, $2a < r < 2a + r_p$, where the stress is better approximated by the tensile yield stress, σ_{ys} (see Figure 2.9b for reference), which is anticipated to be in the order of double the shear yield strength for such consolidated sediments (Gauglitz *et al.*, 1995) prior to the onset of gas generation. The capacity of a material to resist fracture can be characterised by the fracture toughness, K_{1c}, a material property determined from the critical stress at the onset of fracture, σ_c, observed for a number of crack sizes. This fracture toughness, defined for a penny shaped crack, or oblate spheroid, in eq. (2.18), typically scales with inverse yield stress, as high strength materials tend to exhibit less plastic deformation at the crack tip then low strength, ductile materials (Mughrabi, 1992). However, following this logic, materials of very low strength may exhibit plastic regions at fracture similar in scale to the crack length. Under these conditions Figure 2.9b makes it clear that LEFM will no longer apply. Boudreau (2012) discusses fracture toughness values in the 80-1300 Pa $\sqrt{\text{m}}$ range in relation to marine soft sediments, increasing substantially with depth (Boudreau, 2012).

$$K_{1c} = \frac{2}{\pi}\Delta P_c\sqrt{\pi a} \tag{2.18}$$

Normal to the crack's longest axis, and parallel to the tensile stress, the width of the crack is labelled the *crack opening displacement*, COD, which will be maximum, COD_{max}, at the centre of the crack, $x = 0$. The COD can be estimated along the crack length, $0 \leq x \leq a_c$ as a function of the internal bubble pressure, crack length

and the Young's modulus of the material according to eq. (2.19):

$$\begin{aligned} COD &= \frac{4\Delta P}{E}\sqrt{a^2 - x^2} \\ COD_{max} &= \frac{4\Delta P}{E}\sqrt{a^2} \end{aligned} \tag{2.19}$$

This simplified model of the crack is that of an oblate spheroid of major axis a and minor axis $COD_{max}/2$, and so the volume, V, is given by:

$$V_b = \frac{4}{3}\pi a^2 \frac{COD_{max}}{2} = \frac{8\pi a^3 \Delta P}{3E} \tag{2.20}$$

Hence, combining eq. (2.20) with eq. (2.18) enables the characterisation of the critical excess bubble pressure, ΔP_c for crack propagation as a function of crack volume, revealing a $V^{-\frac{1}{5}}$ dependency (Johnson *et al.*, 2002):

$$\Delta P_c = \left(\frac{1}{24}\right)^{\frac{1}{5}} \pi^{\frac{4}{5}} \left(\frac{k_{1c}^6}{V_b E}\right)^{\frac{1}{5}} \approx 1.32 \left(\frac{K_{Ic}^6}{V_b E}\right)^{\frac{1}{5}} \tag{2.21}$$

Following eq. (2.19), LEFM also enables prediction of the aspect ratio, AR, or its inverse, AR^{-1}, of spheroidal cracks within the sediment from the fracture toughness and Young's modulus (Johnson *et al.*, 2002) or alternatively the excess bubble pressure and Poisson's ratio, k_ν, (Barry *et al.*, 2010; Sneddon, 1946) using eq. (2.22):

$$\begin{aligned} AR^{-1} &= \frac{COD_{max}}{a_c} = \frac{2K_{1c}}{E}\sqrt{\frac{\pi}{a_c}} \\ AR^{-1} &= \frac{4(1-k_\nu^2)\Delta P}{\pi E} \end{aligned} \tag{2.22}$$

Thus, LEFM can predict a size and geometry of bubbles in the fracture regime using relatively few material properties, only the fracture toughness, Young's modulus and Poisson's ratio. However, there is not a wealth of literature on Young's moduli for marine sediments (Johnson *et al.*, 2002), and limited information for nuclear sediments (Wells *et al.*, 2010), and where values are available (Raju & Ramana, 1986), they substantially under-predict the COD_{max} observed from x-ray CT (Johnson *et al.*, 2002). Similarly, linear regression of Equation (2.22) and Equation (2.21) results in unrealistically small predicted Young's moduli, four orders of magnitude less than those acoustically measured in Raju & Ramana (1986). Hence, many soft sediments prone to fracturing may exhibit prohibitively large regions of plastic deformation for adequate modelling of fracture propagation using LEFM, despite its qualitative usefulness.

2.8 Mechanisms of gas release

For the purpose of this study, gas release from consolidated soft sediments is characterised as either *chronic*, representing slow continuous release from the bed, or *acute*, typified by episodic releases of larger volumes of gas. Another useful distinction lies between *quiescent* (Sherwood & Eduardo Sáez, 2014) releases from undisturbed sediments and releases induced by external perturbations. *Induced* releases are likely to merit increased attention as waste is evacuated from the MSSS due to the physical disturbances anticipated during transport and stacking of the 3 m^3 storage containers, however this work will focus on chronic and acute releases from macroscopically stagnant wastes, typical for nuclear legacy waste in its current environment.

2.8.1 Chronic release mechanisms

Aqueous diffusion

Gaseous species can be released either as free gas (bubbles) or from the aqueous phase as dissolved gas. Release from the aqueous phase requires that volatile species diffuse through pore water to the bed periphery into a supernatant or, in the absence of a supernatant, traverse an air-water interface at the top of the bed. The relative contribution of diffusive and free gas release appears to vary significantly; Katsman *et al.* (2013) reports that 98 % of methane release from shallow lakes originates from free, rather than dissolved gas. Conversely, Gogo *et al.* (2011) used laser spectroscopy to demonstrate that only 40.7-66.5 % of methane release from peatlands results from the flux of bubbles, supported by bubbling emissions of 17.0-51.5 % of the total methane emissions from wetlands observed in Christensen *et al.* (2003), implying that diffusion losses may be comparable in magnitude to free gas release in some instances.

Buoyant bubble ebullition

Buoyant bubble *ebullition* (Katsman *et al.*, 2013), also referred to as *fluidisation* (Boudreau, 2012) or *bubbling* (Keller & Stallard, 1994), is analogous to bubble release from conventional clear Newtonian fluids. However, consolidated soft sediments differ substantially from Newtonian fluids in that they are able to support a stress, and just as they can resist an excess internal bubble pressure during growth, they can also resist a finite buoyant stress before the bubble begins to rise. The condition where a *viscoplastic* material is able to resist the buoyant stress and hold a bubble static indefinitely is the *stopping condition* (Dubash & Frigaard, 2004). A useful dimensionless term for characterising the stopping condition is the ratio of

yield and buoyancy stresses, which defines the yield parameter, Y_g(Atapattu *et al.*, 1995):

$$Y_g = \frac{\tau}{(\rho_l - \rho_g)gr_b} \approx \frac{\tau}{\rho_l g r_b} \tag{2.23}$$

Some studies (Dubash & Frigaard, 2007; Tsamopoulos *et al.*, 2008) alternatively label this ratio the Bingham number, Bn, which conventionally defines the ratio of buoyancy and viscous stresses, $\frac{\tau r_b}{\mu_0 u_b}$, however it is argued that the Bingham number reduces to the yield parameter in the low velocity limit where the Froude number, $\mathrm{Fr} = \frac{u_b}{\sqrt{g r_b}}$ is much less than unity (Dubash & Frigaard, 2004). The stopping condition requires that the yield parameter exceeds a critical value, $Y_g > Y_{gc}$ (Dubash & Frigaard, 2004, 2007). The buoyant stress scales with bubble radius and so the yield parameter diminishes during bubble growth, implying that growth to a critical radius, r_{bc}, which scales with the yield stress, is required for buoyant release. Hence, characterisation of viscoplastic flow behaviour above the yield stress is irrelevant to the stopping condition. Until the bubble begins to rise, all it sees is the yield stress; the consistency, power law index and type of yield stress fluid will impact the subsequent bubble velocity but are inconsequential to whether a bubble is retained or released (Dubash & Frigaard, 2004).

The simplicity of this stopping criteria and the possibility of formulating optically transparent viscoplastic test materials from cross-linked polymer solutions, such as Carbopol (Astarita & Apuzzo, 1965; Atapattu *et al.*, 1995; Dubash & Frigaard, 2007; Tsamopoulos *et al.*, 2008), implies that the experimental determination of the critical yield parameter ought to be trivial. However, efforts to experimentally determine critical yield parameters have encountered a number of issues:

- Achieving a solitary static bubble within yield stress fluid is surprisingly difficult (Dubash & Frigaard, 2007). A bubble generated at a submerged orifice will remain attached until the surface tension force at the orifice, $F_\gamma = \pi d_o \sigma$, (Pamperin & Rath, 1995) and the yield stress of the fluid are overcome, where d_o is the orifice diameter. Hence, any bubble which detaches will have significant excess buoyant force and will rise through the fluid, requiring extrapolation back to the zero-velocity condition rather than direct observation of static bubbles.

- Extrapolation back to a zero velocity condition requires repeatability which is also difficult to achieve with laboratory viscoplastic fluids (Atapattu *et al.*, 1995). Creeping sphere motion in Carbopol has been shown to exhibit shear history dependence for up to 72 h after a previous disturbance (Dubash & Frigaard, 2007).

- As bubbles grow and the yield parameter increases, the influence of surface tension diminishes in relation to the yield stress, $\tau > \frac{\gamma}{r_b}$ (Dubash & Frigaard, 2004), resulting in diverse, complex, non-spherical bubble geometries and a more ambiguous relationship between the critical yield parameter and the bubble size at release.

There appears to be mild disagreement in the literature regarding appropriate values for the yield parameter. Two theoretical models were developed in Dubash & Frigaard (2004) to predict the critical yield parameter for particular bubble geometries; the two models (1) bound the velocity field using a minimum strain rate, $\dot{\varepsilon_{min}}$, condition and (2) bound the stress field by minimising the stress within the non-yielding region of the fluid respectively (Beris *et al.*, 1985; Dubash & Frigaard, 2004). For a spherical bubble these models predict critical yield parameters in the range of $\frac{1}{\sqrt{3}} < Y_{gc} < \frac{1}{\sqrt{2}}$. However, experimental validation in Dubash & Frigaard (2007) suggests these values are somewhat conservative, while finite element analysis in Beris *et al.* (1985) also determined a much smaller critical yield parameter of 0.143.

This finds excellent agreement with the theoretical analsyis in Wheeler (1990) where the elastic-perfectly plastic sediment model in Wheeler *et al.* (1989) is extended to predict expansion at the shallow surface and contraction at the tail. The model anticipates buoyancy to yield stress ratios of 7.5-8 , corresponding to yield parameters (the inverse of this ratio) of 0.125-0.133 (Wheeler, 1990). Slightly smaller values, in the 0.023-0.061 range were found for falling bronze and stainless steel spheres within Carbopol solutions in Atapattu *et al.* (1995). Assuming critical yield parameters in the broad 0.023-0.143 range, CMS of 100 Pa yield stress and 1500 $\mathrm{kg\,m^{-3}}$ density would inhibit the rise of bubbles less than 0.048-0.295 m. Bubbles of around 3 mm diameter were found to be more typical following hydrogen peroxide decomposition within 7 Pa yield stress sediments of kaolin and bentonite (Sherwood & Eduardo Sáez, 2014), raising questions as to whether ebullition is realistic under quiescent sediment conditions.

Keller & Stallard (1994) notes that gas flux by bubble ebullition in marine soft sediments closely correlates with wind speed measurements, as shown by Figure 2.10 (Keller & Stallard, 1994), and diminishes with increased water depth above the sediment, implying that most bubble ebullition is indeed induced by transient rather than quiescent ambient conditions. Furthermore, Wheeler (1990) argues that under cyclic loading the critical yield parameter, and therefore the critical bubble diameter for ebullient release, can be significantly diminished in comparison to purely quiescent conditions, enabling the bubble to ratchet upward through the sediment by incrementally expanding at the shallow surface and contracting at the shallow surface. Ultimately, it would appear that conditions are unfavourable

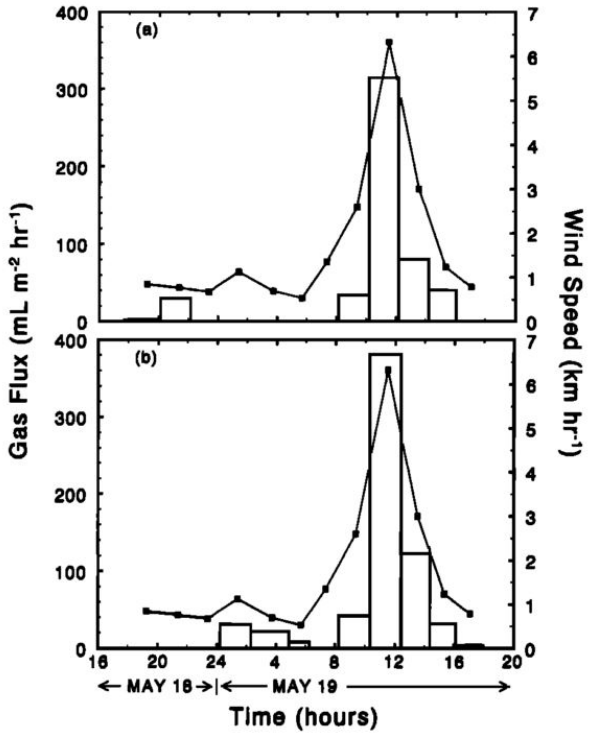

Figure 2.10: Correlation between gas flux from marine soft sediments by bubble ebullition (bars) and wind velocity (lines) (Keller & Stallard, 1994)

for buoyant bubble release under stagnant conditions for all but very low strength sediments, atypical within the MSSS containers.

Bubble rise by viscoelastic fracture

Algar *et al.* (2011a) and Algar *et al.* (2011b) present an alternative mechanism for rise of individual bubbles which may be applicable within sediments strong enough to inhibit quiescent ebullition. When a vertically oriented crack within a pressure field which increases linearly with depth grows to sufficient dimensions, the pressure difference across the height of the bubble becomes significant causing stratification of gas within the bubble (Algar *et al.*, 2011a). Fracture propagation into the plastic region at the shallow surface of the bubble, or crack *tip*, will induce a compressive stress at the crack tail forcing it to close, resulting in a characteristic *teardrop* shaped bubble. Repeated fracturing at the advancing crack tip and annealing at the crack tail causes the bubble to rise by *tunneling* through the sediment (Dorgan *et al.*, 2005).

The stress intensity factor at the crack tip, $K_1^{<+a>}$ is given by eq. (2.24) (Algar *et al.*, 2011a):

$$K_1^{<+a>} = \frac{10}{3\pi}\rho_s g a\sqrt{\pi a} + \frac{2}{\pi}P^{<-a>}\sqrt{\pi a} \tag{2.24}$$

where $P^{<-a>}$ is the pressure at the crack tail. Rise by fracture propagation

will occur when this stress intensity factor exceeds the fracture toughness. This criterion is used to define a critical crack length above which the bubble will rise, $2a_{cr}$ (Algar *et al.*, 2011a):

$$a_{cr} = \left(\frac{3K_{1c}\sqrt{\pi}}{10\rho_s g} \right)^{2/3} \tag{2.25}$$

Following eq. (2.22), the corresponding crack volume at release is given by eq. (2.26):

$$V_{cr} = \frac{16(1-k_\nu)^2 \rho_s g a^4}{3E} \tag{2.26}$$

In the aftermath of bubble release the partially annealed sediment will have a lower fracture toughness than the undisturbed material prior to release, thereby enabling the subsequent release of smaller cracks in the locality (Algar *et al.*, 2011a).

Channel formation

Merging of cracks formed by tensile fracture as described in Section 2.7 with near surface drainage channels, typically only a few tens of centimetres deep, can result in much larger channels sometimes several metres in depth (van Kessel & van Kesteren, 2002). Soft sediments can support stable channels up to a maximum depth of l_{max} (van Kessel & van Kesteren, 2002):

$$l_{max} = \frac{\tau(1+e)}{K_0(\rho_s - \rho_l)g} \left(1 + ln\left(\frac{r_{ch}^2 - d_p^2}{d_p} \right) + ln\left(\frac{E}{2\tau(1+k_\nu)} \right) \right) \tag{2.27}$$

where r_{ch} is the channel radius, d_p is the apparent particle size, whether individual grains or flocs, K_0 is the ratio of horizontal to vertical effective stress (equivalent to $\frac{k_\nu}{1-k_\nu}$) and e is the void ratio given by:

$$e = \frac{\rho_s - \rho_l}{\rho_l - \rho_g} > 1 \tag{2.28}$$

These channels can transport both gas and water from the bed, with deep channels enabling significant bubble rise velocities sufficient to erode the channel walls over time (van Kessel & van Kesteren, 2002). Following eq. (2.27), highly consolidated, high yield stress sediments can support stable open drainage channels to much greater depths. van Kessel & van Kesteren (2002) discusses sediments with yield stresses in the order of 10 kPa required for the formation of stable channels on a scale of several metres at low deformation, indicating a chronic release mechanism unique to very highly consolidated waste deposits.

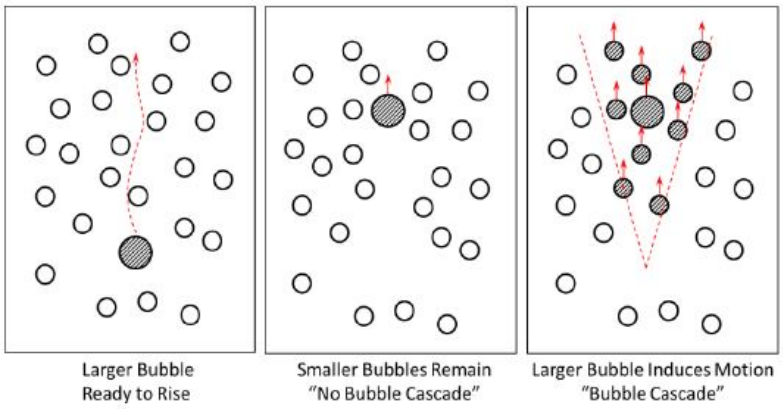

Figure 2.11: Schematic demonstrating a cascade of bubbles liberated by the motion of a local buoyant bubble (Gauglitz *et al.*, 2015)

2.8.2 Acute release mechanisms

Bubble cascades

Bubble cascades refer to the liberation of a pulse of retained bubbles following a mechanical perturbation (Sherwood & Eduardo Sáez, 2014), or in the path, or indeed wake (Vidal *et al.*, 2011), of a buoyant rising bubble, as illustrated by Figure 2.11 (Gauglitz *et al.*, 2015). When a bubble begins to rise within a viscoplastic fluid, local fluid will yield due to the flow field of the bubble. Fast and deformed bubbles, consistent with high Bond numbers (buoyancy dominates surface tension) and low Bingham numbers (viscous stress dominates the yield stress), induce a broader region of fluid to yield and are hence likely to capture a greater number of bubbles within a cascade (Tripathi *et al.*, 2015; Tsamopoulos *et al.*, 2008). Furthermore, as the bubble rises and the pressure field of the sediment decreases the bubble expands and accelerates, generating an expanding flow-field and liberating more bubbles, each of which will then induce their own flow field and yield additional sediment. Enlargement in bubble volume with decreasing depth, h, due to depressurisation, $P_0 - \rho g h$, and coalescence with bubbles in its path can be estimated using Equation (2.29) (Sherwood & Eduardo Sáez, 2014):

$$\frac{\mathrm{d}V_b}{\mathrm{d}h} = \frac{\rho g V_b}{P_0 - \rho g h} + \frac{\pi \nu}{4}\left(2\left(\frac{6V_b}{\pi}\right)^{1/3} + d_{bi}\right)^2 \tag{2.29}$$

where ν is the void fraction and d_{bi} is the initial bubble diameter immediately before ebullition. Thus an ebullient bubble 3 mm in diameter, 0.4 m below the surface within a 1200 kg m^{-3} sediment of 20 % voidage would expand to 176 mm at the surface (Sherwood & Eduardo Sáez, 2014), an increase of nearly two orders of magnitude and thus shearing a vastly greater surface of sediment than the original bubble size distribution might suggest.

Gauglitz *et al.* (2015) observed bubble cascades within bentonite and kaolin suspensions of up to 90 Pa yield stress, indicating that bubble cascades represent a phenomenon particular to low strength *slurries*. The percentage of the bubble population released by a bubble cascade varied greatly with the vessel geometry, cascades enabled release of between 14 and 99 % of bubbles within a time-scale of 20 s of a single buoyant bubble release within columns of 0.58-1.78 m diameter (Gauglitz *et al.*, 2015). Hence, bubble cascades have been characterised as an acute release mechanism even though they can be triggered by the quiescent release of a single, relatively small ebullient bubble.

Rollover events

Rayleigh-Taylor instabilities, buoyant displacement releases, or rollover events are used interchangeably in the literature to describe acute releases driven by the bulk buoyancy of a consolidated soft sediment beneath a convective supernatant; evidence for such acute releases was summarised in Section 2.3. Full rollover considers the case where the consolidated sediment swells to sufficient void fraction that its bulk density is reduced below that of the overlying supernatant (Ali *et al.*, 2000), characterised by the void fraction, ν, exceeding that required for neutral buoyancy, ν_{NB}, where the bulk sediment, ρ_s, and supernatant densities, ρ_l, reach equilibrium. Total inversion of the consolidated sediment and supernatant through a complete rollover event would redress the instability in the waste configuration and explain the sudden large upward transfer of decay heat within Hanford tanks as shown in Figure 2.3d. However, Allemann (1992) argues that gas release is better explained by a theory of *partial rollover*.

Partial rollover occurs when a buoyant region of the consolidated sediment, or *gob* (Allemann, 1992), breaks free of the cohesive bonds of the bulk sediment matrix and rises to the surface. The rising gob expands due to to the reducing hydrostatic head and accelerates towards the surface. The stress imparted by surface tension or collision with a floating crust (Bryan *et al.*, 1992) causes the gob to fully or partially disintegrate (Stewart *et al.*, 1996). Some gas is released immediately, resulting in the significant drop in waste level that is characteristic of buoyant displacements, while some small bubbles may *fizz* out of the gob at a slower rate (Allemann, 1992). Eventually, when the gas fraction of the gob has sufficiently decreased, the gob descends back to the consolidated waste level and its retained gas fraction is compressed by the increasing hydrostatic load.

Acute gas release by partial rollover requires that sufficient buoyant potential energy, E_{bp}, is converted to kinetic energy to overcome the energy required to *yield* the gob, E_τ, on collision at the top of the waste layer and liberate the retained

gas. An expression for the ratio of potential energy to yielding energy, or *excess buoyant potential energy*, is given in eq. (4.10) (Stewart *et al.*, 1996):

$$\frac{E_{bp}}{E_\tau} = \frac{\nu P_a k_h}{(1-\nu)\varepsilon_\tau \tau}\left(\left(1+\frac{1}{k_h}\right) ln(1+k_h) - k_{by}\right) > 2.6$$
$$k_h = \frac{\rho_l g L}{P_a} \tag{2.30}$$
$$k_{by} = \frac{\nu_{nb}(1-\nu)}{\nu(1-\nu_{nb})}$$

where k_h and k_{by} define the hydrostatic head and excess buoyancy respectively, L is the depth of the supernatant, P_a is the ambient pressure and ε_τ is the *strain at thixotropic transition*, typically around 1 (Stewart *et al.*, 1996). Acute gas releases therefore become more realistic with added supernatant depth, increased void fraction and diminishing yield stress. The buoyant potential energy ratio also also demonstrates that partial rollover can be triggered by a drop in ambient pressure as well as by chronic bed swell, and that acute gas release by partial rollover does not necessarily require that the sediment achieves bulk buoyancy ($\nu > \nu_{NB}$), however the potential for gas release enhances significantly with increased voidage above the point of neutral buoyancy.

It has been deemed that the single-shell tanks at Hanford lack a supernatant layer deep enough to achieve sufficient excess buoyant potential energy for gas release under quiescent conditions, however the waste configuration of the double-shell tanks is more vulnerable to gas release by partial rollover (Stewart *et al.*, 1996). One particular double-shell tank, SY-101, discussed in Section 2.3, has exhibited violent buoyant releases sufficiently large in scale to release over 50 % of the gas within the consolidated bed (Stewart *et al.*, 1996). Analysis of large buoyant gas releases from SY-101 implied that a buoyant potential energy ratio in the order of 5-10 would be required, however scaled experiments indicated a more conservative ratio of 2.6 for acute gas release (Stewart *et al.*, 1996).

2.9 Conclusions

The 22 compartments of the MSSS at Sellafield contain 100s m^3 of consolidated Magnox corrosion products with an uncertain voidage of hydrogen, while an unknown inventory of uncorroded metallic swarf continues to generate flammable gas at an ambiguous rate. These uncertainties are numerous given the urgency with which the MSSS must be safely evacuated of waste and decommissioned (Le Clere, 2011). While acute hydrogen release hazards from CMS waste are acknowledged in the literature (Averill *et al.*, 2015; Hastings *et al.*, 2007), there is no published

research into the extent of gas retention, or *holdup* within Magnox waste. Observations of hydrogen holdup within American nuclear legacy waste in underground silos provide evidence for large acute gas releases by partial rollover (Allemann, 1992) and bubble cascades (Sherwood & Eduardo Sáez, 2014), punctuating the chronic gas release by bubble ebullition (Keller & Stallard, 1994), vertical fracture propagation (Algar *et al.*, 2011a) and transport along open drainage channels (van Kessel & van Kesteren, 2002). However, no adequate mechanism has been presented to account for chronic, quiescent gas release from intermediate strength sediments, sufficiently strong to overcome the buoyancy of individual, centimetre-scale bubbles, but lacking the strength to support stable drainage channels of appreciable depth.

A body of research on methane retention within marine sediments presents some useful mechanisms for bubble growth which qualitatively explain the inverted teardrop (Boudreau, 2012; Tripathi *et al.*, 2015) and penny-shaped crack (Algar & Boudreau, 2010; Gardiner *et al.*, 2003; Johnson *et al.*, 2002) bubble geometries observed under x-ray CT (Barry *et al.*, 2010). However, the optically opaque nature of soft sediments (Hunter *et al.*, 2011) and their complex *elastoviscoplastic* (Terrones & Gauglitz, 2003) response to stresses imposed by a growing bubble, make the provision of a comprehensive mathematical framework for these growth mechanisms far from trivial. The LEFM model used to describe crack propagation by tensile fracture may well be limited by a prohibitively large region of plastic deformation around the crack (Broek, 1982), while elastic-plastic cavity expansion models appear limited to perfectly spherical bubbles (Terrones & Gauglitz, 2003), which may only be realistic for small immature bubbles where surface tension dominates the yield stress.

Consequently, there appears to be considerable scope for further research into gas retention within consolidated soft sediments, complementing the interest from diverse industries, including marine science (Boudreau, 2012), nuclear science (Kam *et al.*, 2001b) and wastewater treatment (van Kessel & van Kesteren, 2002). Particular consideration might be afforded to the following unanswered questions:

- What extent of gas holdup is realistic within CMS and what is the impact of sediment consolidation, or increased yield stress, on the potential for acute gas release?
- How does the nature of the retained bubble population evolve, in terms of size distribution and shape, with the mechanical properties of the sediment?
- How is gas released from intermediate strength sediments in the absence of external mechanical perturbations?

- Does brucite support stable three-phase contact at the bubble interface and how does this impact gas migration and bubble coalescence?
- How does the sedimentary pore structure evolve with sediment consolidation and how does the sediment microstructure influence bubble growth and rise dynamics in contrast to single-phase elastoviscoplastic materials considered elsewhere in the literature (Fraggedakis *et al.*, 2016; Johnson *et al.*, 2002; Sherwood & Eduardo Sáez, 2014)?

Chapter 3

Characterisation of Magnox legacy waste test materials

3.1 Introduction

Prior to investigating the gas retention behaviour of Magnox legacy waste at laboratory scale, suitable test materials must be selected and characterised in order to understand the sediment response to bubble growth. The stopping condition Atapattu *et al.* (1995); Dubash & Frigaard (2004), which dictates whether a bubble can be held static within a soft sediment, is governed by the shear yield stress, while the relationship between a bubble's internal pressure and its growth dynamics is dictated by the stress-strain behaviour of the sediment (Terrones & Gauglitz, 2003). The particle size is crucial in determining the geometry of retained bubbles, with bubbles more likely to deform and intrude between coarse particles (Kam & Rossen, 1999) and fine-grained sediments more likely to expand elastically or fracture (Jain & Juanes, 2009; Katsman *et al.*, 2013) during bubble growth. The stability of particles at the bubble-porewater interface can determine the capacity for growth by Ostwald ripening or coalescence (Pitois *et al.*, 2015). This chapter presents the results of vane rheology, energy dispersive x-ray spectroscopy, x-ray diffraction, micro-tomography, light scattering and dynamic foaming tests, amongst other techniques, in order to characterise some of these critical sediment behaviours for two CMS test materials used throughout this study.

3.2 Materials and methods

3.2.1 Materials

The radioactivity within Magnox-era legacy buildings inhibits direct sampling of CMS for remote experimental work, necessitating the selection of suitable test materials for use as analogues. Since none of the microstructural, mechanical or interfacial properties of soft sediments are anticipated to be influenced by their radioactivity, the considerable health and safety complications accompanying experimental work with active samples were not justified. Extensive consideration has been given to the provision of suitable non-active test materials for Magnox legacy waste trials (Blackburn & Thompson, 2013) and two of the approved test materials, routinely used by Sellafield Ltd for research and development, are employed throughout this study. The first is Versamag (Martin Marietta Magnesia Specialties LLC, USA) (Martin Marietta Magnesia Specialities, 2014), a dry commercial $Mg(OH)_2$ powder of high purity, containing only trace amounts of magnesium and calcium oxides as impurities (Martin Marietta Magnesia Specialities, 2014). Soft sediments of this white precipitated powder are prepared by the addition of mains water and agitation for 30 min using an overhead stirrer with an axial flow impeller. Thus, the solids concentration can be chosen to achieve particular density and yield stress conditions encountered at different stages of CMS consolidation.

The second was a bespoke manufactured test material named *corroded magnesium sludge* (CMgS) produced by Sellafield Ltd and the National Nuclear Laboratory (NNL) using a synthesis route closer to conditions within the Magnox Swarf Storage Silos. Large quantities of commercial magnesium metal raspings (Magnesium Electron Ltd) were heated in water baths doped with sodium chloride in order to achieve accelerated corrosion, mimicking the strategy used to enhance corrosion within the early MSSS containers (Baldwin, 2003). The raspings were periodically raked to expose fresh metallic surface and enhance the corrosion rate. Uncorroded metal was then separated from the corrosion products using a 200 µm sieve before the $Mg(OH)_2$ product was thickened to approximately 10-15 % w/w in a settling tank and then to 40 % w/w by centrifugation. The product was then mixed with crushed Hydromag G $Mg(OH)_2$ (Celtic Chemicals, UK) to manipulate the particle size distribution towards that of CMS and enhance the sludge yield stress at low concentrations. The resulting CMgS product has been used previously for various research and development trials at Sellafield before recovery and centrifugation back to 40 % w/w for use in this study.

As a wet sludge of around 40 % w/w solids content, specific density and yield stress conditions were less simple to precisely specify than for the commercial

$Mg(OH)_2$ powder. Instead, each time a sample was taken the solids concentration of a 50 ml sub-sample was estimated from the mass loss following 12 h of drying in an oven at 100 °C, before the sample was diluted to the desired condition. Difficulties were experienced when consolidating the CMgS to higher solids concentrations than the 40 % w/w bulk concentration provided and so work with the CMgS focused on the poorly consolidated conditions more typical of legacy pond sludge than highly consolidated silo wastes. Analysis of the particle size distribution, chemical and morphological composition, rheology and wetting behaviour was undertaken as detailed in Section 3.2.2.

3.2.2 Particle characterisation techniques

Zeta potential and pH characterisation

Zeta potential, ζ, and pH were measured using a ZetaProbe (Colloidal Dynamics, USA) (HidalgoAlvarez *et al.*, 1996) to characterise the stability of magnesium hydroxide in aqueous environments, which influences the size and shape of $Mg(OH)_2$ aggregates in suspension. The ZetaProbe uses the *electrokinetic sonic amplitude* (ESA) technique, whereby a high frequency, 0.2-20 MHz, electric field is generated between two electrodes submerged within a particulate suspension. The electric field causes suspended particles close to the probes to oscillate generating an ultrasound wave. The potential difference between the applied field at the electrode and the ultrasound wave, in addition to the phase lag, can be used to characterise zeta potential. The ZetaProbe was calibrated using a solution of potassium silico tungstate (KSiW) ions, recommended by Colloidal Dynamics for its stable ESA signal. The ZetaProbe electrodes were placed in $Mg(OH)_2$ samples of 150 ml volume and five zeta potential readings were logged at 1 min intervals.

The suspension pH was measured with an Oakton Acorn pH 6 Meter, calibrated using voltage-pH correlations and standard solutions of pH 4, 7 and 10. The pH probe was installed beside the ZetaProbe electrodes to determine the iso-electric point (IEP), representing the pH at which the net electrical charge of particles in suspension is zero and the inter-particle interactions become exclusively attractive.

Particle sizing

A Mastersizer 2000E (Malvern Instruments, UK) laser diffraction particle size analyser was used to measure particle size distributions (PSD) of the two test materials. Laser diffraction is a very widely employed particle sizing technique based on the observation that small spheres scatter incident light with greater angular variation than large particles; the intensity distribution of scattered light is thus used to estimate a volume weighted size distribution. The Mastersizer is a particularly

ubiquitous instrument used to deploy the technique across many disciplines (Adi *et al.*, 2006; Biggs & Lant, 2000; Goossens, 2008; Sperazza *et al.*, 2004). Dilute suspensions were sonicated for 10 min prior to transfer to the Mastersizer dispersion unit. An axial flow impeller at 2500 rpm is used to disperse particles and induce flow from the dispersion unit to the measurement domain. It is assumed that the combined shear of the sonication and Mastersizer impeller was sufficient to break down large aggregates in the suspension to their shear resistant constituent particles.

Particle imaging techniques

High resolution scanning electron micrographs (SEM) were captured of the two test materials using an EVO MA15 microscope (Carl Zeiss, Germany) at the Leeds Electron Microscopy and Spectroscopy Centre. Samples were sputter coated with a 10 nm film of either gold of iridium prior to imaging in order to improve the signal to noise ratio (Song *et al.*, 2011). Images were also captured of $Mg(OH)_2$ aggregates in suspension using a flow particle image analyzer (Sysmex FPIA-2100, Malvern Instruments, UK) (Komabayashi & Spångberg, 2008) and a particle vision and measurement (PVM) instrument (Barrett & Glennon, 2002; Greaves *et al.*, 2008) (Mettler Toledo, US).

X-ray microtomography (μCT)

X-ray microtomography (μCT) (Moreno-Atanasio *et al.*, 2010; Yao *et al.*, 2010) was employed to generate a three-dimensional radiodensity map through dried and wet sludge samples of the two test materials for the identification of high density physical heterogeneities too large for the Mastersizer to detect. The wet soft sediment samples were sampled using 3 mm cellophane tubes while fragments of the dried test materials, dried for 24 h at 100 °C, were scanned on a sample stub. A Skyscan 1172 (Bruker Corporation, Germany) provided an x-ray source of 80 kV voltage and 124 µA current while the sample was rotated in 0.2° intervals through 360° over 4-11 h. The 1801 projections were then reconstructed into 4000×4000 pixel tomographs of 1.28-3.44 µm resolution. Bruker's CT-Vox software was used to render the stack of x-ray tomographs into a three-dimensional volume. The opacity of the bulk material was then reduced to reveal any high radiodensity physical heterogeneities within either sample.

Energy dispersive x-ray spectroscopy (EDX)

Elemental analysis was undertaken by energy dispersive x-ray spectroscopy (EDX) to identify chemical contaminants within the test materials. An 80 mm^2 X-Max

silicon drift detector (Oxford Instruments, UK) associated with the EVO MA15 (Carl Zeiss, Germany) SEM was used to detect x-ray radiation up to 6 keV emitted by atoms within the sample following excitation by an incident electron beam. AZtecEnergy software (Oxford Instruments, UK) was used to identify the atomic abundance of various elements from their characteristic emission peaks within the EDX energy spectra.

X-ray diffraction (XRD)

An X'Pert (PANalytical, Netherlands) powder x-ray diffractometer was used to compare the crystal structure of a dried sample of CMgS with commercial $Mg(OH)_2$ by x-ray diffraction (XRD). The X'Pert's copper anode generates $Cu - K\alpha$ (zhong Li *et al.*, 2009) x-rays of 1.54 Å wavelength, which were focused into a beam through anti-scatter slits onto the sample, sweeping through incident angles of $5 < 2\theta < 65°$. Characteristic intensity peaks of constructive interference were cross-referenced with XRD patterns of various known crystalline phases to identify the structures within each sample.

3.2.3 Soft sediment mechanical and rheological behaviour

The mechanical strength of soft sediments was characterized according to their shear yield stress, which was determined using two alternative vane method approaches (Dzuy & Boger, 1985). First, a Brookfield DV-11+ Pro viscometer (Brookfield AMETEK, USA) was used to rotate four blade vanes of either 6.3 or 10.8 mm diameter at 0.5 rpm within the sediment to observe the measured torque, T, response over time. The vanes were submerged such that the top of the vane aligned with the surface of the sample and so the sheared surface area contained only the bottom face and the vertical wall of an effective cylinder. Torque-time correlations were obtained for samples of 30-52 % w/w solids concentration for the commercial $Mg(OH)_2$ and 30.7-38.8 % w/w for the CMgS. The shear yield stress was determined from the maximum torque response and the vane dimensions according to eq. (3.1) (Dzuy & Boger, 1985):

$$T_{max} = \frac{\pi D^3}{2}\left(\frac{H}{D} + \frac{1}{6}\right)\tau \tag{3.1}$$

where H and D are the height and diameter of the vane respectively. These results were validated using a Bohlin Gemini rheometer (Malvern Instruments Ltd., UK), which benefits from greater measurement sensitivity and coolant flow around the sample cup for temperature regulation. A four blade vane of 24 mm diameter was inserted into the sample, with a 5 mm clearance, for 60 s of pre-shear before

allowing a further 60 s for the bed to recover. The shear stress was then ramped at logarithmic intervals to observe the stress at which the instantaneous viscosity exhibits a sharp decrease, coinciding with a rapid increase in strain, thus indicating the yield stress of the sample (Barnes, 1999).

A series of creep tests were also conducted using the Bohlin Gemini vane-cup geometry to investigate any viscoelastic response to prolonged stress (Goñi *et al.*, 2015; Uhlherr *et al.*, 2005). Following 60 s of pre-shear above the yield stress and 120 s of recovery time, in order to remove hysteresis effects from transferring the sample and submerging the vane, samples of 37.5 % w/w $Mg(OH)_2$ soft sediment and 38.9 % w/w CMgS were subjected to a series of incrementally increased creep stress for 1000 s until the samples flowed freely. Deformation of the samples was observed through the increase in strain, $\gamma(t)$, over time, obtained from the product of the instantaneous compliance, $J(t)$, and the applied stress, τ_{creep} (Jeldres *et al.*, 2014).

$$\gamma(t) = J(t)\tau_{creep} \tag{3.2}$$

3.2.4 Characterisation of the three phase interface

Particles which demonstrate hydrophobic behaviour are able to adsorb to the surface of bubbles to form a monolayer (Ali *et al.*, 2000). The monolayers around these *armoured* bubbles can inhibit coalescence and coarsening by Ostwald ripening and thus stabilise foams (Pitois *et al.*, 2015). Stable particle-gas contact also allows bubbles to *de-wet* pore walls within soft sediments and thereby reduce resistance to bubble invasion into adjacent pore-space according to the Young-Laplace relationship in eq. (2.10) (Boudreau, 2012), which has a significant impact on the geometry of retained bubbles (Kam *et al.*, 2001b; Wheeler, 1988a) and the potential avenues for volatile transport through consolidated sediments (van Kessel & van Kesteren, 2002). On the basis that conventional microscopy methods for characterising three phase contact angles are inherently unsuitable for non-ideal mineral surfaces (Chau, 2009), two alternative techniques are described below to (1) investigate the stability of $Mg(OH)_2$ monolayers at an air-water interface through a series of Langmuir-Blodgett experiments (Derkach *et al.*, 2009; Hunter *et al.*, 2009; Kundu *et al.*, 2005; Ybert *et al.*, 2002) and (2) investigate the capacity of $Mg(OH)_2$ to stabilise dynamic foams, or *dynamic foaming potential*, using Bikerman foam tests (Fryer *et al.*, 2011; Pugh, 2007; Tan *et al.*, 2005).

Langmuir-Blodgett experiments

$Mg(OH)_2$ monolayers were prepared at the surface of an 80 cm^2 Langmuir-Blodgett trough, shown in Figure 3.1. The trough was first cleaned with methanol, millipore

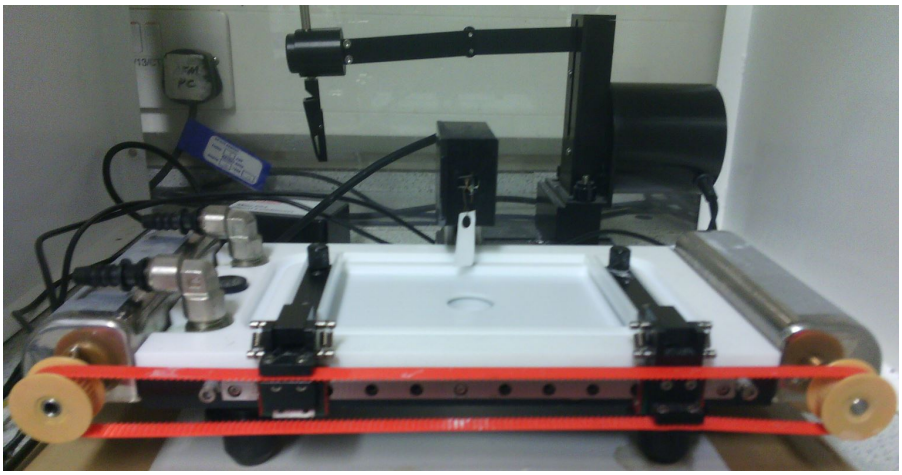

Figure 3.1: Image of the 80 cm^2 Langmuir-Blodgett trough used to prepare and compress $Mg(OH)_2$ monolayers while monitoring changes in surface pressure

water, aspirated dry, filled with water and the surface aspirated clean; this cleaning process was repeated until a surface pressure increase of less than 0.3 $mN\,m^{-1}$ was observed on closing the barriers to 20 cm^2.

A 3.9 % w/w dispersion of magnesium hydroxide in isopropanol, considered to be a suitable dispersant and water-immiscible solvent, was prepared and sonicated for 10 min. The monolayer was then prepared by transferring a 1 ml volume of the suspension to the trough interface by dabbing droplets from the bevelled tip of a 500 µl micro-syringe across the air-water interface. A 10 min period was allowed for isopropanol to evaporate from the monolayer prior to experimentation. Tests were then conducted using a *compression-expansion* cycle where the barriers converged from 80 to 20 cm^2 over 13 min, remained still for 5 min and then diverged back to 80 cm^2 over 13 min. Surface pressure measurements were determined from a force balance on a 1 cm wide Wilhelmy plate attached to a microbalance (Derkach *et al.*, 2009).

Bikerman foam tests

Bikerman foam tests were conducted by bubbling air into aqueous $Mg(OH)_2$ suspensions of 2, 4 and 8 % v/v, or 4.6, 9.0 and 17.1 % w/w, through a 46-60 µm pore fritted glass disk at the base of a 34 mm diameter glass Bikerman column, as demonstrated by the schematic in Figure 3.2 (Fryer *et al.*, 2011). Prior to experimentation, the column was thoroughly cleaned with ethanol and then water in order to remove any traces of surfactants or dust particles which enhance and diminish foamability respectively. The height of the top of the foam was recorded at 10 s intervals against the millimetre calibrations at the column wall until the rate of bubble formation at the fritted disk achieved a dynamic equilibrium with the rate of bubble collapse at the top of the foam and a constant, maximum foam

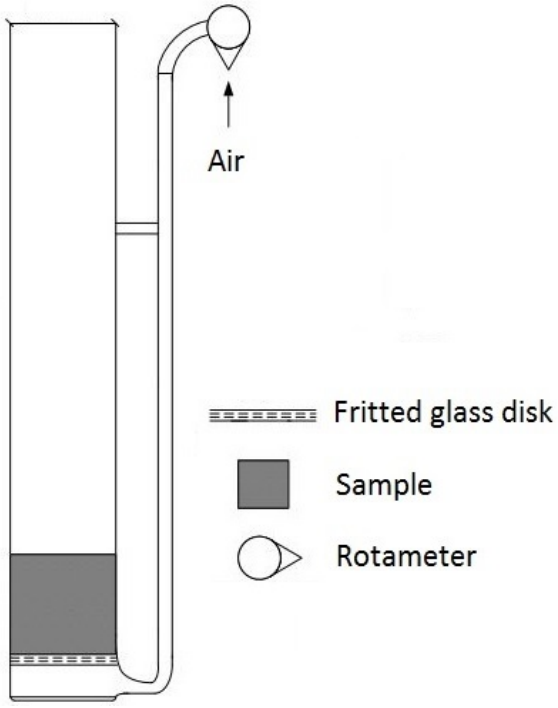

Figure 3.2: Schematic of a Bikerman column with an in-line rotameter for dynamic foam height analysis, modified from Fryer *et al.* (2011)

height, H_{max}, was observed. A range of air flow rates, $\dot{V}$, up to 134.7 ml min^{-1} were investigated using an *in-line* rotameter (Supelco Analytical, USA), in order to investigate maximum foam height as a function of gas velocity, u_g. Bikerman (1973); Pugh (2007); Tan *et al.* (2005) all observed linear proportionality between gas velocity and maximum foam height, with their ratio providing a *dynamic foam stability* factor (Aktas *et al.*, 2008; Barbian *et al.*, 2005; Bikerman, 1973), Σ, in seconds.

$$\Sigma = \frac{V_f, max}{\dot{V}} = \frac{H_{max} A}{\dot{V}} = \frac{H_{max}}{u_g} \tag{3.3}$$

where $V_{F,max}$ is the maximum foam volume and A is the cross-sectional area of the column. A second useful characteristic time-scale is the average bubble lifetime, $\mathcal{T}$, (Barbian *et al.*, 2003) which dictates the rate of foam rise according to eq. (3.4) (Barbian *et al.*, 2005; Bikerman, 1973):

$$H(t) = H_{max}\left(1 - \exp\left(-\frac{t}{\mathcal{T}}\right)\right) \tag{3.4}$$

3.3 Results and discussion

3.3.1 Particle size, structure and composition

Laser scattering particle size distributions (PSD) of the commercial $Mg(OH)_2$ and CMgS test materials are presented in Figure 3.3. The Versamag demonstrated the narrower size distribution, with particles of 0.6-100 µm and a median particle size of 4.4 µm. The CMgS shares the same primary mode, and a similar median diameter of 4.8 µm, however the CMgS exhibited an additional coarser mode centred around 200 µm with some particles detected right up to the 1000 µm limit of the Mastersizer, possibly indicating the presence of some very large millimetre scale particles.

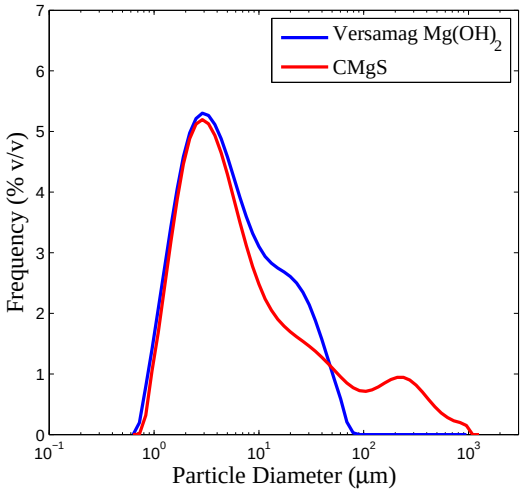

Figure 3.3: Laser scattering particle size distributions for commercial $Mg(OH)_2$ (Versamag) and corroded magnesium sludge (CMgS) test materials acquired using a Malvern Mastersizer 2000

Aqueous suspensions of $Mg(OH)_2$ are reported to exhibit low electrophoretic mobility (Schott, 1981) and hence a strong tendency for rapid aggregation (Brakalov, 1985). Characterisation of the ζ – potential of Versamag suspensions within the *self-buffering* pH range of 10.03 ± 0.13 yielded very low magnitude potentials in the range of 0.5-3.2 mV. Thus, $Mg(OH)_2$ self buffered to an alkaline pH close to the isoelectric point (IEP), which is consistent with IEP measurements in the 10.8-11 range in Biggs *et al.* (2007) and Schott (1981). Consequently, the size and structure of $Mg(OH)_2$ in aqueous suspension will be governed by its aggregation kinetics (Brakalov, 1985; zhong Li *et al.*, 2009), which may be highly sensitive to the shear environment of a particular particle sizing technique.

Evidence of this aggregation behaviour is provided in Figure 3.4, where $Mg(OH)_2$ aggregates are observed at three imaging scales. A scanning electron micrograph of dry Versamag powder in Figure 3.4a shows a 3 µm cluster of hexagonal *platelets*,

with facial dimensions up to 400 nm and thicknesses of less than 50 nm. These constituent platelets are consistent with brucite *crystallites* observed in Gregson *et al.* (2011) and zhong Li *et al.* (2009). The cluster or *primary agglomerate* itself is similar in scale to the primary modes of the Versamag and CMgS PSDs in Figure 3.3, suggesting that these small agglomerates are more resistant to the high shear conditions of the Mastersizer than larger aggregates. A larger, 22 µm diameter, aggregate in Figure 3.4b, captured using the Sysmex FPIA, shows the outline of the primary agglomerates within a larger aggregate. Figure 3.4c reveals the presence of very large *macro-aggregates*, the largest of 157 µm diameter, within a dilute suspension and under low shear agitation.

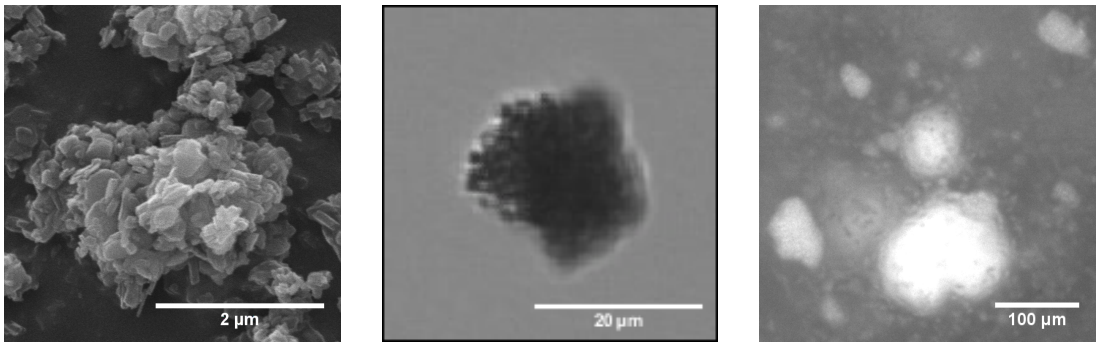

(a) (b) (c)

Figure 3.4: Images of $Mg(OH)_2$ acquired (with decreasing magnification from left to right) using (a) scanning electron microscopy (SEM), (b) Sysmex flow particle image analysis (FPIA) and (c) particle vision and measurement (PVM)

These large, loosely bound macro-aggregates are likely to be significant in governing the sedimentation dynamics of Magnox corrosion products transferred from the base of the FGMSP to the SPP1 tanks (Biggs *et al.*, 2007), however the microstructure of consolidated $Mg(OH)_2$ soft sediments, having undergone significant compressional dewatering, is likely dictated by the shear resistant primary agglomerates and crystallites shown in Figure 3.4a. For the CMgS, the Mastersizer PSD revealed a range of robust, shear resistant particles greater than 100 µm diameter, while coarser particles still, too large for the laser scattering measurement technique to detect, are clearly visible when handling the test material. X-ray microtomography (μCT) was employed to investigate whether this coarse particle fraction could be distinguished from the bulk material by its radiodensity; μCT reconstructions of $Mg(OH)_2$ and CMgS soft sediments, both dried for 8 h at 100 °C, acquired using a Bruker Skyscan, are shown in Figure 3.5.

Away from the large voids and thermal fractures, artefacts of drying the samples, the dried Versamag μCT reconstruction in Figure 3.5a appears largely homogeneous in density. Conversely, the CMgS sample in Figure 3.5c demonstrates several high radiodensity *hotspots*. This disparity is more apparent in Figures 3.5b

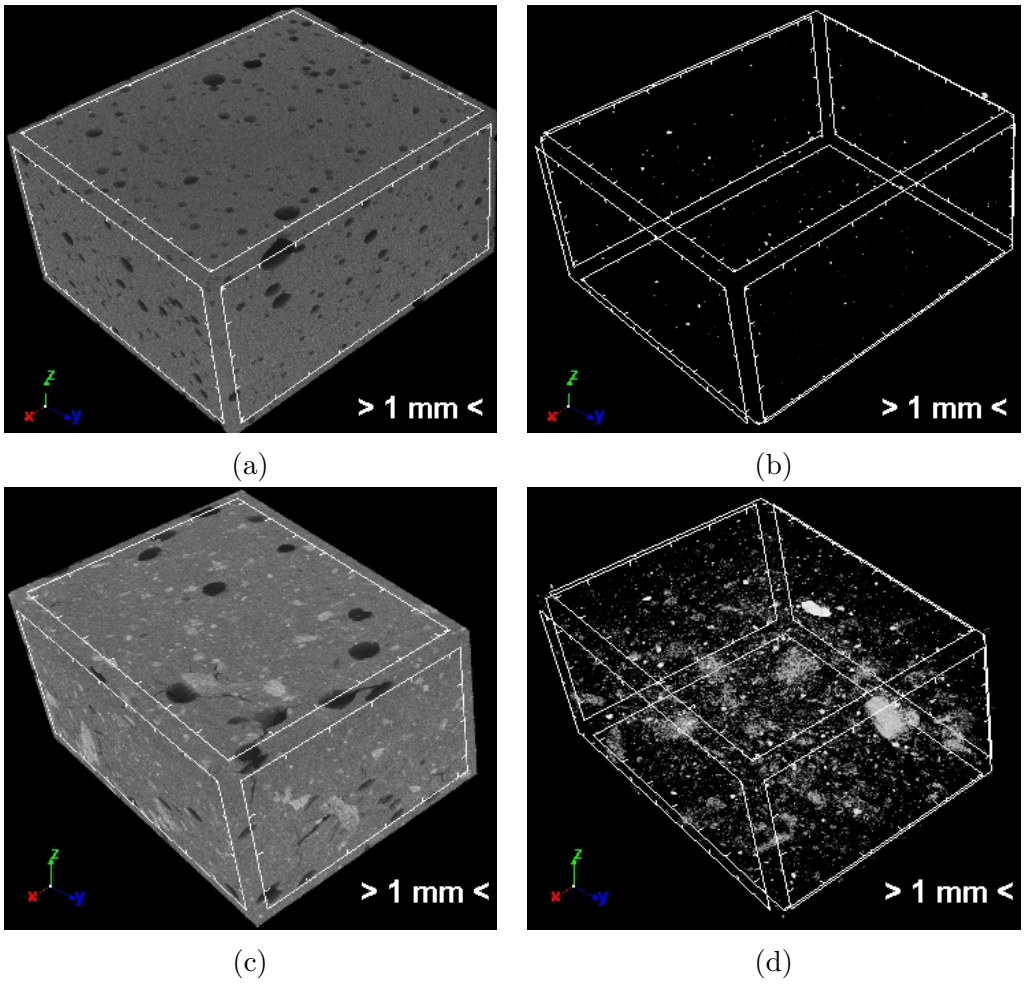

(a) (b)

(c) (d)

Figure 3.5: Three dimensional x-ray micro-tomography reconstructions of (a, b) dried $Mg(OH)_2$ soft sediments and (c, d) dired CMgS. The opacity of the bulk material has been minimised in (b) and (d) to observe high radiodensity heterogeneities within each test material.

and 3.5d where the *opacity* of the uniform bulk sediment and low radiodensity voids has been significantly reduced to isolate the high density heterogeneities. A number of hotspots are similar in scale to the millimetre calibrations indicated on the bounding box and are so much denser than the surrounding bulk material that they are unlikely to be $Mg(OH)_2$ aggregates. Some of these hotspots could represent (1) uncorroded magnesium metal raspings, which were not captured by the 200 µm sieve or removed by sedimentation, (2) magnesium oxide from the added crushed Hydromag which has not hydrated, or (3) foreign species which contaminated the test material during previous large-scale trials before it was recycled for this research.

Typically, gas bubbles retained by consolidated soft sediments are many times larger than the grains of the surrounding sediment (Wheeler, 1988a), as excessive Laplace pressures prevent stable sub-micron, pore scale bubbles. During bubble growth by elastic-plastic cavity expansion(Terrones & Gauglitz, 2003), solids and pore-water are understood to flow away from the larger bubbles together, behaving as one continuous phase (Boudreau, 2012; Wheeler, 1988a). However, coarse, dense particles embedded within the bulk $Mg(OH)_2$ matrix may resist displacement and instead deform the bubble. Equally, particles two orders of magnitude larger than the median particle size act as obstacles in the pore structure which may inhibit gas invasion through the pore-space or disrupt the typical linear elastic stress field around the tip of a crack, as shown in Figure 2.9b, and thereby curtail fracture propagation. Efforts were undertaken to characterise the elemental composition of the two test materials by EDX analysis in the hope of identifying this coarse, dense particle fraction observed under μCT.

Four EDX spectra, shown in Figure 3.7 and quantified in Table 3.1, were generated for regions indicated within each of the four scanning electron micrographs in Figure 3.6. Spectra 1 and 2 correspond to typical regions of the bulk phases of Versamag and CMgS respectively, consistent with the agglomerates of hexagonal platelets in Figure 3.4a. The predominantly oxygen and magnesium contents, present in a 2:1 atomic ratio, are anticipated for brucite-rich (Gregson *et al.*, 2011) sediments. The trace amounts of silicon, sulphur, chlorine and calcium are common oxides found in commercial $Mg(OH)_2$ powders synthesised by hydration and precipitation of calcined dolomitic lime, $CaO \cdot MgO$ (Blackburn & Thompson, 2013; Martin Marietta Magnesia Specialities, 2014). A sample of CMgS was then diluted to allow the large, heavy particles to sediment out for collection before they were washed, dried and transferred to an SEM stub. One particularly coarse particle, 2.4 mm across its longest axis, isolated by this approach is shown in Figure 3.6d. Despite its significant physical dissimilarity from the brucite micrographs in Figures 3.6a and 3.6b the EDX spectrum is indistinguishable, implying either (1) brucite deposition at the surface of a large dense foreign particle or (2) substantial

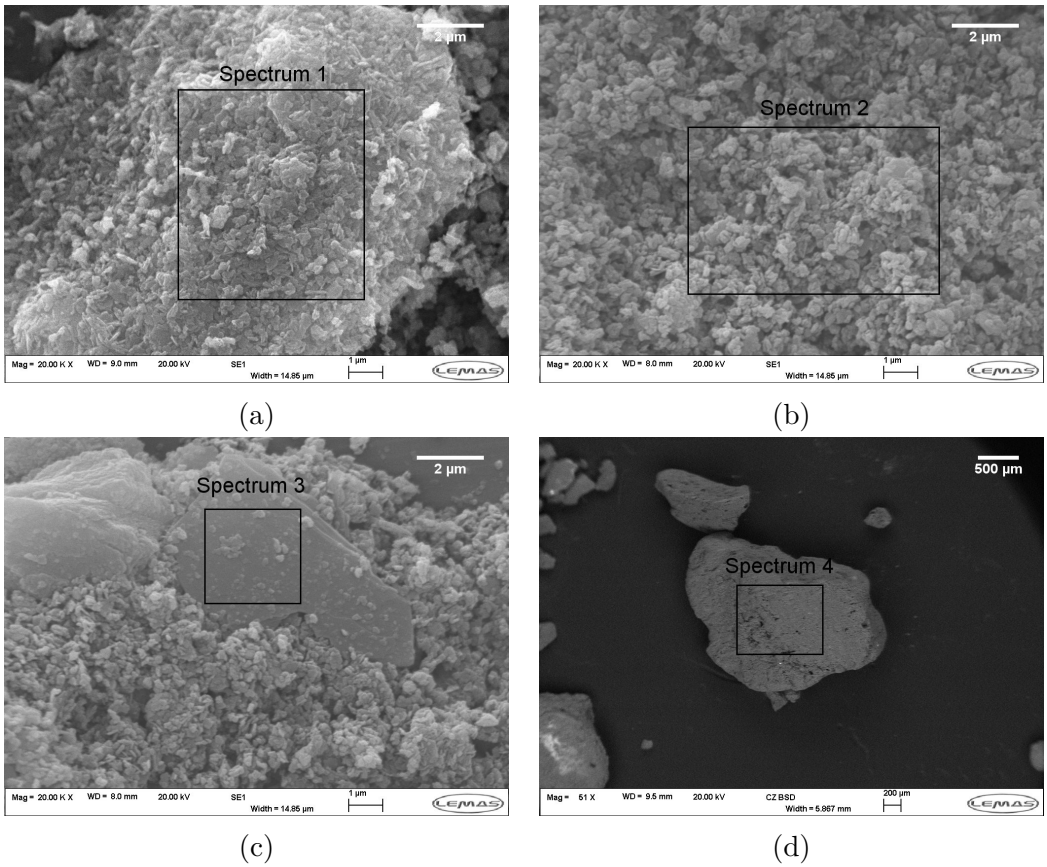

Figure 3.6: Four scanning electron micrographs of the bulk phase of (a) Versamag and (b) CMgS, (c) a large crystal impurity within the CMgS and (d) a very large, dense millimetre scale particle within CMgS; the black box regions were analysed for their atomic composition using energy-dispersive x-ray specroscopy (EDX), presented in Figure 3.7 and table 3.1

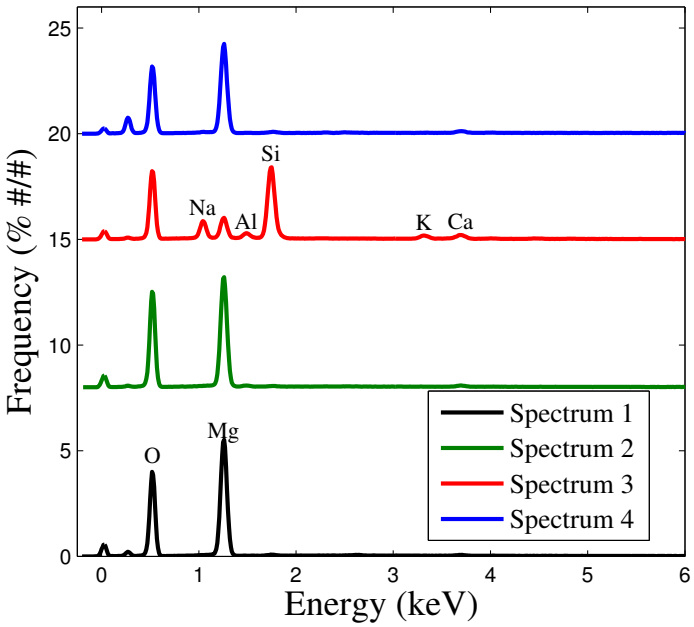

Figure 3.7: Four EDX spectra corresponding to the micrographs in Figure 3.6 indicating the elements which best account for each EDX peak

corrosion at the surface of some metallic magnesium to at least the 1-2 µm depth the EDX is able to probe. The brucite structure at the surface of Figure 3.6d appears similar to the globular aggregate morphology observed in Henrist *et al.* (2003) following synthesis at elevated temperatures. Comparison of this macroscopic particle with the 500 µm scale bar, 2.5 times larger than the sieve mesh used to segregate corrosion products from uncorroded metal, reinforces the μCT observation that the CMgS has obtained a coarser particle fraction since its original synthesis.

Table 3.1: A summary of the relative atomic abundance of each element identified from the four EDX spectra in Figure 3.7

Element	Atomic abundance (%)			
	Spectrum 1	Spectrum 2	Spectrum 3	Spectrum 4
O	63.54	66.43	65.57	64.99
Mg	35.69	33.02	6.64	33.80
Si	0.31	0.12	17.37	0.29
S		0.04		0.20
Cl	0.19			
Ca	0.27	0.38		0.73
Al			1.31	
Na			6.93	
K			0.89	
Ba			0.17	

Further SEM examination of the CMgS revealed the large flat crystal in Figure 3.6c, distinguishable from the brucite crystallites in both its scale and its non-hexagonal morphology. In addition to the magnesium and oxygen present in every sample, the EDX analysis revealed silicon, sodium, aluminium and potassium in order of decreasing atomic abundance. This atomic spectrum is consistent with the quartz, SiO_2, muscovite, $(KF)_2(Al_2O_3)_3(SiO_2)_6(H_2O)$, and illite, $(AlMgFe)_2(SiAl)_4O_{10}[(OH)_2H_2O]$, minerals found in slate (Knipe, 1981). Discussion with Sellafield Ltd. revealed that crushed slate had been added to the test material in order to represent the large, dense component of CMS, consisting of uncorroded metal fragments and wind blown sand within the open-air ponds.

X-ray diffraction (XRD) tests were performed on the two test materials for more detailed assessment of the crystal structure of the bulk phase. A sweep of incident x-ray angles in the range of $5 < 2\theta < 65°$ generated the XRD spectra presented in Figure 3.8. The two diffraction patterns are consistent with Brucite XRD fingerprints from various studies (Henrist *et al.*, 2003; Ramesh & Sreenivasa, 2015; Song *et al.*, 2011; zhong Li *et al.*, 2009), revealing the five major peaks listed in Table 3.2. These five intensity peaks were identified as distinct families of brucite lattice planes based on the XRD analysis in Henrist *et al.* (2003).

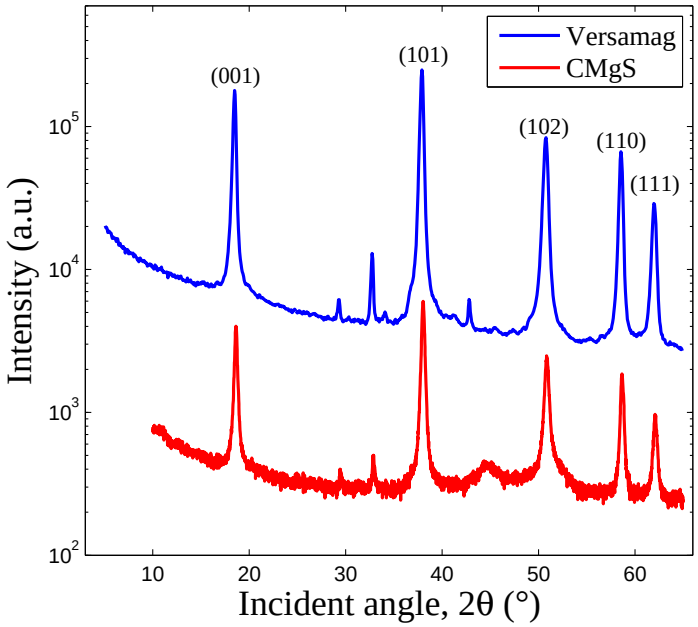

Figure 3.8: X-ray diffraction (XRD) patterns for commercial $Mg(OH)_2$ (Versamag) and corroded magnesium sludge (CMgS) [XRD measurements undertaken with Wei Ding and Johannes Botha, University of Leeds]

zhong Li *et al.* (2009) and Henrist *et al.* (2003) found that the ratio of the 001 and 101 lattice plane intensity peaks, I_{001}/I_{101}, was sensitive to various preparation conditions, including background ion concentrations, pH, temperature and the presence of surfactants during synthesis, and that this ratio has a profound impact on particle size, morphology and dispersion properties, however this ratio, at 0.45-0.48 , did not greatly differ between the two test materials. In fact the ratios of each of the five common dominant peaks in Table 3.2 as well as the minor intensity peaks at 29.4 and 32.9° imply similar crystal structure for the bulk phase of the two materials. The small peak at 42.8° unique to the commercial $Mg(OH)_2$ and the broad *amorphous hump* observed in the 43.5-47.0° range of the CMgS spectrum represent the only points of departure between the XRD spectra, and the magnitude of the amorphous hump is too close in scale to the underlying noise to justify quantitative analysis.

3.3.2 Mechanical deformation behaviour of magnesium hydroxide soft sediments

Vane rheology was employed to investigate whether the coarse particle fraction within the CMgS test material significantly altered the bulk mechanical behaviour, observed across a range of solids concentrations, from that of the commercial $Mg(OH)_2$. An example torque-time relationship, obtained using the Brookfield

Table 3.2: Summary of the major intensity peaks identified from the XRD spectra in Figure 3.8; the respective brucite crystal planes are identified from Henrist *et al.* (2003)

$2\theta\,(^\circ)$		I_i/I_{101}		Brucite plane
$Mg(OH)_2$	CMgS	$Mg(OH)_2$	CMgS	
18.47	18.63	0.48	0.45	001
37.90	38.02	1.00	1.00	101
50.77	50.92	0.41	0.31	102
58.54	58.64	0.40	0.35	110
61.96	62.07	0.18	0.20	111

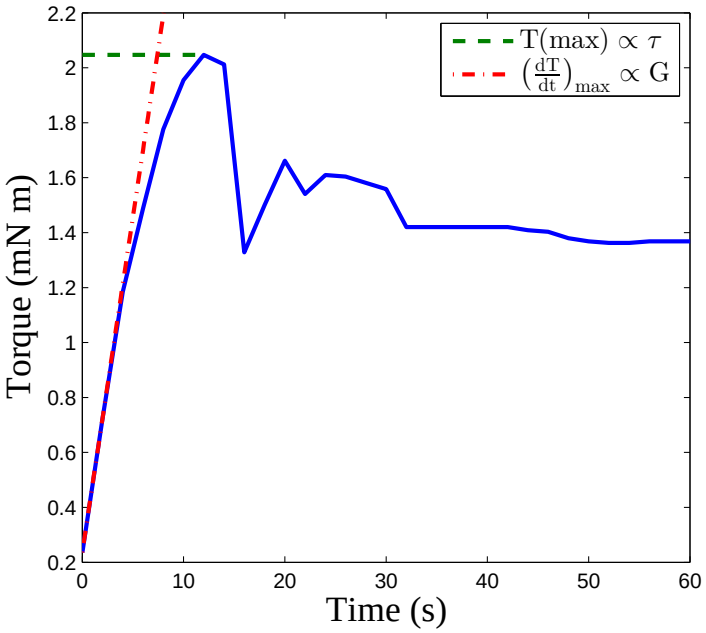

Figure 3.9: Example torque-time profile from the 0.5 rpm rotation of a four blade vane within % w/w $Mg(OH)_2$ soft sediment demonstrating the maximum torque and maximum torque gradient

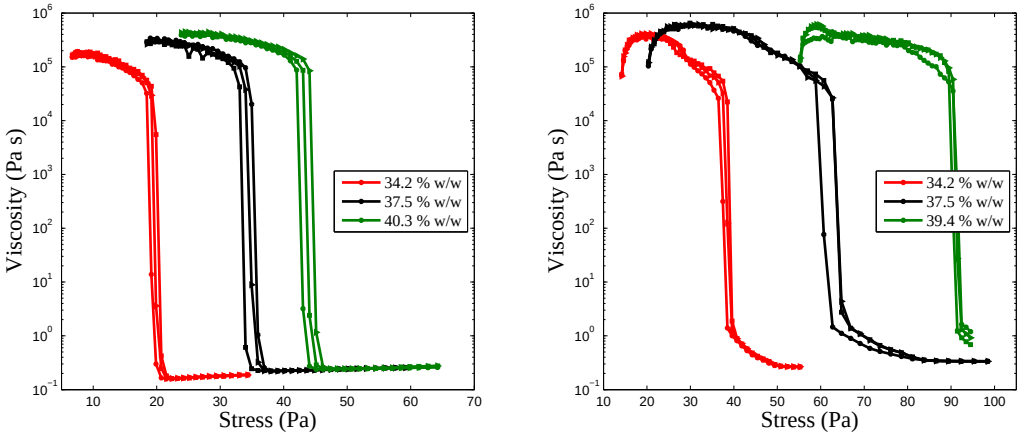

(a) (b)

Figure 3.10: Stress controlled flow curves passing through an observed yield stress for (a) Versamag $Mg(OH)_2$ soft sediments and (b) CMgS

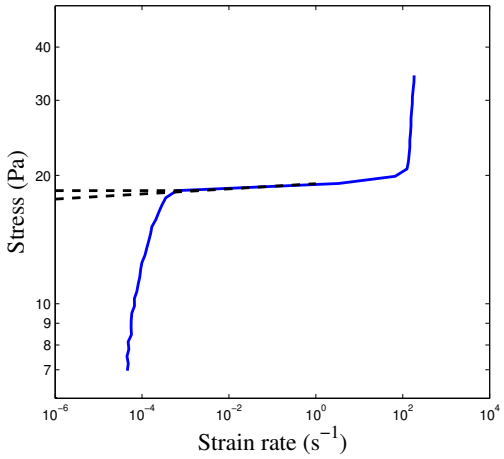

Figure 3.11: Comparative yield stress determination from (1) the imposed stress immediately prior to a decrease in viscosity by several orders of magnitude or (2) extrapolation to the point of near-zero strain rate

DV-11+ Pro viscometer, is demonstrated for a 45 % w/w $Mg(OH)_2$ soft sediment in Figure 3.9. The 2.05 mN m maximum torque, obtained with the smaller, 6.3 mm diameter, vane, corresponds to a yield stress of 320 Pa according to eq. (3.1) (Dzuy & Boger, 1985). Three repeat tests at the same solids concentration demonstrated reasonable agreement, with yield stresses measured of 315 ± 7 Pa. The convenience of this approach is that the small vane geometries available and negligible wall effects between the sheared surface and the much larger sample container enabled the characterisation of yield stresses up to 830 Pa, which will be summarised in Figure 3.12. The drawback is that this approach is relatively crude in comparison to isothermal, stress-contolled viscometry and so a Bohlin Gemini rheometer was used to validate the results.

Stress controlled flow curves for $Mg(OH)_2$ soft sediments at three solids con-

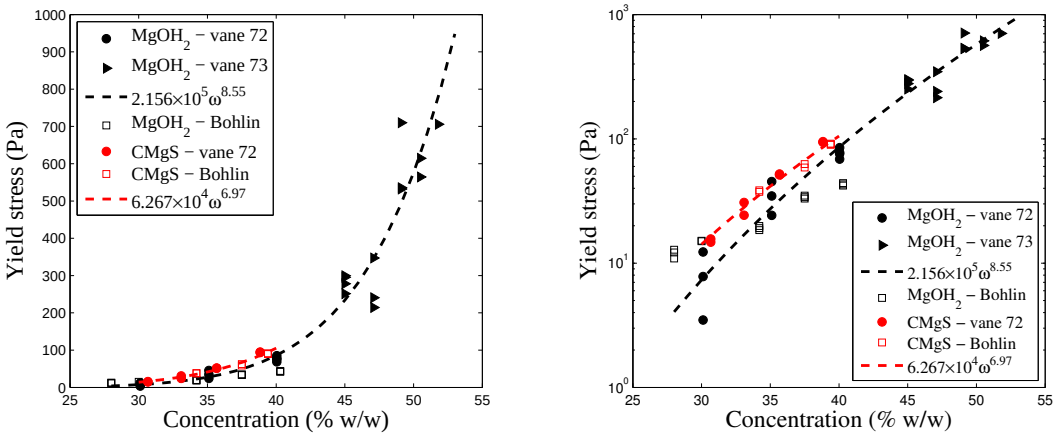

Figure 3.12: Commercial $Mg(OH)_2$ (Versamag) and CMgS soft sediment shear yield stresses within the 28-52 % w/w concentration range, acquired using a Brookfield DV-II Pro viscometer and Bohlin Gemini rheometer shown on (a) linear and (b) semilog axes in order to highlight the disparity between the test materials in the low concentration regime. The Brookfield yield stress data was acquired using two vanes (72 and 73) of 10.8 and 6.3 mm diameter respectively, with the smaller vane employed for sediment concentrations above 40 % w/w

centrations are presented in Figure 3.10a. The nine flow curves demonstrate the same characteristic behaviour, with a high viscosity plateau at low shear stresses, a yield stress, indicated by the six orders of magnitude decrease in viscosity over a very narrow stress range, and a secondary low viscosity plateau above the yield point. The rapid fall in viscosity at the yield point is accompanied by an equally rapid increase in strain, as the vane readily deforms the sediment on transition to more fluid-like behavior above the yield stress (Nguyen & Boger, 1992). Figure 3.11 demonstrates that there is little disparity in the apparent yield stress whether it is defined by the stress determined by extrapolation to a near zero strain rate of $1 \times 10^{-6}\,s^{-1}$ or by the stress which immediately preceeds the several orders of magnitude decrease in viscosity or increase in strain. The transition from Newtonian plateau to continuous flow occurs over such a small stress increment that the disparity between these definitions of the yield stress differs less than the variance between repeat flow curves. Hence, the transition stress which marks the end of the Newtonian plateau is used to define the yield stress (Barnes, 1999).

The yield stress at each solids concentration demonstrates good repeatability between samples and increases with solids concentration. This behaviour is mirrored by the CMgS flow curves in Figure 3.10b, however significantly greater stresses are required for equivalent concentration samples to yield. This is more apparent in Figure 3.12, which aggregates all the yield stress-concentration data, acquired with both instruments for both test materials.

For the commercial $Mg(OH)_2$ sediments, the smaller Brookfield vane (vane

73) was required for samples above 40 % w/w concentration to operate within the maximum torque limits of the viscometer, but resulted in slightly greater scatter in the measured yield stress. This is influenced by a number of factors: (1) the uncertainty in the yield stress measurements increases as the area of the sheared surface is reduced, (2) samples with higher solids content are more difficult to homogeneously mix, and (3) these increased uncertainties coincide with a region of sharp yield stress increase with solids concentration. Nonetheless, the collated data for the commercial $Mg(OH)_2$ from both instruments generated a power law fit with concentration, shown in eq. (3.5), with a robust coefficient of determination, R^2, of 0.96.

$$\tau = 2.156 \times 10^5 \omega^{8.55} \tag{3.5}$$

where the solids concentration is expressed as a weight fraction ($0 < \omega < 1$) to provide a shear yield stress in pascals. The Brookfield and Bohlin data demonstrated particularly good agreement for the CMgS samples, however yield stress analysis was limited to samples of up to 40 % w/w. The corresponding power law relationship with concentration is given in eq. (3.6).

$$\tau = 6.267 \times 10^4 \omega^{6.97} \tag{3.6}$$

Presentation of the shear yield stress on a logarithmic scale in Figure 3.12b better demonstrates the disparity between the test materials. CMgS sediments in the 30-40 % w/w concentration range were observed to yield at roughly double the shear stress of the commercial $Mg(OH)_2$ sediments. Investigations of gas holdup within Hanford sediments has used primarily kaolin and bentontite clay sediments as non-active analogues (Gauglitz *et al.*, 2015; Sherwood & Eduardo Sáez, 2014). Kaolin suspensions exhibit much lower yield stresses than $Mg(OH)_2$ sediments of equivalent solids content, while the reverse is true for Bentonite clay which rapidly increases in shear yield stress with added solids concentration (Gauglitz *et al.*, 2015). Best agreement in concentration-shear yield stress conditions between the two $Mg(OH)_2$ test materials in this study and research and development test materials used by PNNL were observed for kaolin-bentonite mixtures in ratios of 90 : 10 to 80 : 20 (Gauglitz *et al.*, 2015).

The apparently elastic or solid-like response at low stress and viscous, fluid-like, response above the yield stress, demosntrated in Figure 3.10 typifies viscoplastic behaviour (Bird *et al.*, 1983; Liddell & Boger, 1996). However, the four creep profiles for 37.5 % w/w $Mg(OH)_2$ in Figure 3.13a, performed using an imposed stress below the yield stress, $20 \leq \tau_{creep} \leq 33$ Pa, suggest this interpretation does not fully capture the complex sediment rheology. While the series of creep profiles in Figure 3.13a demonstrate a dominantly elastic response up to the yield stress, the

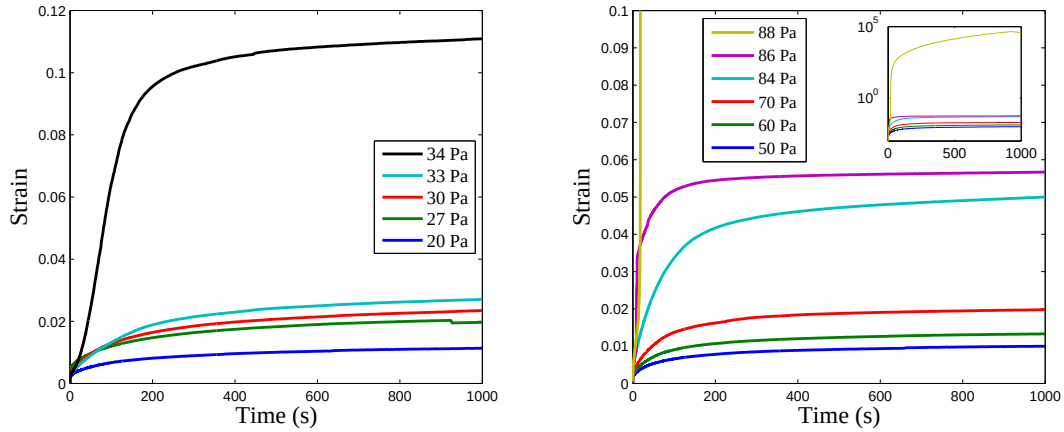

(a) (b)

Figure 3.13: Creep profiles at a series of constant stress conditions for (a) 36.0 % w/w $Mg(OH)_2$ soft sediment and (b) 38.9 % w/w CMgS

continued linear rise in strain after 400 s, once the contribution of the instantaneous and delayed elastic compliances have diminished, demonstrates a viscous response to protracted creep below the yield point, similar to observations for kaolin in Uhlherr *et al.* (2005). This could indicate that bubbles with sufficient excess bubble pressures, retained within soft sediments for long periods, may exhibit chronic viscous deformation at the bubble boundary and become more spherical over time. The departure from this type of creep behaviour in the 34 Pa test, with much more extensive deformation of the sample during the first 100 s, indicates the transition to more fluid-like behaviour (Jeldres *et al.*, 2014; Liddell & Boger, 1996; Uhlherr *et al.*, 2005), indicating a yield stress in the 33-34 Pa range, which is consistent with the 37.5 % w/w flow curves in Figure 3.10a.

Six creep profiles are presented for 38.9 % w/w CMgS in Figure 3.13b. The profiles at applied stresses of 50-84 Pa demonstrate similar behaviour to the commercial $Mg(OH)_2$. The dominant response is characterised by a delayed elastic compliance, with an exponential decay in the increase in strain towards a plateau, however, a truly flat plateau is never achieved due to a continued linear rise in strain, thereby demonstrating the viscous compliance. Conversely, the creep curve at 86 Pa, the highest stress before the sample is observed to yield, demonstrates a classically elastic response for the duration of the test. The inset to Figure 3.13b, representing strain on a logarithmic scale, shows a 6 order of magnitude increase in strain at an applied stress of 88 Pa indicating a yield stress in the 86-88 Pa range. The creep tests, combined with the stress-strain flow behaviour justifies the characterisation of consolidated soft sediments in Terrones & Gauglitz (2003) as elastoviscoplastic materials (Fraggedakis *et al.*, 2016; Saramito, 2009).

The creep tests reinforce the observation from the flow curves in Figure 3.10 and yield stress summary in Figure 3.12, that CMgS is able to withstand greater

stresses than an equally consolidated $Mg(OH)_2$ soft sediment before yielding. The broader particle size distribution and presence of very large, dense contaminants within the CMgS also implies a greater tendency for the CMgS to consolidate under gravity. It has proved difficult to replicate the very high yield stress conditions believed to exist within certain MSSS containers at laboratory scale, since CMS has consolidated under large hydrostatic loads over many decades. Furthermore, the standard commercial rheometers available for this work limited shear yield stress characterisation to sediments of less than 830 Pa, although sediments of up to 54 % w/w solids content have been achieved, which correspond to yield stress conditions of up to 1112 Pa on extrapolation of eq. (3.5). There is considerable uncertainty regarding the precise condition of waste within the MSSS and decommissioning activities currently being undertaken at Sellafield make young low-intermediate yield stress sludge much more realistic. CMS from the floor of the FGMSP undergoes considerable dilution and shearing during mobilisation and transport to SPP1. Crane extraction of consolidated waste from the MSSS and transfer to 3 m^3 containers resembles a *slump test* (Gauglitz *et al.*, 2015; Sofrá & Boger, 2002) sometimes used to characterise yield stress in the minerals industry. CMS released from the crane grab will slump under its own weight, breaking many of the slowly formed inter-aggregate bonds. Hence, there remains a considerable interest in low and intermediate yield stress sediments in addition to the kilopascal yield stress conditions typically associated with the MSSS containers (Hunter *et al.*, 2011).

In addition to the shear yield stress, the shear modulus, G, is identified in eq. (2.11) as critical to whether a spherical bubble can expand its host cavity (van Kessel & van Kesteren, 2002). Sherwood & Meeten (1991) and Alderman *et al.* (1991) state that the same vane rheometry data in Figure 3.9 used to determine the shear yield stress can be used to estimate the shear modulus from the maximum gradient of the torque-time profile according to eq. (3.7):

$$G = \frac{1}{4\pi u_\theta H}\left(\frac{dT}{dt}\right)_{max}\left(\frac{1}{R^2} - \frac{1}{R_c^2}\right) \tag{3.7}$$

where u_θ is the angular velocity of the vane, H is the vane length, and R and R_c are the radii of the vane and container respectively. Applying this correlation generates the shear modulus values summarised in Figure 3.14. The technique appears to be sensitive to the vane geometry, demonstrating poor continuity between the large vane data for solids concentrations less than 40 % w/w and the small vane data at elevated concentrations. While these shear modulus data should be considered with caution, the data appears similar in magnitude to the shear yield stress data within this 30-50 % w/w sediment concentration range. Hence, the inverse yield strain, $\gamma_s^{-1} = \frac{G}{\tau}$, lies within the range of 0.7-1.4 and so a crude estimate of

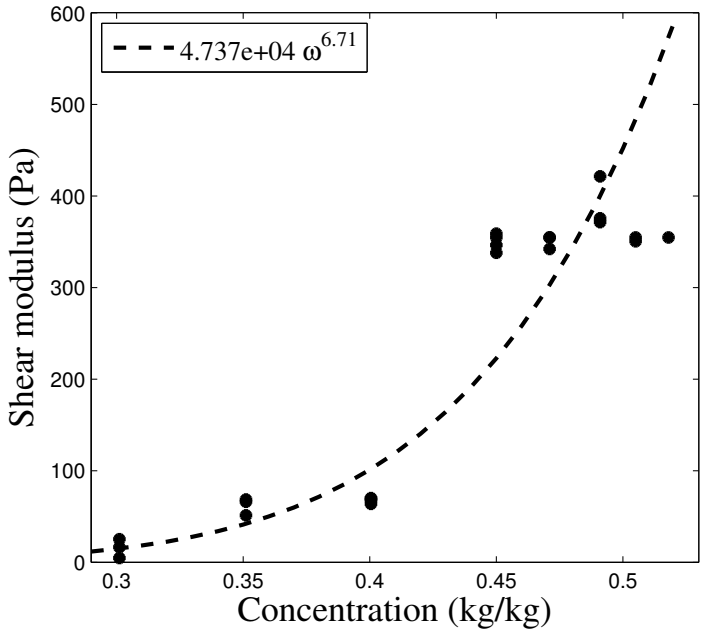

Figure 3.14: The shear modulus of magnesium hydroxide soft sediments obtained using the vane method

the excess bubble pressure for cavity expansion can be written as $\Delta P_e = \frac{4}{3}\tau \pm 40\,\%$, indicating that the excess bubble pressure for cavity expansion exhibits a similar magnitude to the yield stress.

3.3.3 Behaviour at the three phase interface

Three *compression-expansion* Langmuir-Blodgett isotherms are presented in Figure 3.15. Each isotherm demonstrates a significant, 34-46 $\mathrm{mN\,m^{-1}}$, increase in surface pressure as the monolayer undergoes compression, indicating that a large number of $Mg(OH)_2$ particles are supported at the three phase interface. Isotherms 2 and 3 are most comparable in shape. Compression of the monolayer through the *condensed phase* (Ybert *et al.*, 2002) sees a rapid increase in surface pressure until the monolayers occupy 34 and 41 $\mathrm{cm^2}$ of the trough surface respectively, at which point the monolayers appear to yield to form a more stable three-dimensional phase (Kundu *et al.*, 2005). Thereafter, each isotherm demonstrates significant hysteresis during the expansion cycle, indicative of a relatively inelastic monolayer (Hunter *et al.*, 2009). Isotherm 1 does not exhibit such a clear *yielding* of the monolayer, however the significant increase in surface pressure and expansion cycle hysteresis are consistent in each instance.

The dashed vertical line at an area of 50.7 $\mathrm{cm^2}$ in Figure 3.15 represents the surface area that would be occupied by the added mass of $Mg(OH)_2$ in a uniform monolayer of 4.4 µm spheres arranged with perfect hexagonal packing (Hunter *et al.*, 2009). Following Figure 3.4a, the primary agglomerates do not appear to

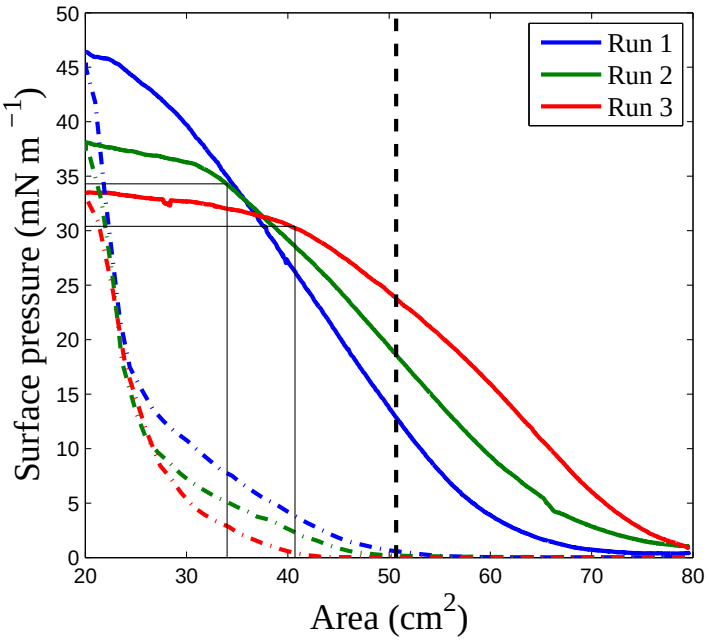

Figure 3.15: Three Langmuir-Blodgett isotherms observed during compression (solid) and expansion (dashed) of a $Mg(OH)_2$ monolayer at an air-water interface

be perfectly spherical, while the laser scattering particle sizing in Figure 3.3 does not reveal a monodisperse distribution; however, the surface area value of 50.7 cm^2 indicates a conservative estimate of the surface area of the monolayer at collapse if all particles were supported at the interface. In reality, the surface areas occupied by the monolayers at collapse for isotherms 2 and 3 were 20 and 33 % below that of the ideal monolayer, implying that between a fifth and a third of solids are perfectly wetted by water and fall into the sub-sphase, thereby exhibiting no finite contact angle. By the same measure, and given adequate time to stabilise, the majority of $Mg(OH)_2$ particles are indeed supported at the air-water interface.

Bubbling air through aqueous $Mg(OH)_2$ suspensions of 2-8 %v/v in a Bikerman column demonstrated poor capacity for the brucite particles to stabilise a dynamic foam. This is demonstrated by the image in Figure 3.16 where no stable foam is observed even at this relatively high air flow rate of 122.1 ml min^{-1}. This does not necessarily contradict the observation of a stable monolayer during the Langmuir-Blodgett experiments as particles were stabilised at the air-water interface over long contact times, > 10 min, during the slow evaporation of the isopropanol spring solvent. These dynamic foaming tests are characterised by particle-bubble contact times in the order of seconds or even less, which appear to be inadequate for particles to stabilise at the interface (Aktas *et al.*, 2008). While any finite contact angle will enable monolayer formation on a Langmuir trough, contact angles of at least 40° are reportedly required to form a stable foam (Hunter *et al.*, 2009), while contact angles of 70 and 85° are reported to best stabilise dynamic mono- and

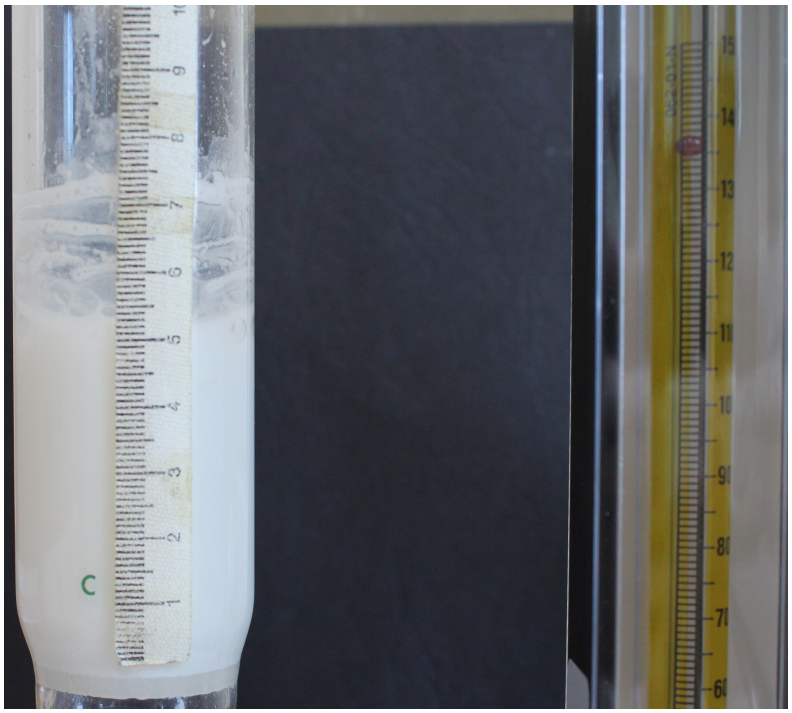

Figure 3.16: Image from a dynamic foam test within a Bikerman column taken while bubbling air through a 2 % v/v $Mg(OH)_2$ suspensions at 122.1 ml min^{-1}

bi-layer foam films respectively (Kaptay, 2006). Furthermore, even for dynamic foaming tests employing stabilising agents with optimum wetting characteristics, a relatively small, < 10 %, percentage of particles in the dispersion interact at the interface (Hunter *et al.*, 2009).

Gas generation governed by the corrosion of Magnox cladding and by radiolysis is a chronic process, with bubble growth proceeding on a time scale of weeks and months. Given the surface activity observed during the Langmuir-Blodgett experiments, these time-scales would appear to be adequate for some particles to stabilise at the bubble interface (Ali *et al.*, 2000) and form armoured bubbles (Pitois *et al.*, 2015). Consequently, $Mg(OH)_2$ at bubble interfaces could enable a chronic foam formation and inhibit bubble coalescence with soft sediments, however realistic contact angles in the order of 40° are unlikely to favourably influence the energetics of capillary invasion. Since the excess bubble pressure required to intrude into adjacent pore-space scales with the inverse pore throat radius and the cosine of the contact angle (Kam & Rossen, 1999), a three-phase contact angle of 40° only diminishes that excess pressure by 23 % against a perfectly pore-wetting continuous phase, and so capillary invasion will almost exclusively be dictated by the scale of sedimentary pores. However, floatation of particles within the Hanford tanks, leading to the formation of a floating crust (Page *et al.*, 2018), is considered to be driven by organic constituents within the waste matrix (Bryan *et al.*, 1992), which were carefully avoided during these experiments. Real CMS contains humic and fulvic acids generated by decayed organics within the open air FGMSP (Gregson

et al., 2011) which become surface-sorbed to hydrotalcites in the sludge matrix (Amin & Jayson, 1996; Gregson *et al.*, 2011) and could greatly enhance particle stability at the three-phase interface.

3.4 Conclusions

Two test materials, commonly used for research and development by Sellafield Ltd. as non-active analogues for CMS, have been characterised in terms of their chemical composition, particle size distributions, shear deformation behaviour and three phase wetting characteristics ahead of an investigation into their gas retention behaviour at laboratory scale. Following EDX and XRD analysis, the commercial magnesium hydroxide and corroded magnesium sludge (CMgS) test materials were found to consist predominantly of brucite, $Mg(OH)_2$, although the CMgS also contained additional coarse crystals, $\approx 20\,\mu m$, rich in silicon, sodium and aluminium understood to be crushed slate. Under SEM, the brucite component of both test materials exists as primary agglomerates of hexagonal platelet crystallites, consistent with observations in Gregson *et al.* (2011) and zhong Li *et al.* (2009). The commercial $Mg(OH)_2$ and CMgS have similar laser scattering derived median particle diameters of 4.4 and 4.8 µm respectively, however the CMgS contains a secondary mode of particles centred around 200 µm, while μCT revealed a significant number of millimetre-scale particles, much denser than the bulk sediment and outside the detection range of the laser scattering measurement technique. EDX revealed no elemental disparity between the $\approx 4\,\mu m$ primary agglomerates and the $> 1\,mm$, with magnesium and oxygen present in a 1:2 atomic ratio, indicating a second, high density brucite morphology.

Vane rheology demonstrated a complex elastoviscoplastic sediment response to shear deformation (Fraggedakis *et al.*, 2016; Saramito, 2009), with a distinct yield stress which increases rapidly with solids concentration, $\tau \propto \omega^{6.97-8.55}$, and a dominantly elastic response to creep below the yield stress but also a notable viscous compliance. The CMgS exhibited yield stresses roughly double those of the commercial $Mg(OH)_2$ at equivalent solids concentrations within the 30-40 % w/w range and thus an equivalent yield stress will coincide with a more porous microstructure for CMgS. Both test materials demonstrate greater yield strength than equivalent concentrations of kaolin, used extensively to simulate Hanford tank waste during gas retention studies (Sherwood & Eduardo Sáez, 2014). Langmuir-Blodgett experiments revealed that a majority of brucite particles added to the trough were supported at the air-water interface, arranged in a monolayer with a relatively inelastic response to compression and expansion (Hunter *et al.*, 2009; Ybert *et al.*, 2002), raising the possibility for armoured bubbles (Pitois *et al.*, 2015) within consolidated

soft sediments, which could inhibit coalescence and promote foam formation. However, $Mg(OH)_2$ demonstrated a poor capacity to stabilise dynamic foams within a Bikerman column (Barbian *et al.*, 2005), indicating that long contact times are required for particles to stabilise at the interface, which may be more realistic for chronic hydrogen generation by corrosion within the MSSS.

Chapter 4

The evolution of bubble populations retained by magnesium hydroxide soft sediments experiencing *in situ* gas generation

4.1 Introduction

The condition of waste within the MSSS containers, the extent of gas holdup within, and the size and shape of the retained bubble populations are all subject to significant uncertainty, with monitoring greatly inhibited by dose levels in some areas of up to 200 REM h^{-1}, equivalent to a permissible daily working time of less than a second (Smith, 2006). Characterising bubble populations within non-active sediments is not trivial due to the optically opaque nature of sludge. X-ray computed tomography (CT) has been employed to visualise bubbles in opaque environments with a degree of success, but much of this work has focused on individual bubbles injected from a submerged orifice (Barry *et al.*, 2010; Best *et al.*, 2006). Estimating the size and shape distribution for a diverse bubble population, nucleated *in situ* from volatile solutes within sedimentary pore water, would represent substantial progress, particularly for bubbles within $Mg(OH)_2$ sediments for which no research attention has yet been afforded in the publicly available literature.

This chapter presents a series of laboratory scale gas retention tests, using hydrogen peroxide decomposition for *in situ* oxygen generation within consolidated

$Mg(OH)_2$ soft sediments, with the aim of establishing the yield stress conditions which give rise to the most credible acute hydrogen release hazards. This scaled down and accelerated perspective of gas retention within the MSSS containers will also be further investigated using large-scale clinical CT in order to infer the likely mechanisms for bubble growth from the bubble geometries and reveal any macroscopic features which might promote chronic gas transport from the bed.

4.2 Materials and methods

The commercial $Mg(OH)_2$ (Versamag) test material, characterised in terms of its particle size, mechanical and interfacial properties in Chapter 3, was used for all of the experimental work in this chapter. Consolidated soft sediments were prepared by the addition of tap water and agitation for 30 min using an overhead stirrer with an axial flow impeller. *In situ* gas generation was achieved by addition of 35 % w/w hydrogen peroxide (Merck Chemicals, Germany) which decomposes within the bed to form oxygen bubbles according to eq. (5.4):

$$H_2O_2 \longrightarrow H_2O + \frac{1}{2}O_2 \tag{4.1}$$

It is generally accepted that the composition of the gas plays a limited role in the bubbles' buoyancy and the physics governing gas retention and release (Boudreau, 2012), and so it was assumed that oxygen bubbles provide an acceptable analogue for hydrogen, while also benefiting from more controllable reaction kinetics than hydrogen production from metal corrosion. However, the marginally greater solubility of oxygen in water may facilitate more rapid bubble coarsening due to Ostwald ripening. A 4.4 ml volume of hydrogen peroxide was added for each litre of sediment, decomposing to a gas volume corresponding to 60 % of the initial bed volume, consistent with the methodologies outlined by Gauglitz *et al.* (2015) and Sherwood & Eduardo Sáez (2014).

4.2.1 Laboratory scale gas retention tests

A series of laboratory scale tests were conducted to investigate the capacity for gas retention and release under different bed yield stress conditions. A 1 l volume of soft sediment was prepared and pumped to a 118 mm diameter acrylic test cylinder using a peristaltic pump. Hydrogen peroxide was injected into the soft sediment either at the mixing stage (stage 1) or by slow continuous injection during the 2 min transfer period (stage 2) as demonstrated in Figure 4.1. Optical images of the test vessel were captured at 8 min intervals while the hydrogen peroxide decomposed

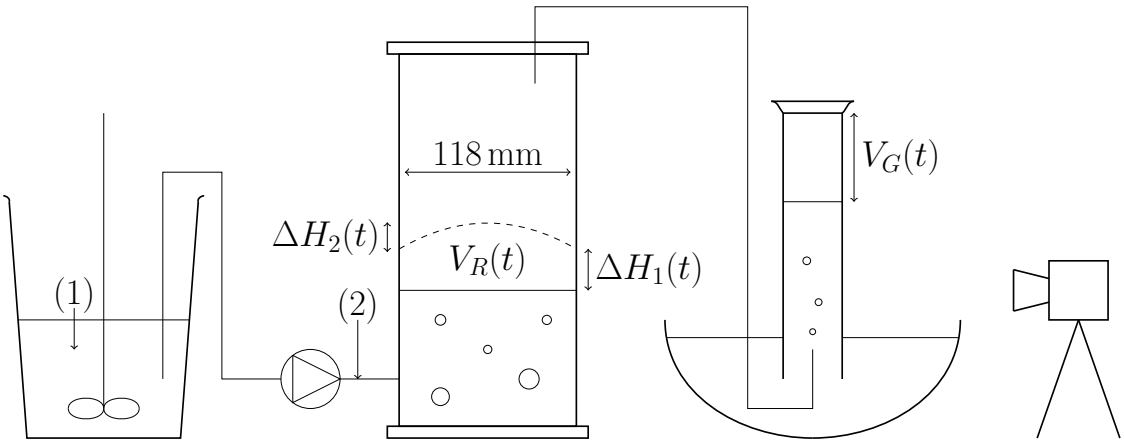

Figure 4.1: Schematic of the laboratory scale gas retention tests identifying two alternative hydrogen peroxide injection points, 1 and 2; the dashed line represents the surface of the soft sediment at time t

to form oxygen bubbles causing the bed to expand. The generated gas volume, $V_G(t)$, was monitored over time by measuring the volume of water displaced from an adjacent upturned measuring cylinder in a water bath. The retained gas volume, $V_R(t)$, was determined from the net increase in bed volume during gas generation. The sediment height, both at the cylinder wall and at the centre of the test vessel, was measured to millimetre precision from the images of the bed, referencing the measuring scale on the test cylinder wall for calibration. The instantaneous bed volume was estimated by representing the bed as a cylinder with a spherical cap according to eq. (4.2):

$$V_R(t) = \pi R^2 \Delta H_1(t) + \frac{1}{3}\pi \Delta H_2(t)^2 \left(3R - \Delta H_2(t)\right) \tag{4.2}$$

where R is the test cylinder radius, $\Delta H_1(t)$ is the increase in bed height at the wall and $\Delta H_2(t)$ is the difference in height between the domed sediment peak and the bed height at the wall (see Figure 4.1). The bed void fraction, $\nu(t)$, can be calculated at any instant using eq. (4.3):

$$\nu(t) = \frac{V_R(t)}{V(t)} \tag{4.3}$$

where $V(t)$ is the instantaneous total bed volume. The capacity of each soft sediment to retain gas is characterized according to the maximum void fraction, ν_{max}, or *gas holdup* (Frank *et al.*, 2012; Gauglitz *et al.*, 2015), observed during the experiments. Since the gas generation profiles were designed for consistency between tests, bed expansion is governed by the rate of gas release. The instantaneous volume of gas which has escaped the bed, $V_E(t)$, is implied from the difference

between the generated and retained volumes:

$$V_G(t) = V_R(t) + V_E(t) \tag{4.4}$$

The density, ρ, of a magnesium hydroxide soft sediment of known solids weight fraction, ω, and void fraction, ν, can be determined using eq. (4.5):

$$\rho(\omega, \nu) = (1 - \nu)\rho_s = \frac{1 - \nu}{\left(\frac{\omega}{\rho_p} + \frac{1-\omega}{\rho_l}\right)} \tag{4.5}$$

where ρ_s is the gas free bulk soft sediment density, ρ_p and ρ_l are the sedimentary particle and fluid densities. Hence, it is possible to determine the void fraction at which the soft sediment bulk density would become buoyant with respect to an aqueous supernatant, $\rho(\omega, \nu) < \rho_l$ (or neutral buoyancy condition ν_{NB}) and complete rollover becomes feasible.

In addition to establishing the conditions at which rollover events are *possible* from their maximum void fractions, the occurrence of Rayleigh-Taylor instabilities is observable if these tests are performed with an aqueous supernatant above the consolidated sediment layer. A 0.5 l volume of water was dyed yellow using a Fluorescein (Sigma Aldrich, Germany) staining agent with the chemical formula $C_{20}H_5O_5$, in order to improve the colour contrast between bed and supernatant, and pumped to the test cylinder after the soft sediment had fully transferred. Optical images of the test vessel were captured at 4 min intervals in order to determine the frequency of rollover events as well as the change in total waste immediately after such release events. These tests were performed for beds of 30, 35, 40 and 45 % w/w solids concentration.

4.2.2 X-ray computed tomography

The laboratory scale gas retention tests provide a good indication of bulk bed swell under different sediment conditions but reveal little about the bubble population retained within the optically opaque bed. A Brivo CT385 medical x-ray computed tomography (CT) scanner (GE Healthcare, UK) was employed to provide insight into the size, shape and number density of the retained bubble population within soft sediments of 30, 40, 45 and 54 % w/w solids concentration, reflecting the broad range of density and yield stress conditions anticipated within Magnox waste tanks (Hunter *et al.*, 2011). The test vessel geometry was replaced with a sideways mounted clear acrylic cylinder of 30 cm diameter and 15 cm length in order to ensure that x-ray attenuation through the sample was as axisymmetric as possible, thereby minimizing artefacts. Sediment preparation was scaled up from 1 l to

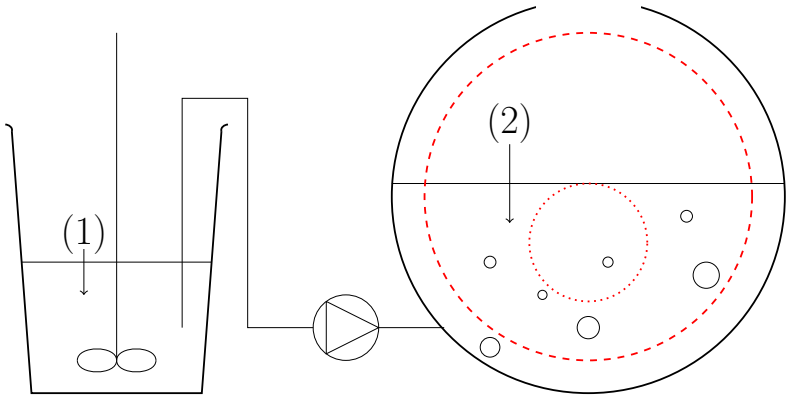

Figure 4.2: Schematic of the modified gas retention tests for optimised CT imaging, identifying two alternative hydrogen peroxide injection points, 1 and 2, and two alternative imaging fields of view in red

6.5 l to utilize the greater test vessel capacity. The effect of non-homogeneous gas generation through the test material was investigated by injecting hydrogen peroxide into the soft sediment during transfer to the test vessel (stage 2), as represented in Figure 4.2.

Figure 4.2 also demonstrates the two imaging fields of view (FOV) investigated. The small FOV captures a volume 49 times smaller than the large FOV, but achieves almost double the pixel resolution and half the axial slice separation, as detailed in Table 4.1. The small FOV was captured more frequently and so was primarily used to examine transient changes in the bubble population. The large FOV was used to ensure a representative sample size and observe the larger macro-features propagating through the bed. The pixel resolution of the large FOV is two orders of magnitude larger than the median sediment grain size, so only mature bubbles significantly larger than the scale of capillaries within the sediment are observed.

Table 4.1: X-ray CT imaging parameters for two imaging fields of view

	Large FOV	Small FOV
X-ray voltage (kV_p)	120	120
X-ray tube current (mA)	40	79
FOV diameter (mm)	250	96
Pixel resolution (µm)	488	250
Slice separation (µm)	1250	625
Number of axial slices	112	32
Axial FOV depth (mm)	138.8	19.4
Total FOV volume (mm^3)	6.81×10^6	1.40×10^5

X-ray CT image analysis

The statistics of the retained bubble population were determined by three dimensional analysis using FIJI-ImageJ software (Schindelin *et al.*, 2012). A stack of CT images was first thresholded to create binary images of black bubbles against white soft sediment. Discrete bubbles were then identified by inter-connecting the black voxels which were face, edge or corner adjacent using the 3D object counter algorithm provided by Bolte & Cordelières (2006). The volume, V, surface area, A, and co-ordinates of each individual bubble were then recorded for further analysis using Matlab (Mathworks, v. R2013b). The bubble size is represented using the equivalent spherical diameter, $d_b = \sqrt[3]{\frac{6V}{\pi}}$, while the bubble shape was analyzed using a digital sphericity, Ψ_{dig}, defined in eq. (4.6). Traditional sphericity calculations performed on bubbles comprised of regular cuboid voxels will be artificially low as the angular voxels exaggerate the surface area of the bubble. Since the sphericity of even a perfect digital sphere cannot exceed the sphericity of a cube ($\Psi_{cube} = \left(\frac{\pi}{6}\right)^{\frac{1}{3}} \approx 0.806$), the digital sphericity normalizes the conventional sphericity against that of a cube to provide ceiling values closer to unity.

$$\Psi_{dig} = \frac{\pi^{\frac{1}{3}}(6V)^{2/3}}{A}\left(\frac{6}{\pi}\right)^{\frac{1}{3}} = \frac{6}{A}V^{\frac{2}{3}} \tag{4.6}$$

Since thresholding represents the critical stage of image post-processing, sensitivity analysis was undertaken to investigate the impact of the chosen threshold value on the ultimate bubble statistics. Using the example of the 40 % w/w soft sediment, the Renyi entropy algorithm (Kapur *et al.*, 1985) was applied to calculate a threshold radiodensity of −315 HU, and a range of ±38 HU around this value was investigated, as shown in Figure 4.3. The range of threshold values had a negligible impact on the resulting bubble diameter histogram, with standard deviations of 2.5 % and 4.2 % observed in the 50$^{\text{th}}$, $d_{b,50}$, and 90$^{\text{th}}$, $d_{b,90}$, percentiles of the equivalent spherical bubble size distributions respectively. However, while the bubble size distribution within this observable size range was not particularly sensitive to thresholding, the number of mature bubbles consisting of more than 5 voxels within the FOV varied significantly between 961 and 1731 (shown in the legend of Figure 4.3). This discrepancy reflects the large number of small bubbles close to the pixel resolution, and the fact that small bubbles are predominantly comprised of surface voxels with intermediate radiodensities between those of the bulk sediment and oxygen. Nonetheless, the influence of the thresholding value on the exact measurement of the bubble number density was not considered significant as the study's focus was on the transient trends in the number, size and shape of mature bubbles within the population, which were less sensitive to the given threshold value.

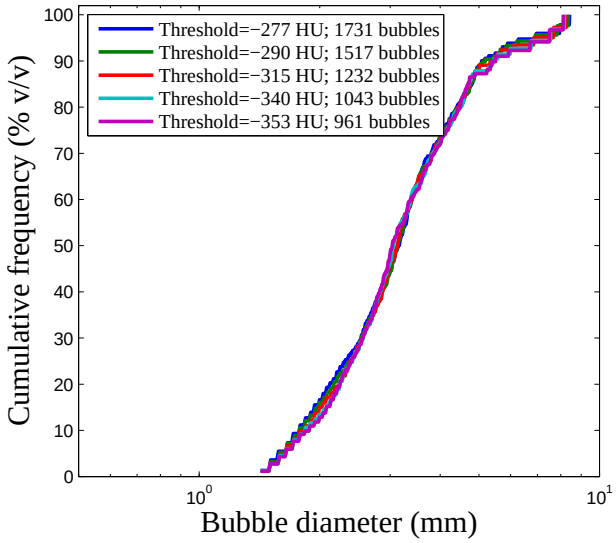

Figure 4.3: Sensitivity of bubble population statistics to the threshold radiodensity value used during image post-processing; the statistics relate to bubbles within the large FOV of a 40 % w/w sediment after 6 h of gas generation

Transient changes in the bubble population were examined using a process of *hyperstacking*. Collating multiple stacks of two-dimensional tomographs at known time intervals into a hyperstack enables panning along the depth of the FOV and through time. By *flattening* the hyperstack, different time frames can be represented using a colour progression, enabling visualization of changes in the number, size, shape and position of bubbles within the FOV.

4.3 Results

4.3.1 Laboratory scale gas retention tests

Injecting hydrogen peroxide into 28-45 % w/w magnesium hydroxide soft sediments at stage 2 in Figure 4.1 resulted in the gas generation profiles shown in Figure 4.4a. Increasing solids concentration in the bed demonstrated no enhanced catalytic effect on the rate of hydrogen peroxide decomposition. Good repeatability was achieved between the four gas generation profiles in Figure 4.4a and complete conversion of 4 ml hydrogen peroxide generated 548 ± 62 ml oxygen in 14-18 h. The total volume of oxygen generated was in line with expectations as 4 ml of 35 % w/w hydrogen peroxide solution contains 4.65×10^{-2} mol H_2O_2, decomposing to 2.33×10^{-2} mol O_2, which would occupy a 568 ml volume in the gas phase at 25 °C and 1 atm. The rate of gas generation exponentially decays as the hydrogen peroxide is consumed, observed as a pseudo first order reaction in the form of eq. (4.7):

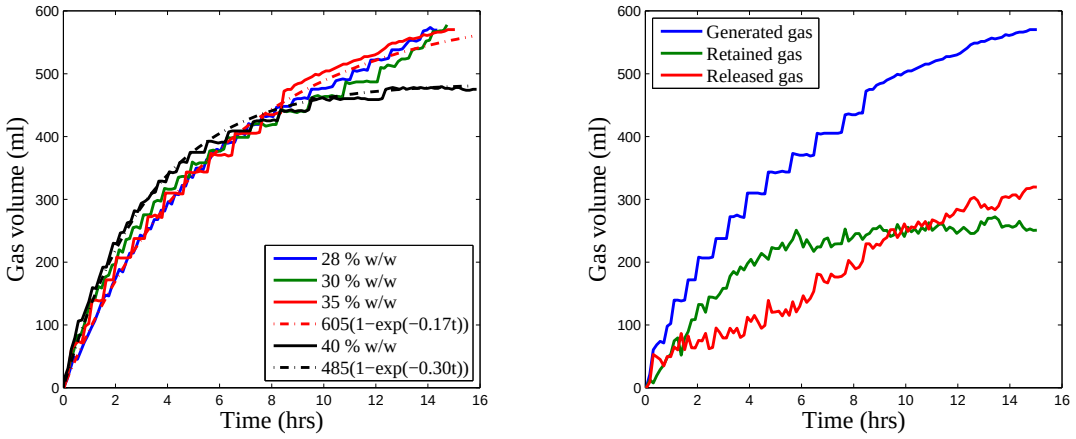

(a) (b)

Figure 4.4: Laboratory scale gas retention test profiles achieved by injecting hydrogen peroxide at point 2 in Figure 4.2, including (a) example gas generation profiles within 28-40 % w/w (4-85 Pa) soft sediments and (b) gas generation, retention and release profiles within 35 % w/w (27 Pa) soft sediment

$$V_G(t) = V_{G,f}(1 - exp(-kt)) \tag{4.7}$$

where $V_{G,f}$ is the final volume of gas generated and k is a first order reaction kinetic constant in the order of 0.17-0.3 h^{-1} for these laboratory scale tests. Two dashed line profiles in Figure 4.4a represent example fits in accordance with eq. (4.7). The rate of oxygen production was sensitive to local temperature conditions and so subsequent tests conducted within a CT scanner exhibited accelerated hydrogen peroxide decomposition, approaching completion within 8 h due to the heat generated by operating the scanner, corresponding to kinetic constants closer to 0.4 h^{-1}. The variation in total generated gas volume can be attributed to fluctuations in ambient temperature and the precision of the syringe used to inject the hydrogen peroxide; since 1 ml 35 % w/w hydrogen peroxide decomposed to around 137 ml oxygen, the total gas volume was sensitive to the precise volume of gas generating reagent introduced. Nonetheless, these gas generation profiles demonstrate sufficient repeatability across the relevant bed concentration range.

Figure 4.4b demonstrates gas generation, retention and implied release profiles observed during 15 h of *in situ* gas generation in a 35 % w/w magnesium hydroxide soft sediment of 27 Pa shear yield stress. During the first 4 h around two thirds of the gas generated is retained by the bed, after which the rate of bed expansion decreased, with the bed attaining a maximum void fraction of 0.27. At 27 % voidage, the bulk density of the bed is reduced to 10 % below that of water, indicating a significant possibility of rollover events in the presence of a supernatant. The absence of a supernatant for these tests precluded large episodic releases due to Rayleigh-Taylor instabilities, and gas appeared to be continuously released from the bed at

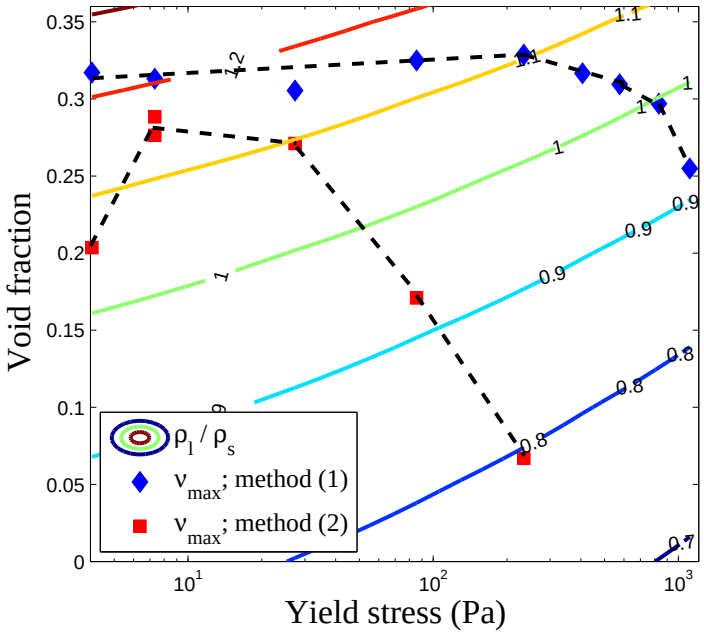

Figure 4.5: The maximum void fractions observed under different shear yield stress conditions and alternative gas generation methods: (1) injection at the sample homogenisation stage and (2) continuous injection into the flow during transfer to the test vessel (see Figure 4.2); the density countour map demonstrates the feasibility of periodic rollover events

a near constant rate of 21 ml h^{-1} (red line, Figure 4.4b), with just over half of the total gas generated escaping the bed over the course of the 15 h experiment. This methodology was repeated for bed concentrations of 28-54 % w/w, corresponding to varied yield stress conditions in the range of 4-1112 Pa. The gas retention and release profiles obeyed similar trends across the yield stress range, but the maximum void fractions varied between each soft sediment and are presented in Figure 4.5.

Injection of hydrogen peroxide at stage 2 (see Figure 4.1) generated a parabolic trend in the gas holdup across the 4-234 Pa yield stress range, implying enhanced rates of continuous gas release below 7 Pa and above 27 Pa shear yield stress. Below 7 Pa yield stress, the buoyant force of even relatively small bubbles should be sufficient to fluidize the weakly consolidated, milky sediment (Dubash & Frigaard, 2007; van Kessel & van Kesteren, 2002). The reduction in holdup above 27 Pa yield stress appears to relate to a more complicated phenomenon. The rate of gas release by fluidisation, or ebullition, should progressively decrease with increased bed yield stress (Atapattu *et al.*, 1995; van Kessel & van Kesteren, 2002), while gas release along stable open channels is more typically associated with significantly more consolidated beds with yield stresses greater than 1 kPa (van Kessel & van Kesteren, 2002). Thus, neither mechanism adequately explains the significantly increased rate of gas release from beds of 84-234 Pa yield stress. It was felt that a potential cause may be related to mixing inhomogeneity, with continuous peroxide injection

into the feedline resulting in a non-uniform distribution of volatiles, leading to the creation of localized release pathways. Consequently an alternative approach was investigated by introducing hydrogen peroxide at the sample homogenization stage (indicated by stage 1 in Figure 4.1), ensuring more thorough mixing of gas generating reagents through the soft sediment.

Homogenisation of hydrogen peroxide through the sediment resulted in consistently high void fractions of 0.3-0.33 across a broad range of yield stress conditions up to 600 Pa, while gas holdup only receded in the 600-1200 Pa range. The reduced holdup in the 600-1200 Pa range coincides with bed conditions that have previously been associated with the continuous release of gas along stable open channels (van Kessel & van Kesteren, 2002). The reason for this disparity in bed expansion between the two approaches to peroxide introduction was uncertain, and so both experimental approaches were explored using x-ray CT imaging to identify whether differences between the retained bubble populations reveal alternative mechanisms for gas release.

Cross-referencing the experimental maximum void fractions with the density contour lines, calculated using eq. (4.5), in Figure 4.5 reveals critical yield stress conditions where bed swell reduces the bulk sediment density to below that of water, invoking the potential for rollover events and acute gas release. The green contour line demonstrates the neutral buoyancy condition as a function of gas free yield strength and void fraction. Under the more homogeneous gas generation conditions assumed with injection method 1, the capacity for rollover events remains feasible for highly consolidated bed conditions of up to 800 Pa yield stress. CMS legacy waste in the MSSS at Sellafield has consolidated over several decades under large lithostatic loads to achieve yield stress conditions believed to be in excess of 1 kPa (Hastings *et al.*, 2007; Hunter *et al.*, 2011; McCracken & Eilbeck, 2005). These highly consolidated, highly heterogeneous bed conditions appear to facilitate sufficient continuous gas release to mitigate the risk of large periodic releases; however, evacuating aging facilities of these legacy wastes requires their mobilization, dilution and homogenization for transportation and storage in new modular containers. Consequently, these processing steps would appear to make the conditions conducive to rollover events more credible, based on the observations at this reduced experimental scale.

Acute gas releases in the presence of a supernatant

Repeat gas retention tests were performed in the presence of a Fluorescein dyed supernatant; time-lapse image sequences for 30 and 45 % w/w sediments are presented in Figure 4.6. The 30 % w/w bed, of 7 Pa yield stress, swells to a voidage of 7 % during the first 24 min of gas generation before becoming unstable. The image

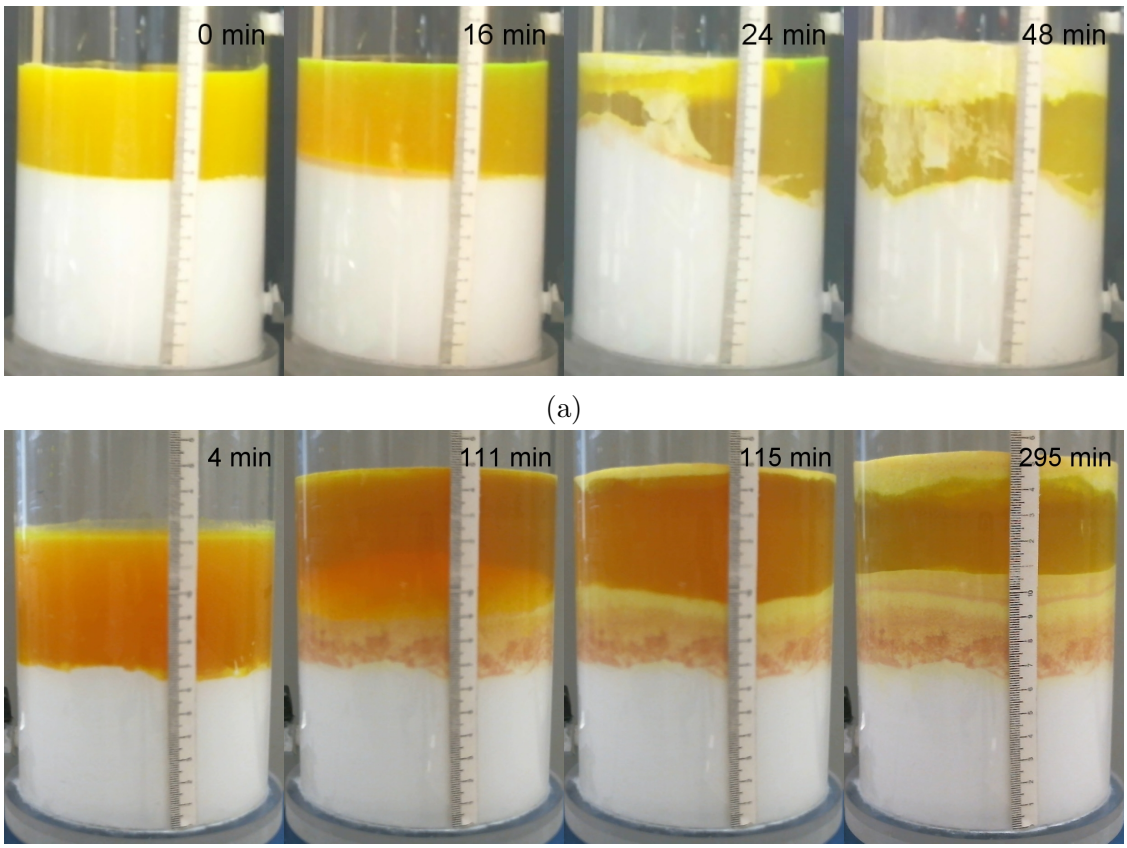

(a)

(b)

Figure 4.6: Image sequences recoded to demonstrate bed swell and release events exhibited by (a) 30 %w/w (7 Pa) and (b) 45 %w/w (238 Pa) $Mg(OH)_2$ soft sediments subject to *in situ* gas generation by hydrogen peroxide decomposition

at 24 min is captured during the first acute release event and expelled $Mg(OH)_2$ is seen to accumulate at the surface as a floating foam or *crust* layer, consistent with observations at the Hanford underground storage tanks where solid crusts up to 1.3 m thick have been recorded (Allemann, 1992; Bryan *et al.*, 1992; Page *et al.*, 2018). Given that the bulk density of the sediment at 7 % voidage remains 12 % greater than the supernatant, gas release is best explained by partial rollover, which does not require that the bulk sediment exceeds the neutral buoyancy condition. A second release event at 48 min, similar in magnitude, sees the crust roughly double in thickness. The sheer white bed colour throughout the experiment appears to exclude the possibility of significant mass transfer between the lower regions of the bed and the fluorescent yellow supernatant, which might be anticipated on full rollover.

The 45 % w/w sediment exhibits similar phenomena, with the bed swelling to 27 % voidage before liberating a portion of solids from the bed to the top of the supernatant after 115 min, and then again at 295 min. In this instance, the high sediment void fraction at release exceeds the neutral buoyancy condition, achieving a bulk sediment density 4 % less than that of water. While some mass exchange is observed between the supernatant and the top third of the bed, there is negligible evidence of a catastrophic rollover liberating gas from the lower portion of the bed. The instability event is not accompanied by a drop in the total height of the bed and supernatant, which would signify gas release to the ullage. The theory of partial rollover, discussed in Section 2.8.2, establishes that gas will only be transfered to the ullage if sufficient buoyant potential energy is converted to kinetic energy that the buoyant gob breaks apart on collision with the supernatant-ullage interface. The ratio of buoyant potential energy to the energy required to yield the gob is repeated in eq. (4.8)(Stewart *et al.*, 1996):

$$\begin{aligned} \frac{W_{bp}}{W_\tau} &= \frac{\nu P_a k_h}{(1-\nu)\varepsilon_\tau \tau}\left(\left(1+\frac{1}{k_h}\right) ln(1+k_h) - k_{by}\right) > 2.6 \\ k_h &= \frac{\rho_l g L}{P_a} \\ k_{by} &= \frac{\nu_{nb}(1-\nu)}{\nu(1-\nu_{nb})} \end{aligned} \tag{4.8}$$

This excess buoyant potential energy increases with the dimensionless lithostatic head, k_h, which scales with the supernatant depth, L. Hence, scaling down the experiment from a 600 m^3 silo container to a litre-scale test with a supernatant only centimetres deep greatly reduces the stress on the gob and so the gas liberated from the bed remains trapped within the floating foam layer. Following, eq. (4.5), the neutrally buoyant void fraction can be expressed in terms of the mass fraction

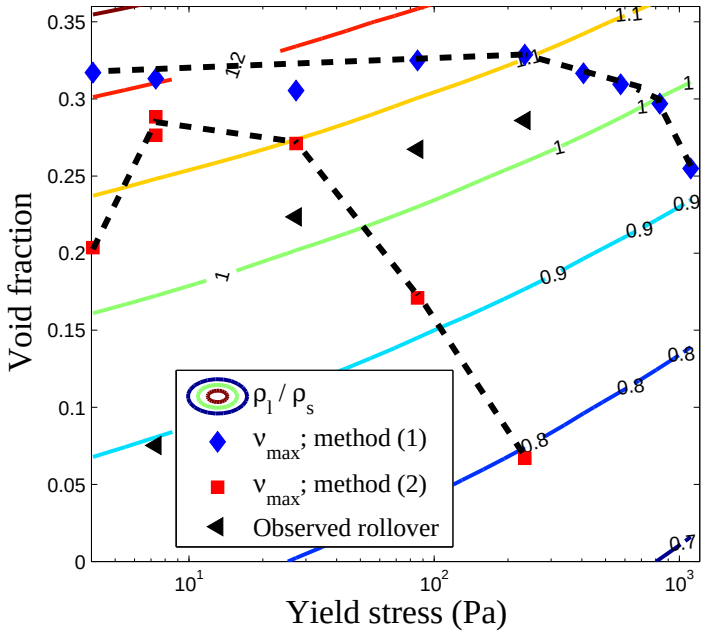

Figure 4.7: Summary of the void fractions at which four sediments of 7-238 Pa yield stress exhibited their first partial rollover event, aggregated with the gas retention tests in the absence of a supernatant from Figure 4.5

of solids in the soft sediment, the fluid and solids densities:

$$\begin{aligned} \frac{1-\nu_{NB}}{\left(\frac{\omega}{\rho_p}+\frac{1-\omega}{\rho_l}\right)} &= \rho_l \\ \therefore \nu_{NB} &= \omega\left(1-\frac{\rho_l}{\rho_p}\right) \end{aligned} \tag{4.9}$$

Substituting for the neutrally buoyant void fraction allows eq. (4.8) to be expressed as:

$$\frac{W_{bp}}{W_\tau} = \frac{\nu\rho_l gL}{(1-\nu)\varepsilon_\tau \tau}\left(\left(1+\frac{P_a}{\rho_l gL}\right) ln\left|1+\frac{\rho_l gL}{P_a}\right| - \frac{\omega\left(1-\frac{\rho_l}{\rho_p}\right)(1-\nu)}{\nu\left(1-\omega\left(1-\frac{\rho_l}{\rho_p}\right)\right)}\right) > 2.6 \tag{4.10}$$

The void fractions at which acute release was observed were added to Figure 4.5 and presented in Figure 4.7. Soft sediments of 35-45 % w/w, or 30-234 Pa yield stress, became unstable once the bulk sediment density fell to 3-5 % less than that of water. The exceptional case was the 30 % w/w, or 7 Pa yield stress, sediment, which quickly became unstable and exhibited partial rollover at a relatively low voidage. From the void fractions at which each sediment became unstable, it is possible to predict whether acute gas release is likely at increased scale using eq. (4.10). Table 4.2 summarises the buoyant potential energy ratios which would be observed for supernatants of 0.1, 1 and 5 m depth.

Table 4.2: Estimation of buoyant potential energy ratios for *gobs* of liberated sediment following partial rollover at various supernatant depths according to eq. (4.10) (Stewart *et al.*, 1996); the conditions most likely to result in acute gas release are shown in bold

ω	τ (Pa)	ν	ν_{NB}	k_{by}	$\frac{E_{bp}}{E_\tau}$ (L = 0.1 m)	$\frac{E_{bp}}{E_\tau}$ (L = 1 m)	$\frac{E_{bp}}{E_\tau}$ (L = 5 m)
0.30	7	0.08	0.17	2.57	-17.1	-166.7	-744.5
0.35	30	0.22	0.20	0.88	1.3	**17.2**	**170.2**
0.40	86	0.27	0.23	0.82	0.8	**9.4**	**80.9**
0.45	234	0.29	0.26	0.88	0.2	**2.9**	**27.9**

From Table 4.2, the conditions at which partial rollover was observed within the 7 Pa yield stress sediment are not likely to manifest in acute gas release, no matter how deep the overlying supernatant. Since partial rollover occurred at a very low gas fraction, the gob is buoyant with respect to the bulk sediment, but not with respect to the supernatant and so the gob will decelerate from the top of the bed through the supernatant and never achieve a realistic kinetic energy to overcome its modest yield stress. A greater concern for such low strength sediments would be acute release from a bubble cascade (Sherwood & Eduardo Sáez, 2014), since a mild perturbation could potentially induce ebullient bubble release. At supernatant depths of only 0.1 m, similar to the experimental scale in Figure 4.6, there appears to be insufficient buoyant potential energy to break apart any of the buoyant gobs and liberate the enclosed gas. Scale up to 1 m deep supernatants increases the buoyant potential energy by an order of magnitude, making acute gas release probable for the 27-86 Pa sediments, while the higher yield stress, 234 Pa, sediment represents a borderline case. Further scale up to a supernatant depth of 5 m appears to virtually guarantee violent acute gas release when intermediate yield stress, 30-234 Pa sediments exhibit partial rollover.

To summarise, sediments of > 500 Pa yield stress are unlikely to experience partial rollover if a supernatant to bed density ratio, $\frac{\rho_l}{\rho_s}$, of 1.05 is required to achieve instability, and a supernatant several metres deep would be required for sufficient buoyant potential energy to yield the liberated gob and release the gas within. However, intermediate yield stress conditions of 30-234 Pa demonstrate sufficient gas holdup to exceed neutral buoyancy and will readily break apart on rising through supernatants of modest depths of around 1 m, thereby presenting a genuine acute release hazard at process scale. A number of measures could mitigate against flammability hazards, including (1) the provision of a sufficiently large ullage capacity that the lower flammability limit can never be approached on acute release, (2) by dewatering CMS to high yield stress conditions which facilitate higher levels of continuous gas release and diminish the possibility for acute gas release on partial rollover, (3) by limiting the depth of the supernatant layer thereby reducing the buoyant potential energy of a liberated gob, or (4) use

of a denser supernatant fluid, thereby making partial rollover events more likely and more frequent, but much milder and less likely to manifest in acute gas release.

For a better understanding of the conditions which give rise to significant gas holdup and high potential for acute gas release it is necessary to appreciate the size, shape and mobility of retained bubbles, rather than just the bulk sediment behaviour, which were investigated through a series of x-ray CT scans.

4.3.2 X-ray computed tomography

The four soft sediments of 30, 40, 45 and 54 %w/w solids concentration imaged using x-ray CT correspond to yield stresses of 7, 86, 234 and 1112 Pa. In order to enable visualisation and quantitative analysis of the retained bubble population, the raw radiodensity distribution through the sample was converted to a stack of 8-bit grey-scale images, bi-level thresholded to reveal black bubbles and white bulk sediment and then black voxels were interconnected in three-dimensional space to identify and label discrete objects using the Bolte & Cordelières (2006) algorithm. Each of these post-processing steps are demonstrated in Figure 4.8. Truncated bubbles in contact with the edge of the field of view were excluded from subsequent quantitative analysis as their size and shape could not be adequately represented.

Evolution in the bubble size and shape

Using the example of the 1112 Pa sediment, six side-on scout profiles of the bed, presented in Figure 4.9a, demonstrate expansion of the bed during the first 4 h of gas generation, similar to the gas retention profile in Figure 4.4b, with negligible bed swell thereafter. The bulk bed expansion is contrasted with the evolution of the bubble population of an observable scale ($d_b \geq 0.72$ mm) within the small FOV, presented in Figure 4.9b. The $d_{b,50}$ and $d_{b,90}$ bubble diameters appear to achieve steady state sizes within the first hour of gas generation. Expansion of the bulk sediment in Figure 4.9a appears to be mirrored by the increase in the number density, n_b, of bubbles at this observable scale, presented on the right hand axis of Figure 4.9b. The number density of bubbles greater than 0.72 mm equivalent spherical diameter increases rapidly within the first two hours of gas generation, slowing significantly from 2-6 h and remaining relatively stable thereafter. Thus, the data reveal that the population of mature, macroscopic bubbles increases during the period of greatest bed expansion, and slows as the bulk bed volume plateaus. While this evolution in the bubble population appears to imply higher rates of bubble nucleation within the early stages of gas generation, this cannot be monitored directly, as microbubbles are not recognized at this imaging resolution. Indeed, if growth of sub-resolution bubbles to the observable scale proceeds by coalescence or

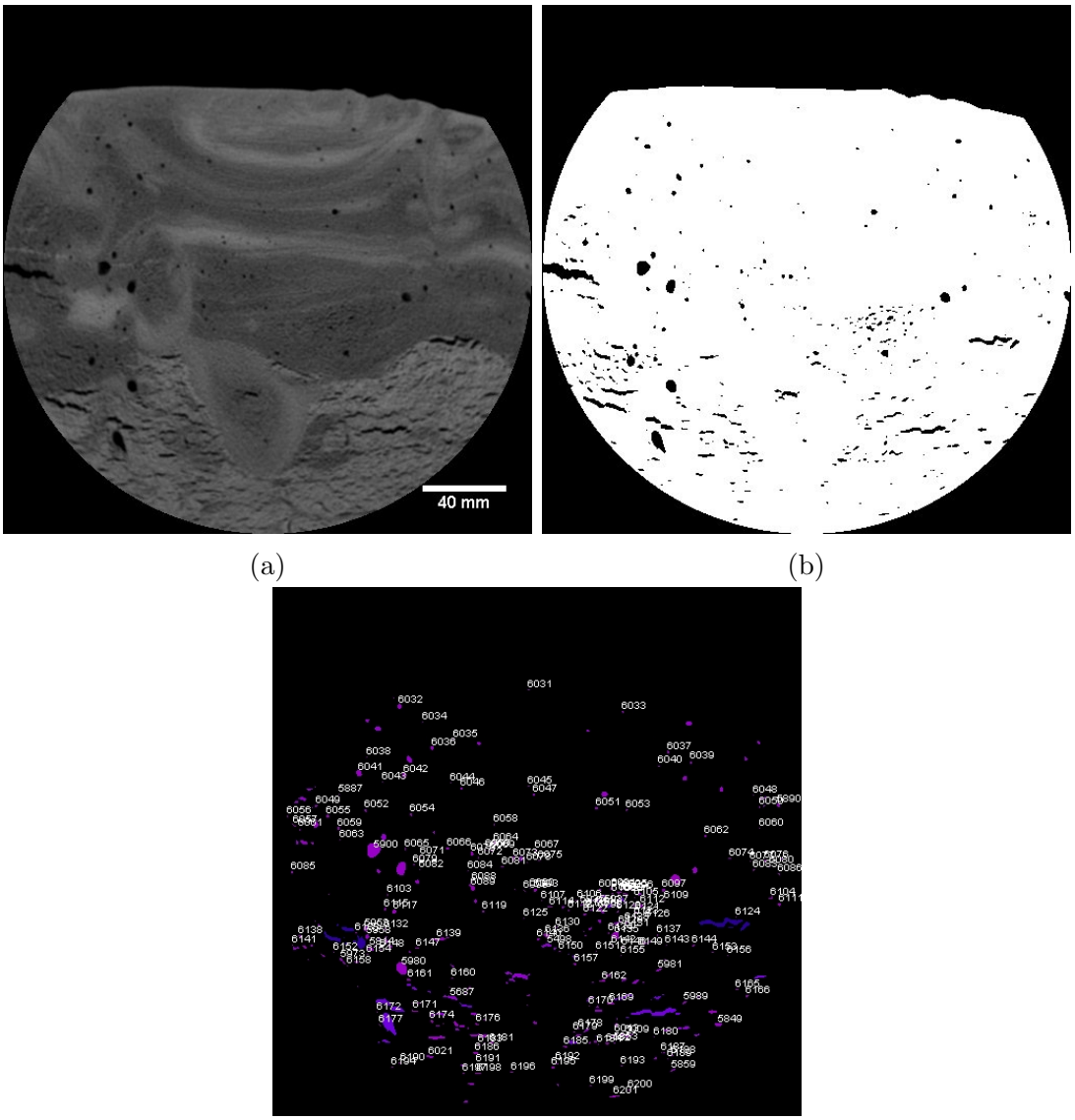

Figure 4.8: Imaging post-processing steps prior to quantitative bubble population analysis demonstrating (a) a typical x-ray CT slice in 8-bit grey-scale, (b) the bi-level thresholded slice revealing black voids against white bulk sediment and (c) identification and labelling of discrete objects in three-dimensional space using the Bolte & Cordelières (2006) algorithm (excluding those in contact with the edge of the field of view); the images relate to 54 % w/w sediment after 6 h *in situ* gas generation

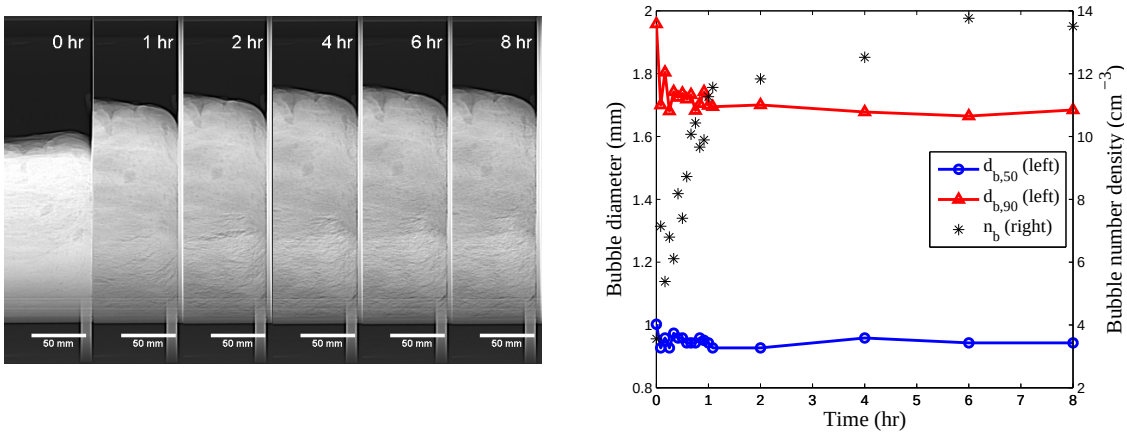

(a) (b)

Figure 4.9: The evolution of retained bubble populations within 1112 Pa yield stress soft sediment including (a) side-on x-ray *scout* images of half the bed showing bulk waste swell during 0-8 h gas generation and (b) the evolution of bubble size and number density with time within the small FOV

by Ostwald ripening, it is possible that the number density of small bubbles could diminish as the population of mature bubbles increases. Conversely, the largest, most mature bubbles exhibit either negligible growth within this time frame, or the gas release mechanism imposes a ceiling in the maximum bubble dimension that the bed is able to support. In either instance, the observable mature bubble population can be considered to reach an equilibrium size distribution and number density, representative of the bed at maximum voidage, after 6 h of hydrogen peroxide decomposition.

This observation of a steady state bubble population within the 1112 Pa yield stress sediment after 6 h of gas generation holds equally true for sediments of 7, 86 and 234 Pa yield stress. Tomographs within the large FOV of all these magnesium hydroxide soft sediments after 6 h gas generation are presented in Figure 4.10, while corresponding size and shape analysis of each of the bubble populations at 2 and 6 h are presented in Figure 4.11. The 7, 86 and 234 Pa tomographs in Figure 4.10 are all characterized by relatively small, regular shaped, dispersed bubbles, the largest of which range from 6.5-9 mm equivalent spherical diameter. Laplace pressures, which promote spherical curvature, scale with inverse bubble diameter, and so small bubbles are anticipated to be highly spherical in nature. The largely spherical nature of mature bubbles within these 7-234 Pa sediments is consistent with a fluid-like response of the sediment to the stress of the growing bubble. However, after excluding the smaller bubbles comprised of fewer than 80 voxels ($d_b \leq 3.56$ mm), Figure 4.9b shows a small but distinct decrease in sphericity with increased yield stress within this range. This is explained by the fact that sediments of increased strength or greater depth typically demonstrate greater anisotropy in

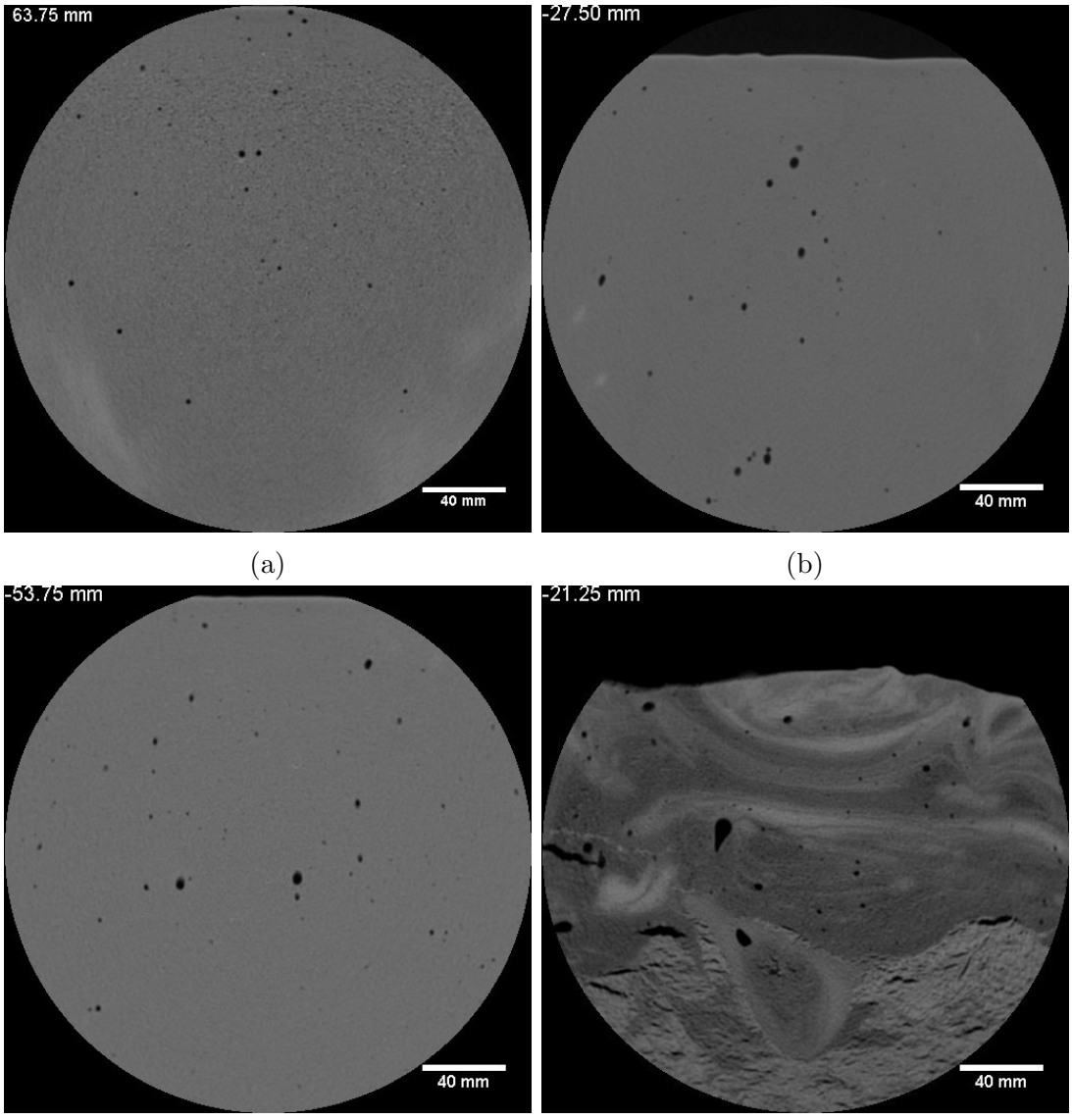

Figure 4.10: X-ray tomographs of bubbles within the large FOV of (a) 7 (b) 86 (c) 234 and (d) 1112 Pa yield stress magnesium hydroxide soft sediments after 6 h gas generation; the values in the top left corner of each image represent the axial distance from the centre of the test vessel

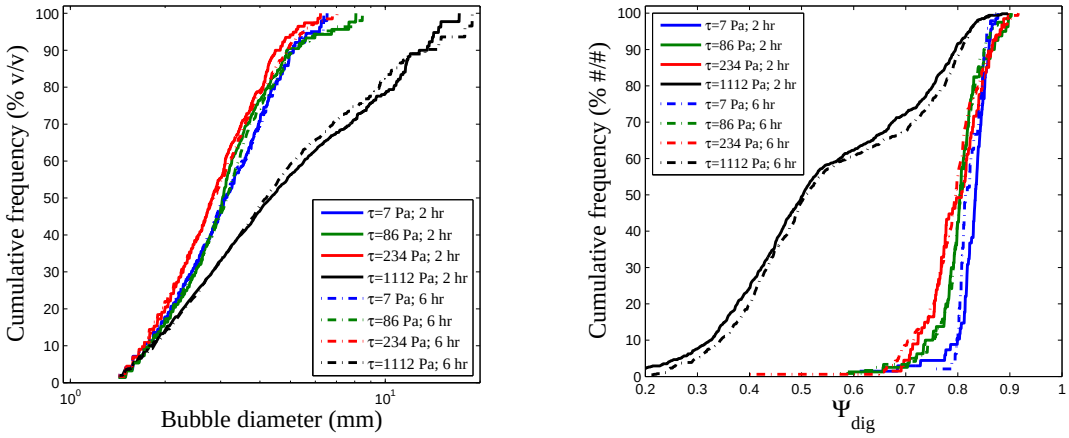

(a) (b)

Figure 4.11: Histograms of (a) bubble diameter (volume weighted, bubbles < 5 voxels excluded) and (b) bubble sphericity (count weighted, bubbles < 80 voxels excluded) within 7-1112 Pa soft sediments after 2 and 6 h gas generation

their stress tensors (Boudreau, 2012), often reported through reductions in Poisson's ratio (Terrones & Gauglitz, 2003; van Kessel & van Kesteren, 2002), thereby promoting less axisymmetric bubble growth. Similarly, Algar & Boudreau (2010) use LEFM modelling to predict an increase in bubble aspect ratios for growth within sediments of increased Young's modulus.

Figure 4.11a demonstrates no significant evolution in the observable bubble size distribution within any of the soft sediments between 2 and 6 h, consistent with the observations from Figure 4.9b. The similarity in bubble size distribution within 30-45 % w/w beds, despite a 33-fold increase in the shear yield stress of the surrounding sediment, seems to conflict with our current understanding of bubble retention in low and intermediate strength beds (Gauglitz *et al.*, 2015; van Kessel & van Kesteren, 2002). Bubble ebullition, possibly inducing bubble cascades, has been considered the main mechanism by which dispersed bubbles are released from these relatively low strength beds (van Kessel & van Kesteren, 2002). As discussed in Section 2.8.1, the ratio of a bubbles' buoyant stress to the sediment yield stress defines a characteristic bubble size for ebullient release (Atapattu *et al.*, 1995; Dubash & Frigaard, 2007; van Kessel & van Kesteren, 2002):

$$d_{b,crit} = Y \frac{\tau}{(\rho_s - \rho_g)g} \tag{4.11}$$

where Y is a material dependant dimensionless *yield parameter* reported in the range of 0.023-0.061 following experimental work in Atapattu *et al.* (1995) and closer to 0.143 according to finite element analysis in Beris *et al.* (1985). The relationship in eq. (4.11) implies that the size of bubble which a bed is able to support increases in proportion to the ratio of a bed's yield stress to its bulk density.

Increasing the solids concentration of the bed from 30 to 45 % w/w sees this ratio increase by a factor of 28, however, this does not manifest in any observable increase in the size distributions of the mature bubble populations within these 7-234 Pa yield stress sediments.

Two theories could explain why the population appears to achieve a steady state size distribution, long before gas production is exhausted, that is seemingly independent of sediment strength within the 7-234 Pa yield stress range. First, the high sphericity of bubbles within these sediments implies a fluid-like response to the stress of the growing bubble. As such, the rate of bubble growth may be limited by diffusion rather than by the elastic resistance of the sediment during bubble growth. Under these circumstances Boudreau *et al.* (2001) model the instantaneous bubble diameter using the expression in eq. (4.12):

$$d_b^2(t) = \frac{4\Phi D_{eff}}{\phi_g}\left(\frac{S(t){R_1}^2}{3D_{eff}} + \phi_1 - \frac{\phi_g}{K_h}\right)t + d_{b,0}^2 \tag{4.12}$$

where, in this instance, the rate of oxygen generation within the pore water, $S(t)$, or source term, is time dependent, as evidenced by the gas generation profiles in Figure 4.4a. The remaining terms include the sediment porosity, Φ, the effective diffusion coefficient for oxygen through the sediment, D_{eff}, which should account for the tortuosity of the diffusion path through the sediment pores, the oxygen concentrations within the bubble, c_g, and within the pore water, c_1, at a radius of R_1, the dimensionless Henry's law coefficient, K_h and the initial bubble diameter, $d_{b,0}$. Given the oxygen generation profiles in Figure 4.4a, it is clear that the source term exponentially diminishes with time, $S(t) = S_0\, exp(-kt)$, where S_0 is the initial source strength. This implies that the bubbles which are nucleated later in the experiment will grow to a smaller ultimate diameter, which could partially explain the plateau in bubble diameter. However, the impact of the exponentially diminishing oxygen source becomes clearer when differentiating eq. (4.12) to generate the expression for bubble growth rate in eq. (4.13):

$$\begin{aligned}\frac{d}{dt}d_b^2(t) &= \frac{4\Phi D_{eff}}{\phi_g}\left(\frac{{R_1}^2}{3D_{eff}}\left(S(t) + \frac{dS(t)}{dt}t\right) + \phi_1 - \frac{\phi_g}{K_h}\right) \\ &= \frac{4\Phi D_{eff}}{\phi_g}\left(\frac{{R_1}^2 S_0}{3D_{eff}}(1-kt)exp(-kt) + \phi_1 - \frac{\phi_g}{K_h}\right)\end{aligned} \tag{4.13}$$

This expression includes a source strength term, $\left(S(t) + \frac{dS(t)}{dt}t\right)$ and a concentration gradient term which drives diffusion towards the bubble, $\left(\phi_1 - \frac{c_g}{K_h}\right)$. The source strength term will rapidly diminish with time due to the exponential component, becoming negative at $t > k^{-1}$ and reaching a minimum at $t = 2k^{-1}$. Thus, for a kinetic constant of $0.4\,h^{-1}$, as observed during the CT experiments, eq. (4.13) predicts that mature bubbles could cease to grow at some time between 2.5 and 5 h,

depending on the magnitude of the concentration gradient within the pore water, despite continued oxygen production for 8 h of experimentation.

Under these circumstances the sediment's capacity to resist stress is entirely neglected, however Algar & Boudreau (2010) describe another mechanism whereby elastic materials, which can support stress, may achieve a *no growth* condition, as previously observed in Gardiner *et al.* (2003). Resistance to bubble growth due to the mechanical strength of the sediment enables the internal pressure of the bubble to rise above ambient pressure, in contrast to growth within conventional viscous fluids which cannot support stress (Algar & Boudreau, 2010). This causes the concentration of oxygen within the bubble to rise, thus causing the concentration gradient which drives diffusion towards the bubble to diminish. For very low source strength or weak supersaturation conditions, a relatively small increase in concentration within the bubble could eliminate the concentration gradient and starve the bubble of oxygen for continued growth. The initial source strength can be characterized from the initial bulk concentration of hydrogen peroxide in the pore water, $\phi_{H_2O_2}$, the stoichiometric ratio of oxygen, $v_{O_2} = 0.5$, and the kinetic constant as follows:

$$\int_0^\infty S_0 exp(-kt) = \frac{S_0}{k} = v_{O_2}\phi_{H_2O_2} \tag{4.14}$$

Using the example of the 86 Pa sediment in Figure 4.10b, which had an initial hydrogen peroxide concentration of 5.9×10^{-2} M and an observed kinetic constant in the order of $0.4\,h^{-1}$, the initial source strength would be $3.29 \times 10^{-6}\,M\,s^{-1}$. Hence, the initial source strength is relatively strong (Algar & Boudreau, 2010), although it will diminish by an order of magnitude every 6 h. The *no growth* condition is more likely attained due to the weak supersaturation of oxygen within the porewater. Every mole of oxygen generated by reaction would saturate the pore water in the bed at a maximum concentration, $\phi_{O_2}(aq)$, of 2.99×10^{-2} M. This concentration is less than a quarter of the critical concentration for homogeneous oxygen nucleation in pure water, ϕ_{nuc}, which is reported at 0.12 M (Bowers *et al.*, 1995), implying that free gas bubbles form by heterogeneous nucleation at a relatively weak supersaturation. Consequently, the rapidly diminishing oxygen source strength which limits diffusion controlled growth and the mild increase in internal bubble pressure required to extinguish the oxygen concentration gradient under these apparently weak supersaturation conditions are both likely to contribute to the cessation of mature bubble growth long before oxygen production is fully exhausted.

The similar bubble size distributions within 7-234 Pa sediment in Figure 4.11a contrast with the 1112 Pa yield stress bed, which retains much larger bubbles of up to 20 mm equivalent spherical diameter. The largest voids exhibit two distinct geometries in Figure 4.10d; some distorted ellipse and inverted teardrop geometries

coexist alongside lateral cracks which are more prevalent within deeper regions of the bed and within brighter regions of sediment (indicative of an elevated solids concentration). This heterogeneity in grey-scale within the bulk sediment, away from the bubbles, in Figure 4.10d demonstrates the difficulties experienced when homogenizing magnesium hydroxide soft sediments with solids concentrations in excess of 50 % w/w. The two distinct void geometries are captured by the bimodal sphericity histogram for bubbles within the 1112 Pa sediment in Figure 4.11b, and are consistent with the cavity expansion and tensile fracture mechanisms for bubble growth. The lowest digital sphericities in Figure 4.11b correspond to fracture sites with the largest aspect ratios. These cracks propagate laterally as the compressive bed stress is lowest normal to the direction of the lithostatic load. Many of the fracture sites imaged within the large FOV of the 1112 Pa material extended to the walls of the test vessel, and so gas diffusion towards these cracks presents a route for continuous gas release from the sediment. The inverted teardrop shapes are consistent with bubbles observed by Katsman (2015), Algar *et al.* (2011a), Takada (1990) and Weertman (1971), who investigated bubbles in a range of viscoelastic materials including marine sediment, gelatin and magma, and are explained by the surrounding pressure field in the soft sediment increasing linearly with depth. As the bubble grows, the pressure difference across the height of the bubble increases, the pressure at the bubble *tail* diminishes and the teardrop geometry emerges as the tail pressure falls to near zero (Algar *et al.*, 2011a). The increase in pressure field with depth also promotes faster growth at the shallow surface of the bubble (Algar *et al.*, 2011a).

Bubble mobility, residence times and release

Figure 4.4b revealed that gas is continuously released from a 27 Pa sediment at a near constant rate of around 21 ml h^{-1}. The slowest gas release was observed when hydrogen peroxide was introduced to sediments of 4-234 Pa at the sample homogenization stage, corresponding to rates of around 17 ml h^{-1}. This continuous gas release must be reconciled with the observations that the size distribution of the mature bubble population remains constant, and independent of yield stress in the 7-234 Pa range, and that there are no major disturbances in the topography or profile of the bed from either the tomographic images of the bed, as shown in Figure 4.9a, or from continuous digital photography of the sediment. Transient x-ray CT was employed to investigate whether the mobility of bubbles within the sediment correlate to the observed rates of gas release.

Figure 4.12 presents tomography of the 7 and 1112 Pa beds across multiple time frames using hyperstacking. Figure 4.12a shows bubbles at 15 min intervals within a 7 Pa $Mg(OH)_2$ soft sediment. A number of small bubbles visible at 0 or 15 min

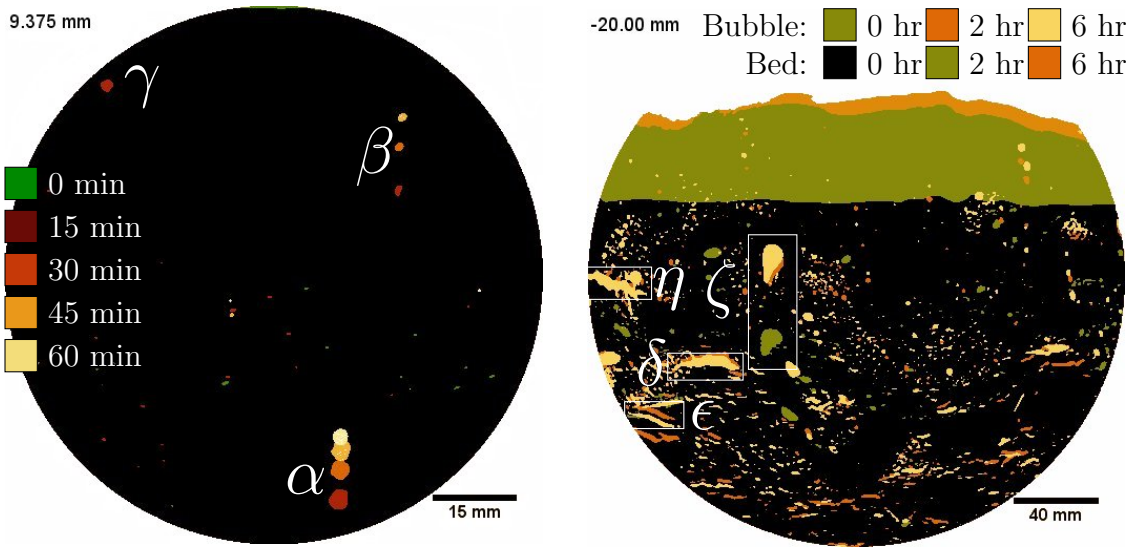

(a) (b)

Figure 4.12: *Hyperstacked* x-ray tomographs of bubbles in 7 and 1112 Pa soft sediments using a colour legend to represent bubbles across multiple time-frames, showing (a) bubbles at 15 minute intervals within the small FOV of a 7 Pa soft sediment and (b) bubbles at 0, 2 and 6 h within the large FOV of a 1112 Pa soft sediment (as the sediment expands due to its increasing voidage the bulk sediment changes from black to green to orange as shown in the legend)

appear only once within this slice through the sediment, indicating residence times within this 96 mm diameter FOV of less than 15 min. Some of these small bubbles could shrink and disappear due to Ostwalt ripening enabling neighbouring bubbles in adjacent tomographs to grow; else, some of these bubbles could grow very quickly to buoyant dimensions ($d_b > d_{b,crit}$) and escape the low strength sediment matrix by fluidisation. In support of the second theory, the bubble labelled 'γ' is only captured within the 30 min scan, suggesting that this bubble grew from sub-pixel dimensions ($d_b \leq 250\,\mu m$) to 2.2 mm diameter in less than 15 min, demonstrating that rapid bubble growth is realistic. The two other labelled bubbles, 'α' and 'β', exhibit longer residence times in the order of 30-45 min and grow at much slower rates of less than $5 \times 10^{-3}\,mm\,min^{-1}$. While bubble α appears to shrink in Figure 4.12a, it is in fact slowly growing while its centre of mass is moving deeper into the FOV; consequently, this two dimensional tomograph captures a smaller slice through a larger total bubble volume, thus highlighting the importance of using three dimensional analysis to characterize the bubble population. In general, the smaller bubbles are observed to grow most quickly, consistent with the square root time dependency of diffusion controlled bubble growth in eq. (4.12)(Boudreau *et al.*, 2001). However, there is substantial variation in the growth rate of similar sized bubbles at different locations in the sediment. A more thorough investigation of bubble growth kinetics would require a modified CT configuration which enables shorter time intervals between scans.

The slow and decelerating rise of the bubbles labelled 'α' and 'β' is considered to be a result of their movement in conjunction with the bulk sediment due to bed expansion, rather than their rise through the sediment by fluidisation, as the rise rates correlate closely with bed expansion rates. The stability of bubble α within the sediment over the initial 45 min period implies a critical bubble diameter greater than 3.6 mm, corresponding to the d_{60} bubble diameter in Figure 4.12a. Conversely, the absence of bubble β from the 60 min tomograph suggests that this 1.6 mm bubble is able to fluidize the bed between the 45 and 60 min frames, thus implying a smaller critical rise diameter.

Atapattu *et al.* (1995) have demonstrated a significant history dependence of creeping sphere motion within non-Newtonian Herschel-Bulkley fluids, where spheres were shown to exhibit elevated terminal velocities after a series of repeat experiments, suggesting that the disturbed fluid behaves with a lower observed viscosity than the undisturbed fluid. Dubash & Frigaard (2007) observed shear history dependence lasting up to 72 h within low strength Carbopol solutions. This hysteresis effect, combined with some spatial heterogeneity in the sediment mechanics, implies that the critical rise diameter exhibits both time and position dependence. The same observation also means that the viscous resistance to bubble growth is spatially and temporally dependent and so growth rates for bubbles of equivalent size may vary greatly even if the material is uniformly supersaturated with volatiles. However, despite the considerable spatial variation in bubble growth rate and likely spatial variation in local yield stress, the fact that the largest bubbles within the small FOV of the 7 Pa sediment, with the largest buoyant force, exhibit the longest residence times in the bed implies that bubble ebullition, as represented by eq. (4.11) (Atapattu *et al.*, 1995; Dubash & Frigaard, 2004), is not the dominant mechanism of gas release, even from this very low strength sediment.

Further evidence that bubble ebullition is unlikely to explain the rates of gas release observed in Figure 4.4b lies in the fact that the mature, observable bubble population represents a small percentage of the total voidage. The average voidage of the bed can be estimated from the bed swell observed in profile *scout* tomographs of the whole bed, as presented in Figure 4.9a, and hence the total volume of free gas within the large FOV tomographs can be attained. Table 4.3 compares the total volume of free gas within the large FOV, V_R, with the total volume of the *observable* bubble population, $V_{R,tom}$, obtained using three dimensional image analysis of tomographs such as those presented in Figure 4.10. The volume of the observable population captures the bubbles greater than 0.83 mm equivalent spherical diameter but excludes any bubbles or fractures extending to the edge of the FOV. The volume fraction of bubbles observable at the tomography resolution, $\nu_{tom} = \frac{V_{R,tom}}{V_R}$, varies between 0.03-1.08 % for 7-234 Pa yield stress sediments, rising to 7.5 % for the highest strength bed (1112 Pa).

Table 4.3: Contribution of the observable ($d_b > 0.83\,\text{mm}$) and sub-resolution bubble populations to the total voidage

τ (Pa)	ν	V_R (ml)	$V_{R,tom}$ (ml)	$100 \times \nu_{tom}$ (%)
7	0.32	2188	0.616	0.03
86	0.29	1829	16.9	0.92
234	0.34	2325	25.1	1.08
1112	0.24	1467	110	7.50

This very small contribution of millimetre scale bubbles to the total voidage, especially within the low strength sediments, suggests that the dominant gas release mechanism is unlikely to be buoyancy driven. Other possibilities for gas release include gas diffusion through sub-resolution channels or *dendritic* bubble networks, or direct mass transfer of dissolved oxygen through the surface of the bed to the ullage. Katsman *et al.* (2013) contends that free gas release dominates that of dissolved volatiles in marine environments by a factor of almost fifty. To test this assertion, the rate at which aqueous oxygen is transferred through the liquid and gas films at the bed boundary, $\dot{V}_{E,aq}$, can be estimated for these laboratory scale experiments using two-film theory (Ibusuki & Aneja, 1984), by assuming both phases are well mixed, combined with the ideal gas law:

$$\dot{V}_{E,aq} = \frac{RT}{P} J A = \frac{RT}{P} K A \frac{\left(c_{O_2}(aq) - \frac{p_{O_2}}{H^{pc}}\right)}{H^{cc}} \tag{4.15}$$

where J is molar flux of oxygen through the surface of the bed, A is the surface area of the bed, K is the overall mass transfer coefficient, and H^{pc} and H^{cc} are dimensional and dimensionless forms of the Henry's law constant for oxygen in water respectively. The liquid side mass transfer resistance is reported to be negligible for the exchange of pollutants between air and water and so the overall coefficient approximates that through the gas film, $K \approx k_g$ (Ibusuki & Aneja, 1984). The gas side mass transfer coefficient can be estimated from the Froessling equation (Froessling, 1938), which states that the Sherwood number, $Sh = \frac{lD}{k_g}$, tends to 2 for a stagnant ullage where $Re \to 0$.

Considering the gas retention test in Figure 4.4b, the diffusion coefficient of $1.76 \times 10^{-5}\,\text{m}^2\,\text{s}^{-1}$ for oxygen in air and the characteristic length scale, l, equal to the 0.118 m test vessel diameter, provides a mass transfer coefficient of $2.98 \times 10^{-4}\,\text{m}\,\text{s}^{-1}$. Thus, assuming the pore water was saturated at the maximum possible oxygen concentration of $2.99 \times 10^{-2}\,\text{M}$, oxygen transport to the ullage would be limited to $0.27\,\text{ml}\,\text{h}^{-1}$, representing only 1.3 % of the observed rate of gas release. Consequently, it appears that gas release from these low strength soft sediments, in the absence of a supernatant, is governed overwhelmingly by transport of free gas at a sub-resolution length-scale, possibly along networks of sub-resolution bubbles. For a smaller imaging field of view, clinical x-ray CT is available at greater resolution, of

around 50 µm (Constantinescu & Mukherjee, 2009; Disselhorst *et al.*, 2010), while synchroton x-rays can achieve tomographic resolutions of 1-3 µm (Berg *et al.*, 2013; Mi *et al.*, 2014) for experimentation at a significantly reduced scale. The following chapter aims to investigate the smaller bubble population and possible avenues for gas transport using smaller scale clinical CT of enhanced resolution.

The growth and motion of retained bubbles is more apparent in Figure 4.12b, as bubbles reside over much longer periods within the high strength 1112 Pa sediment. Large FOV tomographs at 0, 2 and 6 h demonstrate both the bulk expansion of the bed (from black to green to orange) within the sideways mounted cylinder and the growth and movement of bubbles during this period. The inverted teardrop bubble, 'ζ', of 8.9 mm equivalent spherical diameter, is visible within all three time frames, moving in tandem with the local sediment due to bulk bed expansion. During the 6 h of gas generation, the maximum dimension of ζ increases from 12 to 19 mm and the bubble tail narrows to a thin point, similar to phenomena described in Algar *et al.* (2011a). The stability of the largest bubbles of 8-20 mm equivalent spherical diameter on a timescale of hours confirms that ebullition does not play a significant role in gas release from quiescent soft sediments in excess of 1 kPa yield stress. Nonetheless, the rate of gas release from this bed exceeds that from each of the lower strength sediments investigated. Gas transport from the bed is better explained by diffusion along cracks such as those labelled 'δ', 'ϵ' and 'η', especially in the instance of bubble η, as this fracture visibly extends to the periphery of the bed. These lateral cracks are more prevalent within the 2 and 6 h tomographs than at 0 h, indicating that only fairly mature bubbles acquire the excess bubble pressures necessary for tensile fracture. This also accords with LEFM theory which states that a critical crack length, a_c, is required for a crack to propagate (Johnson *et al.*, 2002). Cracks δ and ϵ fall in their positions within the FOV between 2 and 6 h, and hence these local regions of the bed undergo compression while other regions continue to expand. The high radiodensity, high strength and deeper regions, often associated with reduced Poisson ratios (Terrones & Gauglitz, 2003; van Kessel & van Kesteren, 2002), in Figure 4.10d and Figure 4.12b, appear to be more prone to consolidation and exhibit more growth by tensile fracture than viscoelastic cavity expansion.

Gas release during heterogeneous gas generation

All x-ray CT presented and analysed in Figures 8-11 employed *in situ* gas generation by injecting hydrogen peroxide at the sample homogenization stage to achieve a relatively uniform distribution of the gas generating reagent. Figure 4.5 however revealed a significant reduction in the bulk bed expansion using an alternative methodology (where the peroxide was injected into the feed line at a constant rate)

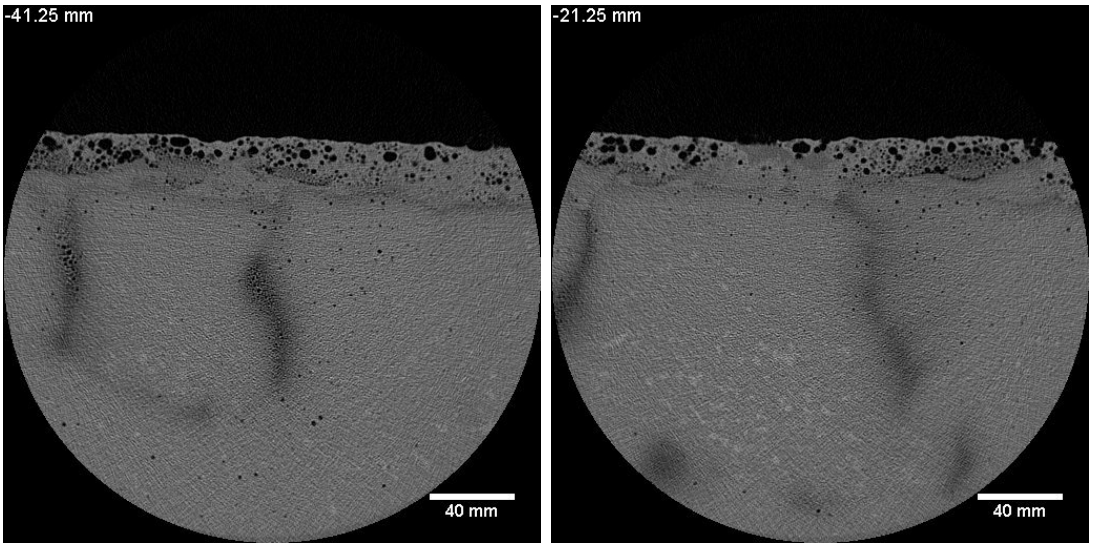

Figure 4.13: X-ray tomographs at two depths within the large FOV of 7 Pa sediment after 6 h gas generation following hydrogen peroxide addition at injection point 2 (see Figure 4.6a)

which manifested in an assumed more heterogeneous distribution of hydrogen peroxide through the bed, evidenced from the lower and more varied total gas holdup. The reason for this disparity is investigated in Figure 4.13, using x-ray CT of a 7 Pa sediment 6 h after hydrogen peroxide introduction at stage 2 in Figure 4.2. The different approach to gas generation is marked by two features within the bed, which are distinct from the otherwise identical bed of equivalent yield stress imaged in Figure 4.10a. First, the bed segregates into a bulk sediment and a foam layer which covers the top 20-30 mm of the bed. The foam layer supports a much greater void fraction than the bulk sediment and includes much larger, less spherical bubbles, often separated by very thin particle films. The formation of this foam layer implies that a portion of solids in the bed have a three phase contact angle greater than zero, consistent with observations from the Langmuir-Blodgett experiments in Section 3.3.3 where a majority of $Mg(OH)_2$ particles were supported at the air-water interface. The foam layer also implies that chronic gas generation and bubble growth is more conducive to the development of a stable foam than the dynamic foamability tests outlined in Figure 3.2 (Fryer *et al.*, 2011). The foam layer supports much too great a gas fraction to remain stable in the presence of an aqueous supernatant and would certainly give rise to a floating foam layer as observed in Figure 4.6 and in certain underground waste tanks at Hanford (Bryan *et al.*, 1992; Kam & Rossen, 1999).

Second, a series of dark streaks propagating through the bulk sediment below the foam layer in Figure 4.13 reveal low radiodensity regions, rich with microbubbles close to the pixel resolution. The poor distribution of hydrogen peroxide through the bed is believed to result in regions of above average oxygen supersaturation and a greater bubble nucleation rate. Enhanced gas transport through these low density,

low strength regions to the walls of the test cylinder and the foam layer could explain the augmented rate of gas release from the bed in Figure 4.13, resulting in the lower maximum voidage of just 6.8 % in comparison to that of 31.8 % observed in Figure 4.10a. Hence, these gas transport pathways could represent an alternative mechanism for gas release from heterogeneous soft sediments, distinct from the stable open channels discussed in van Kessel & van Kesteren (2002), which are visible at the bed surface and are characteristic of beds with much greater yield stress.

Rassat *et al.* (1998) describes a similar mechanism for gas release from low-intermediate strength sediments whereby 'connected paths of distorted round bubbles provide a nearly continuous path for gas release to the surface' following observations within a bentonite clay sediment of 67 Pa yield stress. The two tomographs at different axial depths demonstrate these submerged pathways propagating at multiple locations and along multiple directions through the bed. Significantly, these gas transport pathways provide a localised route for gas release which does not limit bed expansion in other regions of the bed, whereas bubble ebullition represents a global mechanism which can facilitate gas release from any part of the bed. Enhanced gas transport along these pathways to the weakly consolidated top region of the bed could facilitate formation of the stable foam layer, which is not observed within the equivalent 7 Pa sediment in Figure 4.10a. It is noted that any such gas transport pathways which are promoted by non-uniform gas generation may indeed be relatively common in corroding nuclear wastes. Flammable gas generation would be thought of as inherently inhomogeneous in these systems, as it would be focused in localized areas with exposed corroding metallic fuel debris.

4.4 Conclusions

A series of laboratory scale gas retention tests revealed that $Mg(OH)_2$ soft sediments of up to 800 Pa yield stress exhibited gas holdup on a scale that would achieve neutral buoyancy with an aqueous supernatant, raising the possibility for Rayleigh-Taylor instabilities. Sediments of 30-234 Pa yield stress each experienced episodic release events by partial rollover (Allemann, 1992) which would likely facilitate acute gas release in the presence of a 1 m deep supernatant. Reduced gas holdup was observed when gas generating reagents were less homogeneously mixed through the sediment. Under these conditions x-ray CT revealed low radiodensity pathways to the surface thought to result from the nonhomogeneous distribution of volatiles producing localized pockets of gas generation, thereby establishing low density regions rich with microbubbles which present preferential pathways for gas transport. The observation that non-uniform gas generation can enhance chronic

gas release from regions of the bed and reduce the possibility for acute release is reassuring as gas generation within the MSSS is considered inherently inhomogeneous, focused in the localized areas with exposed corroding metallic fuel debris.

Tomography further revealed that the size distribution of mature bubbles remains constant after less than an hour of gas generation, long before the cessation of bed expansion and the exhaustion of gas production. The lack of mature bubble coarsening could be explained by the exponentially diminishing oxygen source strength combined with a diminishing oxygen concentration gradient driven by the increase in internal bubble pressure due to the sediments elastic resistance to bubble growth (Algar & Boudreau, 2010). Sediments of 7-234 Pa yield stress retained steady state bubble populations of high sphericity, consistent with growth by cavity expansion (Terrones & Gauglitz, 2003), and very similar size distributions limited to 6.5-9 mm equivalent spherical diameter. The similarity in size distribution despite a 28-fold increase in the ratio of yield stress to bulk density suggests that the size distribution is not governed by the critical dimensions for bubble ebullition. This is reinforced by the observation that the largest bubbles, with greatest buoyant force, correspond to a small fraction of the total voidage and remain static over long residence times of several hours. However, this raises the question of what mechanism enables the observed chronic gas release from low-intermediate strength quiescent sediments which neither exhibit the macroscopic gas transport pathways associated with more localised gas generation, nor sufficient bubble mobility for global ebullient release.

The most consolidated sediment of 1112 Pa yield stress demonstrated a bimodal sphericity distribution, with the modes corresponding to broadly spherical and inverted teardrop (Algar *et al.*, 2011a) bubble geometries indicative of viscoelastic sediment deformation, and cracks of low sphericity consistent with growth by tensile fracture (Johnson *et al.*, 2002; Katsman, 2015). The fracture sites were more common in deeper and higher density regions and were typically oriented laterally, favouring fracture propagation normal to the compressive load and parallel to the minimum compressive stress. Some fracture sites extended to the container wall and thus present a release route for volatile solutes which diffuse to the fracture. The high strength sediment supported the largest bubbles of up to 20 mm equivalent spherical diameter, which moved in conjunction with the bulk bed expansion but remained macroscopically static for at least 6 h.

Despite shedding light on realistic levels of gas holdup, the upper bound of retained bubble sizes, mature bubble mobility, bubble geometries observed across a range of yield stress conditions, and conditions most conducive to acute release, significant uncertainties remain concerning the $> 92.5\,\%$ of retained bubbles too small for this CT configuration to capture and the implications of this sub-millimetre population for gas release from low-intermediate strength quiescent sediments. How-

ever, having established that the bubble population exhibits negligible evolution after 4-6 h of hydrogen peroxide decomposition, a modified CT configuration, using a smaller sample size and field of view together with longer scan times, can be used to achieve greater imaging resolution and expose this hidden void fraction.

Chapter 5

Enhanced gas migration through permeable bubble networks within consolidated soft sediments

5.1 Introduction

In Chapter 4, large scale clinical CT imaging was employed to demonstrate that large bubbles remain macroscopically static within sediments of 7-1112 Pa yield stress for long residence times. The observation that very low strength (τ = 7 Pa) sediments supported relatively large (< 7 mm ESD) bubbles for at least 6 h, during a period of appreciable chronic gas release, is seemingly at odds with the theory that buoyant bubble ebullition represents the principal mechanism for gas release at low yield stresses, where the ratio of buoyant stress to sediment strength is most favourable to bubble rise (Dubash & Frigaard, 2007; van Kessel & van Kesteren, 2002). Sherwood & Eduardo Sáez (2014) suggested that bubble ebullition, possibly liberating a buoyant flux, or cascade, of bubbles is most likely in the $3 < \tau < 70$ Pa yield stress range. The transient CT imaging in Figure 4.12a indicates that the ebullient yield stress regime may be narrower still, possibly limited to sediments of < 7 Pa yield stress under quiescent conditions (Keller & Stallard, 1994).

This raises the question as to how gas is continuously released from low-intermediate strength sediments (10 Pa $\lesssim \tau \gtrsim$ 1 kPa) which are (1) too strong for buoyant bubble ebullition, (2) too high in fracture toughness for *burrowing* (Dorgan *et al.*, 2005; Mughrabi, 1992), and (3) insufficiently strong to support deep vertical drainage channels (van Kessel & van Kesteren, 2002). Furthermore, any such mechanism must be reconciled with the absence of either vertical motion of large millimetre-scale bubbles or disturbances in topography or profile of the bed, which would

have been apparent in Figure 4.9a. Since > 92.5 % of bubbles were below the detection limit of the large scale clinical tomography in Section 4.3.2, it was postulated that permeable networks of partially coalesced sub-millimetre bubbles or diffusion pathways through fine fractures (van Kessel & van Kesteren, 2002) might present a realistic explanation for gas migration and chronic release. Similarly, Wheeler (1988a) highlighted the possibility that retained free gas within unsaturated soils may be continuous at large void fractions where the *saturation*, given by the ratio of the pore water volume to the combined volumes of pore water and retained gas, falls below a value of around 0.85. However, x-ray CT has yet to be employed to observe viable pathways for gas migration through these intermediate strength sediments.

In this chapter, gas retention is investigated by the homogeneous *in situ* decomposition of hydrogen peroxide within consolidated $Mg(OH)_2$ soft sediments of 30-1112 Pa yield stress, using a Siemens Inveon PET/CT scanner (Constantinescu & Mukherjee, 2009) to image the bubble population at 53.25 µm resolution. Previous research into sedimentary bubbles achieving such tomographic imaging resolution has focused on individual fracture sites propagated from a solitary submerged orifice(Algar *et al.*, 2011a; Best *et al.*, 2006; Johnson *et al.*, 2002), while larger scale CT imaging of diverse bubble populations (see Figures 2.6c, 2.6d and 4.10) has been limited by spatial resolution (Maurer *et al.*, 2016), thus rendering communication between multiple bubble sites and avenues for gas migration invisible. The sediment response to *in situ* bubble growth is interpreted in relation to the two-phase sediment microstructure, which is characterised using low field nuclear magnetic resonance (LFNMR) spectroscopy (D'Orazio *et al.*, 1989; Yao *et al.*, 2010) and cryogenic focused ion beam (cryo-FIB) microscopy. X-ray computed tomography (CT) is coupled to Lattice Boltzmann Method (LBM) and Monte Carlo based simulations, which are proposed for the investigation of gas migration through permeable, connected pathways through the sediment. These computational approaches are highly suitable for characterising flow behaviour through real porous media as they are computationally inexpensive compared with conventional continuum-based computational fluid dynamics (CFD) methods for complex boundary geometries, while the CT reconstructions provide a compatible cubic *lattice* on which to perform the calculations (Selomulya *et al.*, 2006).

5.2 Materials and methods

The same dry commercial $Mg(OH)_2$ powder, Versamag (Martin Marietta Magnesia Specialties LLC, USA), used throughout Chapter 4 was used once again as a non-active analogue for the solid component of CMS. Consolidated soft sediments were

prepared by the addition of tap water and agitation for 30 min using an overhead stirrer with an axial flow impeller. 35, 45 and 54 % w/w sediments were prepared for x-ray tomography imaging, corresponding to diverse shear yield stress conditions of 30, 234 and 1112 Pa respectively, according to the relationship in eq. (3.5).

5.2.1 Soft sediment microstructure characterisation

The soft sediment microstructure was investigated using a combination of low field nuclear magnetic resonance (LFNMR) spectroscopy, mercury intrusion porosimetry (MIP) and cryogenic focused ion beam (cryo-FIB) imaging. LFNMR has proven to be a powerful and non-destructive tool for characterising various porous media, including tight gas sandstones (Xiao *et al.*, 2016) different grades of coal (Yao *et al.*, 2010) and saturated soils (Liu *et al.*, 2016). Following application of a very low external magnetic field, transverse relaxation time (T_2) measurements capture the rate at which protons in the pore filling fluid, water in this instance, lose their magnetic *spin* as a result of collision with the pore walls. Hence, LFNMR can non-destructively probe the pore surface area to volume ratios, S/V, a measure of inverse pore body radius, r_{pb}^{-1}, within water saturated porous materials, such as sludges, slurries and soft sediments. From the resulting transverse relaxation time distribution, slower proton relaxation times correspond to fewer pore wall interactions, consistent with larger pore bodies according to eq. (5.1) (D'Orazio *et al.*, 1989; Yao *et al.*, 2010):

$$\frac{1}{T_2} = \rho_2 \frac{S}{V} \tag{5.1}$$

Translating the relaxation time distribution into a pore size distribution therefore requires the determination of a material dependent proportionality constant, ρ_2, representing the surface relaxivity or transverse relaxation strength (Jaeger *et al.*, 2009). In order to calibrate the transverse relaxation strength a 20 ml sample of soft sediment was dried for 24 h at 100 °C to form a 30 mm diameter disk which was cut into two halves. One half was then re-saturated with water for 24 h before LFNMR analysis, while the other half was analysed using MIP.

MIP uses an applied external pressure to force a non-wetting fluid, mercury, to intrude into a porous sample. The Washburn equation, eq. (5.2), states that the applied pressure, P, required for the non-wetting fluid to invade a pore, with an assumed cylindrical geometry, is inversely proportional to the pore throat radius, r_{th}:

$$r_{th} = \frac{2\gamma cos(\theta)}{P} \approx \frac{0.62}{P} \tag{5.2}$$

For any material which is poorly wetted by mercury the numerator of eq. (5.2) will be equivalent. A mercury vapour-air surface tension, σ, of 485 mN m^{-1} and a high three phase contact angle of 130° are typically used for such advancing or intruding experiments (Anovitz & Cole, 2015). The percentage intrusion into the dried sample during an incremental sweep of applied external pressures can thereby be translated into a distribution of pore throat radii for comparison with the LFNMR distribution for the dried and re-saturated sample. Comparison of the distinctive LFNMR and MIP modes (Yao & Liu, 2012) enables conversion of transverse relaxation times to a more relevant pore length-scale. The ratio of MIP determined modal pore throat radius to LFNMR determined modal relaxation time provides the product of the transverse relaxation strength and the pore throat to body ratio, henceforth referred to as a corrected transverse relaxation strength, $\rho_{2,cor}$, according to eq. (5.3):

$$\frac{2\gamma cos(\theta)}{\bar{P}\bar{T}_2} = \rho_2 \bar{r}_{th}\left(\frac{\bar{S}}{V}\right) = \rho_2 \frac{\bar{r}_{th}}{\bar{r}_{pb}} = \rho_{2,cor}$$
$$r_{th} = \rho_{2,cor} T_2 \tag{5.3}$$

The corrected transverse relaxation strength will be constant only if the pore bodies and throats scale with a fixed ratio, however discrete element method analysis of compacted sands and soils indicates that this assumption is reasonable (Mahmoodlu *et al.*, 2016). Following eq. (5.3) the corrected transverse relaxation strength translates the relaxation time distribution into a more useful pore throat size distribution. Following determination of the corrected transverse relaxation strength using the dried samples, LFNMR analysis was performed using 50 ml samples of 35-54 % w/w magnesium hydroxide soft sediments.

The MIP tests were conducted using a 413 MPa Autopore IV porosimeter (Xiao *et al.*, 2016) (Micromeritics, USA) by increasing the applied pressure from 10 kPa to the 413 MPa ceiling in 42 logarithmic stages and recording the mass of mercury intrusion in milligrams at each interval. LFNMR was undertaken using a MARAN Ultra benchtop NMR analyser (Seland *et al.*, 2007) (Oxford Instruments, UK) operated with 100 scans per sample, to ensure an adequate signal to noise ratio, a magnetic field strength of 0.047 T and 2 MHz resonance frequency. Further measurement specifications include an echo spacing of 100 µs, echo numbers of 4096 and an equilibrium time of 10 s between scans. The resulting echo data were inverted to relaxation times in the 0.1-10 000 ms range with 100 logarithmically spaced intervals.

To supplement the LFNMR and MIP data with an appreciation of the pore geometry, a 40 % w/w $Mg(OH)_2$ soft sediment sample was observed using cryo-FIB imaging. The sample was rapidly frozen by quenching with slush nitrogen before the temperature was increased to and maintained at −90 °C for 8 min in order to

sublime away the majority of the pore-water. The frozen and sublimed sample was then fractured and sputter coated with platinum for the topography to be imaged using a Helios G4 CX DualBeam microscope (FEI, USA) (Matsumoto *et al.*, 2016; Villinger *et al.*, 2015). Images were acquired of the topography of the fractured surface and the interior wall of a borehole etched from the sample by the FIB, or *FIB cross-section*.

5.2.2 Imaging *in situ* bubbles within soft sediments with high resolution x-ray computed tomography (CT)

Gas retention tests were conducted in accordance with the hydrogen peroxide decomposition method outlined in Section 4.2.2 (see Figure 4.2), within a smaller sideways mounted cylinder of 71 mm diameter and 138 mm length. *In situ* gas generation was achieved by the addition of 1.6 ml 35 % w/w hydrogen peroxide (Merck Chemicals, Germany) to a 360 ml volume of soft sediment and agitation for 10 min with an overhead stirrer before transfer to the test cylinder. Following 6 h of gas generation, producing 220 ml O_2 by eq. (5.4), the bed was deemed to have reached a steady state voidage, or maximum gas holdup, and bubble size distribution.

$$H_2O_2 \longrightarrow H_2O + \frac{1}{2}O_2 \tag{5.4}$$

CT scans were undertaken for three commercial magnesium hydroxide soft sediments of 35, 45 and 54 % w/w using an Inveon dual PET/CT scanner (Siemens, Germany) configured with the scanning parameters outlined in Table 5.1. The 53.25 µm voxel resolution captured 4.7-9.1 times more detail in the cross-sectional plane and 11.7-23.5 times more detail in the axial direction than the large clinical CT tests conducted in Section 4.3.2.

Table 5.1: Summary of x-ray CT scanning parameters and comparison with the scanning protocol used in Chapter 4

	Siemens Inveon PET/CT	GE Brivo CT385
X-ray voltage (kVp)	80	120
X-ray tube current (mA)	0.5	40-79
FOV diameter (mm)	81.8	96-250
Pixel resolution (µm)	53.25	250-488
Slice separation (µm)	53.25	625-1250
Number of axial slices	1024	32-112
Total FOV volume	2.86×10^5	1.40×10^5-6.81×10^6

X-ray CT post processing

The reconstructed x-ray tomographs were post processed using FIJI ImageJ (Schindelin *et al.*, 2012) in combination with DigiUtility (Structure Vision Ltd. UK) (Menon *et al.*, 2011). A $600 \times 600 \times 600$ voxel cube was extracted from the centre of the image stack, away from the test-cylinder walls, and then various techniques including bandpass filtering, sharpening and despeckling were used to surpress ring-artefacts (Bentz *et al.*, 2000) and reduce *speckling* noise caused by beam hardening (Boden *et al.*, 2008). Bilevel thresholding was then used to isolate the retained bubble population from the high radiodensity bulk sediment. From the thresholded image stack, each object with face, edge and corner connected voxels was extracted, labelled and its volume recorded using the algorithm outlined in Bolte & Cordelières (2006). These objects include any discrete bubbles retained by the sediment as well as any chains or networks of partially coalesced bubbles which might propagate through the volume.

Characterising partially coalesced or networked bubbles

Where high rates of *partial bubble coalescence* or networks of bubbles are observed, an additional approach is required to characterise the individual bubbles within the network. Automated watershed segmentation is often used for isolating touching objects within digital images; however, this approach is best applied for overlapping objects of narrow size and shape distributions which are atypical based on the images presented in Figure 4.10 and discussed in Algar & Boudreau (2010); Katsman (2015). Instead a *mean empty space* (MES) algorithm was used whereby 10^8 random points were selected within the thresholded void-space and the lengths of three perpendicular chords (in the x, y and z directions) through each of these loci to the nearest sediment boundaries were recorded, providing a comprehensive chord length distribution (CLD) of the individual bubble population within the domain. The discretised CLDs were then translated into bubble size distributions (BSD) by solving the chord length transformation matrix from Li & Wilkinson (2005) using the non-negative least squares (NNLS) algorithm from Lawson & Hanson (1974) in Matlab v. R2013b (Mathworks, USA).

5.2.3 Simulating gas transport through permeable bubble networks

Two alternative three-dimensional computational approaches were employed to characterise gas transport behaviour through soft sediments using the bi-level thresholded CT reconstructions; these are the Lattice Boltzmann Method (LBM) and Monte Carlo gas diffusion (MCGD) models outlined below. For analysing

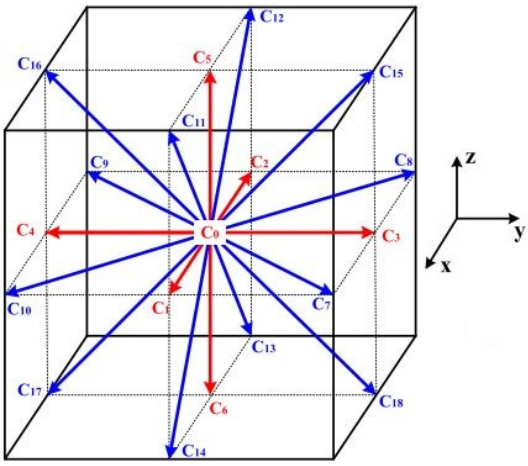

MPF propagation

$$f_i(x + e_i\delta_t, t + \delta_t) = f_i(x, t)$$

Fluid-solid collisions (no-slip)

$$f^*_{-i}(x, t + \delta_t) = f_i(x, t)$$

Fluid-fluid collisions (BGK model)

$$f^*_i(x, t) = f_i(x, t) - \frac{1}{\tau}\left(f_i(x, t) - f^{eq}_i(x, t)\right)$$

$$f^{eq}_i(x, t) = \omega_i \rho' \left[1 + 3e_i\hat{u} + \frac{9}{2}(e_i\hat{u})^2 - \frac{3}{2}\hat{u}^2\right]$$

where $\omega_i = \frac{1}{3}, \frac{1}{16}, \frac{1}{36}$ for $i = 0, 1-6, 7-18$

Figure 5.1: Schematic of the D3Q19 lattice structure (left), reproduced from Guan *et al.* (2017), and a summary of the governing *propagation* (Guan *et al.*, 2017) and *collision* (Quispe *et al.*, 2005; Succi, 2001) models which redistribute the MPFs at each computational time step

one-directional gas transport, a $400 \times 400 \times 400$ voxel CT volume was encased in a solid duct with walls at the boundaries normal to the direction of the pressure or concentration gradient. All simulations were performed using a 3 GHz CPU Intel i5 processor with 2×8 Gb RAM.

Lattice Boltzmann Method (LBM)

LBM represents an alternative numerical scheme to conventional continuum-based CFD methods for simulating fluid flow. While conventional CFD explores numerical solutions to the Navier-Stokes equations at the continuum level, LBM represents the fluid as discrete particles using microscopic collision models and kinetic equations ultimately recovering a continuum solution for macroscopic fluid properties, such as the fluid density, ρ, and superficial fluid velocity, u. A number of studies (Lin *et al.*, 2010; Moreno-Atanasio *et al.*, 2010; Selomulya *et al.*, 2006) have married x-ray CT structures with LBM simulations to predict hydraulic properties of porous media as LBM is computationally inexpensive in comparison to conventional CFD approaches for systems with complex boundary geometries, while the computational lattice nodes at which flow behaviour is resolved are easily mapped onto the domain of cubic voxels generated during CT reconstruction (Selomulya *et al.*, 2006).

LBM simulations were performed using DigiFlow (Structure Vision Ltd. UK), based on a D3Q19 cubic lattice structure (Guadarrama-lara *et al.*, 2015; Guan *et al.*, 2017; Menon *et al.*, 2011) demonstrated in Figure 5.7 (Guan *et al.*, 2017), whereby particles at the central node of a local $3 \times 3 \times 3$ cubic lattice interact with 18 of their 26 nearest neighbours (excluding the 8 extreme corners of the lattice). Each lattice node is thereby associated with 18 mass probability functions (MPF),

$f(x, t, e_i)$, which represent the number of particles with a particular velocity vector, e_i, at a position, x, and time, t.

Particles collide and propagate through the domain, redistributing MPFs between lattice nodes according to the models summarised in Figure 5.7. Collisions are governed by the Bhatnagar-Gross-Krook (BGK) model (Succi, 2001), where a user defined relaxation constant, τ, dictates the rate at which the MPF decays towards the equilibrium value. The relaxation constant relates to the kinematic viscosity of the fluid, $\hat{\nu}$, according to eq. (5.5), where the circumflex accent denotes the dimensionless form of the variable used within the LBM simulation:

$$\boldsymbol{\tau} = \frac{2\hat{\boldsymbol{\nu}} - 1}{6} \tag{5.5}$$

Fluid particle interactions at the solid boundaries are governed by a no-slip boundary condition whereby the MPF is returned to its pre-collision lattice node with a velocity vector equal in magnitude and opposite in direction (Quispe *et al.*, 2005). The MPFs also propagate between neighbouring fluid lattice nodes according to their velocity vectors (Guan *et al.*, 2017). The macroscopic fluid density, $\hat{\rho}$, and velocity, $\hat{u}$ are derived from the MPFs and their associated velocity vectors according to eq. (5.6):

$$\begin{aligned} \hat{\rho} &= \sum_{19}^{1} f_i \\ \hat{u} &= \frac{1}{\hat{\rho}} \sum_{19}^{1} e_i f_i + \tau \frac{\hat{L}}{\Delta \hat{P}} \end{aligned} \tag{5.6}$$

All LBM calculations are performed in dimensionless lattice units (LU), where distance is reported in terms of lattice cell width, $\delta_x = 1$, and time in terms of computational time steps, $\delta_t = 1$. Length scales are easily translated into physical units as the lattice cells have the dimensions of the CT voxel resolution ($\Delta x = 5.325 \times 10^{-5}\,\mathrm{m}$). The computational time step can be derived in physical units as the virtual and physical environments share a common Reynolds number, enabling conversion between virtual and physical velocities using the lattice width, relaxation constant and kinematic viscosity of the permeating fluid, as shown in eq. (5.7).

$$\begin{aligned} \left(\frac{u \Delta x}{\boldsymbol{\nu}}\right) &= \left(\frac{\hat{u} \delta x}{\hat{\boldsymbol{\nu}}}\right) \\ \frac{u}{\hat{u}} &= \frac{\Delta x}{\Delta t} = \frac{\boldsymbol{\nu} \delta x}{\hat{\boldsymbol{\nu}} \Delta x} \\ \Delta t &= \frac{\Delta x^2 (2\boldsymbol{\tau} - 1)}{6\boldsymbol{\nu}} \end{aligned} \tag{5.7}$$

For a relaxation constant of unity and a kinematic viscosity for oxygen of $2.04 \times 10^{-5}\,\mathrm{m^2\,s^{-1}}$, a computational iteration corresponds to $2.32 \times 10^{-5}\,\mathrm{s}$ in real

time. A small pressure gradient, $\nabla\hat{P} = \frac{\Delta\hat{P}}{\hat{L}}$, of 2.5×10^{-4} LU, equivalent to $1.65\,\mathrm{Pa\,m^{-1}}$, was prescribed to induce flow in a desired direction and LBM simulations were run until the superficial velocity of fluid through a cross-section of the domain, including all fluid and solid sites, achieved steady state. The pressure gradient, superficial velocity and fluid viscosity are then used to predict the permeability of the void-space, κ, in m^2 according to Darcy's Law, in eq. (5.8) (Quispe *et al.*, 2005; Selomulya *et al.*, 2006):

$$\kappa = \Delta x^2 \frac{\hat{u}\hat{\boldsymbol{\nu}}\hat{L}\hat{\rho}}{\Delta\hat{P}} \tag{5.8}$$

where $\hat{L}$ is the width of the domain in voxels

Monte Carlo gas diffusion

Monte Carlo gas diffusion (MCGD) simulations were performed using DigiDiffuse software (Structure Vision Ltd. UK), based on a model originally developed for aggregation and sedimentation research (Jia *et al.*, 2000), following a number of studies (Abbasi & Evans, 1983; Evans *et al.*, 1980; Laudone *et al.*, 2008; Zalc *et al.*, 2003) that have employed Monte Carlo style simulations to imitate the seemingly random nature of molecular diffusion within complex porous structures. Here, the simulation domain was constructed of source, porous medium and sink regions each 400 voxel or 21.3 mm wide. The source region, $x = 0 - 400$ voxel, is charged with a fixed concentration, ϕ_s, of *tracer* gas molecules. Tracer molecules diffuse through the porous medium, $x = 400 - 800$ voxel, where tracer molecule concentrations in the void-space, $\phi(x,t)$, increase over time and decay with distance. Tracer molecules which pass through the permeable void-space then accumulate in the enclosed sink region, $x = 800 - 1200$ voxel. Tracer concentrations are taken to be the number of molecules, $\#_M$, per unit volume of void-space, in order to provide a continuous concentration profile through every region of the domain in spite of sudden expansions and constrictions. The concentration within the porous region should therefore be multiplied by the void fraction in order to determine the concentration of oxygen tracers within the entire cubic volume.

Since the macroscopic motion of molecules due to Brownian motion is apparently random, tracer gas molecules are able to randomly move to any of the 26 immediately adjacent sites as long as that site is not occupied by another tracer molecule or a solid boundary. Thus, in contrast to the LBM simulations, the propagation of fluid particles exhibits no dependence on previous computational steps, only the current location of tracer molecules. In the highly improbable instance that every adjacent lattice site is occupied, the move is rejected for that iteration

of the simulation, implying that the net effect of all collisions during that computational iteration return the molecule to its pre-collision lattice node. The rejection of molecular transfer to occupied sites thereby promotes macroscopic diffusion along the direction of the concentration gradient. The evolution in concentration with time relates to the concentration gradient according to Fick's second law of diffusion, the linear form of which is given in eq. (5.9):

$$\frac{d\phi}{dt} = D\frac{d^2\phi}{dx^2} \tag{5.9}$$

where D is the diffusivity, or effective diffusivity, D_{eff} in the case of a porous medium with tortuous diffusion paths. A common analytical solution to eq. (5.9) is defined in eq. (5.10) (Crank, 1979; Laudone *et al.*, 2008) for the boundary conditions of (a) constant source concentration within a plane at $x = 0$, $\phi(0,t) = \phi_0$, and (b) zero concentration infinitely far from the source, $\phi(\infty,t) = 0$:

$$\begin{gathered}\phi(x,t) = \phi_0\, erfc\left(\frac{x}{2\sqrt{Dt}}\right) \\ erfc\left(\frac{x}{2\sqrt{Dt}}\right) = 1 - \frac{2}{\sqrt{\pi}}\int_0^{\frac{x}{2\sqrt{Dt}}} exp\left(-\xi^2\right) d\xi\end{gathered} \tag{5.10}$$

where $erfc$ is the complement, $1 - erf$, to the Gaussian error function (erf). Alternatively, for a source region, $0 \leq x \leq h$, maintained at a constant average concentration, ϕ_s, by replenishing molecules at $x = 0$, and a solid wall at the end of the finite volume, $x = L$, the concentration throughout the domain is better represented using eq. (5.11) (Crank, 1979):

$$\begin{gathered}\phi(x,t) = \frac{\phi_s \boldsymbol{A}}{\boldsymbol{B}} \\ \boldsymbol{A} = \frac{1}{2}\left(erfc\left(\frac{x-h}{2\sqrt{Dt}}\right) - erfc\left(\frac{x+h}{2\sqrt{Dt}}\right) + erfc\left(\frac{2L-h-x}{2\sqrt{Dt}}\right)\right) \\ \boldsymbol{B} = \frac{1}{h}\int_0^h \boldsymbol{A}\, dx\end{gathered} \tag{5.11}$$

where the integral of $\boldsymbol{A}$ across the width of the source region in the denominator ensures that the bulk concentration of tracer particles in the source region remains constant, at ϕ_s. The third term in square brackets captures the reflection and superposition of molecules colliding with the boundary at $x = L$. For an assumed diffusivity, these two analytical solutions provide a mathematical basis to predict the evolution in tracer concentration through time and space in line with the MCGD simulations; the observed diffusivity for each porous medium is found where there is best agreement between the simulated, $\tilde{\phi}(x,t)$, and analytical, $\phi(x,t)$, solutions, quantified by the minimum total absolute error across the width of the porous

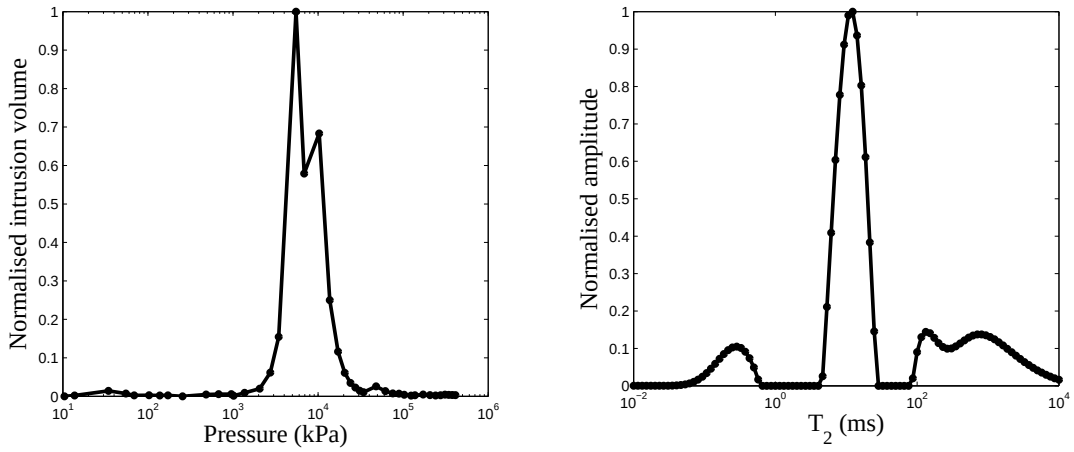

(a) (b)

Figure 5.2: (a) Mercury intrusion porosimetry (MIP) and (b) low-field nuclear magnetic resonance (LFNMR) spectrograms for dried $Mg(OH)_2$ soft sediments

region:

$$D = D_{eff} \text{ when } \mathrm{E} \rightarrow min \text{ where:}$$
$$\mathrm{E} = \sum_{t=1\times10^3\,\mathrm{step}}^{5\times10^5} \sum_{x=400\,\mathrm{voxel}}^{800} \left|\tilde{\phi}(x,t) - \phi(x,t)\right| \tag{5.12}$$

In the case of an open duct, with no geometric obstacles to diffusion, the diffusivity will correspond to the *self-diffusion coefficient*, which is known to be $1.92\times10^{-5}\,\mathrm{m^2\,s^{-1}}$ and $1.60\times10^{-4}\,\mathrm{m^2\,s^{-1}}$ for oxygen (Winter, 1950) and hydrogen (Reichenbacher *et al.*, 1965) respectively. Thus, diffusion through an open duct can be used to calibrate the duration of a computational time step, Δt, in order to translate the effective diffusivities into physical units.

5.3 Results and discussion

5.3.1 Soft sediment microstructure

Mercury intrusion into half a dried disk of $Mg(OH)_2$ is presented in Figure 5.2a beside a LFNMR transverse relaxation time distribution for the other half of the dried disk, following re-saturation with water, in Figure 5.2b. 80 % of the pore-space is intruded by mercury between applied pressures of 2.1-30.9 MPa; applying the Washburn equation, with an advancing contact angle of 130° (Anovitz & Cole, 2015), the centre of this mode corresponds to a pore throat radius of 0.087 µm.

Similarly, the transverse relaxation time distribution demonstrates a distinct mode centred around T_2 = 12.3 ms. The ratio of the MIP determined modal pore throat radius and the modal relaxation time yields a corrected transverse relaxation

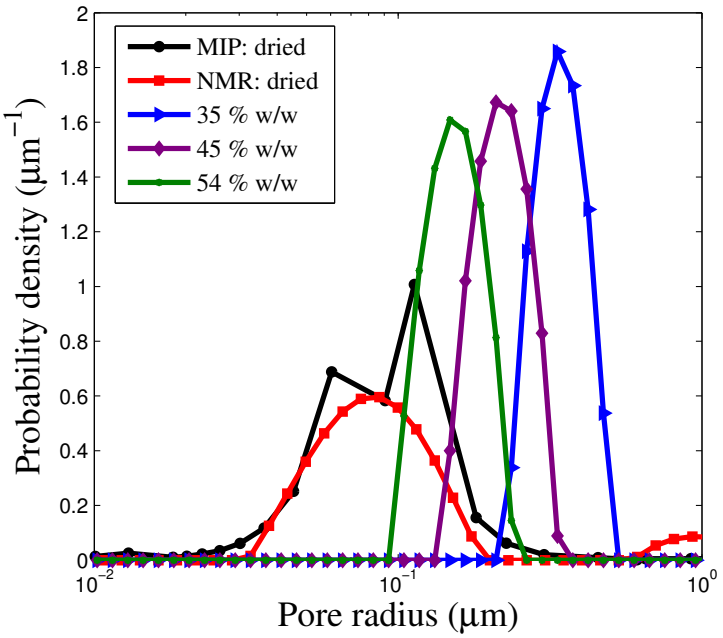

Figure 5.3: Pore throat size distributions for $Mg(OH)_2$ soft sediments of 35-54 % w/w solids concentration obtained by low-field nuclear magnetic resonance (LFNMR) spectroscopy with a mercury intrusion porosimetry (MIP) calibrated *corrected transverse relaxation strength*

strength of $7 \times 10^{-6}\,\mathrm{m\,s^{-1}}$, which is hereafter used to translate relaxation time data into pore throat size distributions for wet soft sediments.

MIP and LFNMR derived pore size distributions for the dried samples and three $Mg(OH)_2$ soft sediments are presented in Figure 5.3. The distributions are normalised to probability density, $p(r_{th})$, values, given by eq. (5.13), whereby the area under each curve is unity and so narrower size distributions manifest with taller peaks.

$$\int_0^\infty p(r_{th})\, \mathrm{d}log_{10}(r_{th}) = 1 \tag{5.13}$$

From Figure 5.3, it is apparent that consolidating soft sediments results in constriction of the sedimentary pores, however consolidation enhances the shear yield stress much more significantly than it constricts the pore throat radii. Increasing the solids concentration from 35 to 54 % w/w sees the modal pore throat radius decrease from 0.335 to 0.148 µm, while the yield stress increases by nearly two orders of magnitude, from 30 to 1112 Pa.

Each of the three $Mg(OH)_2$ soft sediments exhibit very narrow pore size distributions, although the variance increases slightly with solids concentration. Over 92 % of pores within the 35 % w/w sample were measured within the 0.24-0.47 µm range. The remaining 8 % of pores were found within small modes at 3.6-4.5 nm and 9.8-12.3 µm, although it is noted LFNMR can occasionally underestimate the

volume of meso-scale pores (< 50 nm) due to the large echo-spacing (Xiao *et al.*, 2016). Nonetheless, the soft sediment microstructure is dominated by macro-pores (> 50 nm) (Anovitz & Cole, 2015; Xiao *et al.*, 2016) with pore throats an order of magnitude smaller than the median particle size of around 4 µm.

Table 5.2: Summary of modal pore throat radii, $\bar{r}_{th}$, and free water content within $Mg(OH)_2$ soft sediments estimated using LFNMR

Test material	ω (kg/kg)	Water content (kg/kg)		$\bar{r}_{th}$ (µm)
		Total	LFNMR	
$Mg(OH)_2$ (dried & saturated)		0.36	0.36	0.087
$Mg(OH)_2$	0.54	0.46	0.40	0.148
$Mg(OH)_2$	0.45	0.55	0.49	0.210
$Mg(OH)_2$	0.35	0.65	0.60	0.335

The modal pore throat radii are summarised in Table 5.2, along with the LFNMR estimated mass fraction of free water detected in each sample. For the dried and re-saturated sample, the LFNMR estimated free water content corresponds closely to the increase in mass following saturation. Conversely, for the saturated soft sediment samples around 9-13 % of the total water content was not detected by the LFNMR, which could indicate that some of the pore water is not *free* but immobilised within $Mg(OH)_2$ aggregates and meso-scale pores, or bound to the pore walls.

In backscattering detection mode, the cryo-FIB images in Figures 5.4a and 5.4b show a large volume of dark pores in the order of 1.5-2.3 µm wide and occasionally up to 6 µm long. Interpolating between the LFNMR analysis at 35 and 45 % w/w in Table 5.2, the modal pore throat radius is anticipated to be in the order of 0.3 µm. Assuming these throats correspond to the 1.5-2.3 µm wide pores in Figure 5.4a, this implies a pore body to throat ratio in the order of 5-8 . The FIB cross-section in Figure 5.4c demonstrates the continuous nature of the water-filled pores more clearly.

Three mechanisms of bubble growth within soft sediments are frequently discussed; excess bubble pressures required to: (1) invade adjacent pore-space, ΔP_i, (Kam & Rossen, 1999) (2) elastically expand the host pore, ΔP_e, (Terrones & Gauglitz, 2003; van Kessel & van Kesteren, 2002) and (3) propagate an existing fracture, ΔP_f, (Johnson *et al.*, 2002) are summarised in eq. (5.14):

$$\begin{aligned} \Delta P_i &= P_b - P_{pw} = \frac{2\gamma cos(\theta)}{r_{th}} \\ \Delta P_e &= P_b - \sigma = \frac{4}{3}\tau\left(1 - ln\left|\frac{G}{\tau}\right|\right) \\ \Delta P_f &= P_b - \sigma \approx 1.32\left(\frac{K_{Ic}^6}{V_c E}\right)^{\frac{1}{5}} \end{aligned} \tag{5.14}$$

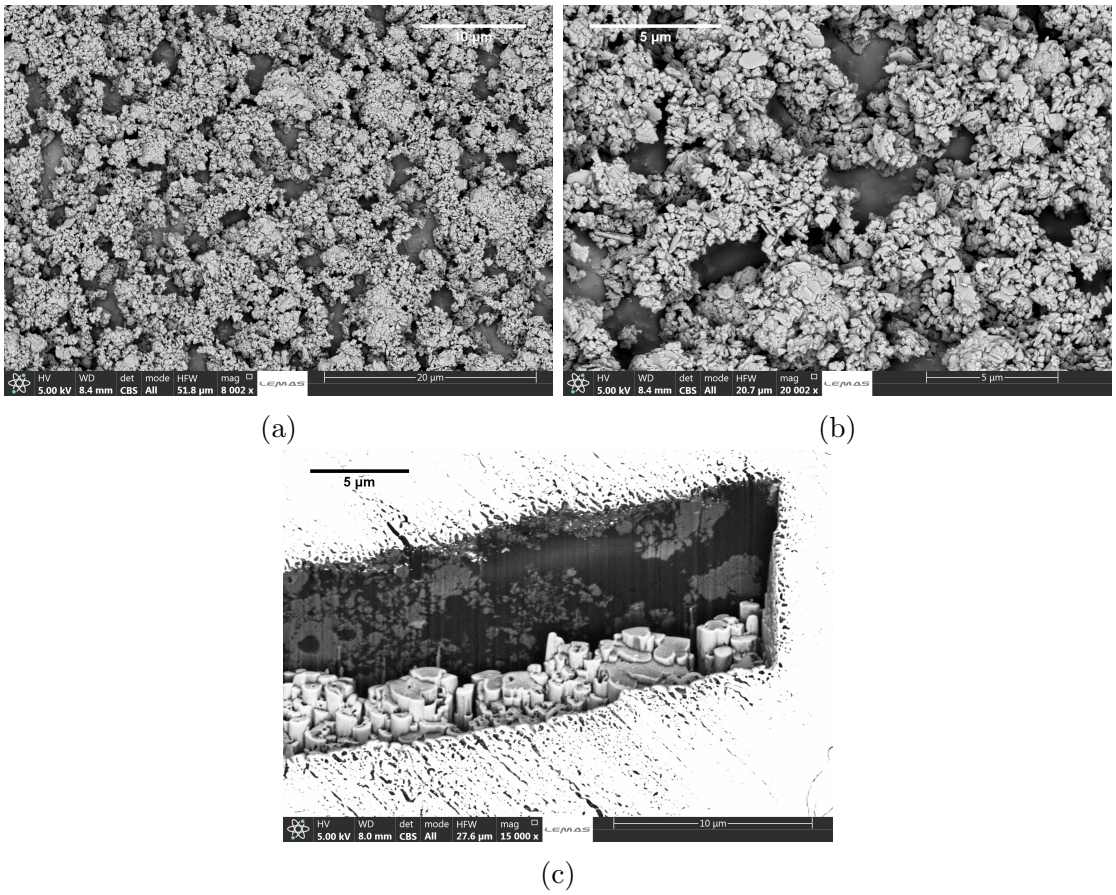

(a) (b)

(c)

Figure 5.4: Focused ion beam (FIB) micrographs of (a-b) the topography of a fractured surface and (c) a vertical FIB cross-section of cryogenically frozen $Mg(OH)_2$ soft sediment

where γ is the surface tension, G is the shear modulus, $K_{I,c}$ is the fracture toughness, V_c is a crack volume and E is the Young's modulus of the sediment. The pore-scales indicated by Table 5.2 and Figure 5.4 appear to preclude capillary invasion as a realistic mode of bubble growth. A non-wetting gas ($cos(\theta) \rightarrow 1$) intruding into a 200 nm diameter pore would entail capillary entry pressures of 1.46 MPa, over three orders of magnitude larger than the shear yield stress of any sample in this study. Bubble growth beyond the pore scale must therefore require some displacement of the sediment matrix. Since the yield stress of the sediment matrix increases much more rapidly than pore dimensions constrict with sediment consolidation, capillary invasion thereby becomes more energetically favourable with sediment consolidation, but remains unrealistic even for kiloPascal yield stress $Mg(OH)_2$ sediments. Furthermore, the fracture toughness of a soft sediment is reported to scale with the inverse square root of the grain size, r_g, (Jain & Juanes, 2009) implying that very fine-grained sediments such as this are more likely to promote fracture than dendritic bubbles consistent with capillary invasion. However, since fracture toughness typically increases with diminishing yield stress (Mughrabi, 1992), broadly spherical bubbles consistent with elastic cavity expansion are anticipated for fine-grained,

low-intermediate yield stress sediments, although fracture propagation may be realistic for kiloPascal yield stress sediments containing sufficiently large initial cracks.

5.3.2 X-ray computed tomography

Figure 5.5 shows typical x-ray CT slices through $Mg(OH)_2$ soft sediments of 30, 234 and 1112 Pa yield stress following 6 h *in situ* gas generation. In each instance, a small number of relatively large (> 1 mm) macro-bubbles of high sphericity are observed, consistent with those identified in Figure 4.10. The 1112 Pa sediment imaged in Figure 5.5c retains larger macro-bubbles than the two lower strength sediments, up to 10 mm in diameter. In each sediment, the vast bulk of the voidage consists of a *honeycomb* of smaller bubbles in the 0.07-0.7 mm diameter range, henceforth referred to as microvoids, many of which appear to be connected. The small bubble population within the high strength 1112 Pa sediment appears more like micro-cracks, oriented laterally, or normal to the compressive load, with significantly greater aspect ratios than the highly spherical microvoids within the 30 Pa sediment.

While 0.07-0.7 mm microvoids are indeed small relative to the macro-bubbles several millimetres in diameter, they remain 2-3 orders of magnitude larger than the undisturbed sedimentary pores observed in Figure 5.4. As such, the microvoids appear to straddle two classic classifications of sedimentary bubbles:(Anderson *et al.*, 1998) type III sediment displacing bubbles which expand the interstitial pores in the sediment and type II *reservoir* bubbles which occupy multiple pores around undisturbed sediment grains. Instead, the tomography appears to demonstrate microvoids which expand their host cavity causing the pore throats to widen in unison with the pore bodies. Eventually, the pore throats widen sufficiently for gas to intrude, allowing neighbouring microvoids to coalesce and form extensive networks. This also implies that the pore geometry and deformability of these low-intermediate strength sediments is not conducive to *snap off* (Ransohoff *et al.*, 1987), whereby gas invading into adjacent pore-space divides at constricted throats and forms separate smaller bubbles.

Microvoid coalescence is a familiar concept to metallurgists as it represents a critical component of fracture propagation (Withers, 2015) and failure within ductile metals (Burghard, 1974). Coalescence between microvoids within aqueous soft sediments may play a similar role in diminishing the fracture toughness of the bulk sediment, however another implication could be that extensive networking of coalesced microvoids establishes pathways for enhanced gas migration and chronic gas release. The connectivity amongst the microvoid population is clearest in Figure 5.5d, where the region of interest outlined in white in Figure 5.5a has been isolated, magnified and processed to diminish speckling and ring artefacts (shown

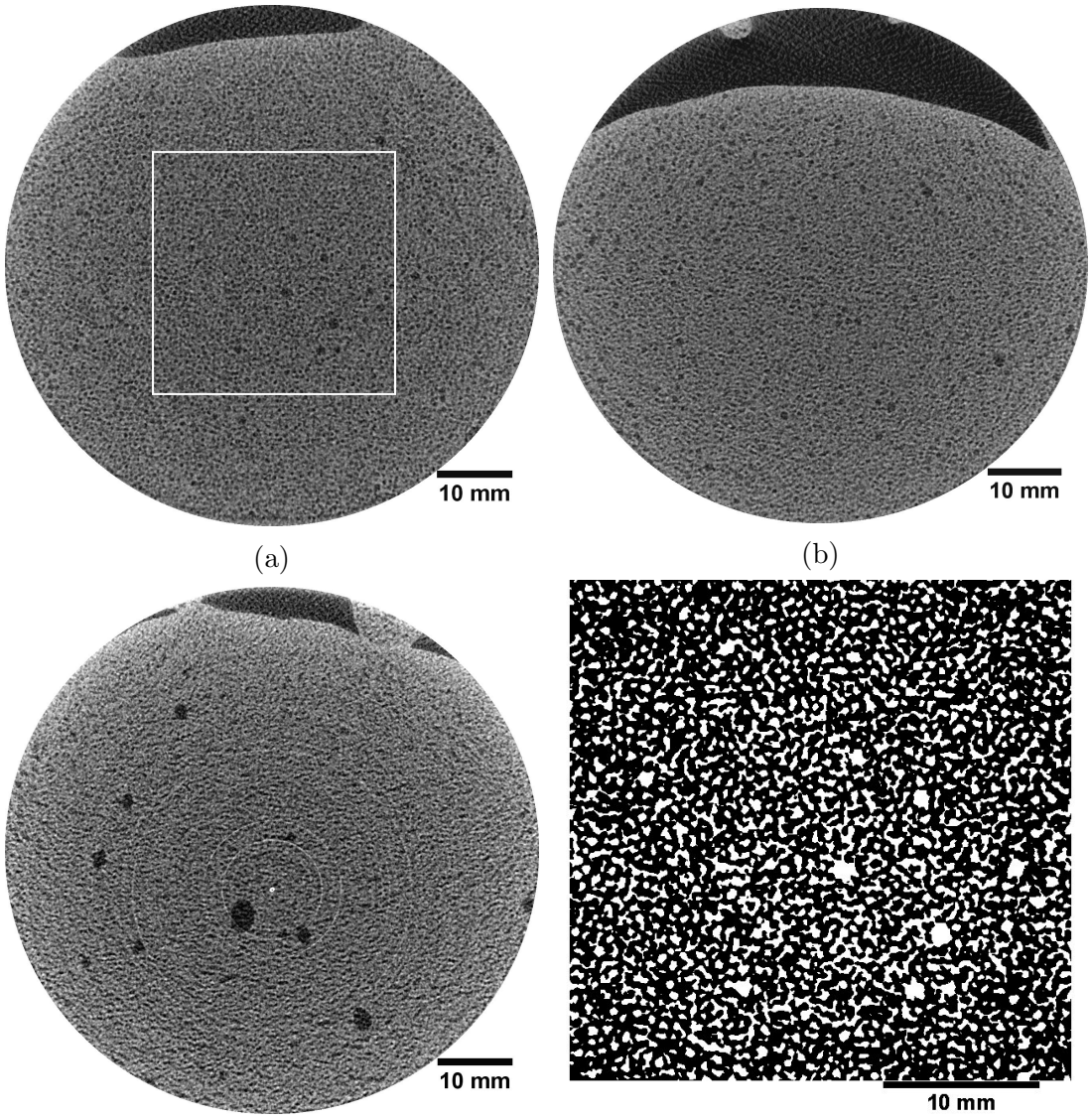

(a) (b) (c) (d)

Figure 5.5: Example x-ray tomographs through the cylindrical cross-section of three $Mg(OH)_2$ soft sediments of (a) 30 Pa, (b) 238 Pa and (c) 1112 Pa yield stress following 6 h in-situ gas generation. The 600×600 pixel region of interest outlined in (a) has been processed and thresholded in (d) to show white bubbles against black sediment

Table 5.3: Characterisation of the voidage properties within 30-1112 Pa yield stress $Mg(OH)_2$ soft sediments following 6 h *in situ* gas generation

τ (Pa)	ν	$\frac{V_g^*}{V_g}$	$\frac{6V_g}{A_g}$ (mm)	$\frac{A_g}{A_s}$	$\bar{AR}^{-1}(\bar{L}_b < 0.5\,\text{mm})$	$\bar{L}_{50}$ (mm)	$\bar{L}_{95}$ (mm)
30	0.31	0.998	0.34	324	0.69	0.47	1.33
238	0.28	0.981	0.34	293	0.53	0.42	1.31
1112	0.34	1.000	0.43	281	0.51	0.50	2.70

most clearly in Figure 5.5c), thresholded and inverted to present white bubbles against a dark soft sediment background. A number of characteristics of the bubble population are summarised in Table 5.3.

The thresholded void fractions of the 600^3 voxel regions of interest lie within the 0.28-0.34 range, which aligns closely to the void fractions of 0.30-0.38 estimated from the increase in bed volume. Thus, essentially the entire bubble population appears to be observable at this 53.25 µm imaging resolution. A crude characteristic dimension of the bubble population can be attained from the total retained gas volume to surface area ratio, $\frac{6V_g}{A_g}$. This characteristic bubble length ranges from 0.34 to 0.43 mm for the three sediments, comfortably larger than than the CT imaging resolution in this study, however it also indicates why only the very mature bubbles are observable under large scale clinical CT with slice separations in the order of 0.625-1.25 mm, as summarised in Table 5.1.

The total interconnected bubble volume was determined by counting the number of face, edge and corner connected bubble voxels using the Bolte & Cordelières (2006) algorithm, revealing that the volume of the continuous gas networks, V_g^*, account for at least 98.1 % of the total free gas volume, V_g, within the 31.95 mm wide region of interest, as detailed in Table 5.3. The bubble network therefore provides a pathway for free gas to migrate through the region of interest by diffusion. Competition between the maximum field of view and the imaging resolution necessary to capture the entire bubble population makes it difficult to estimate the range that the bubble network might span. The field of view could be representative of the sediment on an infinite scale, making 98 % of the retained free gas continuous. Alternatively, the gas could be retained within discontinuous *ganglia* which could span length-scales as little as 0.1 m, barely larger than the 31.95 mm wide field of view, similar to observations of two-phase N_2 – brine flow through porous sandstone (Reynolds *et al.*, 2017) and dense non-aqueous fluid contamination in soils (Wu *et al.*, 2017). In either instance, the extensive connectivity between neighbouring bubbles is likely to have significant implications for gas migration and chronic gas release.

Diffusion through permeable bubble networks would explain chronic gas release from soft sediments much better than aqueous volatile diffusion as gas molecules diffuse much more readily in the gas phase than through an aqueous phase. The

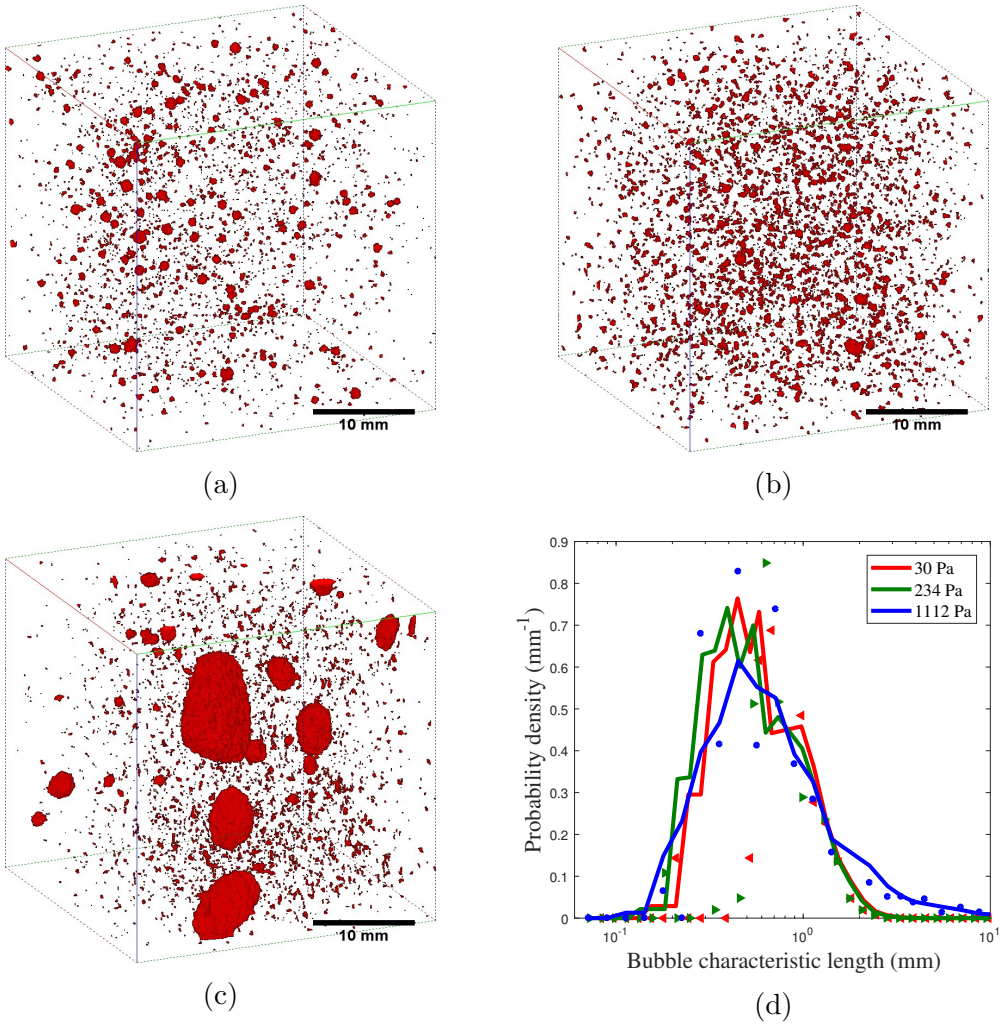

Figure 5.6: Three-dimensional views of *partially eroded* bubble networks indicating the size and shape of individual bubbles within (a) 30 (b) 234 and (c) 1112 Pa soft sediments together with (d) bubble size distribution histograms from chord length analysis

self-diffusion coefficient for oxygen, $1.92 \times 10^{-5}\,\mathrm{m^2\,s^{-1}}$ (Winter, 1950), is four orders of magnitude greater than that of oxygen in water, $3.49 \times 10^{-9}\,\mathrm{m^2\,s^{-1}}$ (Krieger *et al.*, 1967). Furthermore, the ratio of free gas surface area within the bed to the surface area of the interface between the bed and the test cylinder ullage, $\frac{A_g}{A_s}$, indicates there is around 300 times more interfacial area for exchange of volatiles within the bed than at the bed-ullage boundary, and this factor is likely to increase substantially with experimental scale. Hence, conditions are many times more favourable for the release of free gas than for direct release of dissolved oxygen from the aqueous phase, consistent with observations from marine sediments (Katsman *et al.*, 2013). Gas diffusion through permeable bubble networks also reconciles chronic gas release with the observation that the large macro-bubbles which impart the greatest buoyant stress on the sediment and are most likely to rise by ebullition appear to remain static within the bed for several hours.

In order to better visualise the constituent bubbles of each network, a 2-3 voxel

deep film was digitally eroded from the void-space to reduce the connectivity between adjacent bubbles and reveal discrete bubbles, generating the views in Figures 5.6a to 5.6c. These depictions thereby under-represent the volumetric contribution of the microvoid population to the total voidage, but better demonstrate the size and shape of retained bubbles under the different sediment conditions. The microvoid population is more distorted within the higher concentration sediments, with the average inverse aspect ratios, $AR^{-1} = \frac{L_{min}}{L_{max}}$ decreasing significantly, from 0.69 in the 30 Pa sediment to 0.51 at 1112 Pa yield stress. The longest axes of these fine bubbles are typically oriented normal to the compressive load, particularly within the 1112 Pa sediment, indicating that young bubbles grow by preferentially displacing sediment in the direction of minimum compressive stress. The increasing aspect ratio with sediment consolidation thereby accords with the observation that the ratio of lateral to vertical compressive stress, $K_0 = \frac{\sigma_H}{\sigma_V}$, decreases with increased sediment depth and with consolidation (Boudreau, 2012). Preferential bubble deformation in the lateral direction also promotes coalescence in the radial field, instigating a least tortuous diffusion path perpendicular to gravity.

Estimation of bubble aspect ratios as a function of bubble size enabled translation (Lawson & Hanson, 1974; Li & Wilkinson, 2005) of 3×10^8 random chord length measurements of the void-space into the bubble size distributions presented in Figure 5.6d. Bubbles of 0.07-10 mm characteristic length are observed in each instance, with remarkably similar median sizes of 0.42-0.50 mm, summarised in Table 5.3. These sub-millimetre median bubble diameters appear comparatively small compared with previous observations of sedimentary bubbles. Sherwood & Eduardo Sáez (2014) observed bubbles of 3 mm median diameter following hydrogen peroxide decomposition in low strength (τ = 7 Pa) bentonite clay, used as an analogue for nuclear waste slurries stored at Hanford, although the lower limit of detection in this study was unclear. As demonstrated by Figure 5.6c, the 1112 Pa yield stress sample supports a larger fraction of macro-bubbles, with 10.9 % of the voidage consisting of large mature bubbles of $1.5 < \bar{L} = L_{max}\sqrt{AR} < 10$ mm dimensions, while less than 3 % of bubbles within the less consolidated samples exceed 1.5 mm in length. Integration of this large bubble fraction within the much larger void-network may account for their long residence times and why bubbles cease to grow despite continued *in situ* gas generation, since volatiles which diffuse towards networked bubbles may permeate or diffuse through the network rather than promote further growth. LBM and Monte Carlo simulations are employed to characterise gas migration through these sedimentary void-networks.

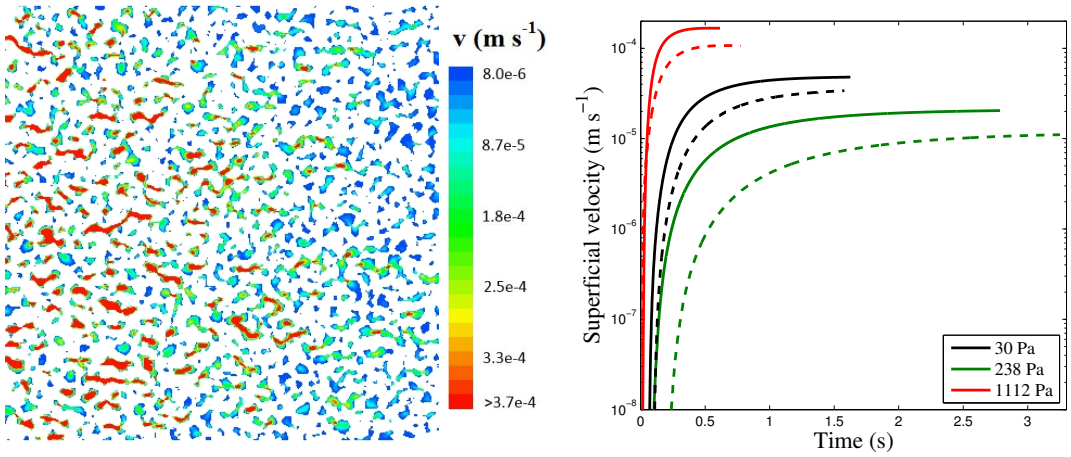

(a) (b)

Figure 5.7: LBM simulations of flow through sedimentary void-networks given a 1.65 Pa m^{-1} lateral pressure gradient, including (a) an example velocity field in the x-y plane through the bubble networks of a 30 Pa yield stress soft sediment, white pixels represent regions of zero flow, including the bulk sediment (solids and porewater) sites and bubbles not connected to the continuous void-network, velocities through the void network are represented using a blue-red colour map with velocity increasing with the colour warmth, and (b) the evolution in superficial velocity at the mid-point of the porous volume in the lateral (solid line) and vertical (dashed line) directions

5.3.3 Characterising the permeability of bubble networks with LBM

Lateral gas flow through the coalesced bubble networks within the 30 Pa yield stress soft sediment was investigated by running an LBM simulation for 70 000 computational iterations, equivalent to 1.62 s, at which point the superficial velocity was observed to achieve steady state; an example two-dimensional velocity field, in the x-y plane, at steady state is shown in Figure 5.7a. Positive velocities in the x-direction, u_x, were observed in 89.9 % of fluid sites, demonstrating continuous flow of gas through the sampled volume. The high velocity regions, indicated by warmer colours, demonstrate preferential flow pathways through the sediment.

The evolution in superficial velocity, or Darcy velocity, through a plane at the mid-point of the volume (x = 200 voxel) is presented for flow through the three soft sediments in Figure 5.7b until steady state conditions were observed. The six profiles represent flow in the lateral, u_x, (solid lines) and vertical, u_y, (dashed lines) directions through the 30, 234, and 1112 Pa yield stress sediments. The principal flow direction for lateral and vertical simulations was specified by both the direction of the imposed pressure gradient and the provision of a solid duct around the sample with walls normal to the pressure gradient. From Darcy's law, eq. (5.8), it is shown that for a given pressure gradient, and fixed viscosity and density of fluid, in this

Table 5.4: The gas permeabilities of bubble networks retained within $Mg(OH)_2$ soft sediments of 30-1112 Pa yield stress

ω (% w/w)	τ (Pa)	ν	κ_H ($\times 10^{-12}$ m^2)	κ_V ($\times 10^{-12}$ m^2)	κ_V/κ_H
35	30	0.31	50.2	30.9	0.61
45	234	0.28	18.6	10.1	0.54
54	1112	0.34	151.6	91.8	0.61

case oxygen, the permeability of the void-space depends only on the superficial velocity, enabling calculation of the lateral, k_H, and vertical, k_V, permeabilities as summarised in Table 5.4.

In each instance, the voidage is 39-46 % less permeable to vertical flow than to horizontal, or lateral, flow ($\kappa_H > \kappa_V$). Since the LBM simulations were performed in a zero-gravity environment, the enhanced permeability to lateral flow must be a consequence of the geometry of the void-network, specifically the tortuosity and constrictivity of the pathways, as the three sediments exhibit similar gas holdup with high bubble connectivity, encompassing > 98 % of the total void fraction. Following Figure 5.6 it was noted that the microvoids are deformed by the sediment with their longest axis oriented perpendicular to the compressive load, or parallel to the minimum compressive stress. Since the deformed bubbles occupy more space normal to gravity, bubbles are more likely to encounter, and coalesce with, neighbouring bubbles in the radial field. This explains the propagation of a less tortuous pathway normal to gravity promoting lateral gas migration.

The LBM simulated permeabilities exhibit the same hierarchy ($\kappa(\tau = 1112\,\text{Pa}) > \kappa(\tau = 30\,\text{Pa}) > \kappa(\tau = 234\,\text{Pa})$) as the void fractions summarised in Table 5.4, with sediments of greatest gas holdup most pervious to gas migration. For geometrically similar microstructures, Quispe *et al.* (2005) discusses a power law relationship between permeability and porosity, or void fraction in this instance, with a cubic exponent. The subtle difference in gas holdup between samples does not therefore account for the range of permeabilities observed, implying that geometric differences between the void-networks significantly influence the gas transport behaviour. Following Figure 5.3, consolidation of the sediment to higher solids concentrations and yield stresses has been shown to constrict the throats connecting pores within the two-phase sediment microstructure. This may manifest in greater constrictivity between the partially coalesced microvoids as the yield stress is increased from 30 to 234 Pa, explaining the reduction in permeability. The reason this trend does not continue to the 1112 Pa sediment is most likely due to the onset of fracture, as observed in Figure 4.10d, particularly amongst the small bubble population, and the merging of these lateral micro-cracks to establish low-tortuosity pathways

However, the hierarchy of the permeability coefficients may be less significant than their magnitude, which lie in the order of 10.1-151.6 $\times 10^{-12}$ m^2, as summarised

in Table 5.4. Permeability coefficients of this magnitude are consistent with highly pervious geological media (Bear, 1972); this is perhaps unsurprising given that the 0.07-10 mm bubbles comprising the void-network are much coarser than typical geological pores. The high magnitude permeabilities imply that gas will readily migrate through these sediments once a long range void-network is established.

The pressure field within soft sediments is said to increase linearly with depth (Algar *et al.*, 2011a), a phenomenon which sometimes causes large bubbles to acquire an inverted teardrop shape as the change in pressure across the height of the bubble can lead to a reduced load at the *tail* causing it to narrow. The increase in pore water pressure with depth will be less than the increase in hydrostatic pressure, $\Delta P = \rho g L$, as the large compressible bubbles transfer a portion of the load to the solid sediment matrix (Wheeler, 1988a). Sediments with substantial gas holdup or even continuous gas may greatly dampen the hydrostatic load. Nonetheless, given the large permeabilities to vertical flow in the order of 10-90 $\times 10^{-12}$ m^2, a mild increase in the ambient pressure field surrounding the bubble network with depth may provide adequate driving force for volatiles to permeate upwards towards the shallow surface of the bed according to Darcy's law, eq. (5.15), a process we will call *stratification*.

$$q = \frac{\dot{V}}{A} = \frac{\kappa_V}{\mu_g}\frac{\Delta P}{L} \tag{5.15}$$

However, since the vertical pressure gradient may be greatly dampened by the large holdup of cavity expanding bubbles and the orientation of individual microvoids and cracks promotes gas migration normal to the compressive load, long range gas migration may be controlled by lateral diffusion, driven by concentration gradients resulting from the continuous *in situ* generation of volitiles, enabling chronic gas release at containment walls. Analysis of lateral diffusion of volatile species through the void-network requires characterisation of the effective diffusivity, which is investigated by Monte Carlo simulation.

5.3.4 Characterising effective diffusivity through permeable bubble networks with Monte Carlo simulations

Figure 5.8 shows a slice through the thresholded 1112 Pa sediment between a source region (left) populated with red tracer molecules and an empty sink region (right) prior to commencement of diffusion. Tracer molecule concentration profiles during a Monte Carlo diffusion simulation through an empty duct are presented at 1×10^5 step intervals in Figure 5.9a. The three regions demarcated by vertical dashed lines represent the source, duct and sink regions from left to right. The blue profile, after 1×10^3 computational steps closely resembles the square-step initial

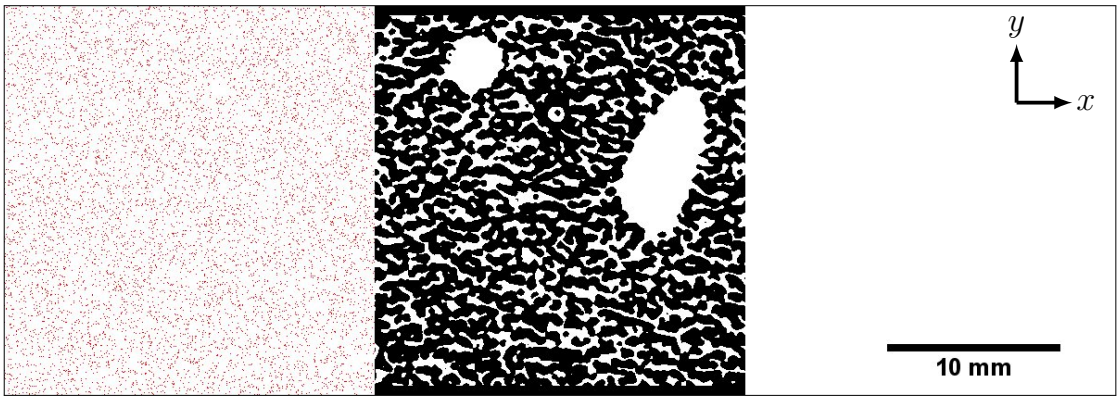

Figure 5.8: An example two-dimensional slice (normal to the z-direction) through the constructed domain for the Monte Carlo gas diffusion (MCGD) simulations at the initial condition; the three regions from left to right represent the source, porous medium and sink regions, where the porous medium is generated from a void-thresholded CT reconstruction of the 54 % w/w sample

condition, indicating minimal diffusion during this time-scale. Subsequent profiles demonstrate the anticipated bell-shaped Gaussian concentration profiles. As the source and sink regions share the same diffusivity as the open duct, a continuous Gaussian distribution extends across the entire 1200 voxel domain, resulting in the concentration at the entry to the duct, $\phi(h,t)$, evolving significantly with time. The reflection and superposition of molecules at the end of the sink region, $x = L$, sees the minimum concentration plateau at increasing concentrations, up to 92 molecule mm^{-3} at the 5×10^5 step.

The thick dashed lines represent analytical solutions obtained using eq. (5.11) with a diffusivity of 4.15×10^{-4} mm^2 step^{-1}, demonstrating excellent agreement with the simulated profiles throughout the 5×10^5 step period, particularly during the first 4×10^5 iterations. The final analytical profile marginally over-predicts the simulated tracer concentration, possibly indicating a slight concentration dependency in the diffusion coefficient, however the small disagreement between the model and the latter stages of the simulation fell within an acceptable tolerance. Oxygen tracer molecules diffuse through oxygen with a self-diffusion coefficient of 19.2 mm^2 s^{-1} (Winter, 1950); comparison of the virtual and physical diffusion coefficients calibrates the duration of a computational iteration, Δt, which was found to be 2.16×10^{-5} s. Each computational time step is therefore five orders of magnitude larger than the collision period for oxygen molecules of 149×10^{-12} s (Hirschfelder *et al.*, 1954), and so a tracer molecule will undergo roughly 1.45×10^5 intermolecular collisions at each iteration of the simulation. Given that a tracer molecule can travel up to $\sqrt{3}$ voxel, or 92 µm, during a computational iteration, intermolecular collisions outweigh wall-collisions many-fold, and so tracer migration is governed by bulk, rather than Knudsen, diffusion.

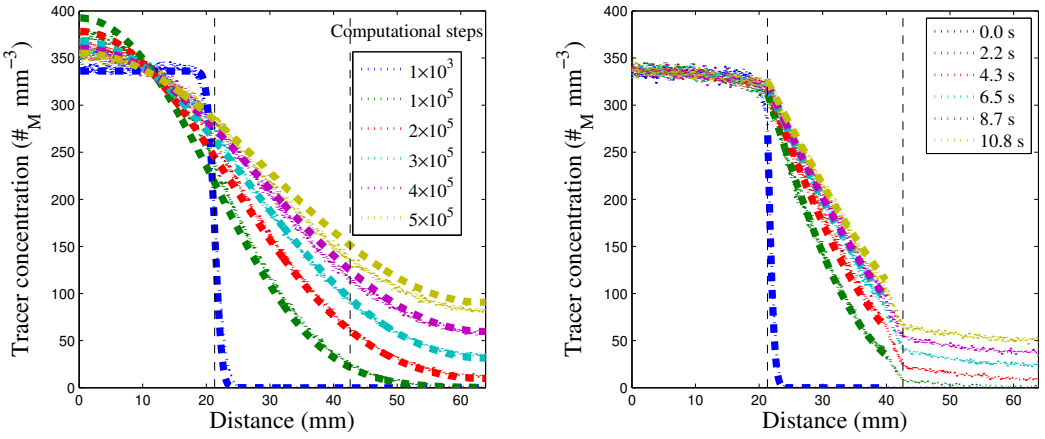

(a) (b)

Figure 5.9: Evolution of oxygen tracer molecule concentration in time and space, $\phi(x,t)$, during Monte Carlo gas diffusion simulations within (a) an open duct and (b) the permeable void networks within 54 % w/w $Mg(OH)_2$ soft sediment (see Figure 5.8); the dotted line profiles are obtained from the simulations, $\phi(x,t)$, the thick dashed lines represent optimised analytical solutions, $\tilde{\phi}(x,t)$, and the vertical dashed lines demarcate the source, porous and sink regions

Tracer molecule concentration profiles through the voidage of the 1112 Pa $Mg(OH)_2$ soft sediment are presented in Figure 5.9b. As for the empty duct, six profiles are shown at regular intervals for the first 5×10^5 step, or 10.8 s, of diffusion. The concentration profiles through the sediment demonstrate the same Gaussian tail shape as through the empty duct, however there is a sudden drop in tracer concentration over the last 50 voxel, or 2.7 mm, of the bed due to the sudden expansion at $x = 2h$. Since the objective is to ascertain the diffusivity through the porous sediment only, the problem can be reformulated to consider only the $x = 400 - 750$ voxel, or 21.3-39.9 mm, region during the first 5×10^5 step. A simpler analytical solution can therefore be found by assuming a planar source concentration at $x = h$ obtained from the simulation, $\hat{\phi}(h,t)$, and by neglecting the reflection of particles at $x = L$, which is not relevant during the early iterations of the simulation, where the diffusion length, $L_D = 2\sqrt{Dt}$, is less than 1200 voxel, or 63.9 mm. This solution is given in eq. (5.16) and the divergence between the simulated and analytical concentration profiles, E, is determined for the truncated, 400-750 voxel, area of interest.

$$\phi(x,t) = \hat{\phi}(h,t)\, erfc\left(\frac{x-h}{2\sqrt{Dt}}\right) \text{ for } x > h$$

$$D = D_{eff} \text{ when } \mathrm{E} \to min \text{ where:} \tag{5.16}$$

$$E = \sum_{t=1\times10^3 \text{ step}}^{5\times10^5} \sum_{x=400 \text{ voxel}}^{750} \left|\hat{\phi}(x,t) - \phi(x,t)\right|$$

The effective diffusion coefficients for each sediment are summarised in Fig-

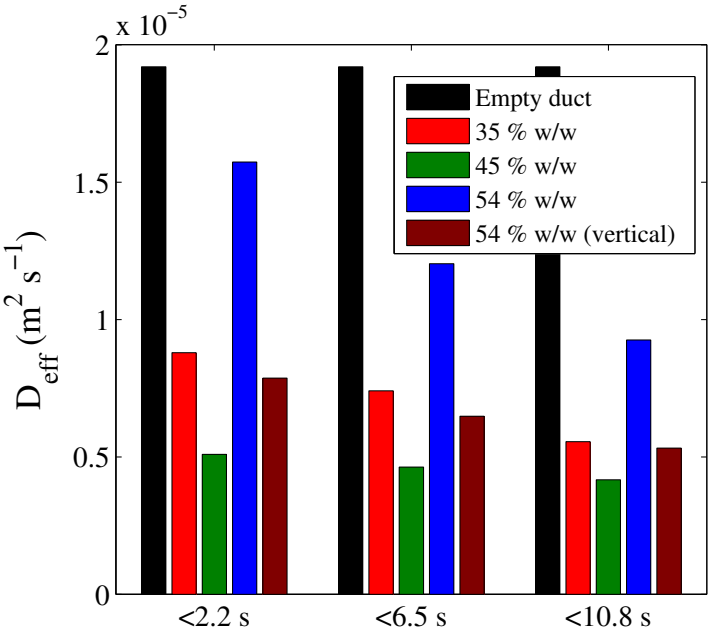

Figure 5.10: Summary of the effective diffusivities for oxygen tracer molucules through an empty duct and through permeable bubble networks within 35-54 % w/w $Mg(OH)_2$ soft sediments

ure 5.10. The diffusion simulations through each of the permeable bubble networks were characterised by the curious observation that diffusion slowed over time, manifesting in effective diffusion coefficients, which diminished by up to 41 % during the simulation. While there is precedent for effective diffusivities through porous media to exhibit some concentration dependence (Crank, 1979), the slowing of diffusion could represent an artefact of the simulation resulting from the coarseness of the voxels relative to the scale of constrictions in the void-network, or *necks* between partially coalesced bubbles. As these constrictions are typically only 1-3 voxel wide, tracer molecules are sometimes forced to diffuse through in single file even though these constrictions are orders of magnitude larger than the mean free paths of oxygen or hydrogen. Hence, as the tracer molecule concentration increases within the voidage, the resistance to diffusion artificially increases. Under these conditions, the predicted diffusivities will be most reliable at the early stages of simulation when the tracer concentration within the soft sediment is low.

The effective diffusion coefficients at each sediment concentration exhibit the same hierarchy as the permeability coefficients, whereby $D_{eff}(\tau = 1112\,\text{Pa}) > D_{eff}(\tau = 30\,\text{Pa}) > D_{eff}(\tau = 234\,\text{Pa})$, although the effective diffusivities lie within a narrower range of 0.4-1.5 $\times 10^{-5}\,\text{m}^2\,\text{s}^{-1}$. Equally, the 1112 Pa sediment demonstrates that diffusive transport proceeds preferentially normal to gravitational compression. This reinforces the arguments made that (1) gas migrates efficiently through high strength sediments with shear yield stresses in the order of a kiloPascal due to the merging of microcracks, (2) at yield stresses below the fracturing regime

sediment consolidation increases the constrictivity of throats between coalesced microvoids and increases the tortuosity of the diffusion path, and (3) microvoids deform with their longest axis favouring the direction of minimum compressive stress, normal to gravity, promoting the formation of lateral rather than vertical transport pathways.

The question remains as to what effective diffusivities in the order of 0.5-1.5 × 10^{-5} m^2 s^{-1} signify for gas migration on the timescales that gas is generated within marine and nuclear sediments. Methanogenic gas generation rates within marine sediments span five orders of magnitude from 1 µmol m^{-3} d^{-1} to 100 mmol m^{-3} d^{-1} (Winterwerp & van Kesteren, 2004). Sludge waste within underground tanks at Hanford generates hydrogen, methane and nitrous oxide at rates in the order of 1 mmol m^{-3} d^{-1} (Sherwood & Eduardo Sáez, 2014), while the hydrogen generation rates within corroded magnox sludge at Sellafield are anticipated to be marginally higher due to the presence of uncorroded metallic cladding swarf. As such, gas generation can be considered a chronic process; even at the fastest gas generation rates in the order of 100 mmol m^{-3} d^{-1} a cubic metre of sediment would require 41 d to generate sufficient volatiles to occupy 0.1 m^3 at ambient temperature and pressure. Within the same time frame, gas can migrate through a continuous void-network with a diffusivity of 1 × 10^{-5} m^2 s^{-1} up to a diffusion length of 11.9 m, comfortably sufficient to diffuse to the walls of nuclear legacy waste containers and facilitate methane release from shallow marine sediments where gas retention is typically greatest as the rich organic content fuels enhanced methanogenesis (Best *et al.*, 2006).

Alternatively, the characteristic time for a one-directional concentration gradient across a given distance, x, to diminish by half, $t_{1/2}$, as a result of diffusion through the void-space can be determined from eq. (5.17).

$$erf\left(\frac{x}{2\sqrt{D_{eff}t_{1/2}}}\right) = 0.5$$
$$\therefore t_{1/2} = 1.099\frac{x^2}{D_{eff}} \tag{5.17}$$

Therefore, a diffusivity of 1 × 10^{-5} m^2 s^{-1} will result in a concentration gradient diminishing by half in 5 d across a 2 m distance, or 32 d across a 5 m distance. Within the same 32 d period no more than 3.2 mol gas is generated per cubic metre of sediment. Hence, diffusion through the void-network appears to be rapid in comparison to the rate of gas generation, implying that the sediment is unlikely to continue to swell once a continuous void-network is established. Furthermore, gas diffusion would proceed even faster if *in situ* hydrogen were generated rather than oxygen, since it has a self-diffusion coefficient of 1.604 × 10^{-4} m^2 s^{-1} (Reichenbacher

et al., 1965), a factor of 8.3 larger than that of oxygen. However, based on x-ray tomography analysis within a 32 mm field of view it cannot necessarily be assumed that the gas phase is continuous over several metres. It is possible that the gas is retained within discontinuous *ganglia* which could span little more than the CT field of view. The latter possibility draws parallels to synchrotron x-ray tomography observations of two-phase N_2 – brine flow through porous sandstone (Reynolds *et al.*, 2017), and dense non-aqueous fluid contamination in soils (Wu *et al.*, 2017).

In the eventuality that the gas phase is not continuous at the metre-scale, three mechanisms could contribute to gas migration over longer distances. Ambient pressure fluctuations which cause the free gas to advance and recede (Kam *et al.*, 2001b) could promote: (1) dynamic connectivity between neighbouring ganglia which is not visible during an instantaneous scan (Reynolds *et al.*, 2017), or (2) ganglion migration through the sediment via Haines jumps (Berg *et al.*, 2013), whereby gas intruding through a pore throat passes into the adjacent pore body manifesting in a sudden drop in capillary pressure, bubble expansion and a rapid transfer of elastic potential energy to kinetic energy (Berg *et al.*, 2013; Gauglitz & Radke, 1989). Berg *et al.* (2013) employed synchrotron x-ray tomography to reveal that Haines jumps can promote gas migration over scales of around 20 individual pore lengths, which, given the distribution of free gas in Figure 5.5, may in turn promote further partial coalescence events. In addition, the large 28-34 % holdup of ≈ 0.4 mm median diameter bubbles provides a large interfacial surface area for continuous exchange of volatiles between the free gas and aqueous phases, while the distance separating bubbles which are not integrated into the continuous network are typically no more than a millimetre. Hence, long range gas migration and chronic release could be explained by (3) a composite mechanism of fast diffusion through highly permeable void-networks, gas exchange at the interface and short range aqueous diffusion. All three processes are likely to operate in tandem to contribute towards an enhanced rate of volatile transport in comparison to aqueous diffusion alone.

The least efficient possible route for gas migration considers only the latter possibility of composite diffusion through static ganglia, 0.1 m in length, and aqueous diffusion across 1 mm distances of intermediate soft sediment. Since aqueous diffusivities are around four orders of magnitude lower than the self-diffusivities of oxygen and hydrogen, gas migration across a 2 m distance would be limited by diffusion through the 20 mm of sedimentary water rather than the 1.98 m of diffusion through the gas phase. Using a conservative assumption that the aqueous diffusivity of oxygen of 3.49×10^{-9} m^2 s^{-1} (Krieger *et al.*, 1967) is diminished by an order of magnitude to correct for the tortuosity of the diffusion path, gas can diffuse across 20 mm of sediment within 3.3 d, around treble the 1.1 d period required

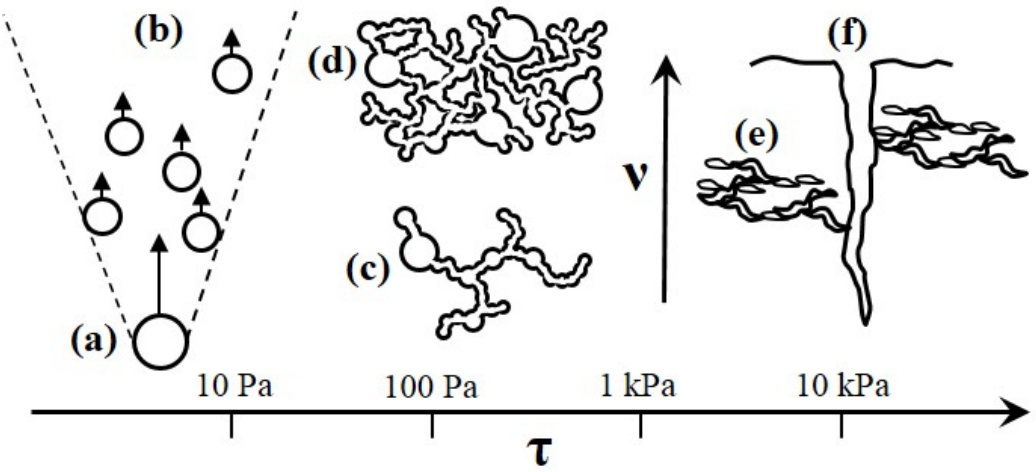

Figure 5.11: Schematic demonstrating alternative chronic gas release mechanisms from consolidated soft sediments under various yield stress and gas holdup conditions, including: (a) buoyant bubble ebullition, possibly inducing (b) bubble cascades (Gauglitz *et al.*, 2015; Sherwood & Eduardo Sáez, 2014), gas migration through (c) discrete ganglia of partially coalesced bubbles or (d) vessel-spanning continuous bubble networks at higher voidages, (e) permeable pathways through coalesced micro-cracks and (f) deep vertical drainage channels (van Kessel & van Kesteren, 2002)

to migrate across a 1.98 m diffusion length through the gas phase. The composite diffusion time of 4.4 d can still be considered rapid in comparison to timescales discussed for chronic gas generation by corrosion, radiolysis and methanogenesis within consolidated soft sediments (Sherwood & Eduardo Sáez, 2014).

Thus, whether the networks of partially coalesced microvoids exist as a continuous vessel-spanning phase or discrete ganglia less than a metre in range, gaseous diffusion appears to present a viable mechanism for chronic gas release from low-intermediate strength sediments able to resist bubble ebullition but unable to support deep drainage channels. The potential for this to represent a widespread mechanism for gas migration across a broad range of sediment yield stress conditions is demonstrated by the schematic in Figure 5.11. The observation that 8 mm bubbles were unable to fluidise $Mg(OH)_2$ sediments of as little as 7 Pa yield stress in Johnson *et al.* (2017) suggests that the lower bound stress at which bubble networks become the principal mechanism for gas migration, under quiescent conditions, could be as low as just a few pascals. Conversely, the upper bound stress at which stable drainage channels are supported to depths of metres lies in the kiloPascal range (van Kessel & van Kesteren, 2002). It therefore appears that the limiting condition for bed swell within 10-1000 Pa yield stress intermediate strength sediments is dictated by the establishment of sufficiently large bubble networks by partial coalescence to enable a faster rate of gas migration than gas generation.

5.4 Conclusions

Magnesium hydroxide soft sediments of 35-54 % w/w solids concentration, or 30-1112 Pa yield stress, exhibited significant bed swell to 28-34 % gas holdup following 6 h *in situ* hydrogen peroxide decomposition. X-ray CT revealed that the voidage consisted of a population of bubbles, 0.07-10 mm in diameter, with extensive partial coalescence between the sub-millimetre microvoids, which resulted in bubble networks which spanned the 32 mm field of view and comprised at least 98 % of the observed free gas. Lattice Boltzmann and Monte Carlo simulations indicate that these networks are highly pervious to gas, with permeabilities of $10.1\text{-}151.6 \times 10^{-12}\,\mathrm{m}^2$ and effective diffusivities for hydrogen of $3.7\text{-}12.5 \times 10^{-5}\,\mathrm{m}^2\,\mathrm{s}^{-1}$, thereby providing avenues for rapid gas migration across the length-scale of the bubble network. Consolidation of the sediments, resulting in an increase in shear yield stress to 1112 Pa and constriction of the water filled pore throats to an LFNMR derived modal size of 148 nm, promoted fracturing amongst the microvoid population, while the larger bubbles maintained a more spherical geometry. Coalescence between laterally oriented micro-cracks established a low-tortuosity pathway for efficient gas transport normal to gravity, with effective diffusivities in the order of $10^{-10}\,\mathrm{m}^2\,\mathrm{s}^{-1}$.

Competition between the maximum scan field of view and imaging resolution required to visualise the smaller microvoids means that the scale of the void-networks remains unclear. Hence, the bubble population may consist of a continuous gas phase encompassing 98 % of all retained free gas, or discontinuous *ganglia* of coalesced bubbles which span lengths of several centimetres, close to the experimental scale of this study. In the latter instance, a combination of (1) dynamic connectivity between neighbouring ganglia, (2) Haines jumps causing the ganglia to migrate and (3) composite diffusion through the gas and aqueous phase can facilitate substantially enhanced gas transport in comparison to aqueous diffusion alone. As the voidage increases to the order of 20-30 % and the distance separating these discrete ganglia diminishes to millimetre scale, composite diffusion through gaseous and aqueous phases appears to facilitate gas release on a shorter time-scale than the chronic rate of gas generation within marine and nuclear waste sediments. The gas transport mechanism identified in this chapter, provides an explanation for the long-standing enigma of how gas escapes from sediments with yield strengths higher than that in which bubble rise, or ebullition (Dubash & Frigaard, 2004), occurs ($\lesssim 10s$ Pa) and lower than that where deep vertical drainage channels form ($\gtrsim$ kPa) (van Kessel & van Kesteren, 2002).

Chapter 6

Gas retention and release from corroded magnesium sludge

6.1 Introduction

The previous two chapters have used x-ray CT to investigate bubbles within consolidated soft sediments of commerical $Mg(OH)_2$, however Chapter 3 introduced a second $Mg(OH)_2$ rich test material, CMgS, which was shown to exhibit significantly greater physical heterogeneity in particle size and density than the commercial $Mg(OH)_2$. The light scattering particle size distribution in Figure 3.3 demonstrated a significant fraction of coarse particles in the 200-1000 µm range which is absent from the commercial $Mg(OH)_2$ sediments. X-ray microtomography, μCT, in Figure 3.5 revealed coarser particles still, including some of millimetre scale, too large for laser scattering detection but visible under μCT due to their much larger density than the typical brucite aggregates. The CMgS therefore appears to exhibit a trimodal particle size distribution with significant heterogeneity in the density distribution through the solid skeleton of the soft sediment.

Modest solids concentrations, $30 < \omega < 40\,\%$ w/w, of CMgS exhibited roughly double the shear yield stresses of equivalent concentrations of commercial $Mg(OH)_2$ in Figure 3.12. The enhanced yield strength at low concentrations and greater heterogeneity in particle size and density make for a more complex test material, but a more realistic analogue for the physically highly complex CMS inventory within the MSSS (Gregson *et al.*, 2011; Hastings *et al.*, 2007; Parry *et al.*, 2011). This chapter applies the MIP, LFNMR and cryo-FIB techniques discussed in Section 5.2.1 to investigate the impact of the broader particle size distribution on the microstructure of consolidated soft sediments, and the two scales of clinical x-ray CT, achieving resolutions of 53.25 and 488 µm respectively, to assess the impact of microstructure on *in situ* bubble growth and the establishment of chronic gas release pathways.

6.2 Materials and methods

Experimentation in this chapter is conducted exclusively using the CMgS test material synthesised by Sellafield Ltd. and NNL by corroding commercial magnesium metal within heated sodium chloride solutions according to the procedure detailed in Section 3.2.1. The solids concentrations of sampled CMgS were estimated from the mass loss from a 50 ml sub-sample following 12 h of drying at 100 °C. The yield stress of the sample is estimated from the solids concentration using the relationship in eq. (3.6) obtained by vane rheology. Experimentation was limited to samples of no more than 42.3 % w/w solids concentration, or 156 Pa yield stress, due to difficulties in dewatering the CMgS to higher solids concentrations.

6.2.1 Microstructure characterisation

A pore size distribution for 42.3 % w/w CMgS was obtained by LFNMR analysis in accordance with the methodology outlined in Section 5.2.1. The transverse relaxation strength was again estimated by performing MIP and LFNMR on two halves of a dried 30 mm disk of CMgS and calibrating a corrected transverse relaxation strength from the ratio of the modal MIP pore throat radius and the modal LFNMR transverse relaxation time. The LFNMR pore size distribution is supported by cryo-FIB microscopy of a 42 % w/w CMgS sample obtained using a Helios G4 CX DualBeam microscope (FEI, USA) (Matsumoto *et al.*, 2016; Villinger *et al.*, 2015), following the same methodology also detailed in Section 5.2.1. Micrographs were captured of both the topography of a fractured and sublimed surface of the frozen sample and a vertical FIB cross-section.

6.2.2 Laboratory scale gas retention tests

Laboratory scale gas retention tests were performed by decomposing hydrogen peroxide within CMgS samples of 29 and 39 % w/w solids concentration, corresponding to shear yield stresses of 11 and 88 Pa respectively. The procedure entailed a slight modification from that outlined in Section 4.2.1, as the condition of the hydrogen peroxide had deteriorated a little during storage since the gas retention tests presented in Figure 4.4. The oxygen yield from a millilitre of hydrogen peroxide had diminished from 136 to 84 ml, implying that a third of the hydrogen peroxide molecules had perished. To generate the desired total gas volume equivalent to 60 % of the initial bed volume, a 7.1 ml, rather than 4.4 ml, volume of hydrogen peroxide was injected into 1 l of CMgS at the mixing stage (stage 1 in Figure 4.1). The hydrogen peroxide was distributed homogeneously through the sample by 2 min mixing with an axial flow impeller attached to an overhead stirrer and then pumped to the

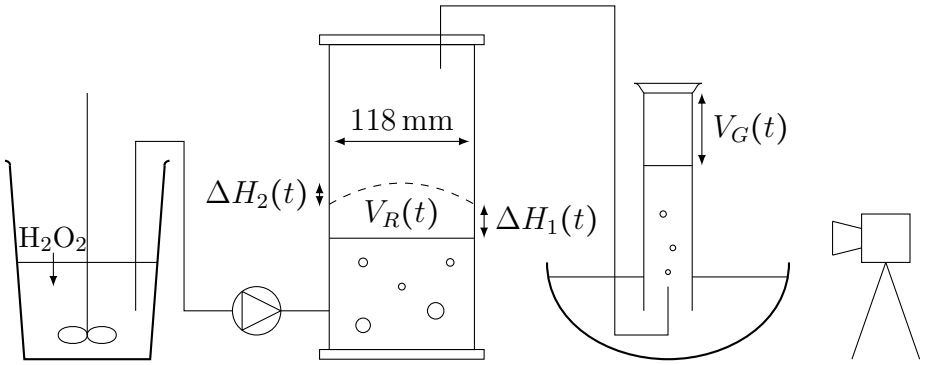

Figure 6.1: Schematic of the laboratory scale gas retention tests used to observe evolution in gas holdup with time during hydrogen peroxide decomposition within CMgS; hydrogen peroxide is well mixed through the sediment using an axial flow impeller

118 mm diameter acrylic test cylinder. The schematic of the experimental method in Figure 4.1 is repeated in Figure 6.1 for clarity:

6.2.3 X-ray computed tomography

X-ray CT scans were performed as oxygen bubbles were generated within two low-intermediate strength CMgS samples of 33.4 and 41.3 % w/w concentration, or shear yield stresses of 30 and 132 Pa respectively. The lower strength sample was imaged after 6 h gas generation within the 71 mm diameter sideways mounted cylinder using the high resolution Inveon dual PET/CT (Siemens, Germany) used throughout Chapter 5. The more consolidated sample was imaged using the Brivo CT385 (GE Healthcare) scanner within the larger 300 mm cylinder, also 150 mm in length, representing an 18-fold increase in experimental scale. Achieving the reduced the scan times and expanded the FOV with the Brivo CT385 necessitated a compromise in pixel resolution from 53.25 µm to 250-488 µm and a 24-fold increase in axial slice separation as detailed in Table 6.1. A smaller 96 mm FOV was scanned at 5 min intervals with the Brivo CT385 during the first hour, while a larger 250 mm diameter FOV was captured again at 2, 4 and 6 h.

Post processing of the tomography data was undertaken using the FIJI-ImageJ (Schindelin *et al.*, 2012) and DigiUtility (Structure Vision Ltd. UK) (Menon *et al.*, 2011) software packages as outlined in Sections 4.2.2 and 5.2.2.

Table 6.1: Summary of x-ray CT scanning parameters and comparison with the scanning protocol used in Chapter 4

	Inveon PET/CT	Brivo CT385	
		Small FOV	Large FOV
X-ray voltage (kVp)	80	120	120
X-ray tube current (mA)	0.5	79	40
FOV diameter (mm)	81.8	96	250
Pixel resolution (µm)	53.25	250	488
Slice separation (µm)	53.25	625	1250
Number of axial slices	1024	32	112
Total FOV volume	2.86×10^5	1.40×10^5	6.81×10^6

6.3 Results and discussion

6.3.1 CMgS microstructure

Mercury intrusion and transverse relaxation time distributions for two halves of a dried disk of CMgS are presented in Figure 6.2a and Figure 6.2b respectively. Similar to the commercial $Mg(OH)_2$, distinct MIP and LFNMR modes are observed in the 4-20 MPa and 2-25 ms ranges respectively. The modal mercury intrusion pressure of 8.2 MPa corresponds to a throat radius of 0.076 µm following application of the Washburn equation, eq. (5.2). The ratio of this modal MIP pore size with the modal transverse relaxation time of 9.3 ms provides a corrected transverse relaxation strength, $\rho_{2,cor}$, of 8.1×10^{-6} m s^{-1}, around 15 % larger than that for the commercial $Mg(OH)_2$ test material, which constitutes reasonable agreement. Given the chemical similarity between the bulk of the two brucite rich test materials, a similar rate of energy transfer from the magnetised protons and sedimentary pore walls is expected. Consequently, disparities between the transverse relaxation time distributions for the CMgS and commercial $Mg(OH)_2$ are likely to reflect real differences in microstructure.

In Figure 6.2, the MIP and LFNMR data for the dried samples have been translated into pore size distributions in micrometres, along with a pore size distribution for a wet CMgS sample of 42.3 % w/w solids concentration or 156 Pa yield stress. As observed for the commercial $Mg(OH)_2$ sediments in Figure 5.3, well over 90 % of the pore volume within the 42.3 % w/w CMgS is connected by throats with radii between 80 and 300 nm, indicative of a macro-porous ($R_{th} > 50$ nm) sediment (Anovitz & Cole, 2015; Xiao *et al.*, 2016).

The modal pore throat radius of 0.152 µm is notably smaller than the 0.21-0.34 µm pores within 35-45 % w/w $Mg(OH)_2$ soft sediments. In fact, comparison of the two test materials in Figure 6.2d and Table 6.2 demonstrates that the 42.3 % w/w CMgS shares a very similar pore throat size distribution to the more consolidated 54 % w/w $Mg(OH)_2$, with it's modal throat radius of 0.148 µm. The

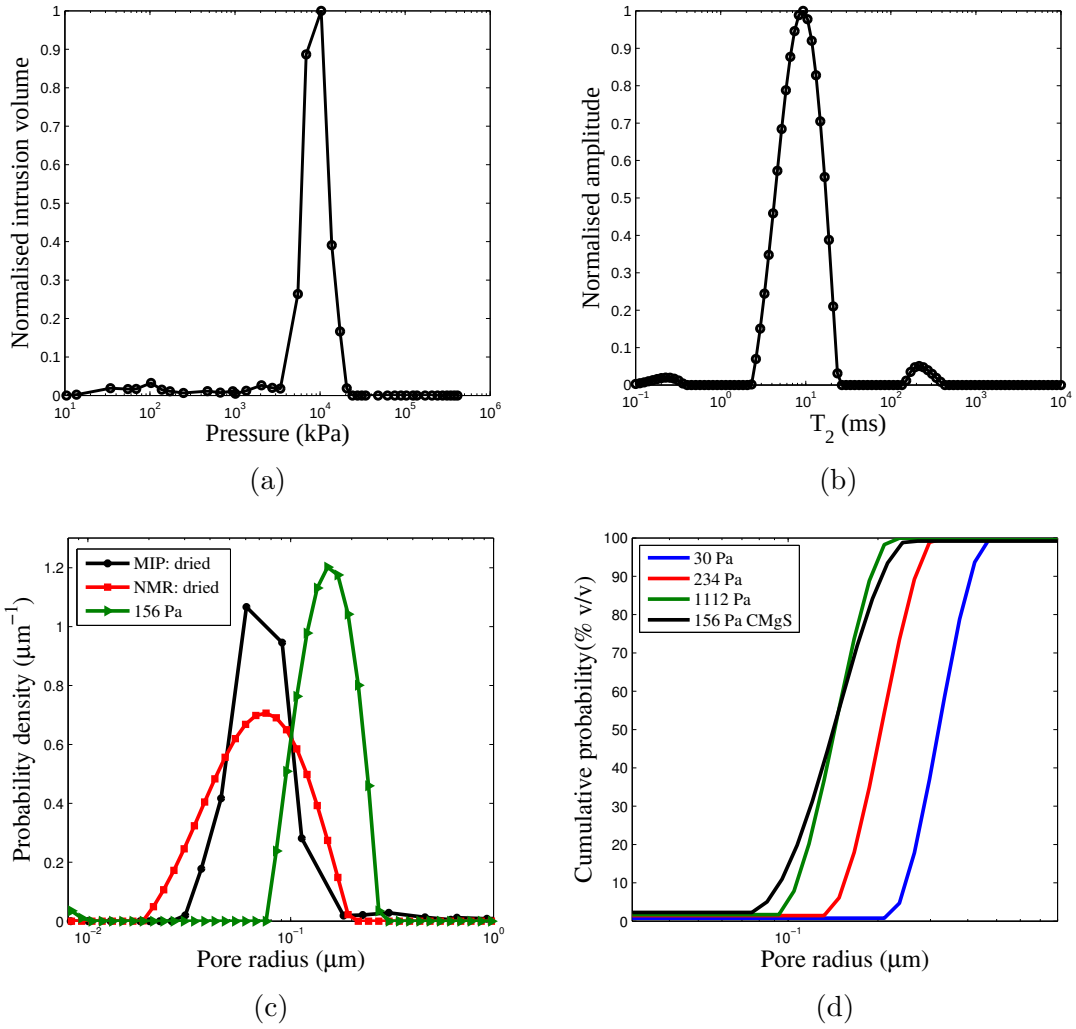

Figure 6.2: (a) Mercury intrusion porosimetry (MIP) and (b) low-field nuclear magnetic resonance (LFNMR) spectra for dried CMgS soft sediments along with (c) a pore size distribution for 42.3 % w/w (156 Pa) CMgS and (d) comparison of pore size distributions for CMgS and commercial $Mg(OH)_2$ sediments of 30-1112 Pa yield stress; the $Mg(OH)_2$ sediment data has been reproduced from Figure 5.3

Table 6.2: Modal pore throat radii, $\bar{r}_{th}$, and free water content within $Mg(OH)_2$ and CMgS soft sediments estimated using LFNMR

Test material	ω (kg/kg)	τ (Pa)	Water content (kg/kg)		$\bar{r}_{th}$ (µm)
			Total	LFNMR	
CMgS (dried & saturated)			0.36	0.34	0.076
CMgS	0.423	156	0.58	0.50	0.152
$Mg(OH)_2$ (dried & saturated)			0.36	0.36	0.087
$Mg(OH)_2$	0.54	1112	0.46	0.40	0.148
$Mg(OH)_2$	0.45	234	0.55	0.49	0.210
$Mg(OH)_2$	0.35	30	0.65	0.60	0.335

CMgS demonstrates a marginally broader pore size distribution than the 54 % w/w commercial $Mg(OH)_2$ sediment; this is consistent with Mahmoodlu *et al.* (2016) where discrete element modelling (DEM) of compacted sand demonstrated that broader particle size distributions correspond to broader pore size distributions. To observe a similar pore throat size distribution to 42.3 % w/w CMgS, a substantially more consolidated sample of commercial $Mg(OH)_2$ is required and this increase in solids concentration has a substantial impact on the sediment's mechanical response to stress. A commercial $Mg(OH)_2$ sediment of comparable microstructure would have a shear yield stress of 1112 Pa, almost an order of magnitude larger than the 156 Pa CMgS.

Alternatively, if CMgS and commercial $Mg(OH)_2$ soft sediments of equivalent shear yield stress are compared, the CMgS will contain a greater water content, and hence a larger total pore volume, as well as greater constrictivity between neighbouring pores as a result of it's narrower pore throats. If an equivalent yield stress sample of CMgS exhibits more voluminuous pores with narrower pore throats, this would appear to: (1) extend the initial phase that the bubble can grow before it occupies the host cavity and starts to encounter the resistance imposed by the stress of the sediment matrix, although this period is still likely to be exceptionally brief, and (2) enhance the resistance to bubble intrusion into adjacent pore-space by capillary invasion. This implies favourable growth of highly spherical bubbles by cavity expansion, but it also indicates that an extended period of growth would be required before the pore throats broaden sufficiently for communication between neighbouring bubbles. The disparity in microstructure would therefore imply a coarser bubble population with reduced connectivity within the CMgS.

Three micrographs obtained by cryo-FIB microscopy are presented in Figure 6.3. The familiar structure of interlocking hexagonal brucite platelets is most clearly shown in Figure 6.3b, however, the macro-porous sediment structure is

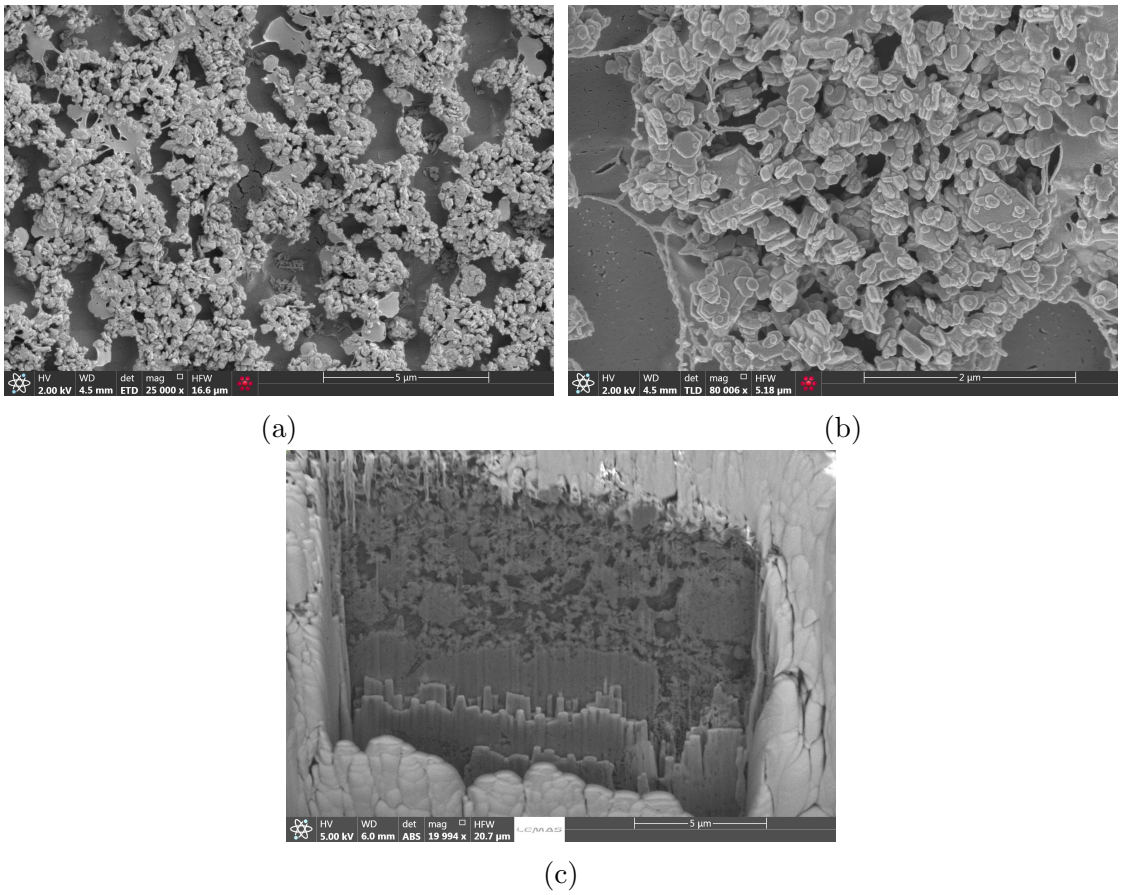

Figure 6.3: Focused ion beam micrographs of (a-b) the topography of a fractured and sublimed surface and (c) a vertical FIB cross-section of a cryogenically frozen sample of 42 % w/w CMgS

better demonstrated by the lower magnification micrograph of the sublimed topography in Figure 6.3a and the vertical FIB cross-section in Figure 6.3c.

Figure 6.3a demonstrates many empty cavities similar in shape to those in Figure 5.4, around 0.6-1.8 µm in width and up to 4 µm long. The pores appear a little smaller within the vertical FIB cross-section in Figure 6.3c at 0.3-0.8 µm across. Thus, the pore body to throat ratio appears of a similar order to the commercial $Mg(OH)_2$ sediments, at around 5-8 , although it is difficult to build a complete understanding of the microstructure from two perpendicular two-dimensional views.

6.3.2 Bubble populations within CMgS observed using high resolution clinical x-ray CT

Figure 6.4 presents high resolution clinical x-ray tomography of bubbles retained within CMgS and commercial $Mg(OH)_2$ soft sediments of 30 Pa yield stress, each acquired using the Inveon PET/CT scanner detailed in Table 6.1. Following 6 h *in situ* gas generation, the disparity between the two bubble populations is stark. The CMgS supports a much coarser population of 1-8 mm equivalent spherical diameter

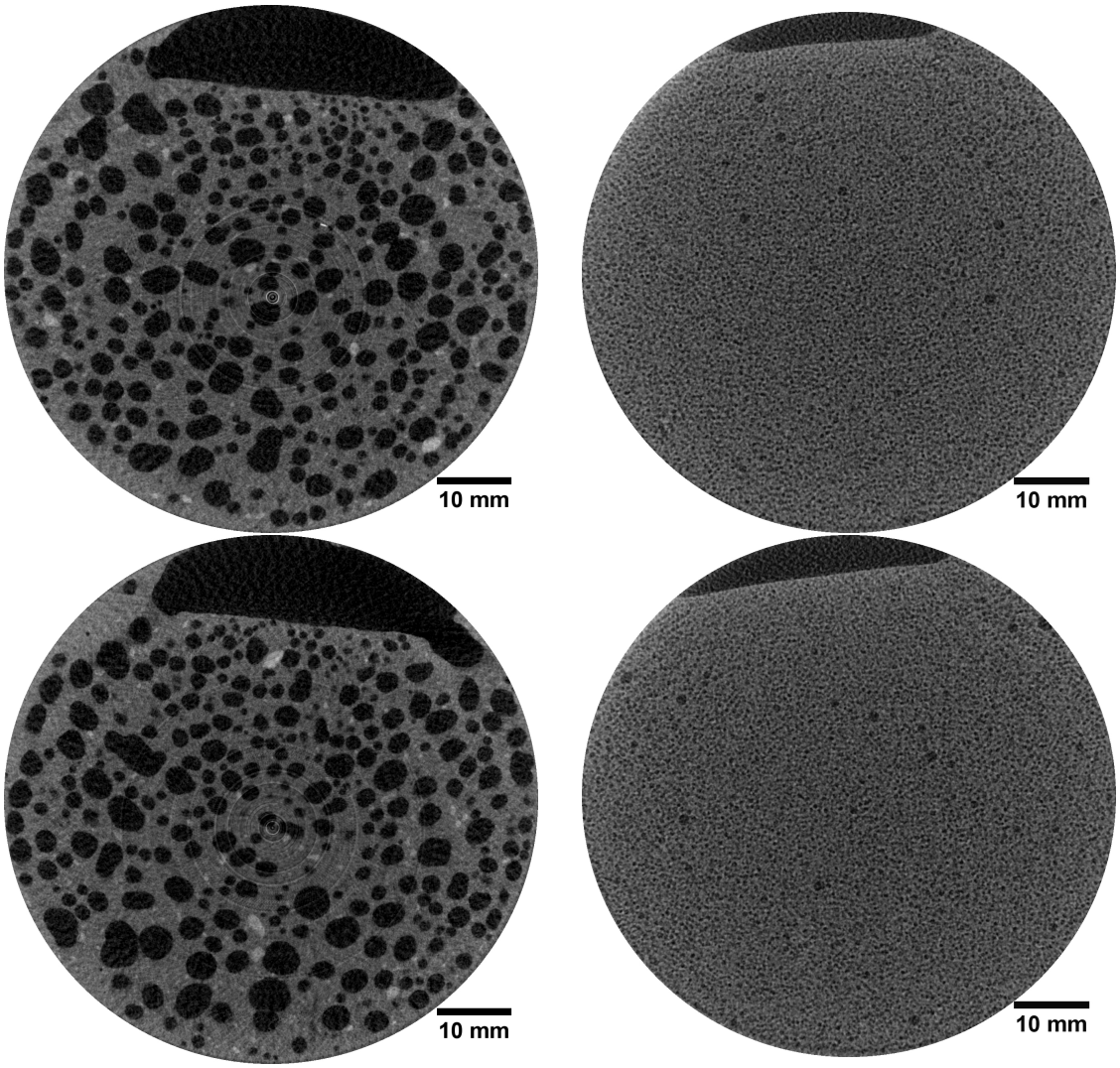

(a) (b)

Figure 6.4: Typical x-ray computed tomography (CT) slices at two axial depths through (a) 30 Pa yields stress CMgS and (b) 30 Pa $Mg(OH)_2$ soft sediment (previously presented in Figure 5.5a) following 6 h *in situ* gas generation; the test materials were imaged within a 7.1 cm diameter side-mounted cylinder using an Inveon PET/CT (Siemens, Germany)

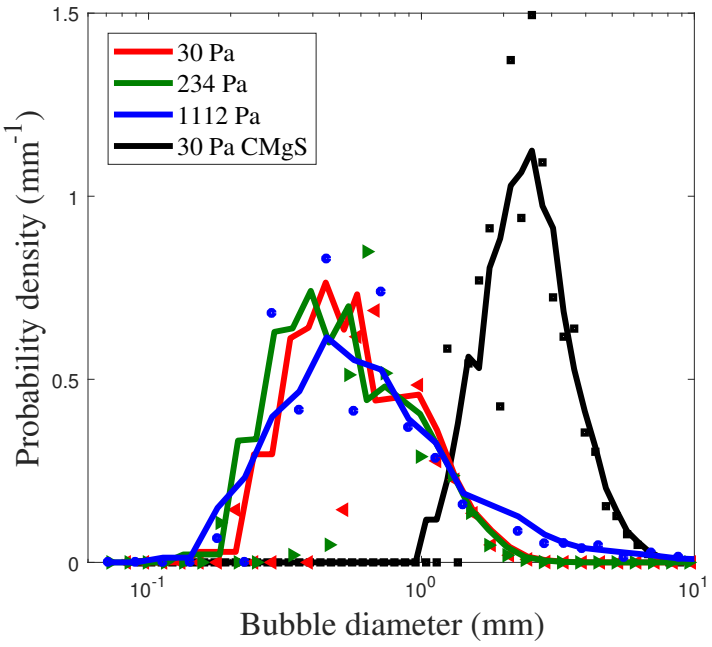

Figure 6.5: Bubble size distributions, translated from chord length distributions, for populations within 30 Pa CMgS and 30, 234 and 1112 Pa $Mg(OH)_2$ soft sediments; the $Mg(OH)_2$ sediment data has been reproduced from Figure 5.6d

bubbles, which comprise the entirety of the 38 % voidage. This represents a significant departure from the bubbles within 30 Pa commercial $Mg(OH)_2$ sediment shown in Figure 6.4b, where millimetre-scale bubbles account for $\ll 1$ % of the total population and partially coalesced sub-millimetre microvoids form networks which span at least several centimetres, but may in fact be continuous on a much larger scale.

Bubble size distributions were obtained by translating chord length distributions by solving the Li & Wilkinson (2005) transformation matrix with a non-negative least squares algorithm (Lawson & Hanson, 1974) as detailed in Section 5.2.2; the BSDs are presented for the 30 Pa yield stress CMgS and three $Mg(OH)_2$ sediments of 30, 234 and 1112 Pa yield stress in Figure 6.5. The disparity in bubble size between the two test materials of equivalent, 30 Pa, yield stress is significantly greater than the impact of enhanced yield stress for the commercial $Mg(OH)_2$ sediments. Given that the two brucite rich test materials share similar chemistry, an equivalent shear yield stress and a similar elastoviscoplastic response, to creep stress with a dominant elastic compliance, the differences in particle size distribution, pore throat size distribution and density heterogeneity within the solid sediment matrix appear to have a significant impact on bubble growth. This implies that while growth of spherical bubbles much larger than the interstitial pores by cavity expansion may be adequately modelled by treating the soft sediment (particles and water) as a single continuous phase (Boudreau, 2012; Wheeler, 1988a), the termination condition for cavity expansion and the ultimate

bubble size distribution may be influenced significantly by the two phase sediment microstructure.

One explanation for the increased fraction of large millimetre-scale bubbles within the CMgS could relate to the coarseness of the PSD. In Brouwer *et al.* (2012), fast x-ray tomography of a fluidised bed reactor revealed that bubble size diminished with an increasing percentage of fine ($\approx 38\,\mu m$) aluminium oxide particles. No explanation for this phenomenon is given in Brouwer *et al.* (2012); however, this could be a result of bubbles' capacity to better support fines in a steric layer at the bubble interface, *armouring* bubbles more effectively and limiting bubble coarsening mechanisms such as coalescence and Ostwald ripening (Pitois *et al.*, 2015; Pugh, 2007). Ostwald ripening is a competitive mechanism for bubble growth (Sherwood & Eduardo Sáez, 2014) whereby large bubbles grow at the expense of smaller neighbouring bubbles which may ultimately disappear altogether. The advantage of this theory is that if the coarser particle size of the CMgS exhibits less effective armouring and therefore diminished resistance to Ostwald ripening, this would explain both the large 2.3 mm median bubble diameter and the substantially diminished population of sub-millimetre microvoids.

A second, and possibly more likely, explanation for the coarseness of the bubble population could relate to the disparity in two-phase microstructure. 30 Pa yield stress CMgS contains 1.6 % w/w fewer solids than an equivalent yield stress of $Mg(OH)_2$. An increased total water content in combination with a high density particle fraction with diminished intra-aggregate water content necessitates a more voluminous network of sedimentary pores. Hence, the CMgS is able to support larger interstitial bubbles before deforming the sediment to create space for further growth. More importantly, the combined MIP and LFNMR analysis also indicated the presence of more constricted pore throats. The extensive microvoid coalescence in the $Mg(OH)_2$ sediments is explained by the pore throats expanding in unison with the host cavity until the capillary entry pressure drops to enable sufficient bubble intrusion for neighbouring bubbles to encounter and coalesce. The more constricted pores within the 30 Pa CMgS demand a more extensive period of cavity expansion before networks can be established across multiple pores. Thus, the CMgS experiences a prolonged period of cavity expansion before growth is interrupted by bubble invasion into adjacent pore-space, resulting in larger bubbles and reduced connectivity.

Furthermore, the large, high density particle fraction appears to play a role in limiting communication between proximate bubbles. In Figure 6.6, magnification in the region of the large, dense particles, previously observed under μCT in Figure 3.5, reveals that the large dense particles act as internal barriers, preventing neighbouring bubbles from approaching. These magnified tomographs also demonstrate deformation in bubble curvature in the viscinity of the large, rigid particles.

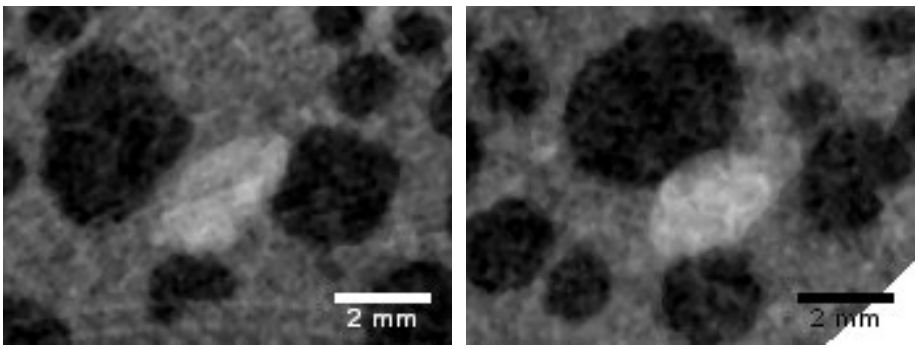

(a) (b)

Figure 6.6: Magnified sections of the micrographs in Figure 6.4a demonstrating the imact of large, dense particles at the growing bubble front

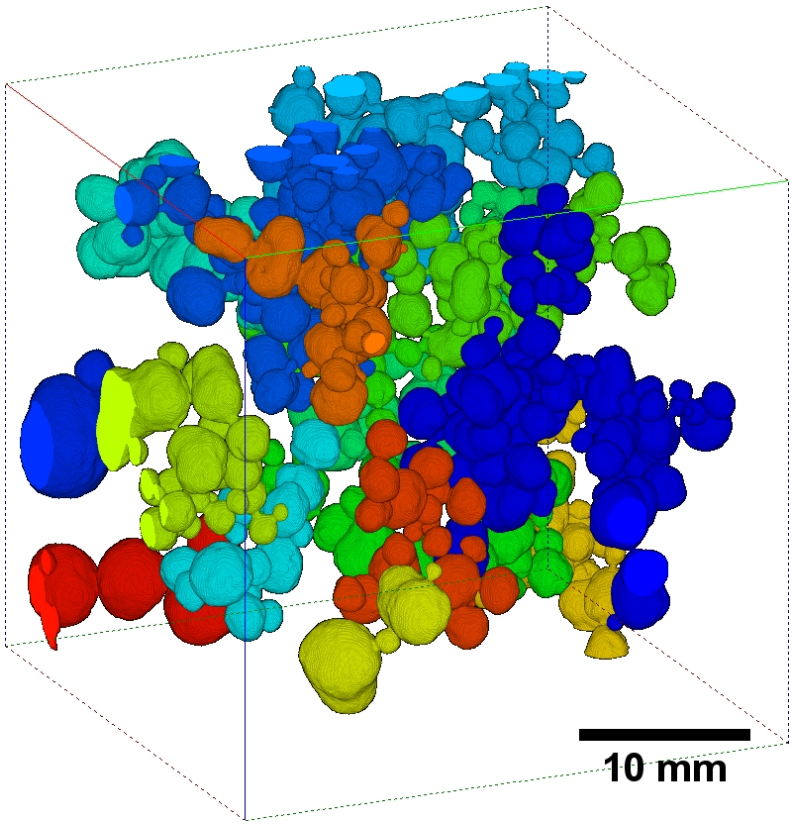

Figure 6.7: Three-dimensional reconstruction of the 16 larges bubble networks within 29 Pa yield stress CMgS; warmer colours represent less voluminous bubble networks

The reduced connectivity between bubbles within the CMgS is demonstrated by Figure 6.7 where the 16 highest volume chains or networks of partially coalesced bubbles within a 32 mm wide cubic FOV are collated and assigned colours ranging in warmth from the largest (blue), to lowest volume (red). Altogether, 1250 distinct bubbles and bubble networks were found within the 32 mm wide FOV. The largest bubble network comprises 42 bubbles, spans 23.2 mm in range and contributes 3.8 % of the total void fraction. Several of the other networks in Figure 6.7 contribute 1-3 % of the voidage within the FOV and contain dozens of coalesced bubbles. This compares with a single network within the 30 Pa $Mg(OH)_2$ sediment which spans the field of view in the x, y and z dimensions and encompasses 99.8 % of the total retained gas volume (discussed in Section 5.3.2).

The significantly coarser bubble population within the CMgS results in a substantially reduced surface area to volume ratio. Not only does this diminish the extent of bubble coalescence but it also increases the resistance to gas exchange between gaseous and aqueous phases. None of the networks within the CMgS provide a continuous pathway through the field of view, indicating that gaseous diffusion through individual networks is a shorter range phenomenon within the CMgS. Combining short range gas diffusion with a greater resistance to volatile exchange between the voidage and pore-water implies a significant reduction in the efficiency of composite gaseous and aqueous diffusion. Thus, the geometry of free gas suggests a significantly diminished rate of gas migration and chronic release from CMgS. to investigate this possibility, the rate of gas release from CMgS is investigated through laboratory-scale gas retention and release tests in Section 6.3.3.

6.3.3 Laboratory scale gas retention tests

Gas generation, retention, and implied release profiles are presented for 11 and 88 Pa yield stress CMgS sediments in Figure 6.8. From the oxygen yield per mole of hydrogen peroxide, it was determined that around a third of the hydrogen peroxide molecules within the 35 % w/w solution had decomposed during storage and so the added peroxide volume was increased to maintain a consistent final volume of gas generation. However, from the gas retention tests in Figure 6.8, it also appears that the peroxide had become less stable, decomposing fully within 2 h rather than 12-16 h in Figure 4.4 or ≈ 8 h during the large scale CT tests in Figure 4.10.

The roughly seven-fold increase in gas generation rate does not constitute a perfect comparison with the experiments in Section 4.3.1. However, the increase in holdup during gas generation is distributed across thousands of < 10 mm bubble sites, and so, whether ≈ 570 ml gas is generated in 2 or 14 h, the strain rates at the bubble-sediment interface remain similarly very small in each instance. Decreasing the timescale of gas generation relative to the timescale of aqueous diffusion

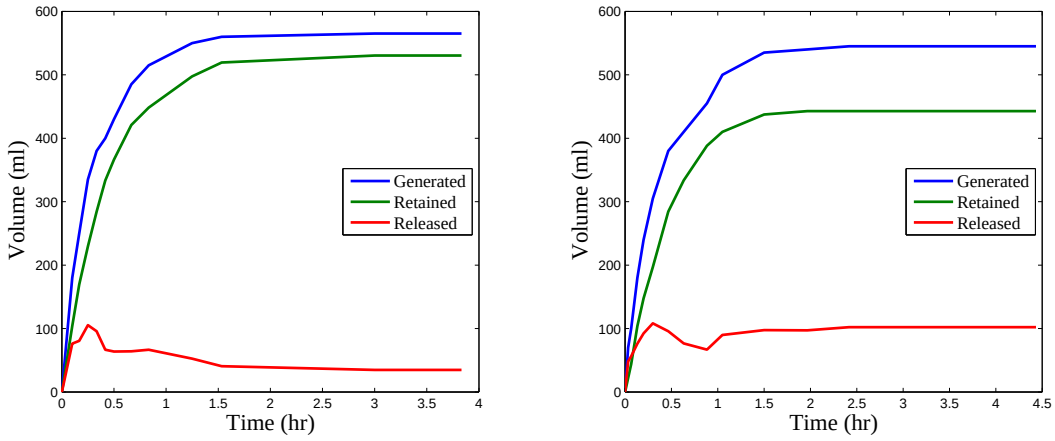

Figure 6.8: Gas generation, retention and implied release profiles during hydrogen peroxide decomposition within 1 l samples of (a) 11 and (b) 88 Pa yield stress CMgS

could impact the bubble size distribution, however the peroxide is homogeneously mixed through the sediment at the commencement of gas generation. Thus, the disparities in microstructure and mechanical behaviour between the two test materials are likely to be far more significant than the impact of faster gas generation in determining the sediment deformation response during bubble growth and the resultant bubble size distribution.

Virtually all the gas generated within the 11 and 88 Pa sediments was retained, causing the beds to swell to large voidages of 38-40 %. Only around 40-100 ml of the 560-580 ml oxygen generated was released from the sediment and no gas release was observed after the first 20 min of gas generation. This contrasts the continuous gas release from 27 Pa yield stress $Mg(OH)_2$ soft sediments at a rate of around 21 ml h^{-1} in Figure 4.4b. The diminished chronic gas release is likely related to the fact the short $\leq$ 23 mm range ganglia of partially coalesced bubbles supported by the CMgS in Figure 6.7 do not enable gas migration rates comparable to the likely vessel-spanning bubble-networks observed within low strength $Mg(OH)_2$ sediments.

Gas can traverse a diffusion length, $L_D = 2\sqrt{Dt}$, equivalent to the 118 mm diameter column radius through a vessel-spanning bubble network with an effective diffusivity of 1×10^{-5} m^2 s^{-1} in approximately 6 min. If the vessel is instead spanned by a 114 mm distance of 4-5 discrete ganglia (of equivalent effective diffusivity), with 4 mm of intermediate sediment with a tortuosity corrected effective diffusivity of 3.5×10^{-10} m^2 s^{-1}, the composite diffusion time increases to 3 h 15 min, longer than the period of gas generation. Furthermore, this composite diffusion time neglects the impact of the reduced interfacial surface area of the coarser bubble population, which will result in slower gas exchange between the aqueous and free gas phases. If the capacity for chronic gas release is dictated, as proposed, by the ratio of the time-scales for gas migration and gas generation, the accelerated gas

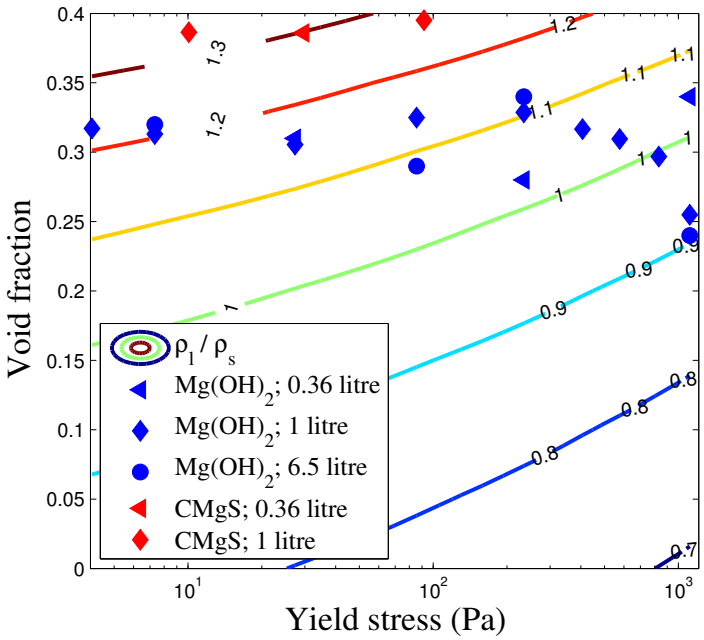

Figure 6.9: Summary of gas holdup within CMgS (red) and commercial $Mg(OH)_2$ (blue) soft sediments across three scales of (1) 0.36 l sideways mounted cylinders, (2) 1 l vertically mounted cylinders and (3) 6.5 l sideways mounted cylinders

generation rate must contribute to the diminished chronic gas release alongside the retarded gas migration through short range discrete ganglia. Thus, the gaseous diffusion model readily accounts for the near-zero gas release rate on a timescale of ≈ 4 h in Figure 6.8.

In the absence of an efficient mechanism for continuous gas release, the 0.36 and 1 l scale CMgS beds in Figure 6.4a and Figure 6.8 respectively exhibit substantial gas holdup, approaching void fractions approaching 0.4. The maximum void fractions for CMgS observed in Figure 6.8 and Figure 6.4a are summarised, alongside with the commercial $Mg(OH)_2$ gas hold up data from Figure 4.5, on a contour plot of bulk sediment density in Figure 6.9.

The large void fractions observed within CMgS, exceeding those observed within the commercial $Mg(OH)_2$ sediments, correspond to a reduction in bulk sediment density to around 25-32 % less than that of water. Hence, based on these 0.36-1 l scale tests, each of these relatively low strength CMgS samples are highly likely to become unstable in the presence of an aqueous supernatant long before the beds swell to their maximum void fraction. Unfortunately, it was not possible with the available CMgS test material to extend these tests into a higher yield stress regime and observe where the gas holdup potential recedes due to the propagation of fracture pathways. The response of high yield stress, physically heterogeneous $Mg(OH)_2$ rich sediments to *in situ* gas generation is crucial to the safe retrieval of CMS from the MSSS, and should represent a focus of future work in preparation

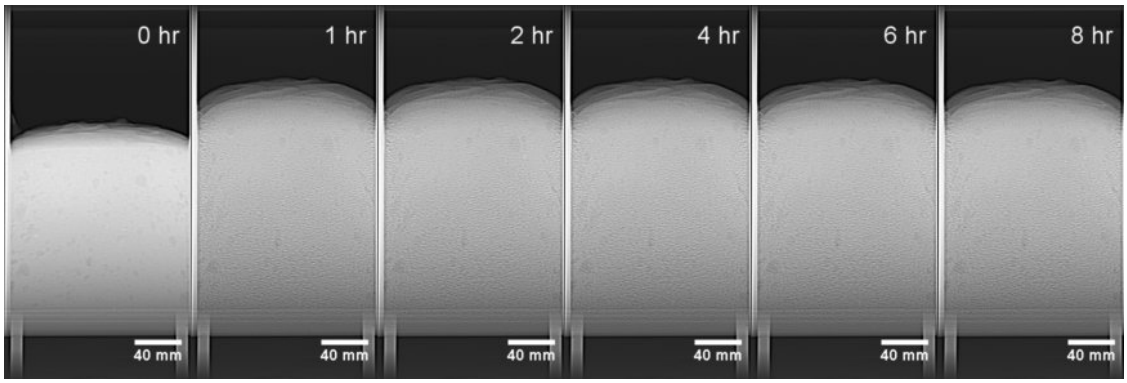

Figure 6.10: Montage of x-ray CT *scout* profiles of 132 Pa CMgS during 8 h *in situ* gas generation

of the decommissioning safety case.

6.3.4 Large scale x-ray computed tomography

A series of side on *scout* profiles of a 132 Pa sediment, captured during the first 8 h after the commencement of gas generation, is shown in Figure 6.10, and demonstrates that bed swell occurred principally within the first hour (mirroring the gas retention tests in Figure 6.8 also performed using the *aged* hydrogen peroxide). The CT scout profiles after 2 h of gas generation confirm that gas holdup had achieved steady state and that bubbles remained stable within the sediment under the quiescent conditions. There was also no evidence of any significant disturbance in the profile or topography of the bed in the images at 0 and 1 h that might explain gas release during the first 20 min gas generation in Figure 6.8.

This large scale CT investigation of bubbles within CMgS differs slightly from the scans of $Mg(OH)_2$ in Section 4.3.2, as the 28 ml volume of peroxide added had not been adjusted to account for the third of the hydrogen peroxide molecules which had perished during storage. Consequently, the gas generating potential was only equivalent to 40 rather than 60 % of the initial bed volume, corresponding to a maximum possible voidage of 28.6 % if all the oxygen generated were retained by the sediment. However, the bed swell observed in Figure 6.10 reveals a maximum voidage of just 15.4 %. Consequently, around 1.4 l of oxygen, over half the total volume generated, was released from the sediment during the period of gas generation without exibiting any disturbances in the profile of the sediment.

X-ray tomographs of a large 250 mm diameter FOV of 132 Pa yield stress CMgS captured 6 h after the commencement of gas generation are presented in Figure 6.11. Despite the significantly lower total void fraction, much more gas appears to be observable at this resolution than within the 86-234 Pa $Mg(OH)_2$ sediments in Figures 4.10b and 4.10c. This is consistent with the coarseness of the bubble population identified within CMgS in Figure 6.5, and supports the theory that the

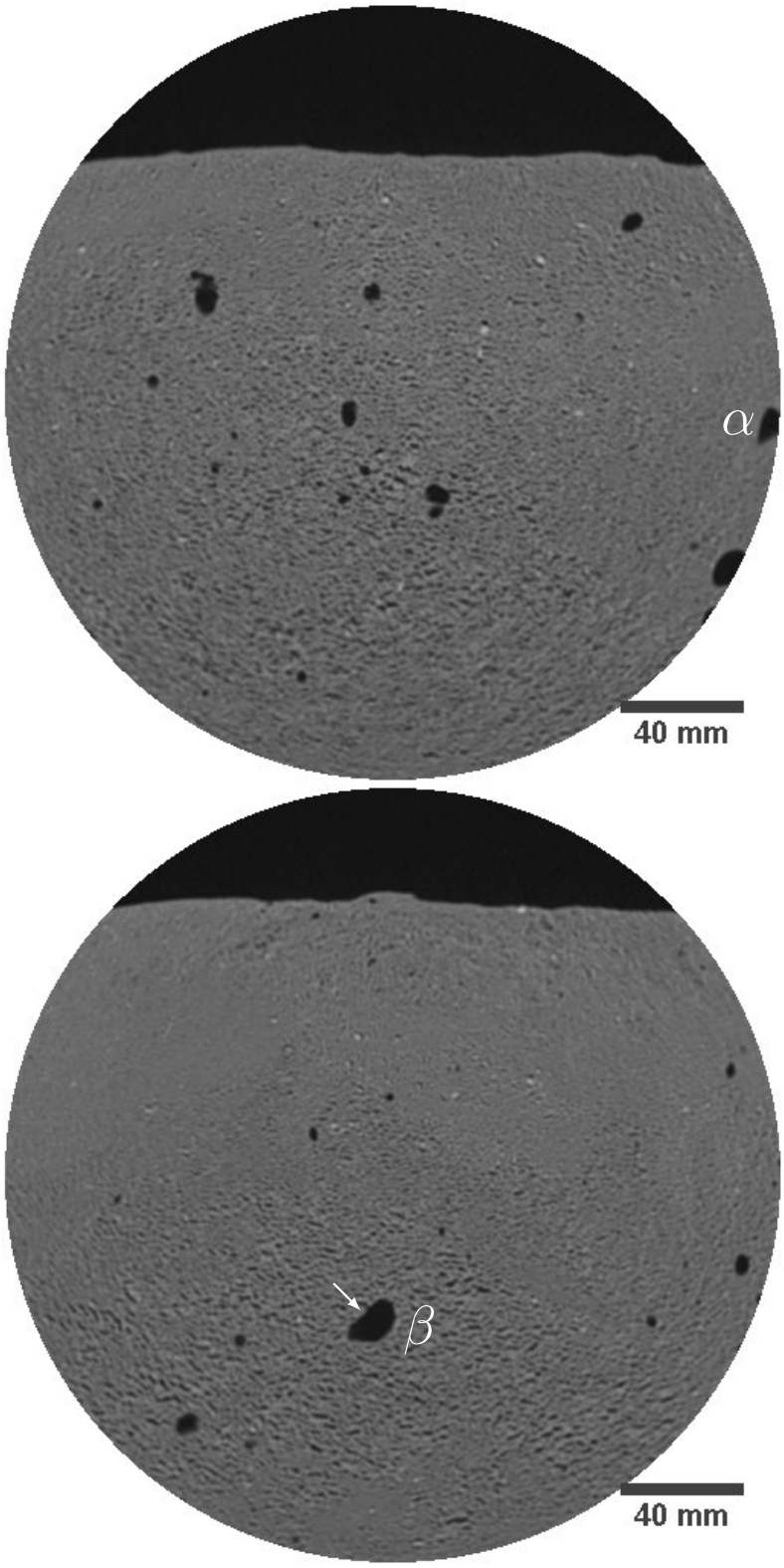

Figure 6.11: Example x-ray tomographs of bubbles retained by 132 Pa CMgS within a 300 mm diameter sideways mounted cylinder

Table 6.3: Contribution of the observable ($d_b > 0.83$ mm) and sub-resolution bubble populations to the total voidage within commercial $Mg(OH)_2$ sediments (reproduced from Table 4.3) and CMgS

τ (Pa)	ν	V_R (ml)	$V_{R,tom}$ (ml)	$100 \times \nu_{tom}$ (%)
7	0.32	2188	0.616	0.03
86	0.29	1829	16.9	0.92
234	0.34	2325	25.1	1.08
1112	0.24	1467	110	7.50
132 **(CMgS)**	0.154	1183	53.8	12.1

coarse particle fraction and narrow sedimentary pore throats promote the growth of larger bubbles. The observable bubble population within this large scale scan corresponds to a void fraction of 0.018, indicating that the mature macro-bubbles, visible at 1.25 mm slice separation and 625 µm pixel resolution, account for 12.1 % of the total voidage, as summarised in Table 6.3. This compares with holdup of < 1.08 % for $Mg(OH)_2$ sediments of comparable (86-238 Pa) shear yield stress.

While the 132 Pa CMgS contains a larger (12.1 %) observable bubble population than equivalent strength $Mg(OH)_2$ sediments, the number of millimetre-scale bubbles remains relatively small in comparison to the 30 Pa sediment in Figure 6.11, where around 95 % of the retained bubbles had equivalent spherical diameters larger than 1.25 mm axial slice separation of these large scale CT tests. Instead, the 132 Pa CMgS most resembles the small scale tomography of 1112 Pa $Mg(OH)_2$ sediment in Figure 5.5c, in that the observable bubble population appears bidisperse. One subset of large bubbles, several millimetres in ESD, appear spheroidal with relatively low aspect ratios, consistent with growth by cavity expansion. A larger volume of bubbles, closer to the 488 µm pixel resolution, appear more elongated, with their longest axis oriented normal to the compressive load.

Given this behaviour, the bulk of the 87.9 % of bubbles below the observable limit are assumed to exist as microcracks, similar to those within the 1112 Pa $Mg(OH)_2$ sediment. Gas migration pathways formed by microcrack coalescence would explain the diminished holdup in comparison to the lower strength CMgS, but would indicates the onset of tensile fracture at much lower yield strength than the $Mg(OH)_2$ sediments. The internal length-scale of the fracture toughness is reportedly dictated by the grain size, resulting in excess bubble pressures for fracture toughness scaling with the inverse square of the particle radius ($\Delta P_f \propto r_p^{-1/2}$) (Jain & Juanes, 2009). Thus, the coarser particle fraction within the CMgS is consistent with an enhanced tendency for fracture. Furthermore, the similarity in pore throat size distribution between 156 Pa CMgS and 1112 Pa $Mg(OH)_2$ in Figure 6.2d also indicates that the microstructure is pivotal in the mechanism for tensile fracture.

The tomographs were thresholded to isolate the visible bubble population for quantitative size and shape analysis, albeit only for the large, mature bubbles.

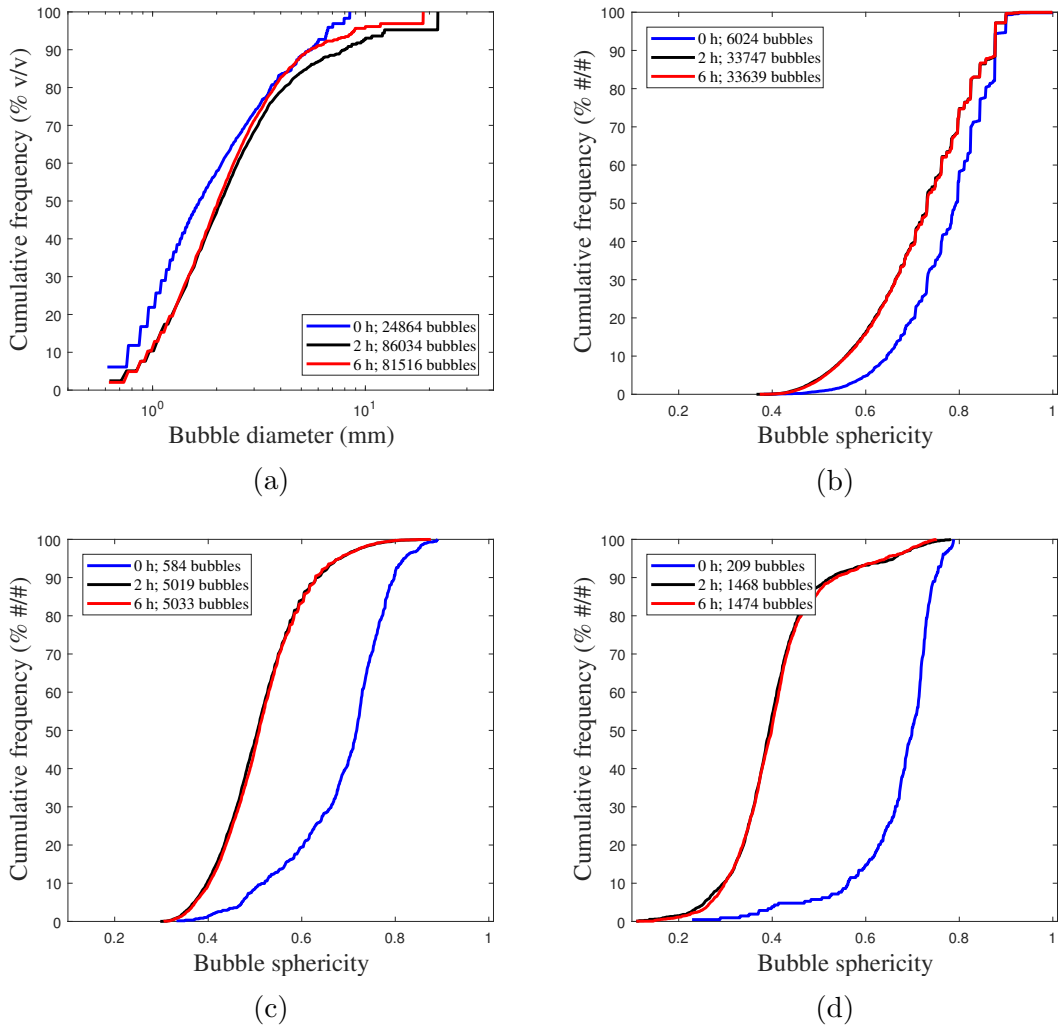

Figure 6.12: Evolution in (a) the size distribution, as well as the number and sphericity of bubbles of (b) 1.42-2.58 mm, (c) 2.58-3.57 mm and (d) > 3.57 mm diameter retained by 132 Pa CMgS

Individual bubbles were identified by connecting adjacent low-radiodensity thresholded voxels using the algorithm from Bolte & Cordelières (2006). Histograms of the equivalent spherical bubble diameters and digital sphericities (see eq. (4.6)) are presented in Figure 6.12.

Unsurprisingly, given the accelerated gas generation kinetics in Figure 6.8 and the fact that bed swell is limited to the first 1-2 h in Figure 6.10, the bubble population undergoes significant evolution within the first 2 h and negligible change between 2 and 6 h. From the bubble size analysis in Figure 6.12a, some large millimetre-scale bubbles were able to form very quickly during the ≈ 10 min period between first introduction of the hydrogen peroxide and conducting the first scan at '0 h'. Within the first 2 h, the largest (8 mm) bubbles grow up to 22 mm ESD, representing a 21-fold increase in volume. However, Figure 6.11 demonstrates that these millimetre-scale macrobubbles are relatively sparse. From Figure 6.12a, bubbles larger than 4 mm contribute less than 20 % of the observable free gas volume

after 2 h gas generation, and therefore only around 2.4 % of the total holdup. During the same 2 h period, the total number of millimetre-scale observable bubbles (indicated in the legend) multiplies by a factor of 3.5, which also accounts for very small portion of the observed bed swell in Figure 6.10. Consequently, as with the $Mg(OH)_2$ soft sediments, bed swell is almost entirely dictated by the increase in the population of bubbles with at least one dimension close to or smaller than the 1.25 mm slice separation, rather than by maturing of fine bubbles to millimetre dimensions or by coarsening of the largest bubbles to centimetre-scale diameters.

Shape analysis of the observable bubble population is conducted separately for different size ranges, or grades, of bubbles in Figures 6.12b to 6.12d. Unfortunately, these size brackets only account for the large cavity expanding bubbles such as those labelled 'α' and 'β'; the finer, more distorted bubbles were too close to the imaging resolution and were comprised of too few voxels to represent their shape accurately. The three size ranges of bubbles (1.42-2.58 , 2.58-3.57 and > 3.57 mm ESD) demonstrate similarly high sphericities at the initial condition. Thereafter, all of these millimetre scale bubbles appear to diminish in sphericity over time. This reduction in sphericity with bubble maturity and increased residence time is increasingly significant for the larger grades of bubble.

Following the observation of a notable viscous compliance during the creep rheology tests in Figure 3.13, which persists long after the initial and delayed elastic compliances have diminished, it was postulated that the opposite evolution in bubble shape might occur, whereby chronic viscous deformation at the bubble-sediment interface might promote bubbles to become more spherical over protracted residence times. Instead, the evolution in bubble shape is exclusively limited to the growth regime; after the first 2 h, once gas generation is exhausted, there does not appear to be any creep deformation at the bubble-sediment interface. Thus, the sediment response to bubble expansion appears to be dominantly elastic in nature, even in response to very low strain rates over periods of hours.

The departure of bubbles away from the initial high sphericity condition with increased residence time still requires explanation. The evolution in BSD between 0 and 2 h in Figure 6.12a offers a partial explanation. The BSD within the smallest (1.42-2.58) and largest (> 3.57 mm) size brackets shifts in favour of a larger bubble size, particularly in the latter instance. It is no surprise that the largest bubbles would be less spherical than the bubbles closer to a millimetre in scale. Smaller bubbles are associated with greater Laplace pressures which promotes spherical curvature and as the bubble grows the yield stress increasingly dominates the surface tension causing bubbles to distort within viscoplastic materials (Dubash & Frigaard, 2004). However, there is negligible change in the BSD within the 2.58-3.57 size bracket which might explain the evolution in bubble shape in Figure 6.12c.

It has been discussed that, within large bubbles, the pressure differential across the height of the bubble can cause stratification of gas towards the top of the bubble, preferential growth at the shallow surface and compression at the bubble tail, causing the bubble to assume an inverted teardrop geometry over time (Algar *et al.*, 2011a). This behaviour is again observed in the bubble labelled 'α' in Figure 6.11 and would account for a reduction in sphericity within the > 3.57 mm subset with increased residence time; however, this bubble shape does not appear to be typical of the large bubble population within the CMgS. The largest bubble observed within these two particular cross-sections, labelled 'β', does not narrow at the tail, instead the bubble encounters greatest resistance to cavity expansion nearer its shallow surface, along the vector indicated by the white arrow. Thus, the anisotropy of the sediment stress-field appears to bear greater influence on bubble shape than the stratification of internal bubble pressure.

A more likely cause of the reduction in bubble sphericity with increased residence time relates to the fact the sediment matrix is deformed at the interface of every growing bubble and so the stress distribution through the sediment matrix evolves significantly throughout the period of bed swell. Hence, sediment displacement at the interface of one growing bubble can induce deformation at the interface of another. This is especially likely to be the case in the vicinity of the large high density heterogeneities within the solid skeleton, as demonstrated by Figure 6.6. Consequently, the longer a bubble resides within an expanding sediment, the more likely the evolution in the sediment structure will in turn deform bubbles away from their spherical initial condition.

Given that the small scale clinical CT imaging in Figure 6.4a and Figure 6.7 demonstrated discrete individual bubbles and short range ganglia of coalesced bubbles, as opposed to the apparently continuous free gas within 30-1112 Pa $Mg(OH)_2$ sediments, the hyperstacking process outlined in Section 4.2.2 is used once more to track the mobility of these discrete bubble features.

Bubble mobility

Bubbles retained by 132 Pa yield stress CMgS are tracked over 5 min intervals within a small FOV and over a 2 h interval within a large FOV in Figure 6.13a and Figure 6.13b respectively. The largest ($d_b \approx 8.5$ mm) bubble within Figure 6.13a, labelled 'γ', gradually rises by 23 mm over the course of 15 min, slowly narrowing at the tail in the process. The same bubble is also identified within the larger FOV after 2 h gas generation and is shown to have risen by 35 mm; a faint orange silhouette at the shallow surface, capturing the bubble after 6 h demonstrates that the bubble remained essentially static from 2-6 h. Several other much smaller ($1 < d_b < 3$ mm)

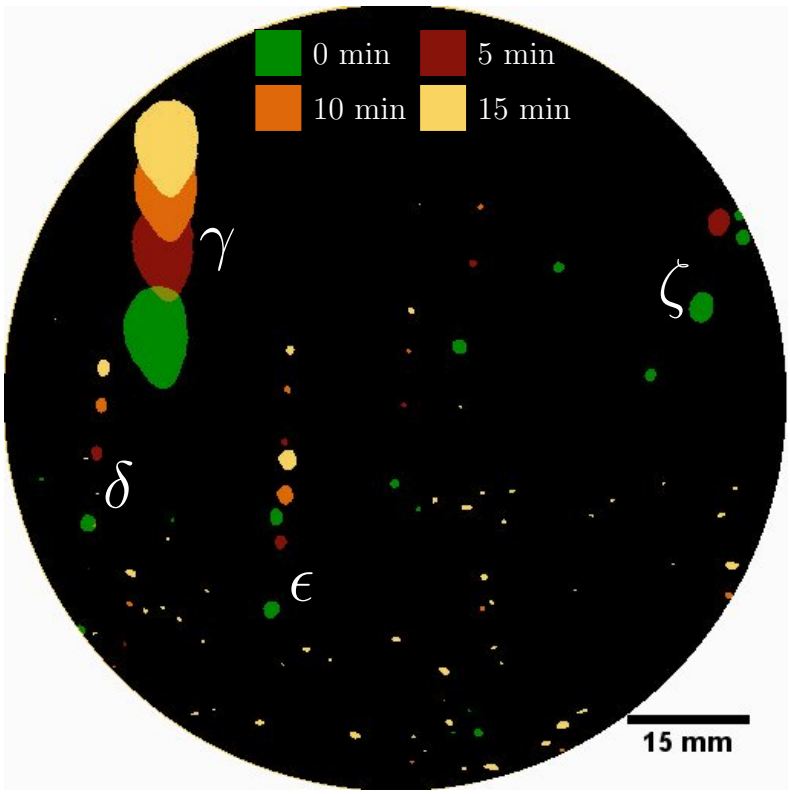

(a)

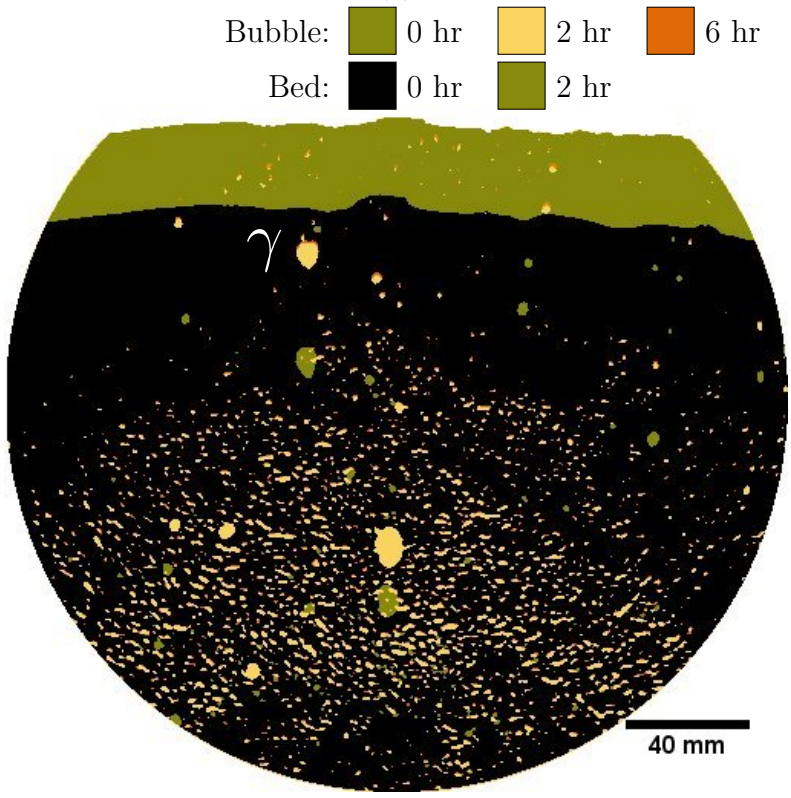

(b)

Figure 6.13: Flattened *hyperstacks* of x-ray tomographs at (a) 5 min intervals for the first 15 min gas generation and (b) a larger FOV at 0, 2 and 6 h gas generation for 132 Pa yield stress CMgS within a 300 mm diameter cylinder

bubbles labelled 'δ', 'ϵ' and 'ζ' rise by almost identical distances over the same period. Hence, as with the $Mg(OH)_2$ sediment hyperstacks in Figure 4.12, the slow and decelerating bubble rise, independent of bubble size or buoyant stress, appears to correspond to bulk bed expansion rather than evidencing bubble migration by ebullition or burrowing (Dorgan *et al.*, 2005).

Thus, the 132 Pa CMgS lies above the ebullient yield stress regime, and yet around 1.4 l gas is able to escape the sediment. In Figure 6.13b it becomes clearer than in the grey-scale images that the observable bubbles at 2 h are concentrated within the deeper half of the bed and largely consist of laterally oriented fractures, similar to the fine cracks observed within the 1112 Pa commercial $Mg(OH)_2$ in Figure 5.5c. These observable cracks, up to 12 mm in length and with aspect ratios as large as 10, are typically separated by distances of less than three pixels, or $<$ 1.9 mm. The short separation distances between observable cracks, combined with the knowledge that 88 % of the holdup exists below the detection limit, provides a strong indication that connected fracture pathways within the deeper half of the sediment could span the 300 mm diameter side mounted cylinder to facilitate chronic release of the excess 1.4 l oxygen not held up within the bed.

On comparison with the smaller scale CT scans in Figure 6.4a, the increase in yield stress from 30 to 132 Pa combined with an increase in scale from 0.36 to 6.5 l manifests in a significant increase in the range of connected bubble-networks, sufficient to facilitate chronic gas release. The increased load at depths below 110 mm appears to greatly impact the mode of bubble growth. At deeper regions within the sediment, cavity expansion appears significantly inhibited in the direction of maximum compressive stress, forcing bubbles to create space for growth normal to gravity, representing another point of comparison with the 1112 Pa $Mg(OH)_2$ sediment, further indicating that microstructure may be more relevant to the onset of tensile fracture than the sediment strength. Thus, attempts to model strain at the bubble-sediment interface which treat the sediment (solids and water) as a single continuous phase and experiments conducted using clear, homogeneous elastoviscoplastic gels are unlikely to capture the full complexity of bubble growth.

The broader particle size distribution, constricted pore throats and enhanced heterogeneity in local density distribution through CMgS, thought to be more representative of real CMS, appears to manifest in fracture propagation within less consolidated sediments. Since low tortuosity pathways of coalesced cracks promote efficient lateral gas diffusion and chronic release, this suggests that the yield stress regime susceptible to large holdup and partial rollover is also narrower than indicated by the $Mg(OH)_2$ sediments. The evolution in bubble shape in favour of high aspect ratio cracks with increased depth, even over scales of just 110 mm, implies that further scale up to the 1 m^3 skips within the 3 m^3 modular storage containers may be significant in establishing further avenues for slow continuous

gas release. This demonstrates the value in conducting additional process-scale trials before decanting MSSS waste into the modular storage containers.

6.4 Conclusions

A test material of consolidated corroded magnesium metal, CMgS, which was found to differ from the commercial $Mg(OH)_2$ test material, used to study gas retention in Chapter 4 and Chapter 5, by its coarse particle fraction, elevated shear yield stresses at low solids concentrations and greater heterogeneity in its local density distribution, was also revealed from LFNMR analysis to exhibit more constricted sedimentary pore throats. These disparities in sediment properties were found to have a significant impact on subsequent bubble growth. 30 Pa yield stress CMgS was shown to exclusively retain coarse 1-8 mm equivalent spherical diameter bubbles and was bereft of the substantial population of sub-millimetre micro-voids which account for over 98 % of gas holdup within an equivalent yield stress sample of commercial $Mg(OH)_2$. Thus, consolidated sediments of similar chemistry, mechanical strength and creep behaviour exhibited significantly different deformation behaviour during bubble growth. It was concluded that, while modelling the sediment (solids and pore water) as a single continuous phase appears adequate for predicting growth of large spherical bubbles by cavity expansion, the two phase microstructure is significant in determining the the termination of cavity expansion due to intrusion through expanded pore throats and partial coalescence between neighbouring bubbles. Consequently, the sediment microstructure greatly impacts both the ultimate bubble size distribution and connectivity between bubbles.

On observing the coarse bubble size distribution, it was proposed that (1) the coarse particle fraction within CMgS may poorly armour bubbles in a steric layer at the bubble surface, thereby diminishing the resistance to bubble coarsening by Ostwald ripening, and (2) that the larger pore volume and more constricted pore throats within CMgS may result in an extended period of cavity expansion before neighbouring bubbles come into contact. The second phenomenon, combined with the diminished interfacial surface area within the bed, resulted in much less extensive bubble networks of up to 42 bubbles, spanning up to 23 mm and comprising < 3.8 % of the total voidage. Composite diffusion through the aqueous phase and these short range ganglia could not account for the same extent of gas migration and chronic release on the time-scale of gas generation as the continuous vessel-spanning networks of free gas within the $Mg(OH)_2$ sediments. Consequently, 0.36-1 l scale CMgS beds swelled to substantial void fractions approaching 40 %, indicating a high probability of acute gas release by partial rollover.

Increasing the experimental scale to 6.5 l and the shear yield stress to 132 Pa saw lateral fractures, previously observed only within kiloPascal strength $Mg(OH)_2$, propagate through the deeper regions of the bed. Implied connectivity between proximate fracture sites and the 88 % of free gas below the observable detection limit would account for the chronic release of 1.4 l O_2 observed at this increased scale and yield stress. Thus, permeable pathways of coalesced microcracks appear plausible within the physically heterogeneous CMgS under substantially less consolidated conditions than the kiloPascal strength $Mg(OH)_2$ sediments in Chapter 5. The onset of fracture at low consolidation is explalined by the similarity in pore throat size distribution between 156 Pa CMgS and 1112 Pa $Mg(OH)_2$, as the microstructure appears to dictate the internal length-scale of the sediment fracture toughness. Establishing chronic release pathways through coalesced fractures within relatively poorly consolidated CMgS represents good news for mitigating against acute flammable gas release as it implies a much narrower yield stress regime susceptible to the high holdup conditions, necessary to achieve neutral buoyancy with an aqueous supernatant under quiescent conditions, than the commercial $Mg(OH)_2$ sediments.

Chapter 7

Conclusions

Nuclear legacy waste sludge, such as that stored at Sellafield, UK and Hanford, USA experiences *in situ* hydrogen generation due to corrosion reactions and radiolysis. Flammable gas bubbles can be immobilised by the strength of the consolidated sediment matrix resulting in bed expansion and potential for acute flammable gas release. This phenomenon has been successfully mimicked at laboratory scale using hydrogen peroxide decomposition to form oxygen bubbles within fine-grained ($\bar{d}_p \approx 4\,\mu m$ diameter) $Mg(OH)_2$ rich sediments across a broad (7-1112 Pa) range of shear yield stress conditions. Sediments of up to 800 Pa yield stress were shown to exhibit gas holdup to voidages of $> 28\,\%$, sufficient to become buoyant with respect to an aqueous supernatant and raising the potential for Rayleigh-Taylor instabilities. Gas holdup diminished within kiloPascal strength sediments where bubbles were observed to grow by induction of large lateral fractures, enabling gas transport towards the test cylinder walls for release.

Litre-scale gas retention tests revealed chronic gas release at relatively constant rates in excess of $21\,ml\,h^{-1}$. Conversely, time lapse x-ray tomography revealed that the largest bubbles ($\approx 7\,mm$ diameter) remained static for periods of several hours within very low strength ($\tau = 7\,Pa$) sediment. Thus, the ratio of the bubbles' buoyant stress to the sediment yield strength appears unfavourable to bubble rise even under poorly consolidated conditions. The absence of vertical bubble motion by ebullition or by fracture burrowing raises the question as to how gas is able to escape from sediments which lack the strength to support deep drainage channels. The millimetre-scale bubbles observed through large-scale (6.5 l) clinical tomography represent $< 1.08\,\%$ of the largest bubbles within 7-238 Pa $Mg(OH)_2$ sediments, while $92.5\,\%$ of bubbles within 1112 Pa sediment were below the observable detection limit. Hence, the long-standing enigma of how gas is released from sediments which are too strong for buoyant bubble migration, but insufficiently strong to promote fracture or support deep drainage channels, was deemed to involve the population of microvoids rendered invisible at this experimental scale.

Small-scale (0.4 l) clinical tomography imaging revealed the entire bubble populations down to their 70 µm diameter minimum. The smallest bubbles were at least 50 times larger than the water-filled pores observed by cryo-FIB microscopy, indicating growth by cavity expansion. Partial coalescence between neighbouring sub-millimetre microvoids resulted in the formation of extensive networks which spanned the 32 mm field of view and comprised > 98 % of the retained free gas, thereby providing pathways for gas migration towards the container walls and bed surface. Lattice-Boltzmann method simulations revealed these bubble networks to be highly pervious to gas, with permeabilities of 10.1-151.6 $\times 10^{-12}$ m^2, potentially enabling hydrogen stratification towards the shallow surface of the bed, driven by the increase in ambient pressure field with sediment depth. Using Monte Carlo based diffusion simulations, effective diffusivities for hydrogen through the bubble networks were found to be in the 3.7-12.5 $\times 10^{-5}$ m^2 s^{-1} range, around four orders of magnitude larger than the diffusivity in water, thereby also enabling enhanced gas migration normal to the lithostatic pressure gradient.

The additional coarse particle fractions of brucite (200-1000 µm) and dense crushed slate (≈ 1 mm) within a second 'corroded magnesium sludge' (CMgS) test material manifested in a number of differences in the sediment microstructure and shear response behaviour. The more physically heterogeneous CMgS exhibited enhanced shear yield stresses in the 30-40 % w/w concentration range, while a combination of low field nuclear magnetic resonance and mercury intrusion porosimetry revealed substantially more constricted pore throat size distribution, typical of a much more consolidated fine brucite sediments. These behavioural differences had significant implications for the characteristics of the retained bubble population, leading to growth of a narrower and coarser bubble size distribution in the 1-8 mm range and substantially reduced connectivity between neighbouring bubbles at low yield strength.

The large bubble size distribution could be explained by enhanced Ostwald ripening, whereby large bubbles grow at the expense of smaller proximate bubbles, possibly due to poor *armouring* of bubbles by the coarse particle fraction. Furthermore, the constricted pore throats may extend the duration of cavity expansion before neighbouring bubbles are able to interact, thus forming large discrete bubbles. A combination of (1) the constricted sedimentary pore throats, (2) the lower bubble surface area to volume ratio and (3) the large dense slate particles forming obstacles to bubble communication explains the reduced connectivity between bubbles. Consequently, rather than forming extensive, seemingly continuous, vessel-spanning bubble networks, bubbles within the CMgS formed short-range discrete ganglia of < 42 partially coalesced bubbles, spanning only around 23 mm in range. Discrete ganglia may enable longer-range gas transport through (1) dynamic connectivity between ganglia driven by expansion of the retained free gas in

response to falling atmospheric pressure, (2) through the continuous exchange of volatiles between the aqueous and gas phases and (3) ganglia migration through the sediment by Haines jumps, albeit at a slower rate than gas migration through continuous vessel-spanning bubble networks.

The capacity for sediments to swell to large void fractions, which present the greatest risk of acute flammable gas release, represents a balance between the rates of gas generation and chronic gas release. Chronic gas release from low-intermediate strength ($10\,\mathrm{Pa} \lesssim \tau \gtrsim 1\,\mathrm{kPa}$) sediments appears to be dictated by the establishment of permeable gas transport pathways, observed here for the first time. Non-homogeneous, or localised, *in situ* gas generation can enable formation of gas transport pathways at lower holdup ($\approx 7\,\%$), thereby limiting subsequent bed swell. Equally, coalescence between fine lateral fractures promotes the formation low-tortuosity pathways for efficient gas transport, inhibiting bed swell to the neutral buoyancy condition. Tensile fracture was observed within kiloPascal strength $Mg(OH)_2$ and less consolidated (132 Pa strength) CMgS, which shared very similar pore throat size distributions, indicating that microstructure dictates the internal length-scale of the fracture toughness. Bubble aspect ratios appear to increase with sediment strength and depth, thereby promoting bubble network propagation and gas transport in the direction of the longer bubble axis, typically normal to the compressive load. Conversely, large spherical bubbles which grow by cavity expansion and mature by Ostwald ripening tend to exhibit poor connectivity, and thus facilitate slower gas migration.

The corroded Magnox sludge currently within the Magnox Swarf Storage Silos is likely to be highly consolidated, with heterogeneous *in situ* gas generation promoted in the vicinity of uncorroded metallic swarf; these characteristics have been consistent with a reduced risk of acute flammable gas release based on the laboratory scale experiments presented. While mobilisation of the waste during decommissioning may result in lower yield stress conditions prone to increased gas holdup, the risk of acute gas release is likely to be mitigated by transfer to $1\,\mathrm{m}^3$ skips due to the reduced buoyant potential energy of sediments stored beneath shallow supernatant layers. However, evacuating the silos into portable containers increases the risk of stress-induced gas releases from physical perturbations during transport, presenting new engineering challenges which require further investigation.

Chapter 8

Future work

The expense and urgency of the task to evacuate legacy buildings at Sellafield, combined with the comparatively small amount of published data in this field, justifies further research into the various engineering challenges presented by *in situ* hydrogen generation in radioactive sludge waste. The contribution of methane release from marine sediments to global greenhouse gas emissions provides a longer term motivation for further fundamental research into the physics of bubble growth within consolidated soft sediments. Based on the findings of this research, some recommended areas for continued research are outlined below:

1. Throughout this research, it has been assumed that the chemical composition of gas retained by consolidated sediments has a negligible impact on the physics of bubble growth (Boudreau, 2012). This assumption has justified the use of hydrogen peroxide decomposition, forming oxygen, to mimic hydrogen bubble growth. The evolution in internal bubble pressure, the deformation behaviour at the bubble-sediment interface, and the driving force for buoyant migration are all seemingly independent of the gas composition. However, the disparity in solubility between oxygen and hydrogen may impact bubble coarsening mechanisms such as Ostwald ripening, and the size distribution of bubbles appears to be significant in determining the range of permeable gas transport pathways for chronic release. Ultra-fine metallic powders have been used by Gauglitz *et al.* (2012) to generate *in situ* hydrogen by corrosion within kaolin test materials on an accelerated time-scale. A similar approach would provide a useful validation of gas retention within $Mg(OH)_2$ sediments, but would require the identification of a corrosion reaction which does not passivate at elevated pH (≈ 10).

2. Gas retention tests have been performed at 0.36-6.5 l scale, with some of the larger scale experiments (see Figures 4.10d and 6.11) revealing an evolution in bubble aspect ratio with increased sediment depth. Thus, there appears to be

value in further work investigating the impact of scale-up on the sediments' capacity for bed swell. Having established a relatively cheap, repeatable and safe approach for mimicking *in situ* bubble growth within $Mg(OH)_2$ sediments, the methodology could quite easily be extended to the scale of the $1\,m^3$ skips to which the CMS waste is due to be transferred and temporarily stored.

3. Chemically similar test materials of equivalent yield stress have been shown to demonstrate some fundamental differences in the characteristics of their retained bubble populations, thought to be due to physical disparities in particle size distribution and microstructure. Cryo-FIB microscopy has shown promise for visualisation of sedimentary pores, however the instrument was only available at the very end of this research. A preliminary investigation has suggested it be possible to achieve a more comprehensive characterisation of the microstructure by using the ion beam to etch back the vertical FIB cross-sections, as shown in Figures 5.4c and 6.3c, in increments of $\approx 20\,nm$ to generate a stack of parallel slices through the sediment. Not only would this enable full three-dimensional analysis of the pore throat and body size distributions, but Monte Carlo diffusion simulations, as presented in Section 5.3.4, through the thresholded pore-space could enable characterisation of the tortuosity corrected aqueous diffusion coefficients for various solutes. This would be highly useful for predicting diffusion controlled bubble growth and gas migration by composite diffusion through the gaseous and aqueous phases. This could also represent a breakthrough in effluent treatment, by enabling prediction of the rate of exchange of water soluble fission products, such as caesium and strontium, between the consolidated bed and the supernatant.

4. A broad range of shear yield strengths have been identified where consolidated $Mg(OH)_2$ sediments support large, near spherical bubbles many times greater than the water-filled sedimentary pores, consistent with growth by cavity expansion. Currently, there appears to be a lack of experimental validation for the theoretical cavity expansion models used to predict strain at the bubble-sediment interface in response to increasing internal bubble pressure (Chadwick, 1959), or fluctuations in atmospheric pressure (Terrones & Gauglitz, 2003), summarised in Section 2.7.1. Measuring internal bubble pressure during growth simply requires an in line pressure transducer between an injection mechanism, such as a syringe pump, and an orifice submerged within the test material, similar to the method outlined by Johnson *et al.* (2002) to investigate pressure changes during bubble growth by tensile fracture. Initial experimentation using clear viscoplastic gels would enable

characterisation of the strain response, or bubble expansion, using a high speed camera. If a birefringent gel such as gelatin is used, cross-polarised light could be employed to observe the stress distribution through the gel in response to bubble growth (Dorgan *et al.*, 2005). Ultimately, this method could be extended to bubbles in two phase optically opaque consolidated soft sediments, however synchrotron tomography might be necessary to observe bubble growth to sufficient spatial and temporal resolution. Furthermore, introduction of a second submerged orifice could potentially enable determination of the evolution in internal bubble pressure during partial coalescence, shedding light on the propagation of gas transport pathways through consolidated sediments.

References

Abbasi, H. & Evans, J.W. (1983). Diffusion of gases in porous solids: Monte Carlo simulations in the Knudsen and ordinary diffusion regimes. *AIChE Journal*, **29**, 617–624. 4, 105

Abegg, F. & Anderson, A.L. (1997). The acoustic turbid layer in muddy sediments of Eckenfoerde Bay, Western Baltic: methane concentration, saturation and bubble characteristics. *Marine Geology*, **137**, 137–147. 2, 28

Adi, H., Larson, I., Chiou, H., Young, P., Traini, D. & Stewart, P. (2006). Agglomerate strength and dispersion of salmeterol xinafoate from powder mixtures for inhalation. *Pharmaceutical Research*, **23**, 2556–2565. 44

Aktas, Z., Cilliers, J.J. & Banford, A.W. (2008). Dynamic froth stability: Particle size, airflow rate and conditioning time effects. *International Journal of Mineral Processing*, **87**, 65–71. 48, 63

Alderman, N.J., Meeten, G.H. & Sherwood, J.D. (1991). Vane rheometry of bentonite gels. *Journal of Non-Newtonian Fluid Mechanics*, **39**, 291–310. 61

Algar, C.K. & Boudreau, B.P. (2010). Stability of bubbles in a linear elastic medium: Implications for bubble growth in marine sediments. *Journal of Geophysical Research: Earth Surface*, **115**, F03012. 14, 23, 39, 85, 87, 95, 102

Algar, C.K., Boudreau, B.P. & Barry, M.A. (2011a). Initial rise of bubbles in cohesive sediments by a process of viscoelastic fracture. *Journal of Geophysical Research: Solid Earth*, **116**, B04207. 1, 2, 22, 25, 28, 34, 35, 39, 88, 92, 95, 98, 118, 145

Algar, C.K., Boudreau, B.P. & Barry, M.A. (2011b). Release of multiple bubbles from cohesive sediments. *Geophysical Research Letters*, **38**, L08606. 34

Ali, S.A., Gauglitz, P.A. & Rossen, W.R. (2000). Stability of solids-coated liquid layers between bubbles. *Industrial and Engineering Chemistry Research*, **39**, 2742–2745. 37, 46, 64

Allemann, R. (1992). Physical mechanisms contributing to the episodic gas release from Hanford tank 241-SY-101. In *Presented at High Level Radioactive Waste Management, Las Vegas*, vol. 1992. x, 2, 10, 11, 12, 18, 37, 39, 78, 94

Amin, S. & Jayson, G.G. (1996). Humic substance uptake by hydrotalcites and PILCs. *Water Research*, **30**, 299–306. 9, 65

Anderson, A.L., Abegg, F., Hawkins, J.A., Duncan, M.E. & Lyons, A.P. (1998). Bubble populations and acoustic interaction with the gassy floor of Eckernforde Bay. *Continental Shelf Research*, **18**, 1807–1838. 19, 111

Anovitz, L.M. & Cole, D.R. (2015). Characterization and analysis of porosity and pore structures. *Reviews in Mineralogy and Geochemistry*, **80**, 61–164. 100, 107, 109, 129

Astarita, G. & Apuzzo, G. (1965). Motion of gas bubbles in non-Newtonian liquids. *AIChE Journal*, **11**, 815–820. 19, 32

Atapattu, D.D., Chhabra, R.P. & Uhlherr, P.H.T. (1995). Creeping sphere motion in Herschel-Bulkley fluids: flow field and drag. *Journal of Non-Newtonian Fluid Mechanics*, **59**, 245–265. 32, 33, 41, 75, 85, 90

Averill, A.F., Ingram, J.M., Battersby, P. & Holborn, P.G. (2014). Ignition of flammable hydrogen/air mixtures by mechanical stimuli. Part 1: Ignition with clean metal surfaces sliding under high load conditions. *International Journal of Hydrogen Energy*, **39**, 18472–18479. 13

Averill, A.F., Ingram, J.M., Battersby, P. & Holborn, P.G. (2015). Ignition of flammable hydrogen in air (and other H2/N2/O2 mixtures) by mechanical stimuli. Part 3: Ignition under conditions of low sliding velocity (<0.8 m/s). *International Journal of Hydrogen Energy*, **40**, 9847–9853. 13, 38

Baldwin, N. (2003). Remediating Sellafield - A new focus for the site. In *Proceedings of Waste Management*, 1–9, Waste Management Symposia, Tucson. 5, 6, 7, 42

Barbian, N., Ventura-Medina, E. & Cilliers, J.J. (2003). Dynamic froth stability in froth flotation. *Minerals Engineering*, **16**, 1111–1116. 48

Barbian, N., Hadler, K., Ventura-Medina, E. & Cilliers, J.J. (2005). The froth stability column: Linking froth stability and flotation performance. *Minerals Engineering*, **18**, 317–324. 48, 66

Barnes, H.A. (1999). The yield stress – a review or '$\pi\alpha\nu\tau\alpha\ \rho\epsilon\iota$' – everything flows? *Journal of Non-Newtonian Fluid Mechanics*, **81**, 133–178. 46, 58

Barrett, P. & Glennon, B. (2002). Characterizing the metastable zone width and solubility curve using Lasentec FBRM and PVM. *Trans IChemE*, **80**, 799–805. 44

Barry, M.A., Boudreau, B.P., Johnson, B.D. & Reed, A.H. (2010). First-order description of the mechanical fracture behavior of fine-grained surficial marine sediments during gas bubble growth. *Journal of Geophysical Research: Earth Surface*, **115**, F04029. 28, 30, 39, 67

Bear, J. (1972). *Dynamics of Fluids in Porous Media*. Dover Civil and Mechanical Engineering Series, Dover Publications Inc., New York. 118

Bentz, D.P., Quenard, D.A., Kunzep, H.M., Baruchel, J., Peyrin, F., Martys, N.S. & Garboczi, E.J. (2000). Microstructure and transport properties of porous building materials . I1 : Three-dimensional X-ray tomographic studies. *Materials and Structures*, **33**, 147–153. 102

Berg, S., Ott, H., Klapp, S.A., Schwing, A., Neiteler, R., Brussee, N., Makurat, A., Leu, L., Enzmann, F., Schwarz, J.O., Kersten, M., Irvine, S. & Stampanoni, M. (2013). Real-time 3D imaging of Haines jumps in porous media flow. *Proceedings of the National Academy of Sciences*, **110**, 3755–3759. 3, 22, 92, 123

Beris, A., Tsamopoulos, J., Armstrong, R. & Brown, R. (1985). Creeping motion of a sphere through a Bingham plastic. *Journal of Fluid Mechanics*, **158**, 219. 33, 85

Best, A., Richardson, M., Boudreau, B., Judd, A., Leifer, I., Lyons, A., Martens, C., Orange, D. & Wheeler, S. (2006). Shallow seabed methane gas could pose coastal hazard. *Eos, Transactions American Geophysical Union*, **87**, 213–217. x, 2, 3, 21, 28, 67, 98, 122

Biggs, C.A. & Lant, P.A. (2000). Activated sludge flocculation: On-line determination of floc size and the effect of shear. *Water Research*, **34**, 2542–2550. 44

Biggs, S., Nabi, R. & Poole, C. (2007). The influence of zeta potential and yield stress on the filtration characteristics of a magnesium hydroxide simulant. In *Proceedings of the 11th International Conference on Environmental Remediation and Radioactive Waste Management: ICEM2007*, 1–7, Bruges. 49, 50

Bikerman, J.J. (1973). *Foams*. Springer Science & Business Media, New York. 48

Bird, B.R., Dai, G. & Yarusso, B.J. (1983). The rheology and flow of viscoplastic materials. *Reviews in Chemical Engineering*, **1**, 1–70. 59

Blackburn, D.R. & Thompson, E.J. (2013). The manufacture and use of sludge test materials for R&D purposes in the treatment and processing of magnox based sludge. In *Proceedings of ASME 15th International Conference on Environmental Remediation and Radioactive Waste Management*, vol. 1, V001T01A009, Brussels. 3, 42, 52

Boden, S., Bieberle, M. & Hampel, U. (2008). Quantitative measurement of gas hold-up distribution in a stirred chemical reactor using X-ray cone-beam computed tomography. *Chemical Engineering Journal*, **139**, 351–362. 102

Bolte, S. & Cordelières, F.P. (2006). A guided tour into subcellular colocalization analysis in light microscopy. *Journal of Microscopy*, **224**, 213–232. xiii, 72, 81, 82, 102, 113, 143

Boudreau, B.P. (2012). The physics of bubbles in surficial, soft, cohesive sediments. *Marine and Petroleum Geology*, **38**, 1–18. 3, 4, 22, 23, 24, 25, 29, 31, 39, 46, 52, 68, 85, 115, 134, 153

Boudreau, B.P., Gardiner, B.S. & Johnson, B.D. (2001). Rate of growth of isolated bubbles in sediments with a diagenetic source of methane. *Limnology and Oceanography*, **46**, 616–622. 14, 17, 86, 89

Boudreau, B.P., Algar, C., Johnson, B.D., Croudace, I., Reed, A., Furukawa, Y., Dorgan, K.M., Jumars, P.A., Grader, A.S. & Gardiner, B.S. (2005). Bubble growth and rise in soft sediments. *Geology*, **33**, 517–520. x, 2, 20, 21, 22, 25

Bowers, P.G., Hofstetter, C., Letter, C.R. & Toomey, R.T. (1995). Supersaturation limit for homogeneous nucleation of oxygen bubbles in water at elevated pressure: 'Superhenry's law'. *Journal of Physical Chemistry*, **99**, 9632–9637. 87

Bradford, P., Case, B., Dearnaley, G., Turner, J. & Woolsey, I. (1976). Ion beam analysis of corrosion films on a high magnesium allow (Magnox Al 80). *Corrosion Science*, **16**, 747–766. 14, 15, 16

Brakalov, L.B. (1985). On the mechanism of magnesium hydroxide ripening. *Chemical Engineering Science*, **40**, 305–312. 49

Broek, D. (1982). *Elementary Engineering Fracture Mechanics*. Martinus Nijhoff Publishers, The Hague. xi, 3, 25, 28, 29, 39

Brouwer, G.C., Wagner, E.C., van Ommen, J.R. & Mudde, R.F. (2012). Effects of pressure and fines content on bubble diameter in a fluidized bed studied using fast X-ray tomography. *Chemical Engineering Journal*, **207-208**, 711–717. 135

Bryan, S.A., Pederson, L.R. & Scheele, R.D. (1992). Crust growth and gas retention in synthetic Hanford waste. In *Proceedings of Waste Management*, vol. 1992, Tucson. 10, 37, 64, 78, 93

Burghard, H.C. (1974). The influence of precipitate morphology on microvoid growth and coalescence in tensile fractures. *Metallurgical Transactions*, **5**, 2083–2094. 111

Burrows, R., Harris, S. & Stevens, N.P.C. (2005). Corrosion electrochemistry of fuel element materials in pond storage conditions. *Chemical Engineering Research and Design*, **83**, 887–892. x, 5, 6, 15, 16, 25

Chadwick, P. (1959). The quasi-static expansion of a spherical cavity in metals and ideal soils. *Quarterly Journal of Mechanics and Applied Mathematics*, **12**, 52–71. 26, 154

Chan, Y.J., Chong, M.F., Law, C.L. & Hassell, D.G. (2009). A review on anaerobic-aerobic treatment of industrial and municipal wastewater. *Chemical Engineering Journal*, **155**, 1–18. 1

Chau, T.T. (2009). A review of techniques for measurement of contact angles and their applicability on mineral surfaces. *Minerals Engineering*, **22**, 213–219. 46

Chen, G., Flury, M., Harsh, J.B. & Lichtner, P.C. (2005). Colloid-facilitated transport of cesium in variably saturated Hanford sediments. *Environmental Science and Technology*, **39**, 3435–3442. 10

Christensen, T., Panikov, N., Mastepanov, M., Joabsson, A., Stewart, A., Öquist, M., Sommerkorn, M., Reynaud, S. & Svensson, B. (2003). Biotic controls on CO2 and CH4 exchange in wetlands – a closed environment study. *Biogeochemistry*, **64**, 337–354. 17, 31

Constantinescu, C.C. & Mukherjee, J. (2009). Performance evaluation of an Inveon PET preclinical scanner. *Physics in Medicine and Biology*, **54**, 2885–2899. 3, 92, 98

Crank, J. (1979). *The Mathematics of Diffusion*. Oxford university press, London. 106, 121

Crill, P.M. & Martens, C.S. (1986). Methane production from bicarbonate and acetate in an anoxic marine sediment. *Geochimeca et Cosmochimica Acta*, **50**, 2089–2097. 17

Cronin, J. & Collier, N. (2012). Corrosion and expansion of grouted Magnox. *Mineralogical Magazine*, **76**, 2901–2909. 7

Delegard, C.H., Sinkov, S.I., Chenault, J.W., Schmidt, A.J., Welsh, T.L. & Pool, K.N. (2014). Determination of uranium metal concentration in irradiated fuel storage basin sludge using selective dissolution. *Journal of Radioanalytical and Nuclear Chemistry*, **299**, 1871–1882. 1, 9

Deng, Y., Harsh, J.B., Flury, M., Young, J.S. & Boyle, J.S. (2006). Mineral formation during simulated leaks of Hanford waste tanks. *Applied Geochemistry*, **21**, 1392–1409. 10

Derkach, S.R., Krägel, J. & Miller, R. (2009). Methods of measuring rheological properties of interfacial layers (Experimental methods of 2D rheology). *Colloid Journal*, **71**, 1–17. 46, 47

Diggle, A. (2012). Formation and persistence of dried regions of MSSS waste (Technical report #35/089/76). Tech. rep., Sellafield Ltd., Seascale. 18

Disselhorst, J.a., Brom, M., Laverman, P., Slump, C.H., Boerman, O.C., Oyen, W.J.G., Gotthardt, M. & Visser, E.P. (2010). Image-quality assessment for several positron emitters using the NEMA NU 4-2008 standards in the Siemens Inveon small-animal PET scanner. *Journal of Nuclear Medicine*, **51**, 610–617. 92

Dobson, K.J., Coban, S.B., McDonald, S.A., Walsh, J.N., Atwood, R.C. & Withers, P.J. (2016). 4-D imaging of sub-second dynamics in pore-scale processes using real-time synchrotron X-ray tomography. *Solid Earth*, **7**, 1059–1073. 3, 22

D'Orazio, F., Tarczon, J.C., Halperin, W.P., Eguchi, K. & Mizusaki, T. (1989). Application of nuclear magnetic resonance pore structure analysis to porous silica glass. *Journal of Applied Physics*, **65**, 742–751. 98, 99

Dorgan, K.M., Jumars, P.A., Johnson, B., Boudreau, B.P. & Landis, E. (2005). Burrow extension by crack propagation. *Nature*, **433**, 475. 22, 25, 27, 34, 97, 147, 155

Draganic, Z. & Draganic, I. (1971). Molecular hydrogen in the gamma-Radiolysis of neutral aqueous solutions. *The Journal of Physical Chemistry*, **75**, 3950–3957. 17

Dubash, N. & Frigaard, I. (2004). Conditions for static bubbles in viscoplastic fluids. *Physics of Fluids*, **16**, 4319–4330. 3, 31, 32, 33, 41, 90, 125, 144

Dubash, N. & Frigaard, I.A. (2007). Propagation and stopping of air bubbles in Carbopol solutions. *Journal of Non-Newtonian Fluid Mechanics*, **142**, 123–134. 19, 32, 33, 75, 85, 90, 97

Dzaugis, M.E., Spivack, A.J. & D'Hondt, S. (2015). A quantitative model of water radiolysis and chemical production rates near radionuclide-containing solids. *Radiation Physics and Chemistry*, **115**, 127–134. 17

Dzuy, N.Q. & Boger, D.V. (1985). Direct yield stress measurement with the vane method. *Journal of Rheology*, **29**, 335–347. 45, 57

Evans, J.W., Abbasi, M.H. & Sarin, A. (1980). A Monte Carlo simulation of the diffusion of gases in porous solids. *Journal of Chemical Physics*, **72**, 2967–2973. 105

Fairhall, G. & Palmer, J. (1992). The encapsulation of Magnox swarf in cement in the United Kingdom. *Cement and Concrete Research*, **22**, 293–298. 1, 5, 6, 7

Faraggi, M. (1973). On the molecular hydrogen formation in the gamma radiolysis of water and aqueous solutions. *International Journal for Radiation Physics and Chemistry*, **5**, 197–206. 16, 17

Forepoint Ltd. (2016). Magnox Swarf Storage Silos. x, 6

Fraggedakis, D., Dimakopoulos, Y. & Tsamopoulos, J. (2016). Yielding the yield stress analysis: A thorough comparison of recently proposed elasto-visco-plastic (EVP) fluid models. *Journal of Non-Newtonian Fluid Mechanics*, **238**, 170–188. 40, 60, 65

Frank, X., Charpentier, J.C., Ma, Y., Midoux, N. & Li, H.Z. (2012). A multiscale approach for modeling bubbles rising in non-Newtonian fluids. *Industrial and Engineering Chemistry Research*, **51**, 2084–2093. 69

Froessling, N. (1938). Über die verdunstung fallender tropfen. *Gerlands Beiträge zur Geophysik*, **52**, 170–215. 91

Fryer, M., O'Flaherty, E. & Gray, N.F. (2011). Evaluating the measurement of activated sludge foam potential. *Water*, **3**, 424–444. xi, 46, 47, 48, 93

Gardiner, B.S., Boudreau, B.P. & Johnson, B.D. (2003). Growth of disk-shaped bubbles in sediments. *Geochimica et Cosmochimica Acta*, **67**, 1485–1494. 2, 4, 28, 39, 87

Gauglitz, P., Rassat, S., Powell, M., Shah, R. & Mahoney, L.A. (1995). Gas bubble retention and its effects on waste properties: retention mechanisms , viscosity, and tensile and shear strengths, PNNL-10740. Tech. rep., Pacific Northwest National Laboratory, Richmond, WA. 29

Gauglitz, P., Buchmiller, W., Probert, S., Owen, A. & Brockman, F. (2012). Strong-sludge gas retention and release mechanisms in clay simulants, PNNL-21167. Tech. rep., Pacific Northwest National Laboratory, Richmond, WA. x, 21, 22, 153

Gauglitz, P.A. & Radke, C.J. (1989). Dynamics of Haines jumps for compressible bubbles in constricted capillaries. *AIChE Journal*, **35**, 230–240. 123

Gauglitz, P.A., St. Laurent, C.M. & Radke, C.J. (1988). Experimental determination of gas-bubble breakup in a constricted cylindrical capillary. *Industrial and Engineering Chemistry Research*, **27**, 1282–1291. 11

Gauglitz, P.A., Bontha, J.R., Daniel, R.C., Mahoney, L.A., Rassat, S.D., Wells, B.E., Bao, J., Boeringa, G.K., Buchmiller, W.C. & Burns, C.A. (2015). *Hydrogen gas retention and release from WTP vessels: summary of preliminary studies*, vol. 24255. Pacific Northwest National Laboratory, Richmond, WA. xi, xvi, 12, 36, 37, 59, 61, 68, 69, 85, 124

Gephart, R.E. & Lundgren, R.E. (1998). *Hanford tank cleanup: a guide to understanding the technical issues*. Battelle Press, Columbus, OH (United States). 10

Gerber, M. (2008). The sludge cleanout of Hanford's K basins. *Radwaste Solutions*, **15**, 20–31. 9

Gogo, S., Guimbaud, C., Laggoun-Défarge, F., Catoire, V. & Robert, C. (2011). In situ quantification of CH4 bubbling events from a peat soil using a new infrared laser spectrometer. *Journal of Soils and Sediments*, **11**, 545–551. 31

Goñi, C., Jeldres, R.I., Toledo, P.G., Stickland, A.D. & Scales, P.J. (2015). A non-linear viscoelastic model for sediments flocculated in the presence of seawater salts. *Colloids and Surfaces A: Physicochemical and Engineering Aspects*, **482**, 500–506. 46

Goossens, D. (2008). Techniques to measure grain-size distributions of loamy sediments: A comparative study of ten instruments for wet analysis. *Sedimentology*, **55**, 65–96. 44

Greaves, D., Boxall, J., Mulligan, J., Montesi, A., Creek, J., Dendy Sloan, E. & Koh, C.A. (2008). Measuring the particle size of a known distribution using the focused beam reflectance measurement technique. *Chemical Engineering Science*, **63**, 5410–5419. 44

Gregson, C.R., Goddard, D.T., Sarsfield, M.J. & Taylor, R.J. (2011). Combined electron microscopy and vibrational spectroscopy study of corroded Magnox sludge from a legacy spent nuclear fuel storage pond. *Journal of Nuclear Materials*, **412**, 145–156. x, 1, 5, 7, 8, 9, 25, 50, 52, 64, 65, 126

Guadarrama-lara, R., Jia, X. & Fairweather, M. (2015). A meso-scale model for fluid-microstructure interactions. *Procedia Engineering*, **102**, 1356–1365. 103

Guan, Y., Guadarrama-lara, R., Jia, X., Zhang, K. & Wen, D. (2017). Lattice Boltzmann simulation of flow past a non-spherical particle. *Advanced Powder Technology*, **28**, 1486–1494. xiv, 103, 104

Hamill, H. (1970). Evidence for very early effects in the radiolysis of water. *Journal of Physical Chemistry*, **74**, 3914–3924. 16, 17

Hastings, J.J., Rhodes, D., Fellerman, A.S., McKendrick, D. & Dixon, C. (2007). New approaches for sludge management in the nuclear industry. *Powder Technology*, **174**, 18–24. x, 1, 2, 5, 6, 7, 8, 9, 25, 38, 76, 126

Hayon, E. & Moreau, M. (1965). Reaction mechanism leading to the formation of molecular hydrogen in the radiation chemistry of water. *Journal of Physical Chemistry*, **69**, 4058–4062. 16, 17

Henrist, C., Mathieu, J., Vogels, C., Rulmont, A. & Cloots, R. (2003). Morphological study of magnesium hydroxide nanoparticles precipitated in dilute aqueous solution. *Journal of Crystal Growth*, **249**, 321–330. xviii, 54, 55, 56

HidalgoAlvarez, R., Martin, A., Fernandez, A., Bastos, D., Martinez, F. & DelasNieves, F.J. (1996). Electrokinetic properties, colloidal stability and aggregation kinetics of polymer colloids. *Adv. Colloid Interface Sci.*, **67**, 1–118. 43

Hirschfelder, J.O., Curtiss, C.F. & Bird, R.B. (1954). *Molecular Theory of Gases and Liquids*. John Wiley & Sons, Inc., New York. 119

Horsley, D. & Hallington, P. (2005). Nuclear power and the management of the radioactive waste legacy. *Chemical Engineering Research and Design*, **83**, 773–776. 5

Hunter, T., Biggs, S., Young, J., Fairweather, M. & Peakall, J. (2011). Ultrasonic techniques for the in situ characterization of nuclear waste sludges. In *Waste Management, Phoenix*, vol. 2011. 2, 39, 61, 70, 76

Hunter, T.N., Wanless, E.J. & Jameson, G.J. (2009). Effect of esterically bonded agents on the monolayer structure and foamability of nano-silica. *Colloids and Surfaces A: Physicochemical and Engineering Aspects*, **334**, 181–190. 46, 62, 63, 64, 65

Ibusuki, T. & Aneja, V.P. (1984). Mass transfer of ammonia into water at environmental concentrations. *Chemical Engineering Science*, **39**, 1143–1155. 91

Ingram, J.M., Averill, A.F., Battersby, P.N., Holborn, P.G. & Nolan, P.F. (2014). Electrostatic ignition of sensitive flammable mixtures: Is charge generation due to bubble bursting in aqueous solutions a credible hazard? *Process Safety and Environmental Protection*, **2**, 750–759. 13

Jackson, S.F., Monk, S.D. & Riaz, Z. (2014). An investigation towards real time dose rate monitoring, and fuel rod detection in a First Generation Magnox Storage Pond (FGMSP). *Applied Radiation and Isotopes*, **94**, 254–259. 5, 6

Jaeger, F., Bowe, S., Van As, H. & Schaumann, G.E. (2009). Evaluation of 1H NMR relaxometry for the assessment of pore-size distribution in soil samples. *European Journal of Soil Science*, **60**, 1052–1064. 99

Jain, A.K. & Juanes, R. (2009). Preferential mode of gas invasion in sediments: grain-scale mechanistic model of coupled multiphase fluid flow and sediment mechanics. *Journal of Geophysical Research: Solid Earth*, **114**, B08101. 3, 4, 20, 25, 41, 110, 142

Jeldres, R.I., Toledo, P.G., Concha, F., Stickland, A.D., Usher, S.P. & Scales, P.J. (2014). Impact of seawater salts on the viscoelastic behavior of flocculated mineral suspensions. *Colloids and Surfaces A: Physicochemical and Engineering Aspects*, **461**, 295–302. 46, 60

Jia, X., Wedlock, D.J. & Williams, R.A. (2000). Simulation of simultaneous aggregation and sedimentation. *Minerals Engineering*, **13**, 1349–1360. 105

Johnson, B.D., Boudreau, B.P., Gardiner, B.S. & Maass, R. (2002). Mechanical response of sediments to bubble growth. *Marine Geology*, **187**, 347–363. 1, 3, 4, 19, 25, 27, 28, 29, 30, 39, 40, 92, 95, 98, 109, 154

Johnson, M., Peakall, J., Fairweather, M., Biggs, S., Harbottle, D. & Hunter, T.N. (2017). Yield stress dependency on the evolution of bubble populations generated in consolidated soft sediments. *AIChE Journal*, **63**, 3728–3742. 124

Kam, S. & Rossen, W. (1999). Anomalous capillary pressure, stress, and stability of solids-coated bubbles. *Journal of Colloid and Interface Science*, **213**, 329–339. 4, 23, 41, 64, 93, 109

Kam, S.I., Gauglitz, P.A. & Rossen, W.R. (2001a). Effective compressibility of a bubbly slurry. I. Theory of the behavior of bubbles trapped in porous media. *Journal of Colloid and Interface Science*, **241**, 248–259. 1

Kam, S.I., Gauglitz, P.A. & Rossen, W.R. (2001b). Effective compressibility of a bubbly slurry. II. Fitting numerical results to field data and implications. *Journal of Colloid and Interface Science*, **241**, 260–268. x, xi, 1, 2, 3, 4, 10, 11, 23, 24, 39, 46, 123

Kaptay, G. (2006). On the equation of the maximum capillary pressure induced by solid particles to stabilize emulsions and foams and on the emulsion stability diagrams. *Colloids and Surfaces A: Physicochemical and Engineering Aspects*, **282-283**, 387–401. 64

Kapur, J.N., Sahoo, P.K. & Wong, A.K.C. (1985). A new method for gray-level picture thresholding using the entropy of the histogram. *Computer Vision, Graphics, and Image Processing*, **29**, 273–285. 72

Katsman, R. (2015). Correlation of shape and size of methane bubbles in fine-grained muddy aquatic sediments with sediment fracture toughness. *Journal of Structural Geology*, **70**, 56–64. 2, 4, 28, 88, 95, 102

Katsman, R., Ostrovsky, I. & Makovsky, Y. (2013). Methane bubble growth in fine-grained muddy aquatic sediment: insight from modeling. *Earth and Planetary Science Letters*, **377-378**, 336–346. 1, 24, 31, 41, 91, 114

Keller, M. & Stallard, R.F. (1994). Methane emission by bubbling from Gatun Lake, Panama. *Journal of Geophysical Research: Atmospheres*, **99**, 8307–8319. xi, 1, 31, 33, 34, 39, 97

Kirby, C. (1987). Galvanic and crevice corrosion effects in Magnox A180 alloy. *Corrosion Science*, **27**. 15, 16

Knipe, R.J. (1981). The interaction of deformation and metamorphism in slates. *Tectonophysics*, **78**, 249–272. 54

Knollmeyer, P. (2006). Progress with K-basins sludge retrieval, stabilization and packaging at the Hanford nuclear site. In *Proceedings of Waste Management*, Tucson. 9

Kohan, L.M., Sanguanmith, S., Meesungnoen, J., Causey, P., Stuartb, C.R. & Jay-Gerin, J.P. (2013). Self-radiolysis of tritiated water. 1. A comparison of the effects of 60Co γ-rays and tritium β-particles on water and aqueous solutions at room temperature. *RSC Advances*, **3**, 19282–19299. 17

Komabayashi, T. & Spångberg, L.S.W. (2008). Comparative analysis of the particle size and shape of commercially available mineral trioxide aggregates and portland cement: a study with a flow particle image analyzer. *Journal of Endodontics*, **34**, 94–98. 44

Krieger, I.M., Wulholland, G.W. & Dickey, C.S. (1967). Diffusion coefficients for gases in liquids from the rates of solution of small gas bubbles. *J. Phys. Chem.*, **71**, 1123–1129. 114, 123

Krupka, K.M., Schaef, H.T., Arey, B.W., Heald, S.M., Deutsch, W.J., Lindberg, M.J. & Cantrell, K.J. (2006). Residual waste from Hanford tanks 241-C-203 and 241-C-204. 1. Solids characterization. *Environmental Science and Technology*, **40**, 3749–3754. 9

Kundu, S., Datta, A. & Hazra, S. (2005). Effect of metal ions on monolayer collapses. *Langmuir*, **21**, 5894–5900. 4, 46, 62

Laudone, G.M., Matthews, G.P. & Gane, P.A.C. (2008). Modelling diffusion from simulated porous structures. *Chemical Engineering Science*, **63**, 1987–1996. 105, 106

Lawson, C. & Hanson, R. (1974). *Solving Least Squares Problems.*. Prentice-Hall, Englewood Cliffs, New Jersey. 102, 115, 134

Le Clere, S. (2011). Magnox Swarf Storage Silo liquor effluent management: Sellafield site, Cumbria, UK. In *Proceedings of ASME 14th International Conference on Environmental Remediation and Radioactive Waste Management*, Parts A and B, 67–75, ASME, Reims. 6, 7, 38

Li, M. & Wilkinson, D. (2005). Determination of non-spherical particle size distribution from chord length measurements. Part 1: Theoretical analysis. *Chemical Engineering Science*, **60**, 3251–3265. 102, 115, 134

Liddell, P.V. & Boger, D.V. (1996). Yield stress measurements with the vane. *Journal of Non-Newtonian Fluid Mechanics*, **63**, 235–261. 59, 60

Lin, C., Videla, A. & Miller, J. (2010). Advanced three-dimensional multi-phase flow simulation in porous media reconstructed from X-ray Microtomography using the HeChenZhang Lattice Boltzmann Model. *Flow Measurement and Instrumentation*, **21**, 255–261. 103

Liu, L., Wilkinson, J., Buchmann, C. & Lorke, A. (2016). The role of sediment structure in gas bubble storage and release. *Journal of Geophysical Research: Biogeosciences*, **121**, 1992–2005. 20, 22, 24, 99

Liu, L., Kock, T.D., Wilkinson, J., Cnudde, V., Xiao, S., Buchmann, C., Uteau, D., Peth, S. & Lorke, A. (2018). Methane bubble growth and migration in aquatic sediments observed by micro-scale X-ray computed tomography. *Environmental Science & Technology*, **52**, 2007–2015. 20, 24

Lukens, W.W., Shuh, D.K., Schroeder, N.C. & Ashley, K.R. (2004). Identification of the non-pertechnetate species in Hanford waste tanks, Tc(I) - carbonyl complexes. *Environmental Science and Technology*, **38**, 229–233. 10

Maher, Z., Ivanov, P., O'Brien, L., Sims, H., Taylor, R.J., Heath, S.L., Livens, F.R., Goddard, D., Kellet, S., Rand, P. & Bryan, N.D. (2016). Americium and plutonium association with magnesium hydroxide colloids in alkaline nuclear industry process environments. *Journal of Nuclear Materials*, **468**, 84–96. 9

Mahmoodlu, M., Raoof, A., Sweijen, T. & van Genuchten, M.T. (2016). Effects of sand compaction and mixing on pore structure and the unsaturated soil hydraulic properties. *Vadose Zone Journal*, **15**, 1–11. 100, 131

Makar, G.L. (1990). Corrosion studies of rapidly solidified magnesium alloys. *Journal of The Electrochemical Society*, **137**, 414–421. 14, 15, 16

Martens, C. & Albert, D. (1995). Biogeochemical processes controlling concentrations and transport of biogenic methane in organic-rich coastal sediments. In T. Wever, ed., *Proceedings of the Workshop on Modelling Methane-Rich Sediments of Eckernförde Bay*, 10–17, Forschungs Bundeswehr Wasserschall Geophysik. 17

Martin Marietta Magnesia Specialities (2014). Magnesium hydroxide MSDS, CAS No. 1309-42-8. 42, 52

Mashal, K., Harsh, J.B., Flury, M., Felmy, A.R. & Zhaq, H. (2004). Colloid formation in Hanford sediments reacted with simulated tank waste. *Environmental Science and Technology*, **38**, 5750–5756. 10

Matsumoto, H., Maki, A., Shen, J.W. & Takeuchi, H. (2016). PM-07A non-linear discrete reconstruction method based on the gray-level quantization unit. *Microscopy*, **65**, i35.1–i35. 101, 127

Maurer, S., Gschwend, D., Wagner, E.C., Schildhauer, T.J., Ruud van Ommen, J., Biollaz, S.M. & Mudde, R.F. (2016). Correlating bubble size and velocity distribution in bubbling fluidized bed based on x-ray tomography. *Chemical Engineering Journal*, **298**, 17–25. 98

McCracken, G. & Eilbeck, M. (2005). Clean up progress on high hazard facilities at Sellafield: Magnox Swarf Storage Silos. In *Proceedings of ANS Topical Meeting on Decommissioning, Decontamination, and Reutilization*, vol. 2005, 161–167. 7, 25, 76

Menon, M., Yuan, Q., Jia, X., Dougill, A.J., Hoon, S.R., Thomas, A.D. & Williams, R.A. (2011). Assessment of physical and hydrological properties of biological soil crusts using X-ray microtomography and modeling. *Journal of Hydrology*, **397**, 47–54. 102, 103, 128

Mi, J., Tan, D. & Lee, T.L. (2014). In situ synchrotron x-ray study of ultrasound cavitation and its effect on solidification microstructures. *Metallurgical and Materials Transactions B*, **46**, 1615–1619. 92

Moreno-Atanasio, R., Williams, R.A. & Jia, X. (2010). Combining x-ray microtomography with computer simulation for analysis of granular and porous materials. *Particuology*, **8**, 81–99. 44, 103

Morris, J., Wickham, S., Richardson, P., Rhodes, C. & Newland, M. (2009). Contingency options for the drying, conditioning and packaging of Magnox spent fuel in the UK. In *Proceedings of The 12th International Conference on ICEM2009 Environmental Remediation and Radioactive Waste Management*, 1–7, Liverpool. 5, 6

Muddle, R.F. (2011). Bubbles in a fluidised bed: A fast x-ray scanner. *AIChE Journal*, **57**, 2684–2690. 2, 22

Mughrabi, H. (1992). *Plastic Deformation and Fracture of Materials*, vol. 6 of *Materials Science and Technology*. 25, 29, 97, 110

Mustaree, S., Meesungnoen, J., Butarbutar, S.L., Causey, P., Stuartc, C.R. & Jay-Gerin, J.P. (2014). Self-radiolysis of tritiated water. 1. A comparison of the effects of 60Co γ-rays and tritium β-particles on water and aqueous solutions at room temperature. *RSC Advances*, **4**, 43572–43581. 17

Nguyen, Q.D. & Boger, D.V. (1992). Measuring the flow properties of yield stress fluids. *Annual Review of Fluid Mechanics*, **24**, 47–88. 4, 58

Orr, R., Godfrey, H., Broan, C., Goddard, D., Woodhouse, G., Durham, P., Diggle, A. & Bradshaw, J. (2017). Kinetics of the reaction between water and uranium hydride prepared under conditions relevant to uranium storage. *Journal of Alloys and Compounds*, **695**, 3727–3735. 2, 13

Page, J.S., Reynolds, J.G., Ely, T.M. & Cooke, G.A. (2018). *Development of a Carbonate Crust on Alkaline Nuclear Waste Sludge at the Hanford Site*, vol. 342. Elsevier B.V. 10, 64, 78

Pamperin, O. & Rath, H.j. (1995). Influence of buoyancy on bubble formation at submerged orifices. *Chemcial Engineering Science*, **50**, 3009–3024. 32

Parry, S.a., O'Brien, L., Fellerman, A.S., Eaves, C.J., Milestone, N.B., Bryan, N.D. & Livens, F.R. (2011). Plutonium behaviour in nuclear fuel storage pond effluents. *Energy & Environmental Science*, **4**, 1462. 1, 5, 6, 7, 9, 126

Pastina, B. & Laverne, J.A. (2001). Effect of molecular hydrogen on hydrogen peroxide in water radiolysis. *Journal of Physical Chemistry A*, **105**, 9316–9322. x, 16, 17

Phillips, C. & Knollmeyer, P. (2006). Back to basins. *Nuclear Engineering International*, **51**, 22–26. 9

Pitois, O., Buisson, M. & Chateau, X. (2015). On the collapse pressure of armored bubbles and drops. *European Physical Journal E*, **38**, 1–7. 41, 46, 64, 65, 135

Potyondy, D.O. & Cundall, P.A. (2004). A bonded-particle model for rock. *International Journal of Rock Mechanics and Mining Sciences*, **41**, 1329–1364. 25

Prugue, X. (2013). Development of a mechanical based system for dry retrieval of single-shell tank waste at Hanford. In *Proceedings of ASME 15th International Conference on Environmental Remediation and Radioactive Waste Management*, 1–5, Brussels. 10

Pugh, R.J. (2007). Foaming in chemical surfactant free aqueous dispersions of anatase (titanium dioxide) particles. *Langmuir*, **23**, 7972–7980. 46, 48, 135

Quispe, J.R., Rozas, R.E. & Toledo, P.G. (2005). Permeability porosity relationship from a geometrical model of shrinking and lattice Boltzmann and Monte Carlo simulations of flow in two-dimensional pore networks. *Chemical Engineering Journal*, **111**, 225–236. xiv, 4, 103, 104, 105, 117

Raju, L.V.S. & Ramana, Y.V. (1986). Physical and elastic properties of marine sediments off Bombay, India. *Marine Geotechnology*, **6**, 359–375. 30

Ramesh, T.N. & Sreenivasa, V.P. (2015). Removal of indigo carmine dye from aqueous solution using magnesium hydroxide as an adsorbent. *Journal of Materials*, **2015**, 1–10. 54

Ransohoff, T.C., Gauglitz, P.A. & Radke, C.J. (1987). Snap-off of gas bubbles in smoothly constricted noncircular capillaries. *AIChE Journal*, **33**, 753–765. 111

Rassat, S., Caley, S., Bredt, P., Gauglitz, P., Rinehart, D. & Forbes, S. (1998). Mechanisms of gas retention and release: Experimental results for Hanford single-shell waste tanks 241-A-101, 241-S-106, and 241-U-103, PNNL-11981. Tech. rep., Pacific Northwest National Laboratory (PNNL), Richland, WA (US). 94

Rassat, S., Mahoney, L., Wells, B., Mendoza, D. & Caldwell, D. (2003). Assessment of physical properties of transuranic waste in Hanford single-shell tanks (PNNL tech. rep. no. 14221). Tech. Rep. March, Pacific Northwest National Laboratory (PNNL), Richland, WA (US). 10

Reddy, S.F., Monk, S.D., Nye, D.W., Colling, B.R. & Stanley, S.J. (2012). Proposal to characterise legacy Sellafield ponds using SONAR and RadLine. *Applied Radiation and Isotopes*, **70**, 1162–1165. 6

Reichenbacher, W., Müller, P. & Klemm, A. (1965). Diffusion von HT, DT und T2 in H2 und D2 bei 24C. *Z. Naturforschg.*, **20**, 1529–1536. 107, 122

Reynolds, C.A., Menke, H., Andrew, M., Blunt, M.J. & Krevor, S. (2017). Dynamic fluid connectivity during steady-state multiphase flow in a sandstone. *Proceedings of the National Academy of Sciences*, **114**, 8187–8192. 3, 22, 113, 123

Rossen, W.R. & Gauglitz, P.A. (1990). Percolation theory of creation and mobilization of foams in porous media. *AIChE Journal*, **36**, 1176–1188. 4

Saramito, P. (2009). A new elastoviscoplastic model based on the Herschel-Bulkley viscoplastic model. *Journal of Non-Newtonian Fluid Mechanics*, **158**, 154–161. 60, 65

Schindelin, J., Arganda-Carreras, I., Frise, E., Kaynig, V., Longair, M., Pietzsch, T., Preibisch, S., Rueden, C., Saalfeld, S., Schmid, B. & Tinevez, J.Y. (2012). Fiji: an open-source platform for biological-image analysis. *Nature Methods*, **9**, 676–682. 72, 102, 128

Schmidt, A.J. & Zacher, A.H. (2007). Composition and Technical Basis for K Basin Settler Sludge Simulant for Inspection, Retrieval, and Pump Testing (PNNL tech. rep. no. 16619 Rev. 1). Tech. rep. 9

Schott, H. (1981). Electrokinetic studies of magnesium hydroxide. *Journal of Pharmaceutical Sciences*, **70**, 486–489. 49

Schwartz, H.A. (1969). Applications of the spur diffusion model to the radiation chemistry of aqueous solutions. *The Journal of Physical and Colloid Chemistry*, **73**, 1928–1937. 16

Seland, J.G., Bruvold, M., Brurok, H., Jynge, P. & Krane, J. (2007). Analyzing equilibrium water exchange between myocardial tissue compartments using dynamical two-dimensional correlation experiments combined with manganese-enhanced relaxography. *Magnetic Resonance in Medicine*, **58**, 674–686. 100

Selomulya, C., Tran, T., Jia, X. & Williams, R. (2006). An integrated methodology to evaluate permeability from measured microstructures. *AIChE Journal*, **52**, 3394–3400. 2, 22, 98, 103, 105

Sherwood, D.J. & Eduardo Sáez, A. (2014). The start of ebullition in quiescent, yield-stress fluids. *Nuclear Engineering and Design*, **270**, 101–108. xvi, 1, 3, 17, 31, 33, 36, 39, 40, 59, 65, 68, 80, 97, 115, 122, 124, 135

Sherwood, J.D. & Meeten, G.H. (1991). The use of the vane to measure the shear modulus of linear elastic solids. *Journal of Non-Newtonian Fluid Mechanics*, **41**, 101–118. 61

Sills, G.C. & Gonzalez, R. (2001). Consolidation of naturally gassy soft soil. *Geotechnique*, **51**, 629–639. 1, 2

Singer, D.M., Zachara, J.M. & Brown, G.E. (2009). Uranium speciation as a function of depth in contaminated Hanford sediments - A micro-XRF, micro-XRD, and micro- and bulk-XAFS study. *Environmental Science and Technology*, **43**, 630–636. 9

Smith, B. (2006). Cleanup progress on high hazard legacy facilities at Sellafield: Magnox Swarf Storage Silos. In *Proceedings of Waste Management*, Waste Management Symposia, Tucson. 2, 7, 67

Sneddon, I. (1946). The distribution of stress in the neighbourhood of a crack in an elastic solid. In *Proceedings of the Royal Society of London A: Mathematical, Physical and Engineering Sciences*, vol. 187, 229–260, The Royal Society. 30

Sofrá, F. & Boger, D.V. (2002). Environmental rheology for waste minimisation in the minerals industry. *Chemical Engineering Journal*, **86**, 319–330. 61

Solbrig, C.W., Krsul, J.R. & Olsen, D.N. (1994). Pyrophoricity of uranium in long-term storage environments. In *Proceedings of Spent nuclear fuel meeting: challenges and initiatives*, USDoE, Washington, DC (United States), Salt Lake City. 2, 13

Song, X., Sun, S., Zhang, D., Wang, J. & Yu, J. (2011). Synthesis and characterization of magnesium hydroxide by batch reaction crystallization. *Chemical Engineering Science*, **5**, 416–421. 44, 54

Sperazza, M., Moore, J.N. & Hendrix, M.S. (2004). High-resolution particle size analysis of naturally occurring very fine-grained sediment through laser diffractometry. *Journal of Sedimentary Research*, **74**, 736–743. 44

Stakebake, J.L. (1981). Kinetic studies of the reaction of plutonium hydride with oxygen. *Nuclear Science and Engineering*, **78**, 386–392. 13

Stewart, C., Brewster, M., Gauglitz, P., Mahoney, L., Meyer, P., Recknagle, K. & Reid, H. (1996). Gas retention and release behavior in Hanford single-shell waste tanks, PNNL-11391. Tech. Rep. December, Pacific Northwest National Laboratory, Richmond, WA. xviii, 37, 38, 78, 80

Streatfield, R. & Hebditch, D. (2006). Gas generation in radioactive wastes-MAGGAS predictive life cycle model. In *Proceedings of Waste Management*, Waste Management Symposia, Tucson. 18

Succi, S. (2001). *The Lattice Boltzmann Equation: for Fluid Dynamics and Beyond*. Oxford University Press, Oxford. xiv, 103, 104

Takada, A. (1990). Experimental study on propagation of liquid-filled crack in gelatin: Shape and velocity in hydrostatic stress condition. *Journal of Geophysical Research: Solid Earth*, **95**, 8471–8481. 88

Tan, S.N., Pugh, R.J., Fornasiero, D., Sedev, R. & Ralston, J. (2005). Foaming of polypropylene glycols and glycol/MIBC mixtures. *Minerals Engineering*, **18**, 179–188. 46, 48

Terrones, G. & Gauglitz, P.A. (2003). Deformation of a spherical bubble in soft solid media under external pressure. *Quarterly Journal of Mechanics and Applied Mathematics*, **56**, 513–525. xi, 1, 3, 4, 12, 26, 27, 39, 41, 52, 60, 85, 92, 95, 109, 154

Totemeier, T.C. (2000). Characterization of uranium corrosion products involved in a uranium hydride pyrophoric event. *Journal of Nuclear Materials*, **278**, 301–311. 13

Tripathi, M.K., Sahu, K.C., Karapetsas, G. & Matar, O.K. (2015). Bubble rise dynamics in a viscoplastic material. *Journal of Non-Newtonian Fluid Mechanics*, **222**, 217–226. 19, 36, 39

Tsamopoulos, J., Dimakopoulos, Y., Chatzidai, N., Karapetsas, G. & Pavlidis, M. (2008). Steady bubble rise and deformation in Newtonian and viscoplastic fluids and conditions for bubble entrapment. *Journal of Fluid Mechanics*, **601**, 123–164. 32, 36

Uhlherr, P.H.T., Guo, J., Tiu, C., Zhang, X.M., Zhou, J.Z.Q. & Fang, T.N. (2005). The shear-induced solid-liquid transition in yield stress materials with chemically different structures. *Journal of Non-Newtonian Fluid Mechanics*, **125**, 101–119. 46, 60

van Kessel, T. & van Kesteren, W.G.M. (2002). Gas production and transport in artificial sludge depots. *Waste Management*, **22**, 19–28. xvi, 1, 3, 24, 25, 35, 39, 46, 61, 75, 76, 85, 92, 94, 97, 98, 109, 124, 125

Vidal, V., Soubiran, F., Divoux, T. & Géminard, J.C. (2011). Degassing cascades in a shear-thinning viscoelastic fluid. *Physical Review E*, **84**, 066302. 36

Villinger, C., Neusser, G., Kranz, C., Walther, P. & Mertens, T. (2015). 3D analysis of HCMV induced-nuclear membrane structures by FIB/SEM tomography: Insight into an unprecedented membrane morphology. *Viruses*, **7**, 5686–5704. 101, 127

Watson, J.H.P. & Ellwood, D.C. (2003). The removal of the pertechnetate ion and actinides from radioactive waste streams at Hanford, Washington, USA and Sellafield, Cumbria, UK: The role of iron-sulfide-containing adsorbent materials. *Nuclear Engineering and Design*, **226**, 375–385. 1, 5, 10

Weertman, J. (1971). Theory of water-filled crevasses in glaciers applied to vertical magma transport beneath oceanic ridges. *Journal of Geophysical Research*, **76**, 1171–1183. 88

Wells, B., J.J., J., Boeringa, G., Bauman, N., Guzman, A., Arduino, P. & Keller, P. (2010). Lateral earth pressure at rest and shear modulus measurements on Hanford sludge simulants (PNNL tech. rep. no. 19829). Tech. Rep. September, Pacific Northwest National Laboratory (PNNL), Richland, WA (US). 10, 30

Wheeler, S. (1990). Movement of large gas bubbles in unsaturated finegrained sediments. *Marine Geotechnology*, **9**, 113–129. 33

Wheeler, S., Sham, W. & Thomas, S. (1989). Gas pressure in unsaturated offshore soils. *Canadian Geotechnical Journal*, **27**, 79–89. xi, 24, 26, 27, 33

Wheeler, S.J. (1988a). A conceptual model for soils containing large gas bubbles. *Geotechnique*, **38**, 389–397. 1, 4, 24, 25, 46, 52, 98, 118, 134

Wheeler, S.J. (1988b). The undrained shear strength of soils containing large gas bubbles. *Géotechnique*, **38**, 399–413. 1

Wheeler, S.J. & Gardner, T.N. (1989). Elastic moduli of soils containing large gas bubbles. *Geotechnique*, **39**, 333–342. 1

Whitney, P., Meyer, P., Wilkins, N., Miller, N., Gao, F. & Wood, A. (1996). Flammable gas data evaluation progress report. Tech. Rep. PNNL-1373, Pacific Northwest National Laboratory. x, 10, 11, 12

Williams, G., Dafydd, H.A.L. & Grace, R. (2013). The localised corrosion of Mg alloy AZ31 in chloride containing electrolyte studied by a scanning vibrating electrode technique. *Electrochimica Acta*, **109**, 489–501. x, 15

Winter, E. (1950). Diffusion properties of gases: Part IV - The self-diffusion coefficients of nitrogen oxygen and carbon dioxide. *Transactions of the Faraday Society*, **47**, 342–347. 107, 114, 119

Winterwerp, J.C. & van Kesteren, W.G.M. (2004). *Introduction to the Physics of Cohesive Sediment Dynamics in the Marine Environment*, vol. 56 of *Developments in Sedimentology*. Elsevier, Amsterdam. 17, 122

Withers, P.J. (2015). Fracture mechanics by three-dimensional crack tip synchrotron x-ray microscopy. *Philosophical Transactions A*, **373**, 20130157. 111

Witwer, K. (2011). Preliminary demonstration of GeoMelt treatment of Hanford's K-basin sludge. In *Proceedings of the 14th International conference on Environmental Remediation and Radioactive Waste Management*, PARTS A AND B, 747–752, American Society of Mechanical Engineers - ASME; New York (United States), Reims. 10

Wu, M., Cheng, Z., Wu, J. & Wu, J. (2017). Precise simulation of long-term DNAPL migration in heterogeneous porous media based on light transmission micro-tomography. *Journal of Environmental Chemical Engineering*, **5**, 725–734. 113, 123

Xiao, D., Lu, Z., Jiang, S. & Lu, S. (2016). Comparison and integration of experimental methods to characterize the full-range pore features of tight gas sandstone – A case study in Songliao Basin of China. *Journal of Natural Gas Science and Engineering*, **34**, 1412–1421. 99, 100, 109, 129

Xiao, D., Jiang, S., Thul, D., Huang, W., Lu, Z. & Lu, S. (2017). Combining rate-controlled porosimetry and NMR to probe full-range pore throat structures and their evolution features in tight sands: A case study in the Songliao Basin, China. *Marine and Petroleum Geology*, **83**, 111–123. 4

Yao, Y. & Liu, D. (2012). Comparison of low-field NMR and mercury intrusion porosimetry in characterizing pore size distributions of coals. *Fuel*, **95**, 152–158. 100

Yao, Y.B., Liu, D.M., Cai, Y.D. & Li, J.Q. (2010). Advanced characterization of pores and fractures in coals by nuclear magnetic resonance and X-ray computed tomography. *Science China Earth Sciences*, **53**, 854–862. 44, 98, 99

Ybert, C., Lu, W., Möller, G. & Knobler, C.M. (2002). Collapse of a monolayer by three mechanisms. *Journal of Physical Chemistry B*, **106**, 2004–2008. 46, 62, 65

Yuan, F., Bennell, J.D. & Davis, A.M. (1992). Acoustic and physical characteristics of gassy sediments in the western Irish Sea. *Continental Shelf Research*, **12**, 1121–1134. 19

Zalc, M., Reyes, C. & Iglesia, E. (2003). Monte-Carlo simulations of surface and gas phase diffusion in complex porous structures. *Chemical Engineering Science*, **58**, 4605–4617. 105

zhong Li, J., gui Huang, J., wen Tian, Y. & sheng Liu, C. (2009). Corrosion action and passivation mechanism of magnesium alloy in fluoride solution. *Transactions of Nonferrous Metals Society of China (English Edition)*, **19**, 50–54. 45, 49, 50, 54, 65